PETROLEUM RESEARCH JOURNAL

TECHNICAL PAPERS

ENGINEERING

A study of vertical multiphase flow in some Libyan oil wells .....
H.H. Al-Attar and A.E. Abughalia 1

Hydrogen embrittlement in low carbon steels .....
H.L. Rizkalla and A. Abdulwahed 31

Fractography exhibited by hydrogen embrittled austenitic stainless steels
F.O. El-Shawesh 35

Nafoora-Augila unit: Reservoir performance and the role of granite productivity – A case study .....*N.A. Berruin and Y.S. Gherryo* 43

EXPLORATION

Enhancement of residual total aeromagnetic anomalies – Using the Hilbert transform ..... *M.R. Bakbak and N.L Mohan* 61

Probability of the validity of the rock component model in complex log interpretation ..... *G. Szigeti* 67

Cretaceous biostratigraphy and palaeogeography of north Egypt and northeast Libya ..... *M.I. Ibrahim, E. Schrank and M.R. Abdel-Kireem* 75

Fossil Phytoclasts in oils from Messlah and Bouri oil fields–Libya: A preliminary study ..... *R.N. Sinha and H.B. Eland* 95

CHEMISTRY

Possibility of manufacturing lube base stocks from Brega crude oil .....
I. Ahmad, A.A. Tuwil, M. Buseiffi, S. Dabah and A. Balat 101

SHORT NOTES

Oxygen causes corrosion failure of heat exchanger .....
M.L Mehta, T.S. El-Mendelssi and A.M. El-Houde 107

Lead levels in surface layers of nearshore sediments of the western coast of Libya .....
A.K. El Hinsheiry, N.S. Kumar, S.A. El Jawashi and I. Ahmad 111

VOLUME 7 - (1424)/(1995)

Petroleum Research Centre
P.O. Box 6431 Tripoli
Great Socialist People's Libyan Arab Jamahiriya

PRJ, Vol. 7 (January 1995); P. 1–30, 13 FIGS, 6 TABLES, 14 CHARTS.

A STUDY OF VERTICAL MULTIPHASE FLOW IN SOME LIBYAN OIL WELLS

H.H. Al-Attar* and A.E. Abughalia**

دراسة حول أدائية الرفع العمودي في بعض الآبار النفطية الليبيـة

حازم حسن العطار وأكرم الهاشمي أبوغالية

تتناول الدراسة أدائية السريان المتعدد الأطوار في ثمانية آبار نفطية يقع خمس منها في حقل بوالطفل وثلاثة في حقل الغاني.

ولتحقيق ذلك تم أولاً وضع برامج حاسوب خاصة لإختبار علاقة بوتيان وكاربنتر وعلاقة هاجدورن وبراون المعروفتين في الصناعة النفطية، باستخدام القياسات الحقلية المتوفرة لتلك الآبار. بعد ذلك استخدمت العلاقات في دراسة تاثير كل من قطر أنبوب الإنتاج واتجاه الحسابات الخاصة بمسار الضغط على أدائية الرفع العمودي وكذلك مساهمة كل حد في المعادلة العامة للطاقة على التدرج الكلي للضغط داخل أنبوب الإنتاج. كما تم تعديل هذه البرامج بهدف إعداد منحنيات ادائية جديدة خاصة بحقل بوالطفل، بحيث يمكن بواسطتها تنبوء ادائية الرفع العمودي في الآبار النفطية لهذا الحقل بدقة أكبر بالمقارنة مع منحنيات الأدائية المتوفرة في المراجع العلمية.

أشارت نتائج الحسابات إلى إمكانية زيادة معدل إنتاج البئر (A–55) في حقل بوالطفل إلى مستوى 6870 برميل لكل يوم باستخدام أنبوب انتاج بقطر 4 بوصة. كذلك وجد أن تأثير وزن الموائع المنتجة يشكل نسبة تتراوح ما بين 80 و90 بالمائة من الفاقد الكلي بالضغط ولجميع الحالات التي تم دراستها.

ABSTRACT

The purpose of this work is to study the performance of multiphase flow in five wells located in Abu-Attifel field and three oil wells located in El-Ghani field. Two computer programs are developed using the "C" Programming Language in an attempt to test the Hagedorn & Brown correlation and the Poettmann & Carpenter correlation, which are widely used in the petroleum industry, against actual field measurements. The two correlations are then used to investigate the effect of tubing size, direction of pressure traverse calculation, the contribution of each term in the general energy equation on the total pressure gradient.

The programs are then modified in order to produce a new set of working charts for Abu-Attifel oil field. The new charts can predict the vertical-lift performance in Abu-Attifel oil wells more accurately than those available in the literature simply because they exhibit a wider range of pressure, depth and production rate. The programs can further be used to produce working charts for any other oil field provided that some production data is available.

INTRODUCTION

Vertical multiphase flow is found in practically every tubing string used in the production of oil today (with the exception of off-shore wells). This fact emphasizes the importance of this topic and explains why it has been a matter of interest to many investigators. Although research in this topic started as early as 1914 by Davis and Weidner [1], it was only from 1952 when Poettmann and Carpenter published their paper [2], that most of the progress towards a solution to the problem of vertical multiphase flow has been made. Most of the approaches use some form of the general energy equation. Some of the correlations have contributed significantly to the ver-

*Petroleum Engineering Departement, Al-Fateh University, Tripoli, G.S.P.L.A.J.
**Schlumberger Co. Tripoli, G.S.P.L.A.J.

tical multiphase problem such as the correlations of Duns and Ros [3], Orkiszewski [4], Hagedorn and Brown [5], Beggs and Brill [6], Govier and Aziz [7] and the correlation of Poettmann and Carpenter. Others, such as Fancher and Brown [8], and Gilbert [9] contributed slightly to the solution of this problem, so as some earlier work by Hagedorn and Brown on viscous effects.

The pressure gradient (rate of change in pressure with respect to unit flow length) for vertical multiphase flow is the sum of three contributing factors: hydrostatic pressure gradient, friction pressure gradient, and acceleration pressure gradient. The effects of chemical reactions between the phases are neglected; however, such factors as viscosity, surface tension and density are included.

In this study, the vertical multiphase flow problem was considered. A two-component production system (tubing head pressure is constant) was assumed. The system consisted of the flow in the porous media, represented by the (I.P.R.) and the flow inside the well, governed by the vertical multiphase flow correlations. All vertical multiphase flow correlations involve lengthy calculations which consist of a series of steps that are repeated many times until the total depth of the well is reached. Hand calculations are very tedious, time consuming, and there is always the possibility of human error, which increases as the calculations are lengthened. Taking into consideration all the facts mentioned previously, it was necessary to develop efficient computer programs which would save time and effort in order to focus the work on the results, comparison, and discussion.

RESULTS AND COMPARISON OF CORRELATIONS

An essential part of this study is to gather a sufficient amount of actual field data in order to check the reliability of our computer programs, and also to compare between both correlations. Production data for eight wells, three wells located in El-Ghani field with the courtesy of Veba Oil Operations, and five wells located in Abu-Attifel field with the courtesy of Agip Oil Company (N.A.M.E.) were obtained. Although the number of wells is not large, the variation in the production data (production rate, depth, crude properties, etc.) compensated the lack of a large number of wells and served the purpose of this study. For instance the production rate ranged from approximately 400 bpd to 7000 bpd and the depth ranged from 6000 feet to 15000 feet.

The production data for all eight wells is listed in Table 1a and Table 1b. The wells in Abu-Attifel are A-1, A-3, A-27, A-52, and A-55, while those of El-Ghani are VVV5, RRR33, and RRR46.

Table 1a. Production Data for Five Wells in Abu-Attifel Field (Concession 100)-(Courtesy of Agip Oil Company (N.A.M.E)

WELL (A-1):

Description	Value
GOR (scf/stb)	1600.000
Oil Gravity (API)	40.000
Water Gravity	1.050
Gas Gravity	0.745
Oil Production Rate (bbl/day)	6905.00
Water Production Rate (bbl/day)	770.00
Tubing Head Pressure (psi)	1817.00
Depth (ft)	14060.00
Pressure Increment Below (1000)	50.00
Pressure Increment Above (1000)	100.00
Tubing Diameter (in)	3.5000
Surface Temperature (f)	220.0000
Bottom Hole Flowing Pressure(psi)	5540.0000
Pseudo critical pressure (psi)	410.0000
Pseudo critical temperature (f)	665.0000

WELL (A-3):

Description	Value
GOR (scf/stb)	1761.000
Oil Gravity (API)	40.000
Water Gravity	1.050
Gas Gravity	0.745
Oil Production Rate (bbl/day)	4099.00
Water Production Rate (bbl/day)	442.00
Tubing Head Pressure (psi)	1224.00
Depth (ft)	14356.00
Pressure Increment Below (1000)	50.00
Pressure Increment Above (1000)	100.00
Tubing Diameter (in)	3.5000
Surface Temperature (f)	212.0000
Bottom Hole Flowing Pressure(psi)	4423.0000
Pseudo critical pressure (psi)	422.0000
Pseudo critical temperature (f)	665.0000

WELL (A-27):

Description	Value
GOR (scf/stb)	2101.000
Oil Gravity (API)	40.000
Water Gravity	0.000
Gas Gravity	0.745
Oil Production Rate (bbl/day)	6782.00
Water Production Rate (bbl/day)	0.00
Tubing Head Pressure (psi)	1692.00
Depth (ft)	14500.00
Pressure Increment Below (1000)	100.00
Pressure Increment Above (1000)	100.00
Tubing Diameter (in)	3.5000
Surface Temperature (f)	220.0000
Bottom Hole Flowing Pressure(psi)	4776.0000
Pseudo critical pressure (psi)	415.0000
Pseudo critical temperature (f)	665.0000

WELL (A-52):

Description	Value
GOR (scf/stb)	1616.000
Oil Gravity (API)	40.000
Water Gravity	0.000
Gas Gravity	0.738
Oil Production Rate (bbl/day)	5430.00
Water Production Rate (bbl/day)	0.00
Tubing Head Pressure (psi)	1509.00
Depth (ft)	15132.00
Pressure Increment Below (1000)	50.00
Pressure Increment Above (1000)	100.00
Tubing Diameter (in)	3.5000
Surface Temperature (f)	220.0000
Bottom Hole Flowing Pressure(psi)	4949.0000
Pseudo critical pressure (psi)	405.0000
Pseudo critical temperature (f)	670.0000

WELL (A-55):

Description	Value
GOR (scf/stb)	1541.000
Oil Gravity (API)	40.000
Water Gravity	0.000
Gas Gravity	0.738
Oil Production Rate (bbl/day)	5441.00
Water Production Rate (bbl/day)	0.00
Tubing Head Pressure (psi)	1630.00
Depth (ft)	14153.00
Pressure Increment Below (1000)	50.00
Pressure Increment Above (1000)	100.00
Tubing Diameter (in)	3.5000
Surface Temperature (f)	212.0000
Bottom Hole Flowing Pressure(psi)	5051.0000
Pseudo critical pressure (psi)	405.0000
Pseudo critical temperature (f)	670.0000

Table 1b. Production Data for Three Wells in El-Ghani Field (Courtesy of Veba Oil Operations)

WELL (VVV5):

Description	Value
GOR (scf/stb)	475.000
Oil Gravity (API)	38.000
Water Gravity	0.000
Gas Gravity	1.055
Oil Production Rate (bbl/day)	1145.00
Water Production Rate (bbl/day)	0.00
Tubing Head Pressure (psi)	440.00
Depth (ft)	6004.00
Pressure Increment Below (1000)	50.00
Pressure Increment Above (1000)	100.00
Tubing Diameter (in)	3.5000
Surface Temperature (f)	1702.0000
Bottom Hole Flowing Pressure(psi)	500.0000
Pseudo critical pressure (psi)	650.0000
Pseudo critical temperature (f)	670.0000

WELL (RRR46):

Description	Value
GOR (scf/stb)	594.000
Oil Gravity (API)	38.000
Water Gravity	0.000
Gas Gravity	1.055
Oil Production Rate (bbl/day)	416.00
Water Production Rate (bbl/day)	0.00
Tubing Head Pressure (psi)	480.00
Depth (ft)	6142.00
Pressure Increment Below (1000)	50.00
Pressure Increment Above (1000)	100.00
Tubing Diameter (in)	3.5000
Surface Temperature (f)	100.0000
Bottom Hole Flowing Pressure(psi)	1681.0000
Pseudo critical pressure (psi)	500.0000
Pseudo critical temperature (f)	650.0000

WELL (RRR33):

Description	Value
GOR (scf/stb)	660.000
Oil Gravity (API)	38.000
Water Gravity	0.000
Gas Gravity	1.055
Oil Production Rate (bbl/day)	707.00
Water Production Rate (bbl/day)	0.00
Tubing Head Pressure (psi)	540.00
Depth (ft)	5916.00
Pressure Increment Below (1000)	50.00
Pressure Increment Above (1000)	100.00
Tubing Diameter (in)	3.5000
Surface Temperature (f)	100.0000
Bottom Hole Flowing Pressure(psi)	1660.0000
Pseudo critical pressure (psi)	500.0000
Pseudo critical temperature (f)	650.0000

In this study a representative well (A-55) is selected to show in detail the calculations involved in each application of the computer programs. The first step after the completion of the computer programs was to calculate the bottom hole flowing pressure (P_{wf}) starting with the tubing head pressure (P_{tf}) and vice versa for all eight wells, to check the reliability of these programs, and compare between the correlations. The results are presented in Table 2 and Table 3.

Table 2 shows the results when the calculations were carried out from top to bottom, starting with the actual tubing head pressure and calculating downwards until reaching the exact depth of the well to obtain a calculated value for (P_{wf}). The error percentage was calculated using the following relation:

$$\text{Error}(\%) = [(P_{wf}|_{cal} - P_{wf}|_{act})/P_{wf}|_{act}] * 100$$

Table 3 shows the result when the calculations were carried out from bottom to top, starting with the actual value of (P_{wf}) and calculating upward until reaching the surface to obtain a calculated value for (P_{tf}). The error percentage was calculated in the same manner as that of Table 2.

From Table 2 and Table 3, it is clear that the two computer programs function within an error range of 1 to 9 percent, which is considered adequate for this study. The cause of this error could be from number of reasons, error from the correlations themselves or from the available data or other technical problems in the tubing such as scale, paraffin, corrosion, etc. It is clear from the two Tables that the two correlations give close results for most of the wells. The Poettmann & Carpenter correlation yielded good results, especially for the Abu-Attifel wells for which the accuracy was very good (average error 2.38%). This is mainly due to the very high production rates which ensure an entirely turbulent flow that can be considered as one phase, but the results for the El-Ghani field were less accurate (average error 5.43%) probably because the flow rates ranged from 400 to 1000 bbl/day, which is considered low to intermediate. The Hagedorn & Brown correlation gave good results and consistent accuracy, for the Abu-Attifel field the average error was 4.25% and for the El-Ghani field the average was 4.51%. The main reason for this similarity in the error percentage is because the Hagedorn & Brown correlation is a generalized correlation with no specific conditions. An important point should be noted from Table 2, and that is the Hagedorn & Brown correlation always produced calculated values greater than the actual, contrary to the Poettmann & Carpenter correlation which under predicted the pressure in most cases.

EFFECT OF DIRECTION ON PRESSURE TRAVERSE

The first application was to show the effect of the direction of calculations on the pressure traverse for both methods.

The pressure traverse calculated in both directions using the Poettmann & Carpenter correlation, is shown in Fig. 1 while the pressure traverse calculated in both directions by the Hagedorn & Brown correlation, is plotted in Fig.2.

Figures 1 and 2 indicate that the plotted pressure traverse in both direction is different for both methods. The only explanation for this difference is that in each of the two directions, either an actual (P_{tf}) or (P_{wf}) value was chosen and the other was calculated. Since the two correlations do not give the exact pressure traverse (No correlation gives an exact pressure traverse), therefore it is impossible to obtain

Table 2. Results of Calculations when Carried out from Top to Bottom.

	HAGEDORN & BROWN			POETTMANN & CARPENTER		
WELL	CALCULATED Pwf (psi)	ACTUAL Pwf psi	ERROR %	CALCULATED Pwf psi	ACTUAL Pwf psi	ERROR %
A-1	5780	5540	4.34	5424	5540	-2.09
A-3	4649	4423	5.12	4517	4423	-2.13
A-27	5046	4776	5.65	4605	4776	-3.58
A-52	5185	4949	4.78	4799	4949	-3.03
A-55	5119	5051	1.36	4880	5051	-3.38
VVV5	1781	1702	4.68	1788	1702	5.05
RRR33	1736	1660	4.57	1759	1660	6.29
RRR46	1753	1681	4.28	1759	1681	4.64

Table 3. Results of Calculations when Carried Out from Bottom to Top.

	POETTMANN & CARPENTER			HAGEDORN & BROWN		
WELL	CALCULATED Ptf (psi)	ACTUAL Ptf psi	ERROR %	CALCULATED Ptf psi	ACTUAL Ptf psi	ERROR %
A-1	1670	1817	-4.09	1729	1817	-4.79
A-3	1130	1224	-7.68	1327	1224	8.41
A-27	1220	1492	-8.2	1624	1492	8.87
A-52	1347	1369	-1.6	1448	1369	5.77
A-55	1588	1630	-2.55	1714	1630	5.17
VVV5	417	440	-5.23	398	440	-9.42
RRR33	503	540	-6.75	506	540	6.29
RRR46	441	480	-8.13	438	480	8.69

the same results when starting with opposite points. Another important point concerning this difference in the plotted pressure traverses is the fact that empirical correlations were used to calculate crude properties such as (R_s) and (β_o), these correlations are functions of temperature and pressure, and give more accurate results when the temperature and pressure are low to intermediate. The pressure and temperature at the surface of the well under study are 1630 Psi and 212°F respectively while at the bottom are 5051 Psi and 288°F respectively. Therefore one would expect that the calculated values of (R_s) and

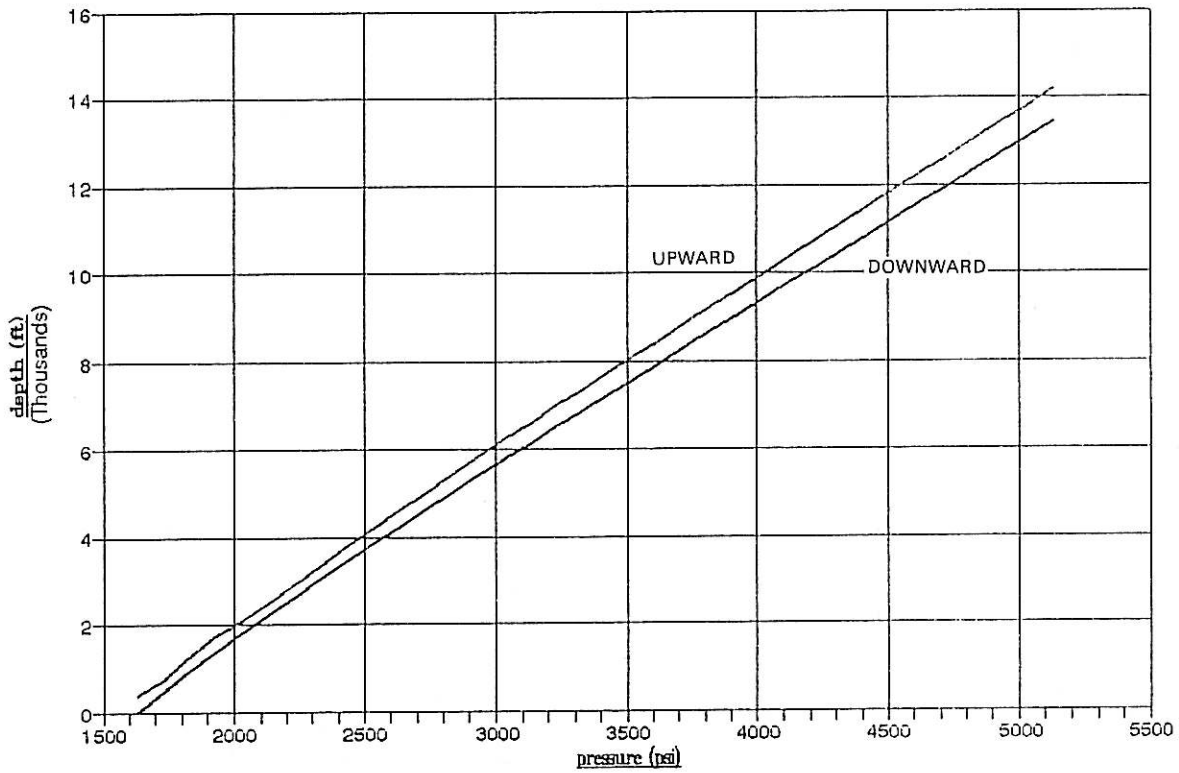


FIG. 1. Pressure traverse in both direction calculated by Poettmann and Carpenter method.

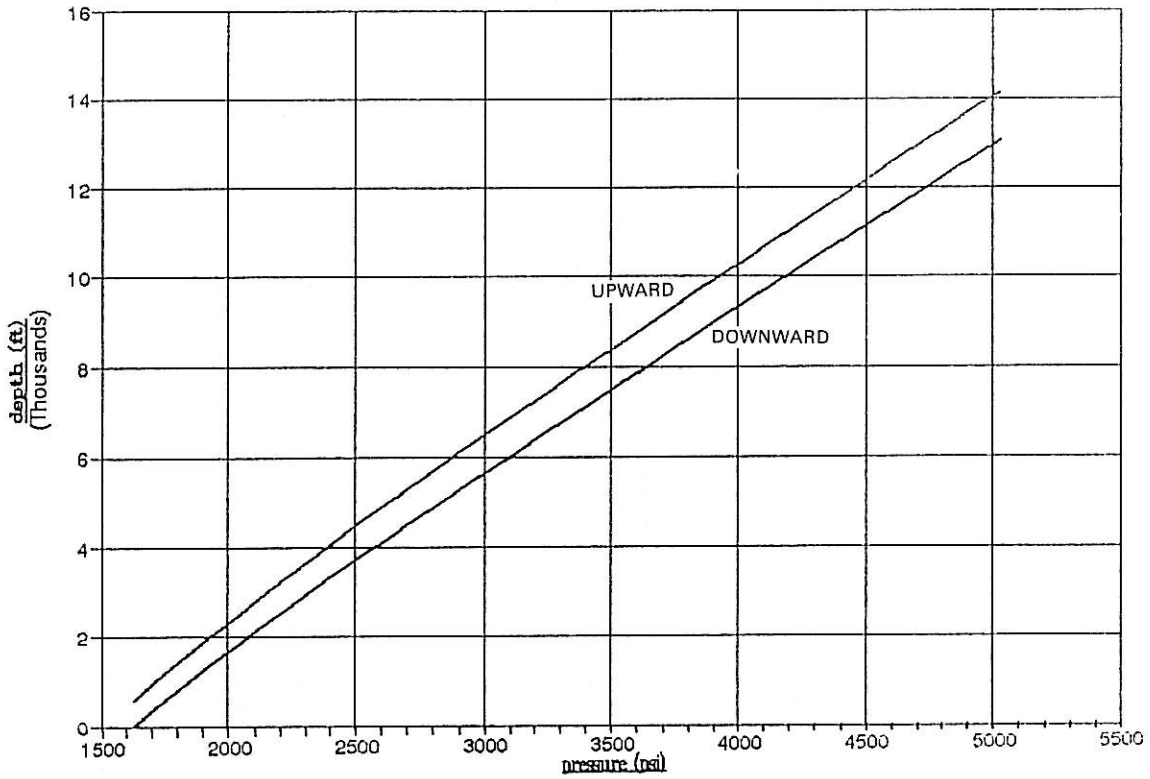


FIG. 2. Pressure traverse in both directions calculated by Hagedorn and Brown method.

(β_o) near the surface to be more accurate which leads to better calculation of the pressure traverse in a downward direction.

EFFECT OF ELEVATION, FRICTION AND ACCELERATION TERMS ON TOTAL PRESSURE LOSS

The second application of the computer programs is to determine the effect of the elevation, friction, and acceleration terms on the total pressure gradient and how much each term contributes to the total pressure loss. In doing so a better understanding of what causes the dissipation of the reservoir energy (pressure), how much is dissipated and where can be achieved. This would be very helpful in the analysis of the vertical multi-phase problem and would be a very useful tool in finding methods that would decrease this loss in vital energy.

The calculations for well (A-55) were carried out for each pressure increment, where the contribution was expressed in (Psi) and added to the actual tubing head pressure (P_{tf}) until the total depth of the well has been reached. At the end of the calculations, the contribution of each term to the total pressure loss is expressed in percentage.

The results from the Hagedorn and Brown correlation are shown in Figures 3a and 3b (Note: For Fig. 3a the contributions are expressed in (Psi) and they are cumulative starting with the actual tubing head pressure (P_{tf}), for Fig. 3b the contributions are represented in percentage of each pressure increment).

The results for the Poettmann & Carpenter correlation are plotted in Fig. 4a and Fig. 4b.

The results show that the predominant factor in the contribution to the total pressure loss is the elevation term. The friction term also has a significant effect, but the acceleration term is quite negligible for most cases. Although this case can be considered somewhat general, the percentages of each term differs from one case to the other depending on other variables such as flow rate, tubing size, and gas liquid ratios. To further express the effect of these variables, Fig. 5 and 6 show the effect of flow rate (for a constant GLR and the same tubing size 3.5 inch) on the total contribution of each term for the specified well (A-55) (Note: The total contribution for each term is expressed in percentage of the total pressure loss).

It is quite clear from Fig. 5 and Fig. 6, that an increase in flow rate means that the friction term becomes more effecting contrary to the elevation term whose influence decreases, but remains dominant. If the calculations were to be done on a smaller tubing size the friction term would have been increased and the elevation term would have been reduced even more. This effect is shown in Figs 7 and 8 where the tubing size is equal to 2.0 inch.

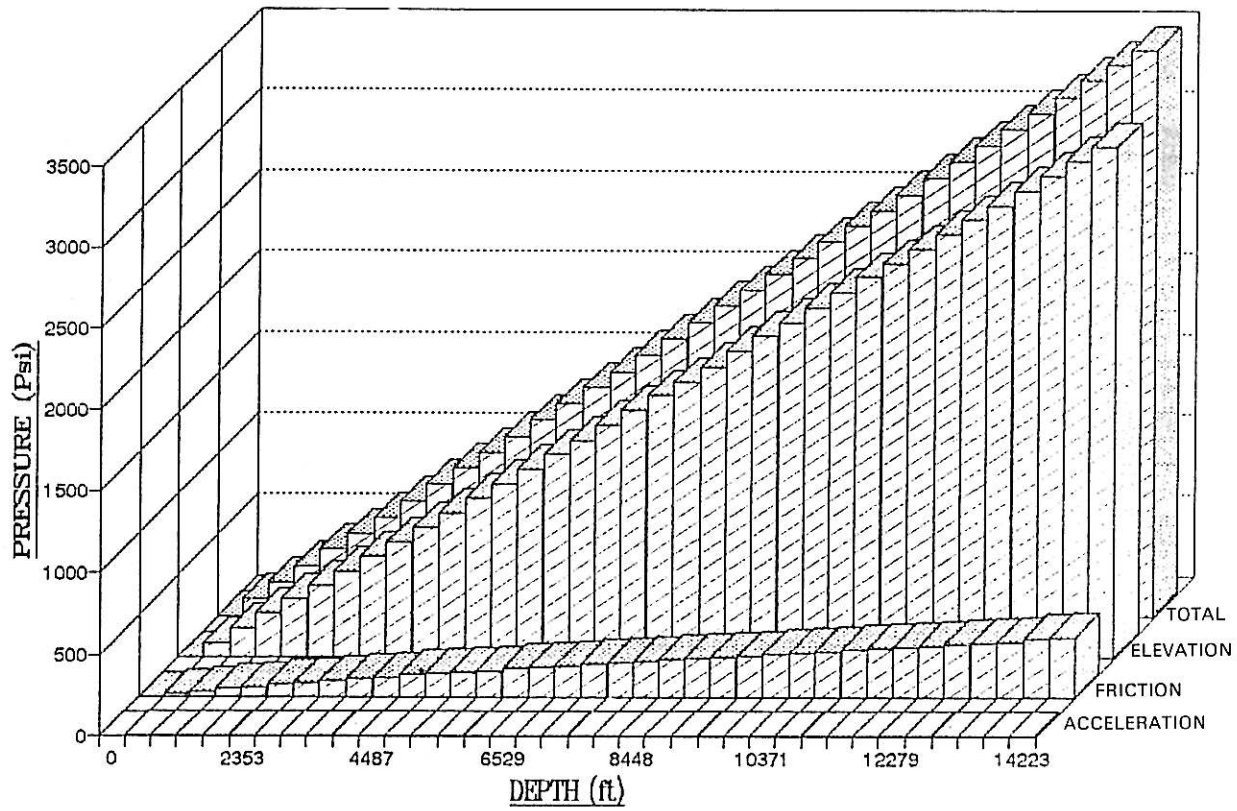


FIG. 3a. Pressure loss contributions by Hagedorn and Brown method.

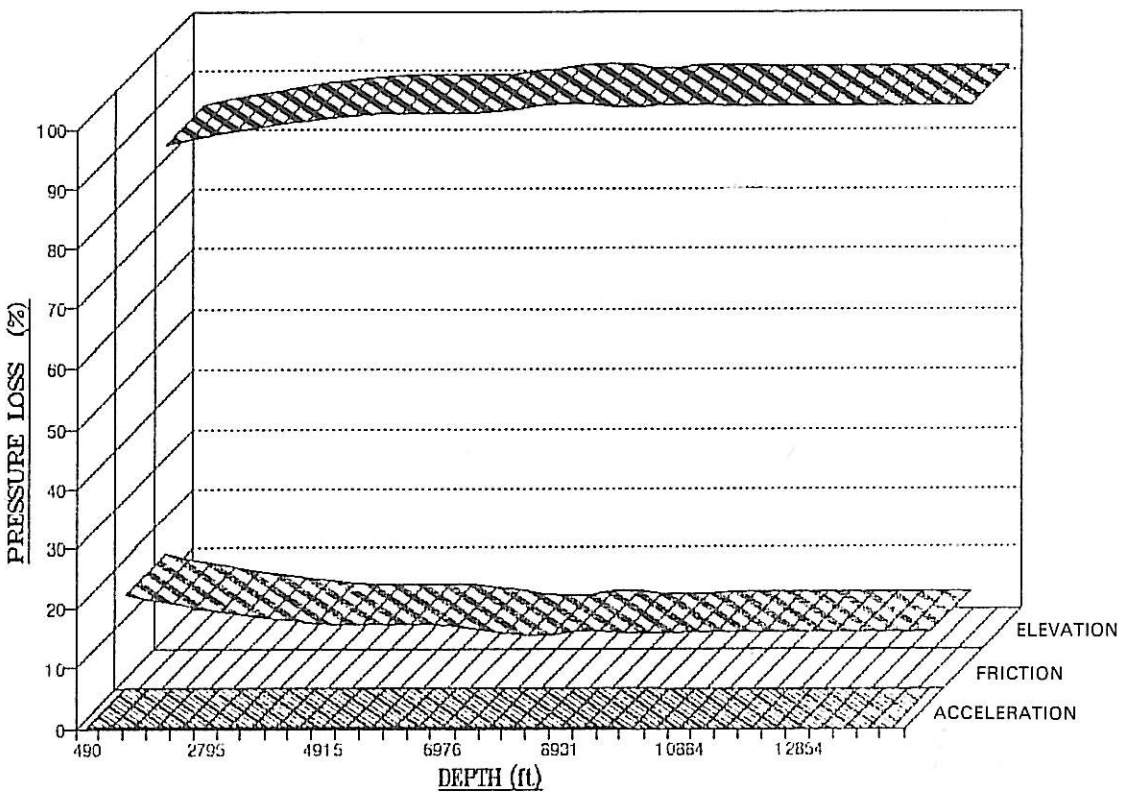


FIG. 3b. Pressure loss contributions as percent of total pressure loss by Hagedorn and Brown method.

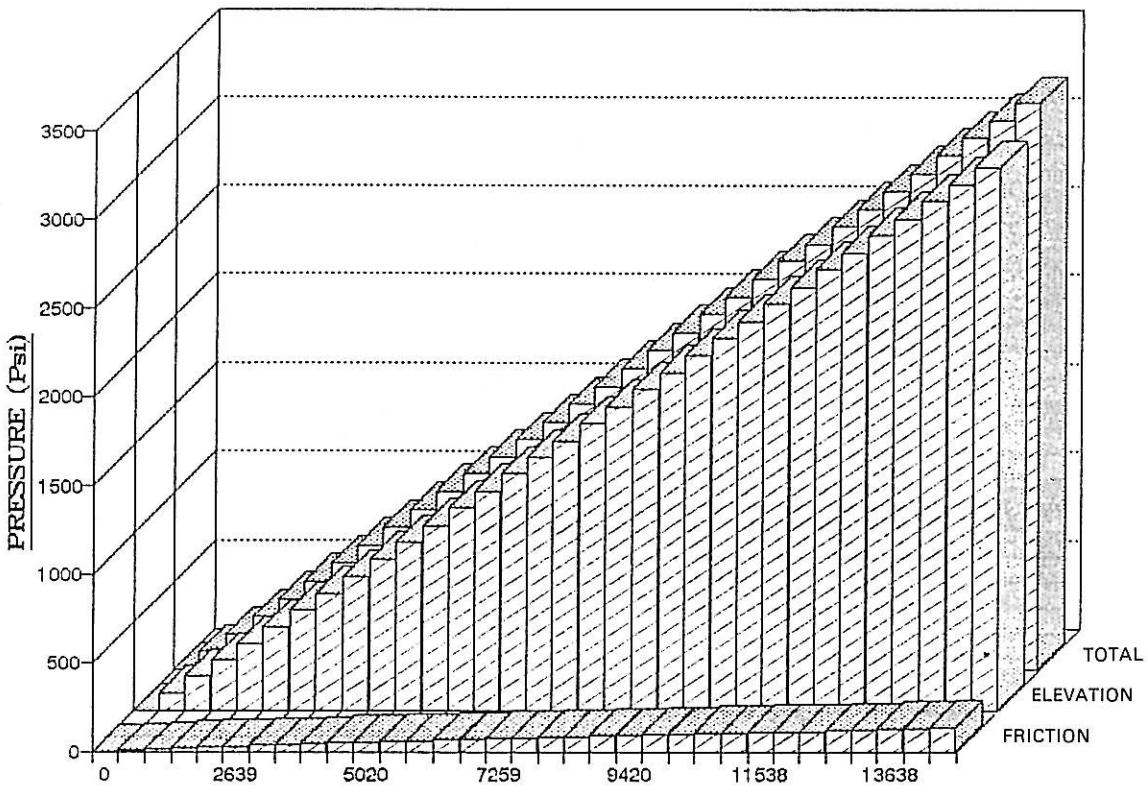


FIG. 4a. Pressure loss contributions by Poettmann and Carpenter method.

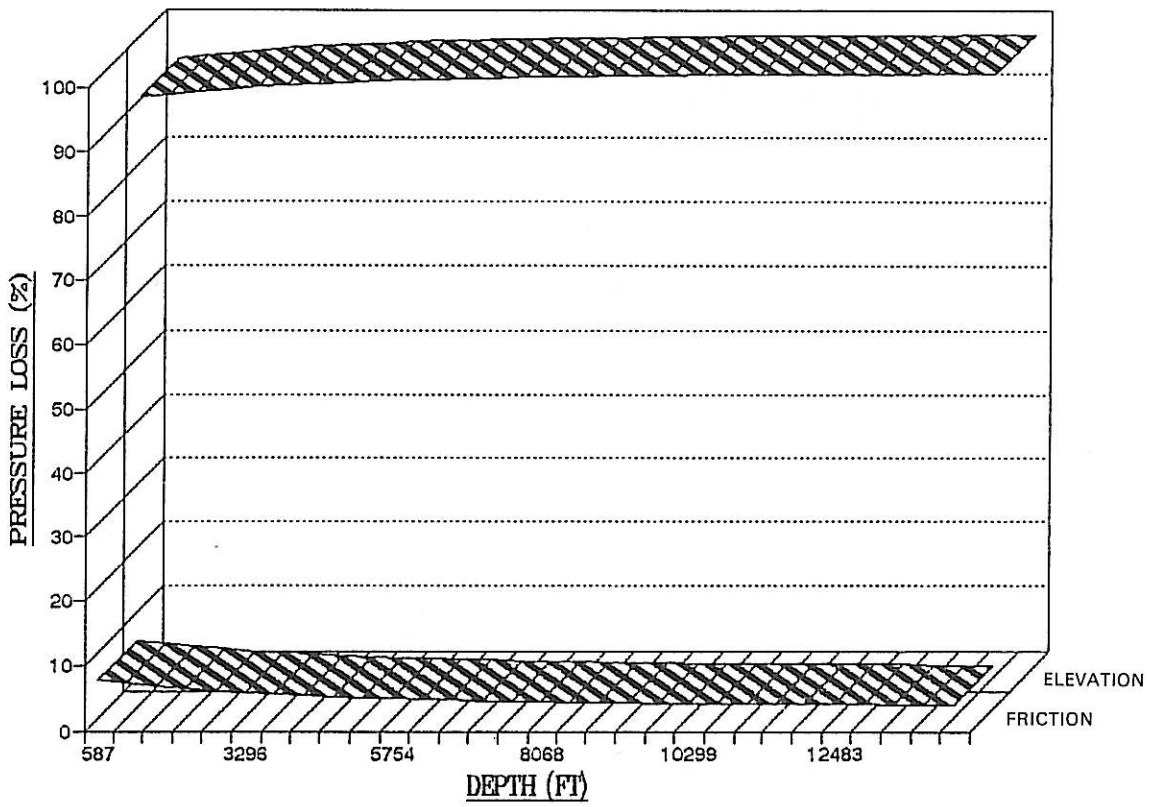


FIG. 4b. Pressure loss contributions as percent of total pressure loss by Poettmann and Carpenter method.

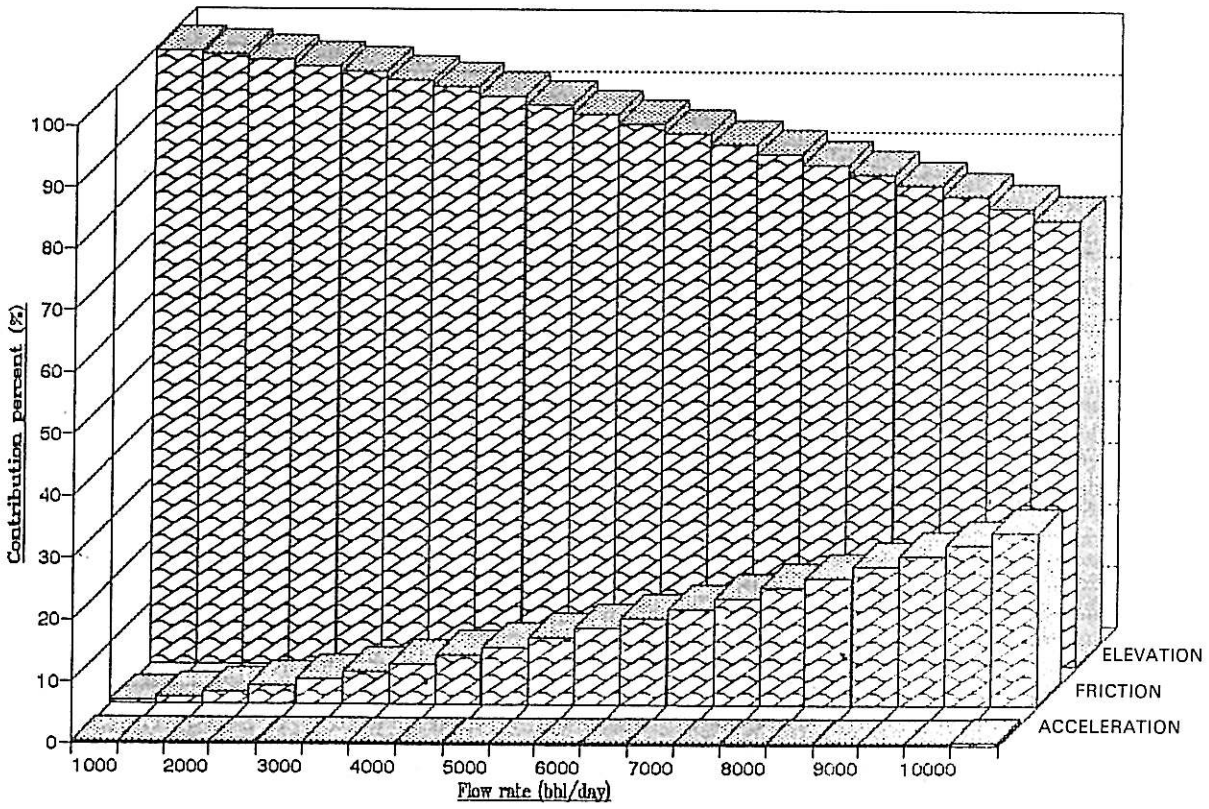


FIG. 5. Effect of flowrate on friction and elevation terms for tubing size of 3.5 inch (Poettmann and Carpenter).

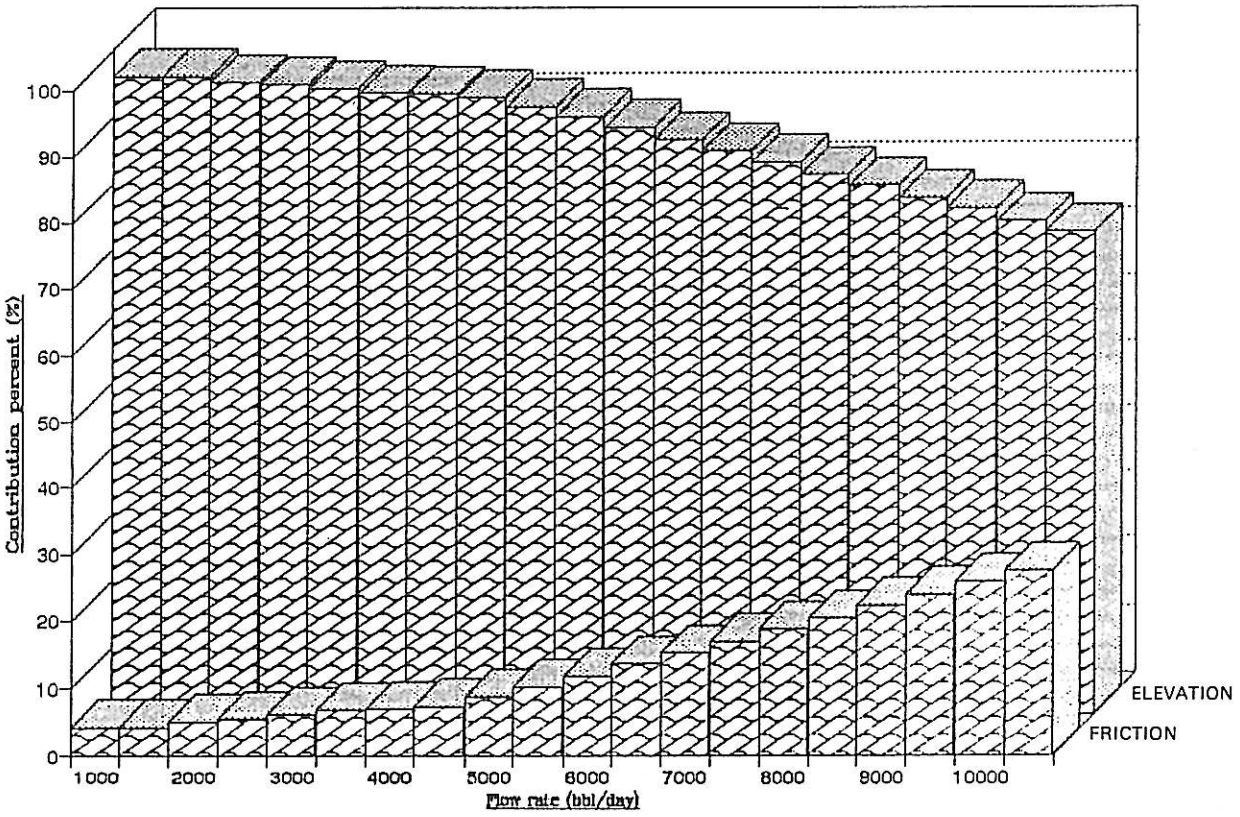


FIG. 6. Effect of flow rate on friction and elevation terms for tubing size of 3.5 inch (Hagedorn and Brown).

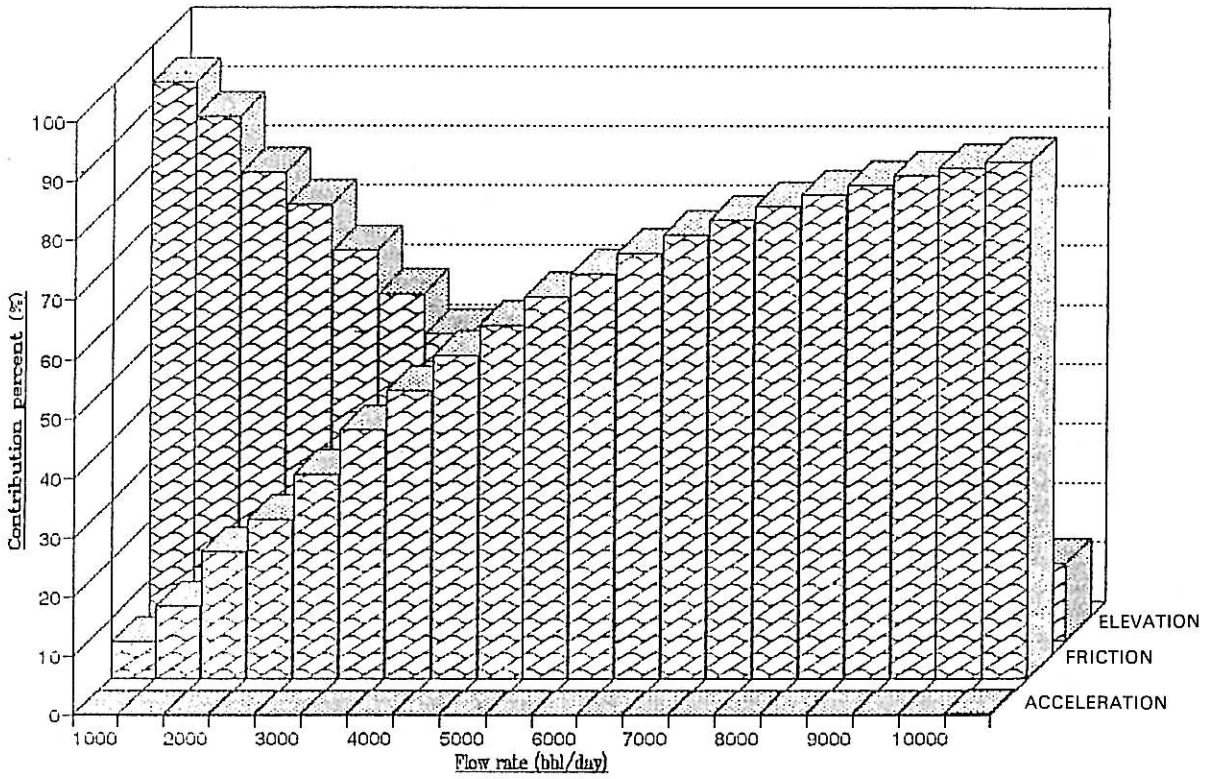


FIG. 7. Effect of flow rate on friction and elevation terms for tubing size of 2.0 inch (Poettmann and Carpenter).

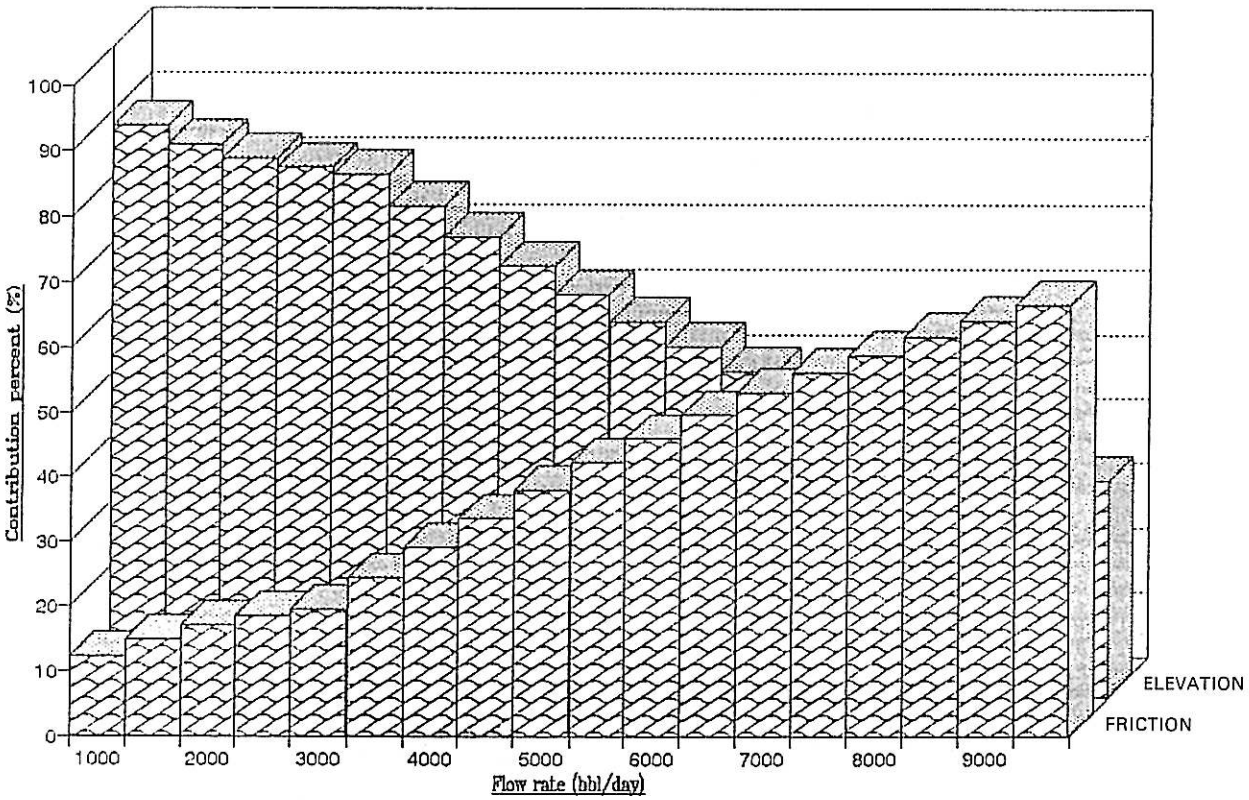


FIG. 8. Effect of flow rate on friction and elevation terms for tubing size of 2.0 inch (Hagedorn and Brown).

The difference in the effect of the terms is very high between the 3.5 and 2.0 inch tubing. In the latter case we notice that the friction contribution reaches 80% of the total pressure loss, this means that most of the energy is consumed (dissipated) in overcoming the friction between the walls of the tubing and the fluids.

EFFECT OF TUBING SIZE ON MAXIMUM PRODUCTION RATE

The third application of the computer programs was to study the effect of tubing size on the maximum production rate possible from a well. The determination of tubing size is extremely important, because the decision about the size should be made prior to drilling. Once the bottom hole flowing pressure is determined for a certain well, calculations are carried out to determine the most suitable tubing size which will achieve the required flow rate and flowing pressure. The maximum fow rate possible from a well is determined from the plot of P_{wf} performance curve and the I.P.R. (Inflow Performance Relationship), the intersection point represents the maximum flow rate possible.

Using the computer programs it was possible to calculate very quickly the P_{wf} performance curves for well (A-55), (the tubing sizes were 2, 2.5, 3, 3.5, and 4 inch, respectively, and the flow rates were from 200 to 10000 bbl/day). The performance curves using both methods were plotted together with the I.P.R in Figs. 9 and 10. For each intersection point on the two plots the contribution of each of the three terms (elevation, friction, and acceleration) is also calculated in order to determine the influences of all the terms and check the possible similarity in their effect for different tubing sizes.

The results for the Hagedorn and Brown, and Poettmann and Carpenter correlations are tabulated in Tables 4 and 5, respectively.

From Tables 4 and 5 and Figs 9 and 10 the followings are noted:

1. The maximum production rate possible from a certain well is proportional to the tubing size used, the greater the tubing size the greater the production rate. It is quite clear that the Poettmann and Carpenter correlation always gave maximum production rates greater than the Hagedorn and Brown correlation. This is mainly because of lower friction losses in the Poettman and Carpenter correlation. There are other factors which play a very important role in determining the tubing size, mainly economical aspects and technical aspects. The economical aspects are concerned with the costs of all possible alterna-

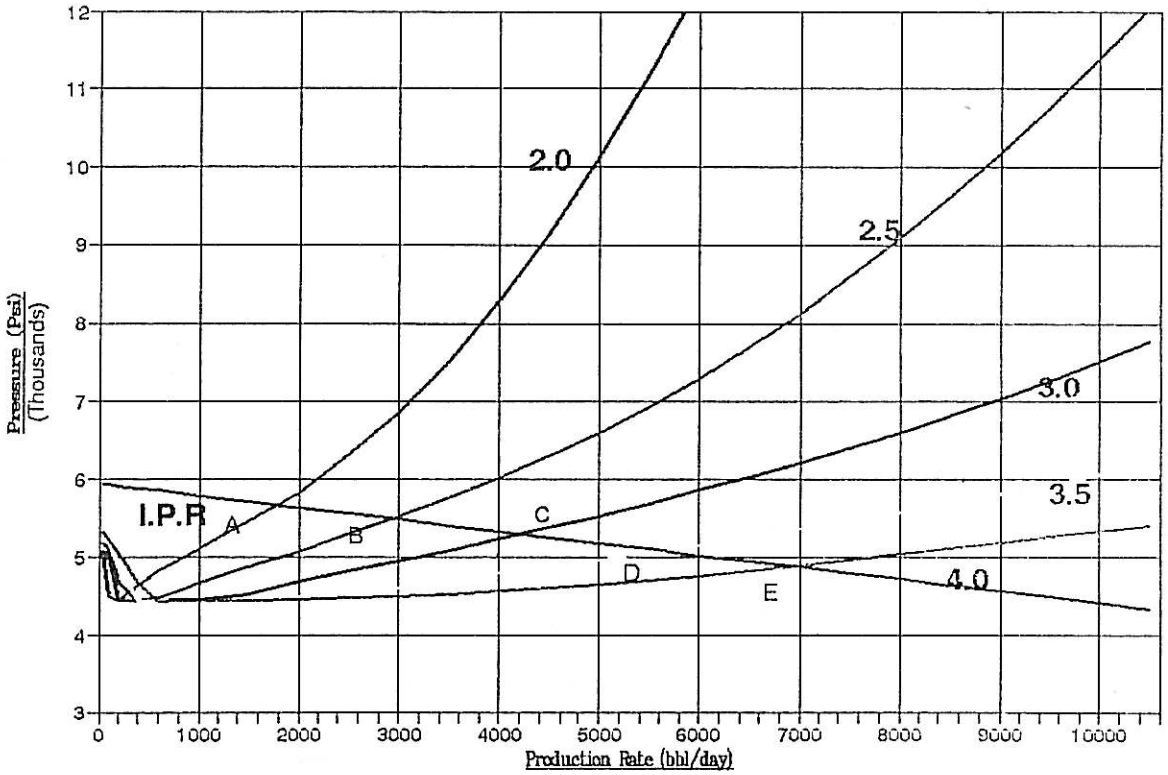


FIG. 9. Well performance curves for different tubing sizes by Hagedorn and Brown; curves A, B, C, D, and E correspond to 2.0, 2.5, 3.0, 3.5, and 4.0 inch tubing sizes, respectively.

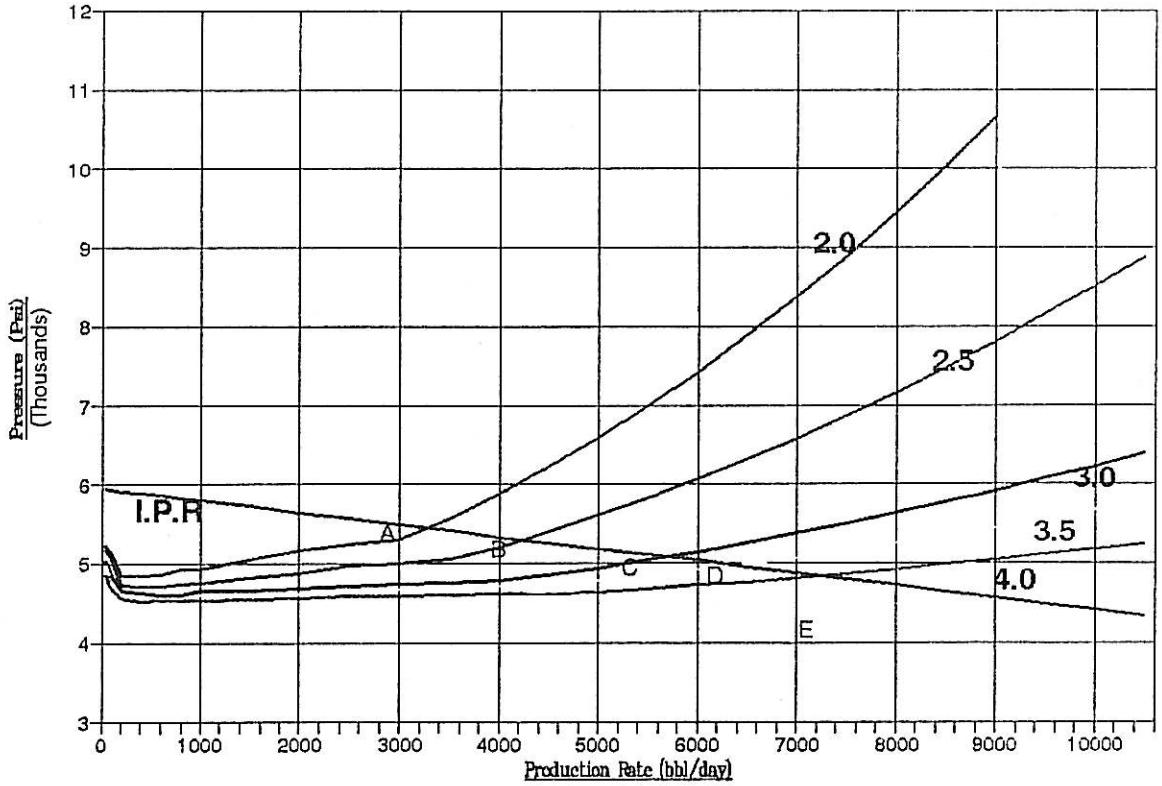


FIG. 10. Well performance curves for different tubing sizes by Poettmann and Carpenter; Curves A, B, C, D, and E correspond to 2.0, 2.5, 3.0, 3.5, and 4.0 inch tubing sizes, respectively.

Table 4. Results of Hagedorn and Brown Correlation

Tubing size Inch	Q_o (bbl/day)	P_{wf} (Psi)	Elevation (%)	Friction (%)
2.0 (a)	1760	5675	83.94	16.03
2.5 (b)	2940	5505	85.76	14.22
3.0 (c)	4200	5310	87.58	12.40
3.5 (d)	5660	5090	89.18	10.80
4.0 (e)	6870	4880	91.25	8.73

Table 5. Results of Poettmann and Carpenter Correlation

Tubing size Inch	Q_o (bbl/day)	P_{wf} (Psi)	Elevation (%)	Friction (%)
2.0 (a)	3250	5720	84.76	15.24
2.5 (b)	4190	5410	86.65	13.35
3.0 (c)	5210	5120	90.12	9.88
3.5 (d)	6250	4950	93.52	6.48
4.0 (e)	7050	4720	95.80	4.20

tives available, for instance, in our case we have a well which has a maximum production rate of 5660 bbl/day using 3.5 inch tubing, this rate can be increased to 6870 bbl/day using 4.0 inch tubing, so the question is, does this increase in production rate justify the extra cost involved in the installation of 4.0 inch tubing? The technical aspects look into the effect of all possible alternatives on the whole producing system (reservoir, tubing, flowlines, etc.), the bottom hole pressure has a profound effect on the reservoir performance and a mutual study between the production engineer and reservoir engineer is inevitable, in order to reach a proper decision concerning the tubing size.

2. The contributions of both the elevation and friction (the acceleration term is considered negligible less than 0.2%) terms are also shown for both methods. It is quite clear that the elevation term is dominant in all cases, but the interesting point is that for the intersection points of the 2.0, 2.5 and 3.0 inch tubing curves from Tables 4 and 5, the percentage of the contributions is quite similar, this is because Poettmann & Carpenter studied these tubing sizes only and the extension of their work to greater tubing sizes should be carried out with caution. For the 3.5 and 4.0 inch tubing the Poettmann & Carpenter correlation gave considerably lower friction contributions than that calculated by the Hagedorn & Brown correlation. This is due to the exclusion of liquid hold-up in the Poettmann & Carpenter correlation.

In general it is safe to state that for all intersection points (maximum production rates), the elevation term constitutes approximately 80% to 90% of the pressure loss while the rest is due to friction, and the acceleration term is considered negligible. The influence of elevation tends to increase with increase of tubing size.

PREPARATION OF WORKING CHARTS

The fourth application of the programs is to prepare working charts and for this application in particular the computer programs are very helpful and beneficial, mainly because the calculations involved are extremely lengthy and tedious and hand calculations are totally out of the question. The basic idea behind the working charts is the immediate access to the multiphase flow correlations, when computer services are not readily on hand. Although the results

are not as exact as computer results, they do provide a very helpful and adequate alternative when problems needing immediate attention arise. One of the main setbacks of the working charts is that they consider certain fluid properties (gas gravity, oil API, WPOR, etc.) and also certain production data (tubing size, flow rates, WOR, GLR), this usually implies some approximation, because one cannot always find working charts that exactly satisfy the actual conditions, contrary to computer calculations where one can input exactly what is needed.

To prepare working charts it is necessary to calculate pressure traverses many times as a function of gas liquid ratio and production rate while the other parameters are held constant. It was possible to achieve this by adding two nested loops to the original computer programs, with the flow rate being the external loop and the gas liquid ratio the internal loop, so that for each flow rate several pressure traverses were obtained, each one representing a gas liquid ratio. This modification in the computer programs produced a massive amount of output which was converted into graphs by means of graphical software. A whole family of working charts has been produced for flow rates ranging from 400 to 8000 bbl/day (See Appendix A and Appendix B).

The working charts were used to calculate Pwf performance curve for well A-55 (representative well) in order to determine the maximum production rate and compare the results with the computer calculations to check their efficiency. Fig. 11 shows the plot of Pwf performance curves for both correlations and the I.P.R. The maximum production rate and the corresponding pressure for the Poettmann & Carpenter correlation are 6350 bbl/day at a pressure of 4925 Psi and for the Hagedorn & Brown correlation the flow rate was 5700 at a pressure of 5175 Psi.

The results obtained by the working charts for the 3.5 inch tubing are slightly greater than those calculated by the computer programs, this difference in the values of the maximum production rate may be attributed to the following reasons:

1. Human error in reading any chart is a known fact.
2. The approximation involved in using working charts. In this case, the actual GLR for well A-55 was 1541 scf/stb and there is no curve for this GLR, therefore an approximate value of 1500 scf/stb was taken.
3. The accuracy of reading values from a chart depends on the scale, since the depth ranged from zero to 33,000 feet and the pressure ranged from zero to 9000 Psi, it was difficult to produce a scale with clear and adequate divisions.

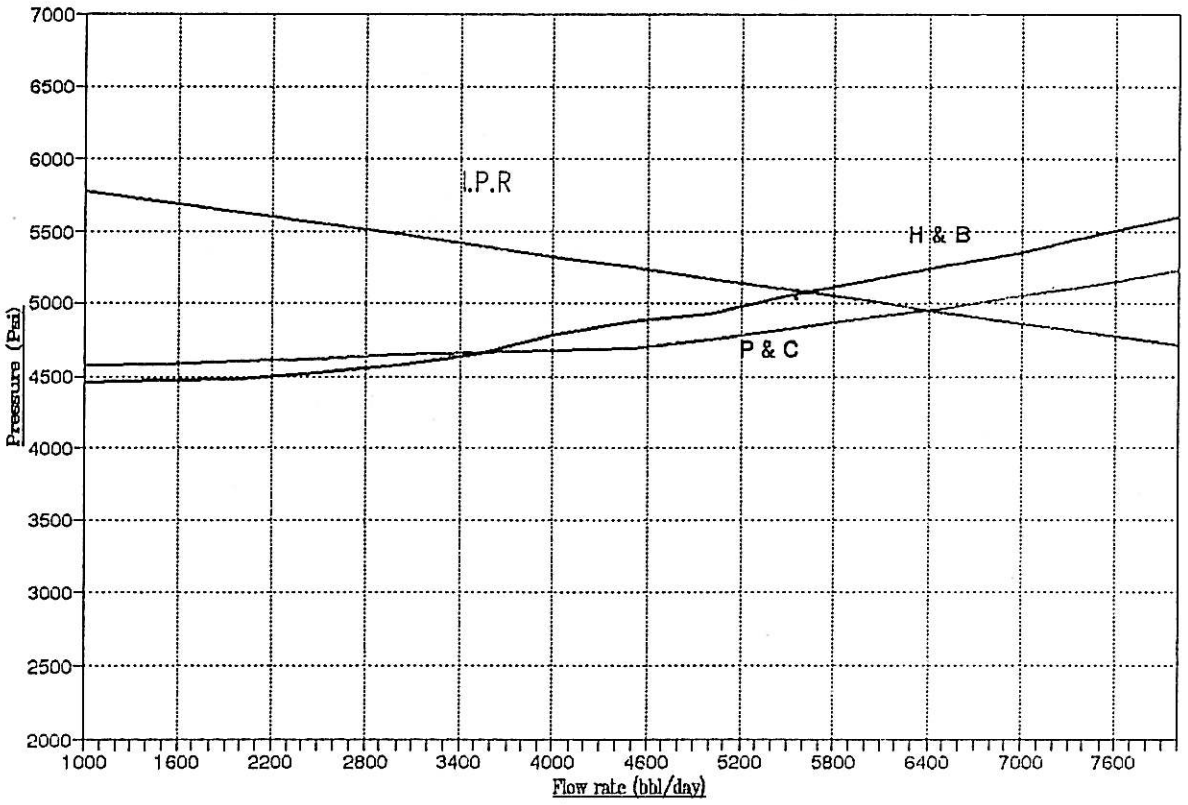


FIG. 11. Well performance curves as predicted by the new working curves for tubing size of 3.5 inch; H & B stands for Hagedorn and Brown whereas P & C stands for Poettmann and Carpenter.

CONCLUSIONS

Although the number of wells in this study is eight, the variation in the production data allows to conclude the following:

- This study and the final results obtained depend greatly on the quality and range of the available field data.
- The fact that empirical correlations were used to calculate fluid physical properties means additional inaccuracies in the results. This also means that the pressure loss prediction method is a combination of a pressure loss correlation and a fluid physical property correlation which should be considered as a unit.
- Both correlations give good results for all wells. The extension of the Poettmann & Carpenter correlation to 3.5 in tubing produces very good results provided that the flow rate is very high (above 2000 bbl/day) and the GLR does not exceed 2500 scf/stb. The Hagedorn & Brown correlation showed ability to predict pressure loss with consistency for all wells.
- The direction of calculations (whether it is upward or downward) has a profound effect on the calculated pressure traverse and a downward direction is recommended.
- For practically all maximum production rates regardless of other variables, the elevation term always constitutes approximately 80% to 90% of the total pressure loss while the rest is due to friction. The acceleration term can be neglected for most cases.
- The accuracy of the working charts depends mainly on their quality, readers accuracy and the approximation involved. The working charts for the Abu-Attifel field are more practical and efficient than those provided by Hagedorn & Brown because the latter charts have depth limitations. By using the computer programs, working charts can be prepared for any field using both correlations.
- The production rate for the representative well (A-55) can be increased to 6870 bbl/day if 4.0 inch tubing were to be installed, but first an economical study must be made to ensure an overall profit due to greater tubing size.

RECOMMENDATIONS

1. For wells producing with very high flow rates and intermediate GLR the Poettmann & Carpenter correlation is suggested, for 3.5 inch tubing the flow rate should exceed 2000 bbl/day. However if there is a wide range of flow rates, GLR and tubing sizes the Hagedorn & Brown correlation gives more consistent accuracy in its results.
2. The direction of calculations should be chosen downwards for greater accuracy and the use of actual fluid physical property data will eliminate the inaccuracies caused by the fluid property correlations.
3. A similar study should be carried out for other vertical multiphase flow correlations, the study should be supported by computer programs and a larger number of wells should be available
4. A two component system was considered in this study consisting of the I.P.R. and P_{wf} performance curves calculated by vertical correlations. The extension of this work to three component systems with the inclusion of horizontal multiphase flow correlations is a must.

ACKNOWLEDGEMENT

The authors would like to thank the management of Agip Oil Co. in Tripoli for permission to publish this paper.

REFERENCES

[1] Davis, G.J., and Weidner, C.E., 1914, "An Investigation of the Air Lift Pump", Bulletin of the University of Wisconsin.

[2] Poettmann, F.H., and Carpenter, P.G., 1952, "The Multiphase Flow of Gas, Oil, and Water Through Vertical Flow Strings with Application to the Design of Gas Lift Installations," Drilling and Production Practice, 257.

[3] Duns, H., Jr., and Ros, N.C.J., "Vertical Flow of Gas and Liquid Mixtures in Wells" 6th. World Petr. Congress, Frankfurt, Germany.

[4] Orkiszewski, J., June, 1967, "Predicting Two-Phase Pressure Drops in Vertical Pipe," Jour. Petr. Tech.

[5] Hagedorn, A.R. April, 1965, and Brown, K.E., "Experimental Study of Pressure Gradients Occuring During Continuous Two-Phase Flow in Small Diameter Vertical Conduits'" Jour. Petr. Tech. 475.

[6] Beggs, H.D. and Brill, J.P. 1973, "A study of Two-Phase Flow in Inclined Pipes," J. Petr. Tech. 607.

[7] Aziz, K., Govier, G.W. and Fogarasi, M., July–Sept., 1972, "Pressure Drop in Wells Producing Oil and Gas," J. Petr. Tech. 38–48.

[8] Fancher, G.H., Jr. and Brown, K.E., (March, 1963), "Prediction of Pressure Gradients for Multiphase Flow in Tubing," Soc. Petr. Eng. Jour. 3, 59.

[9] Gilbert, W.E., 1954, "Flowing and Gas-Lift Well Performance," API Drill. Prod. Practice, 126.

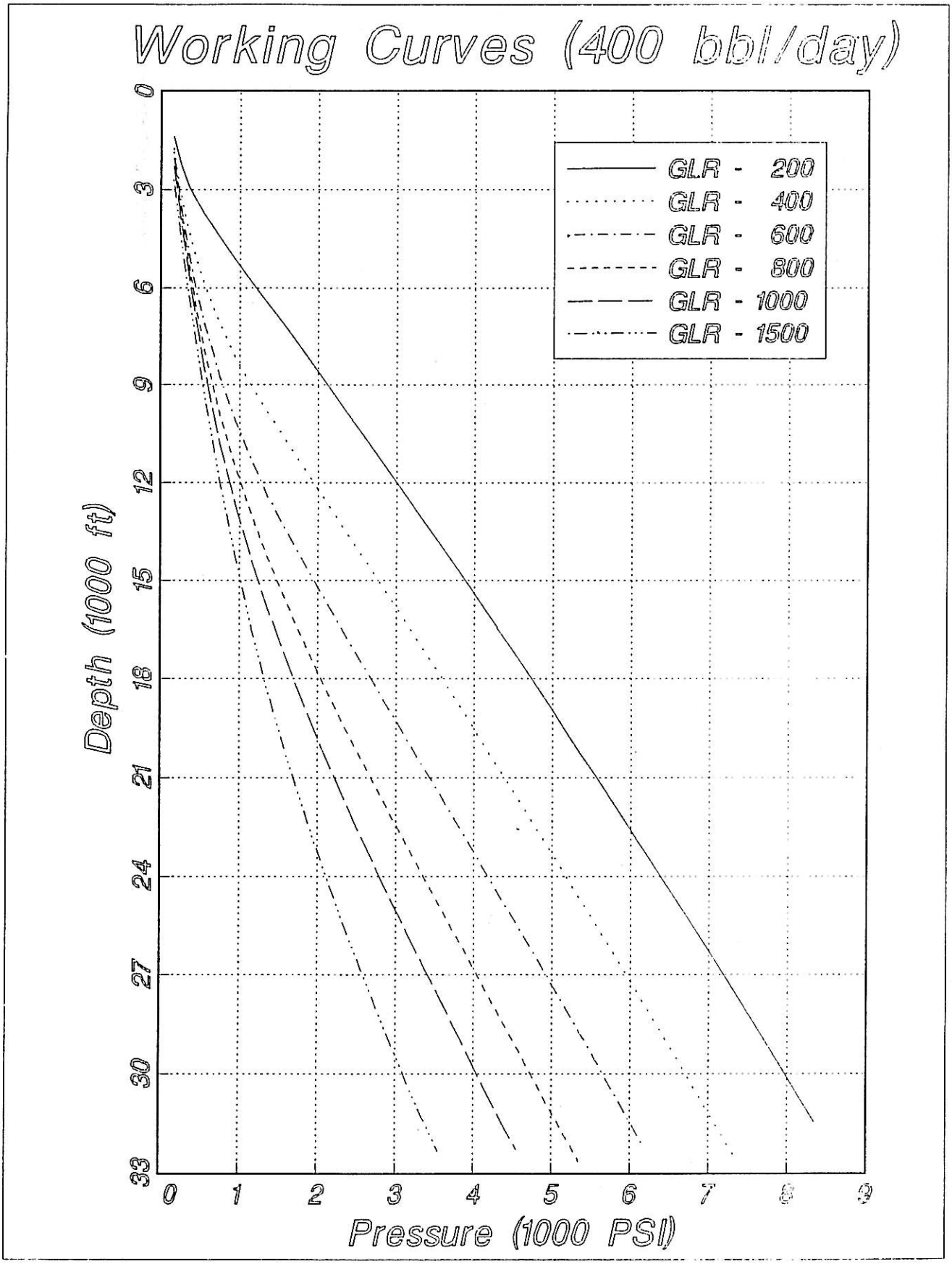
APPENDIX A

The following working charts were calculated using the Hagedorn & Brown Correlation for flow rates of 400 to 8000 bbl/day:

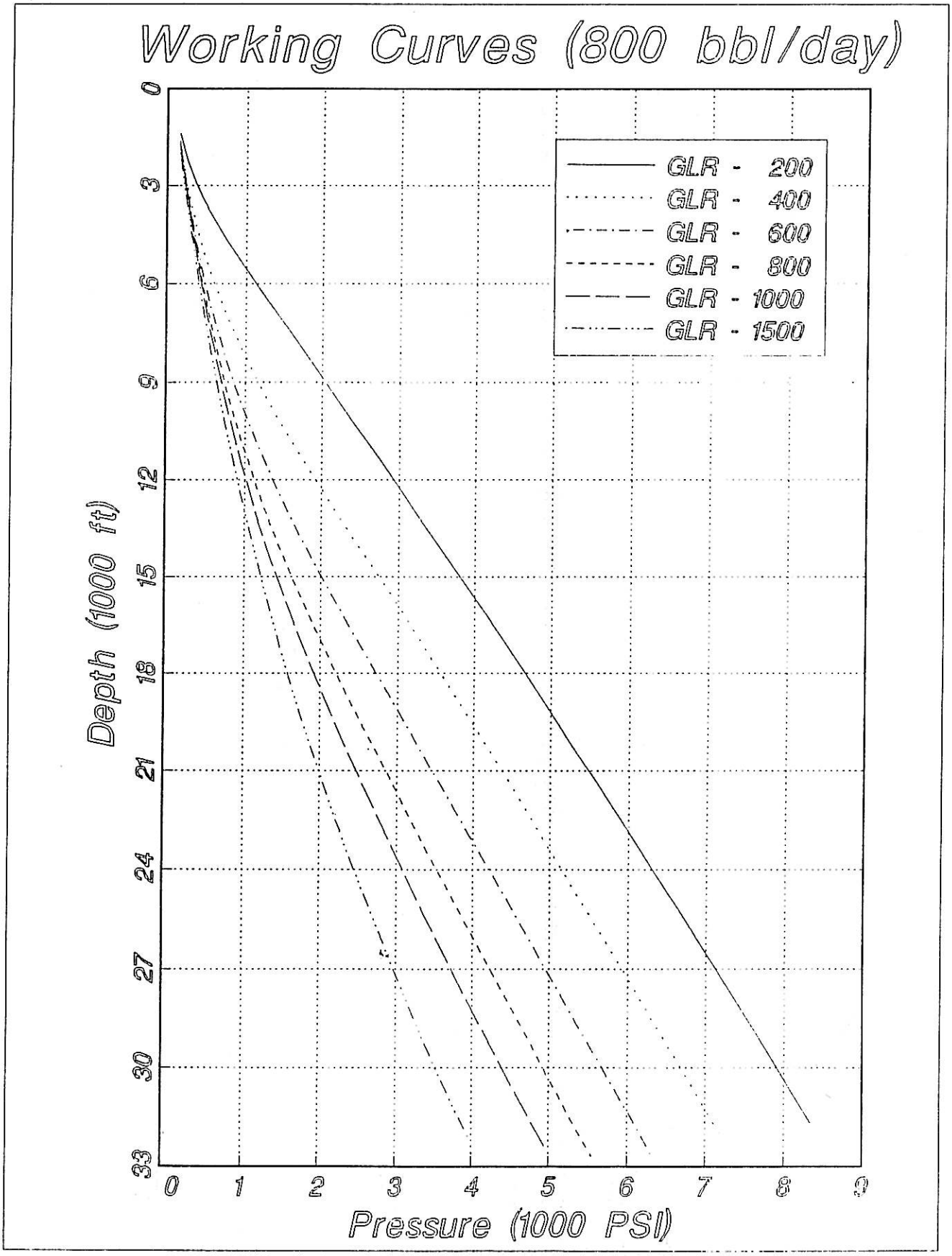
Production Data:

1.	Tubing size	3.5 inch
2.	Oil API gravity	40 API
3.	Gas specific gravity	0.75
4.	Average flowing temp.	245°F

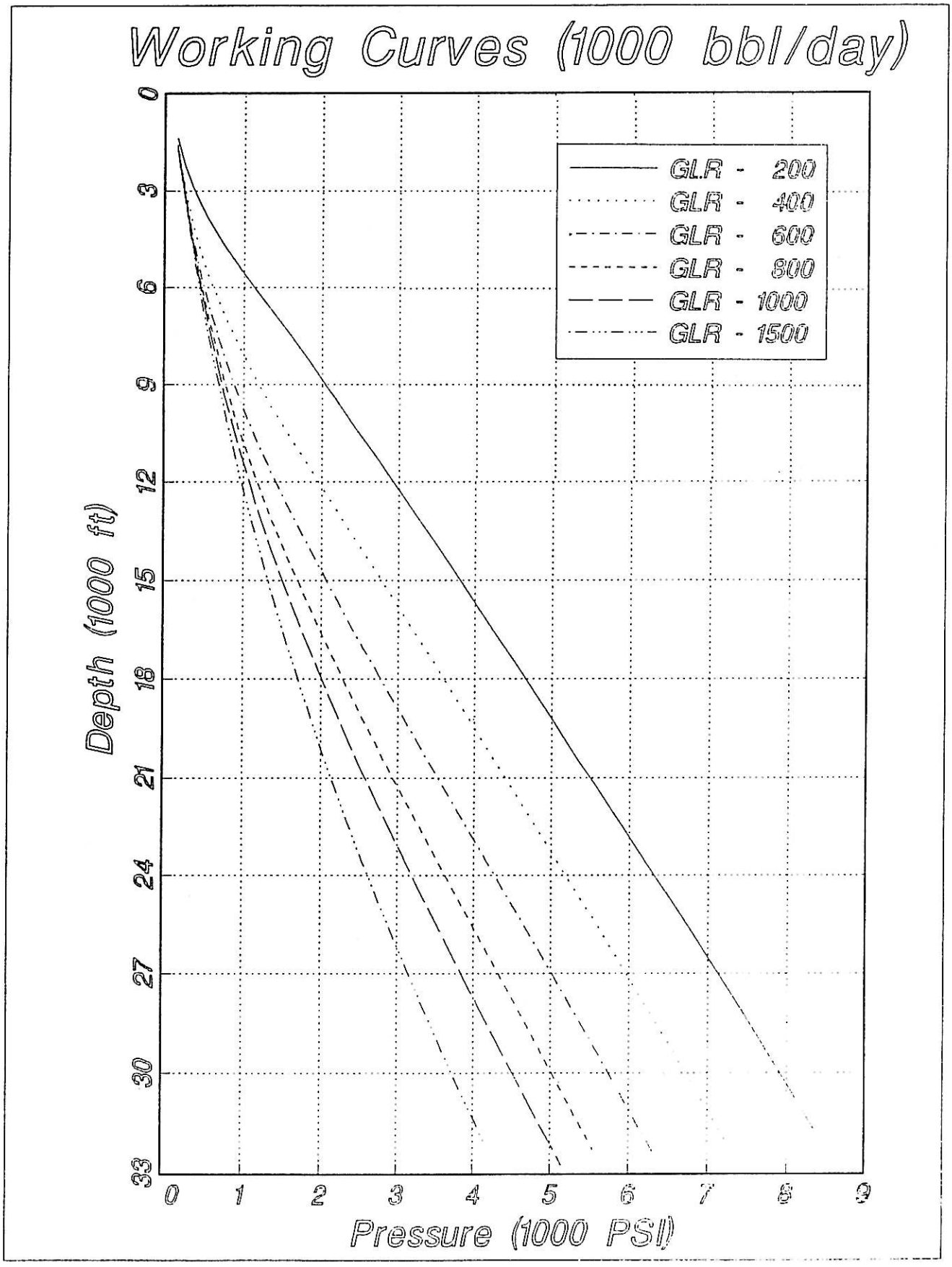
Hagedorn & Brown



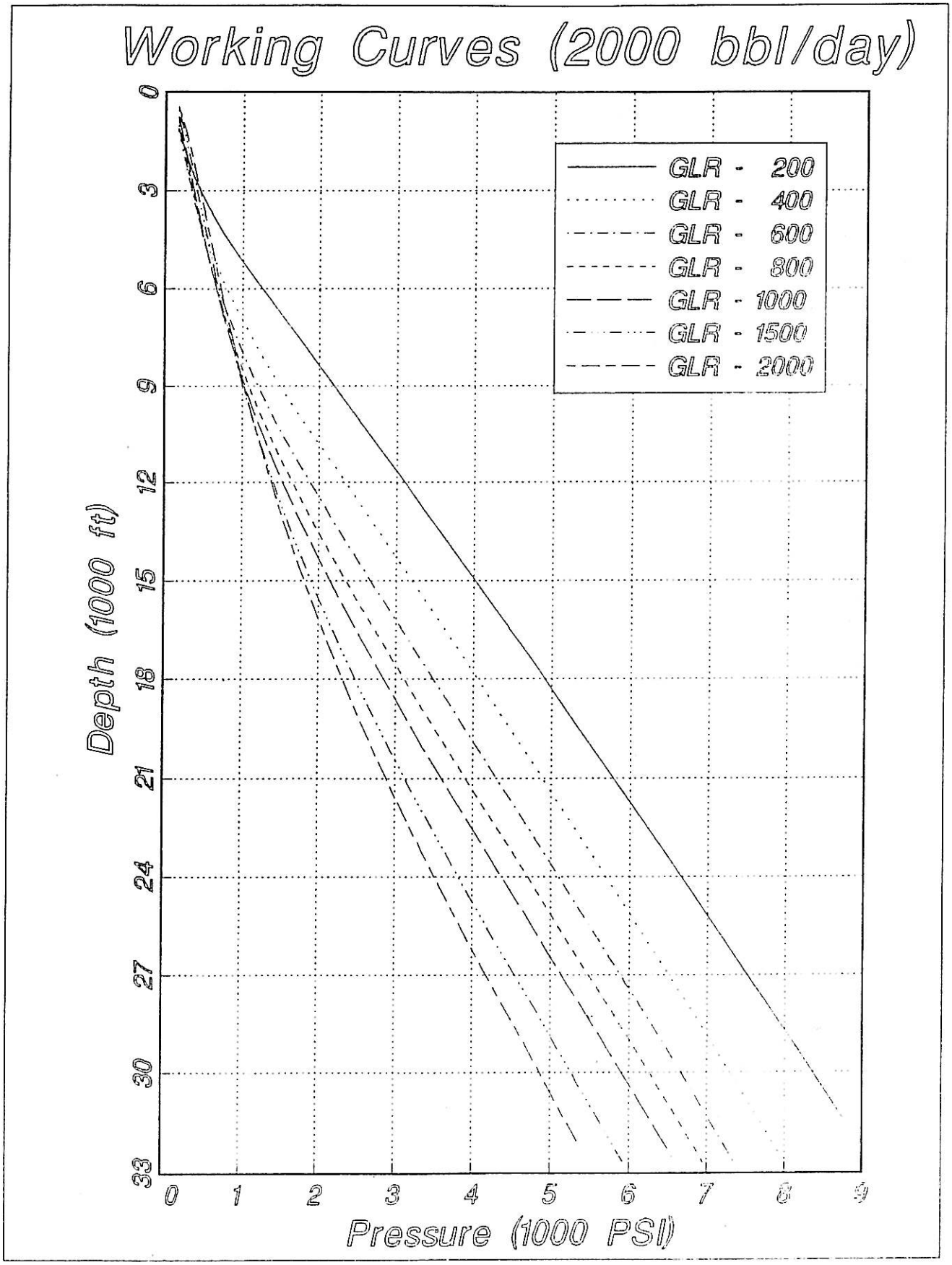
Hagedorn & Brown



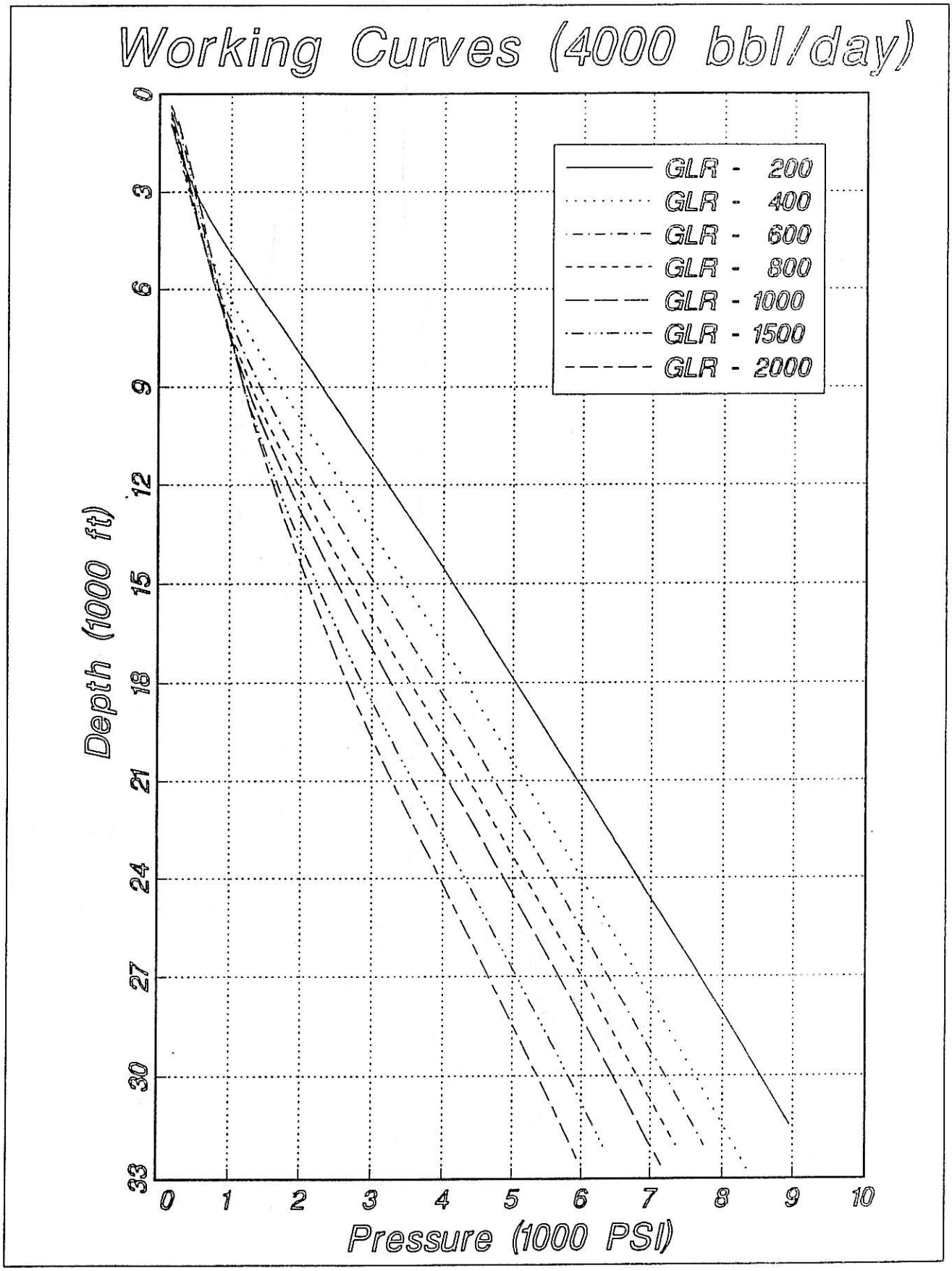
Hagedorn & Brown



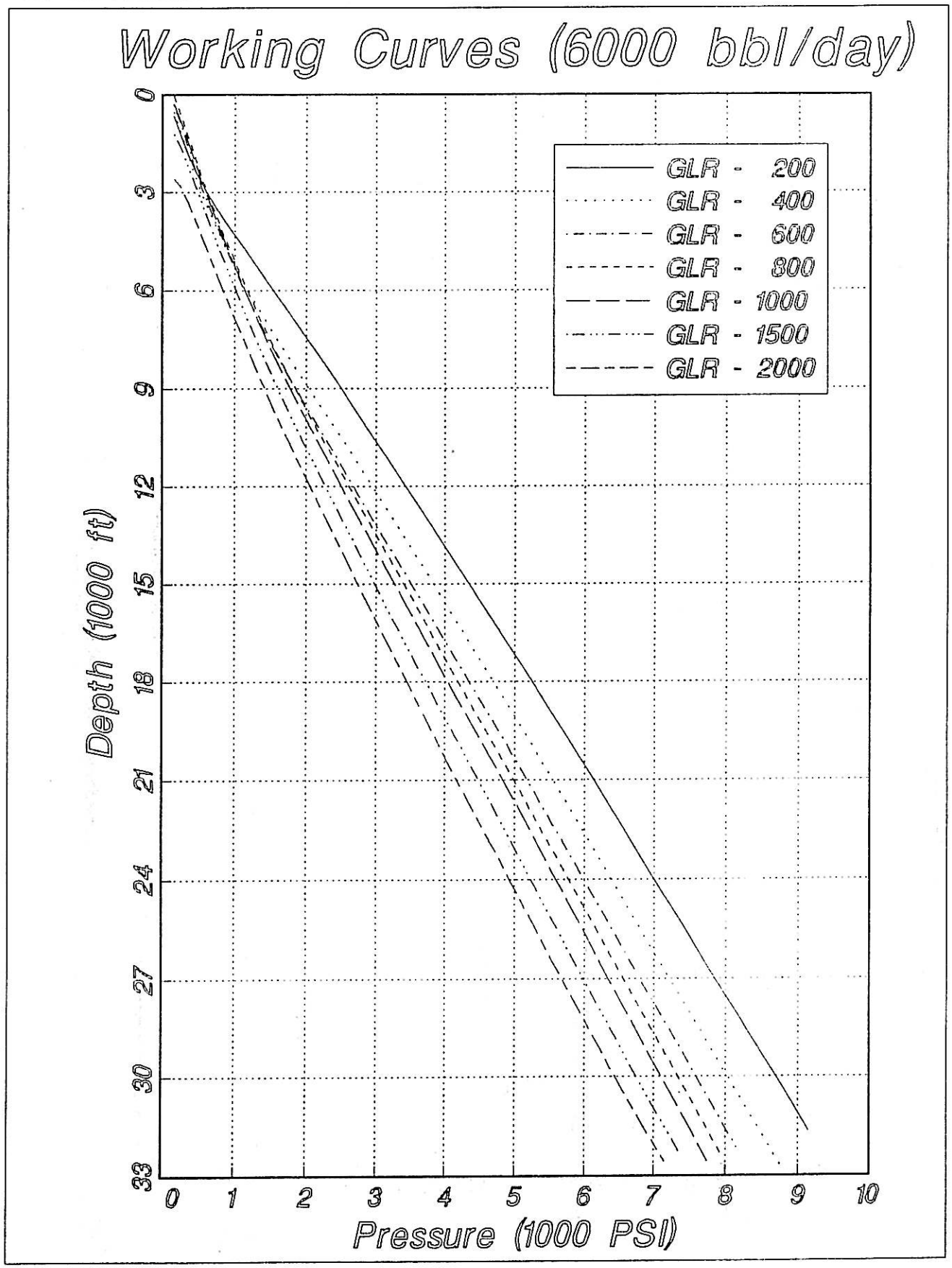
Hagedorn & Brown



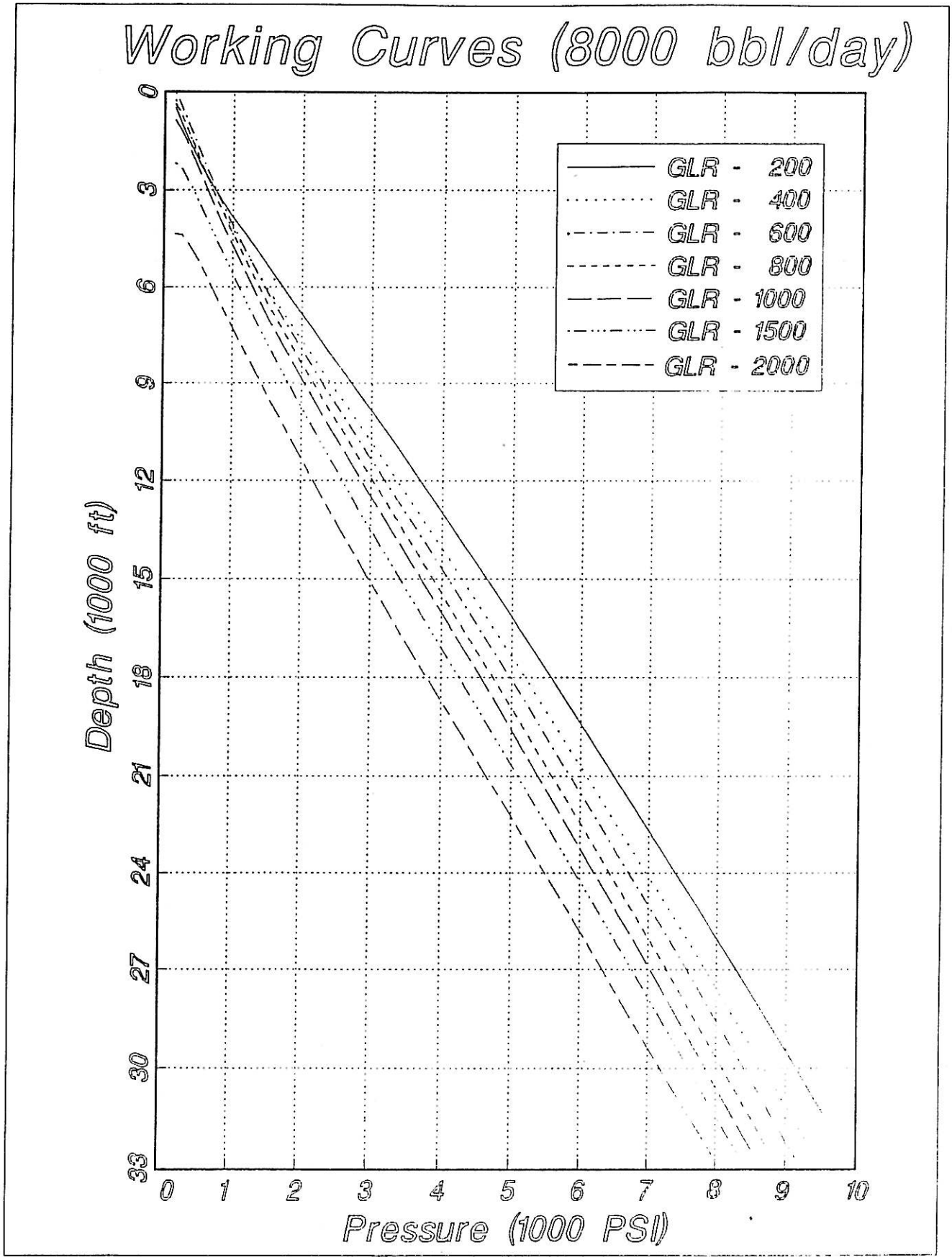
Hagedorn & Brown



Hagedorn & Brown



Hagedorn & Brown



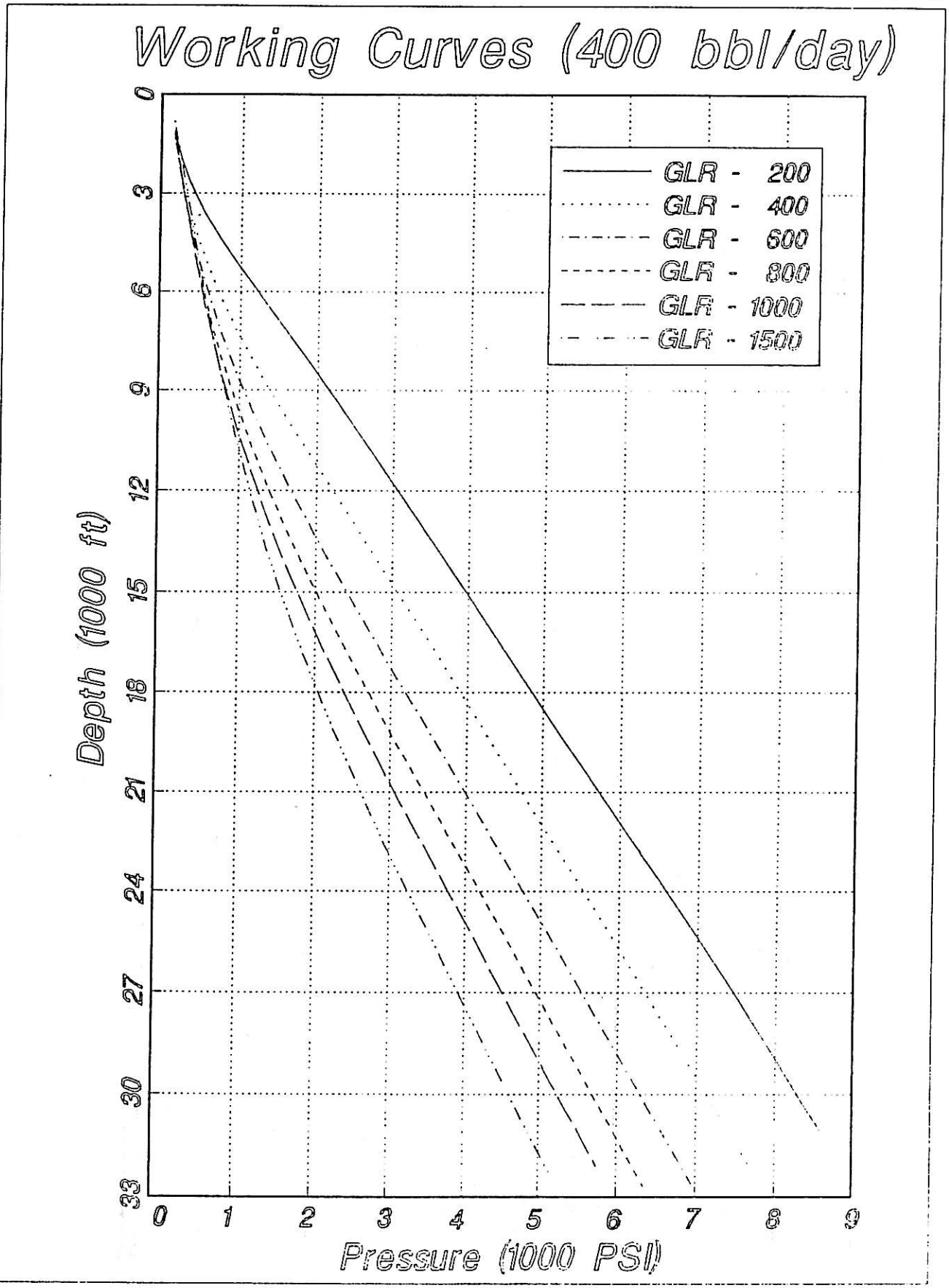
APPENDIX B

The following working charts were calculated using the Poettmann & Carpenter Correlation for flow rates of 400 to 8000 bbl/day:

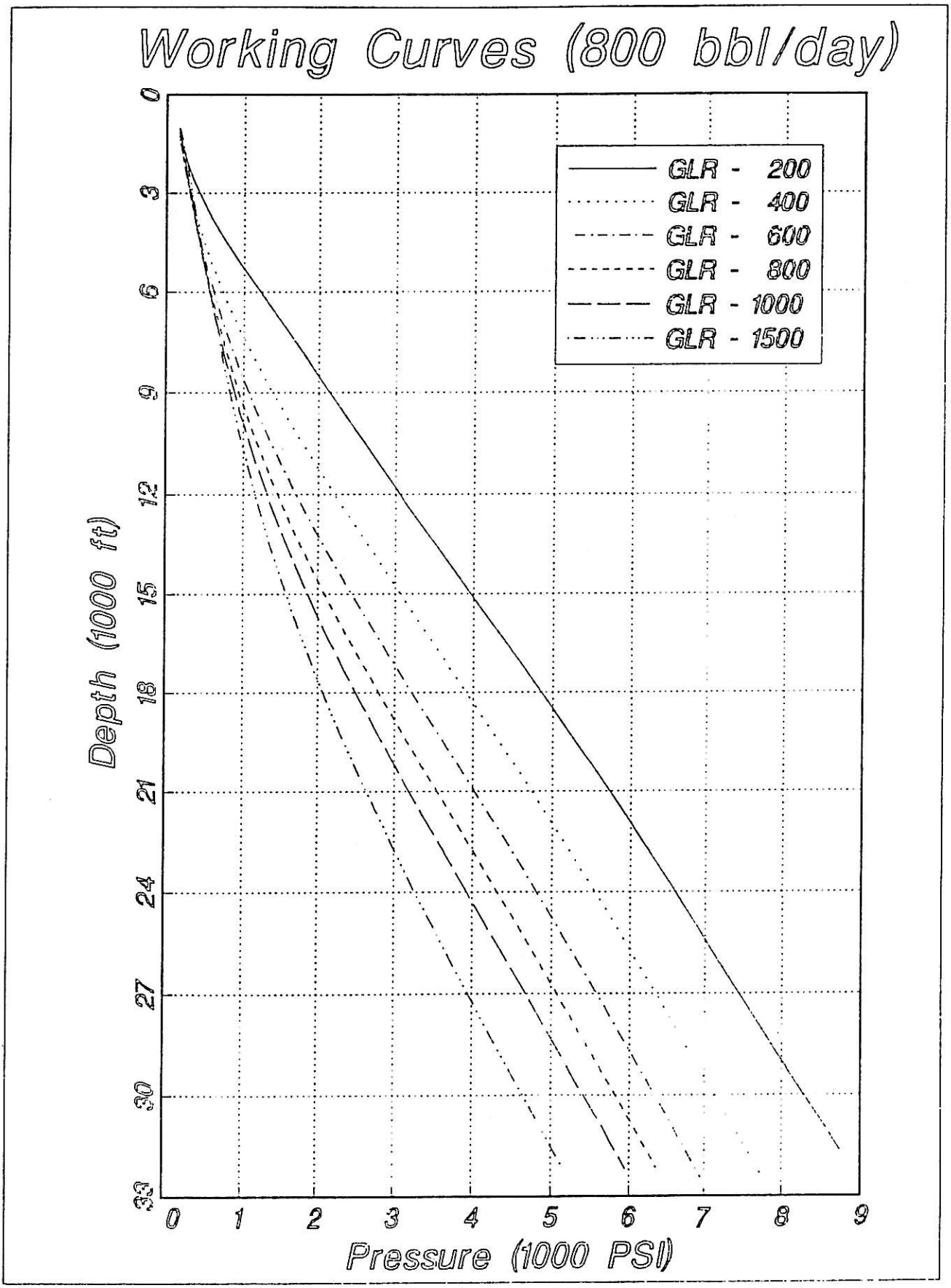
Production Data:

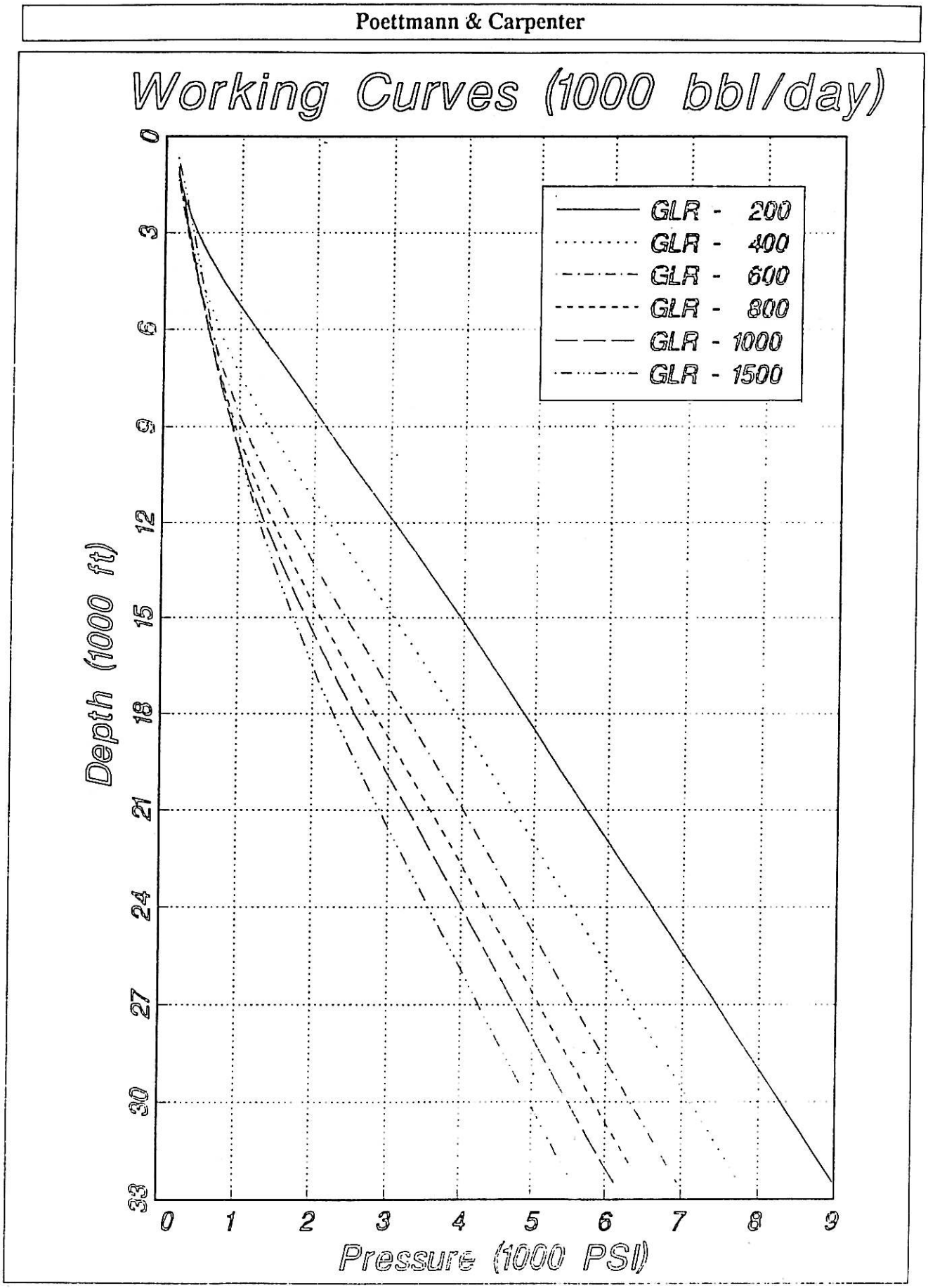
1.	Tubing size	3.5 inch
2.	Oil API gravity	40 API
3.	Gas specific gravity	0.75
4.	Average flowing temp.	245°F

Poettmann & Carpenter

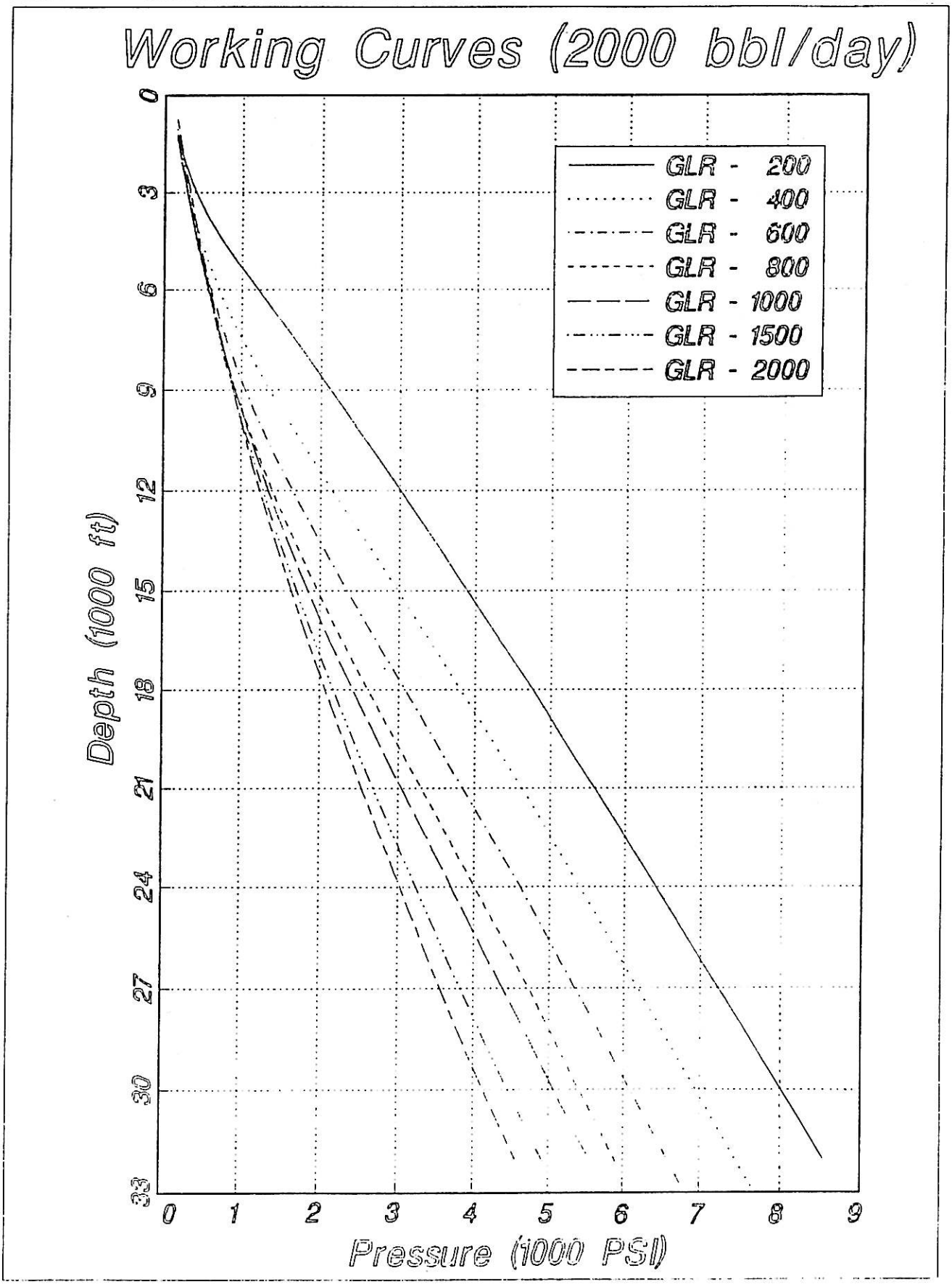


Poettmann & Carpenter

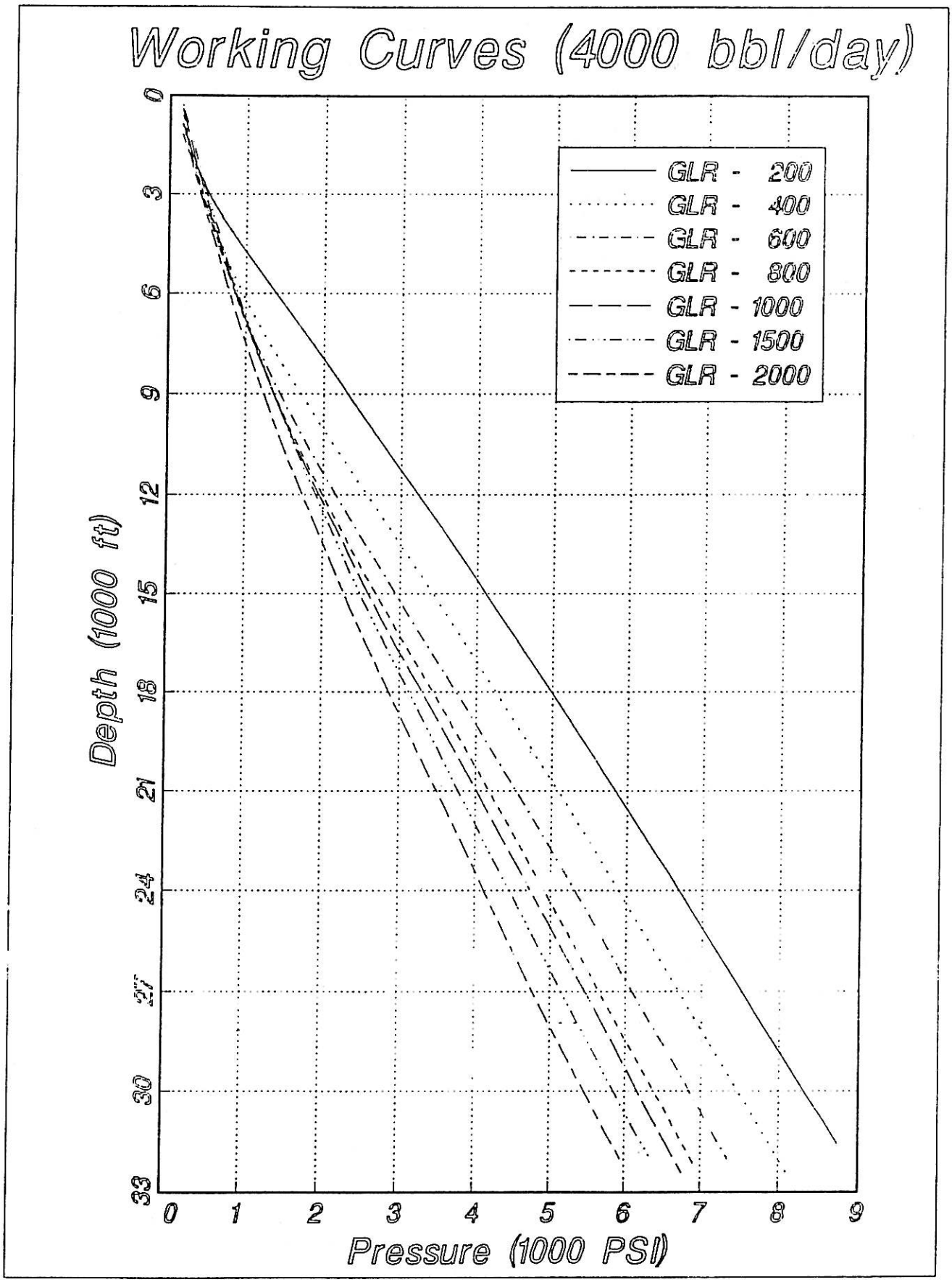



Poettmann & Carpenter
Working Curves (1000 bbl/day)
GLR - 200
GLR - 400
GLR - 600
GLR - 800
GLR - 1000
GLR - 1500
Depth (1000 ft)
0
3
6
9
12
15
18
21
24
27
30
33
0
1
2
3
4
5
6
7
8
9
Pressure (1000 PSI)

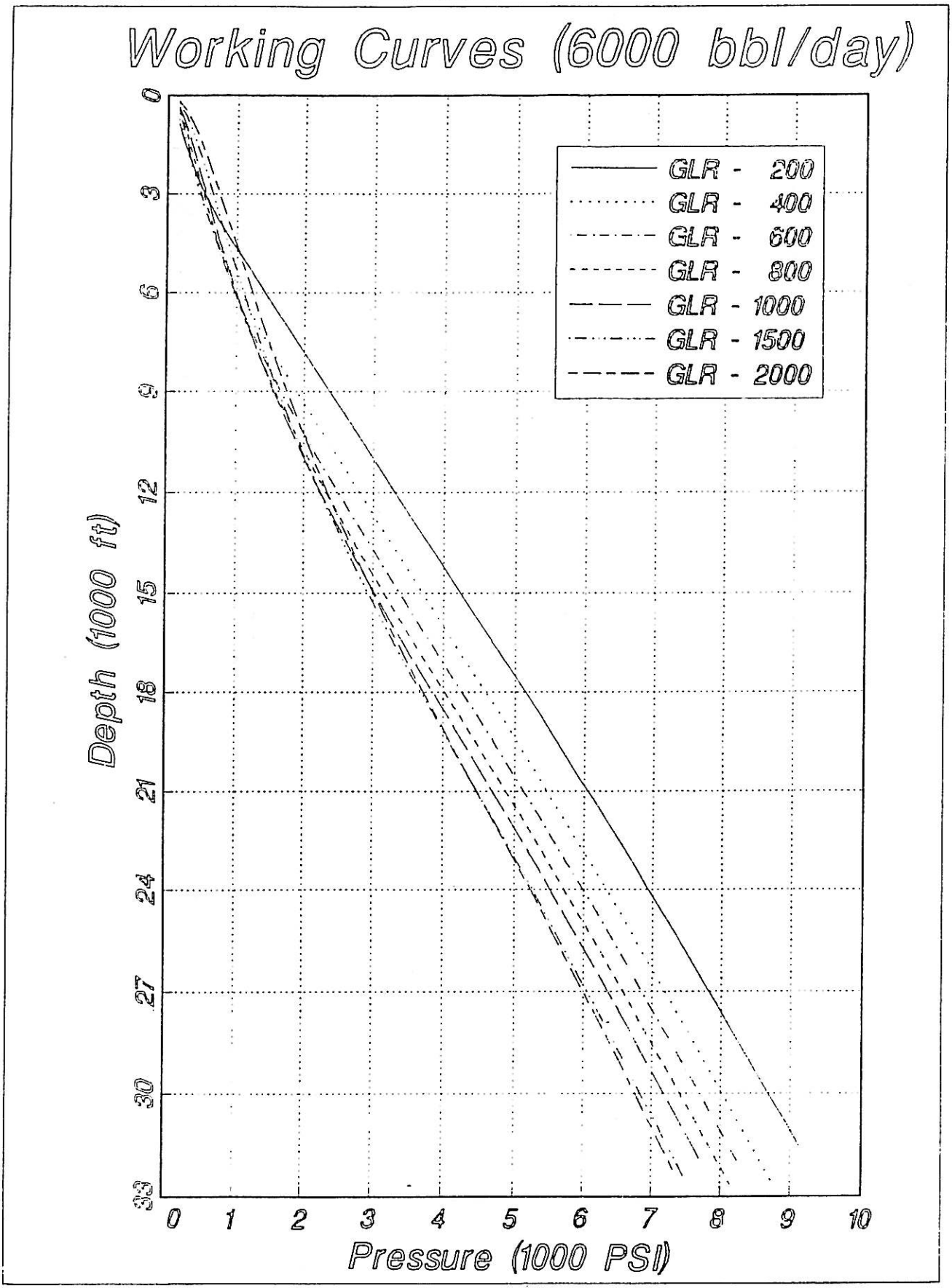
Poettmann & Carpenter



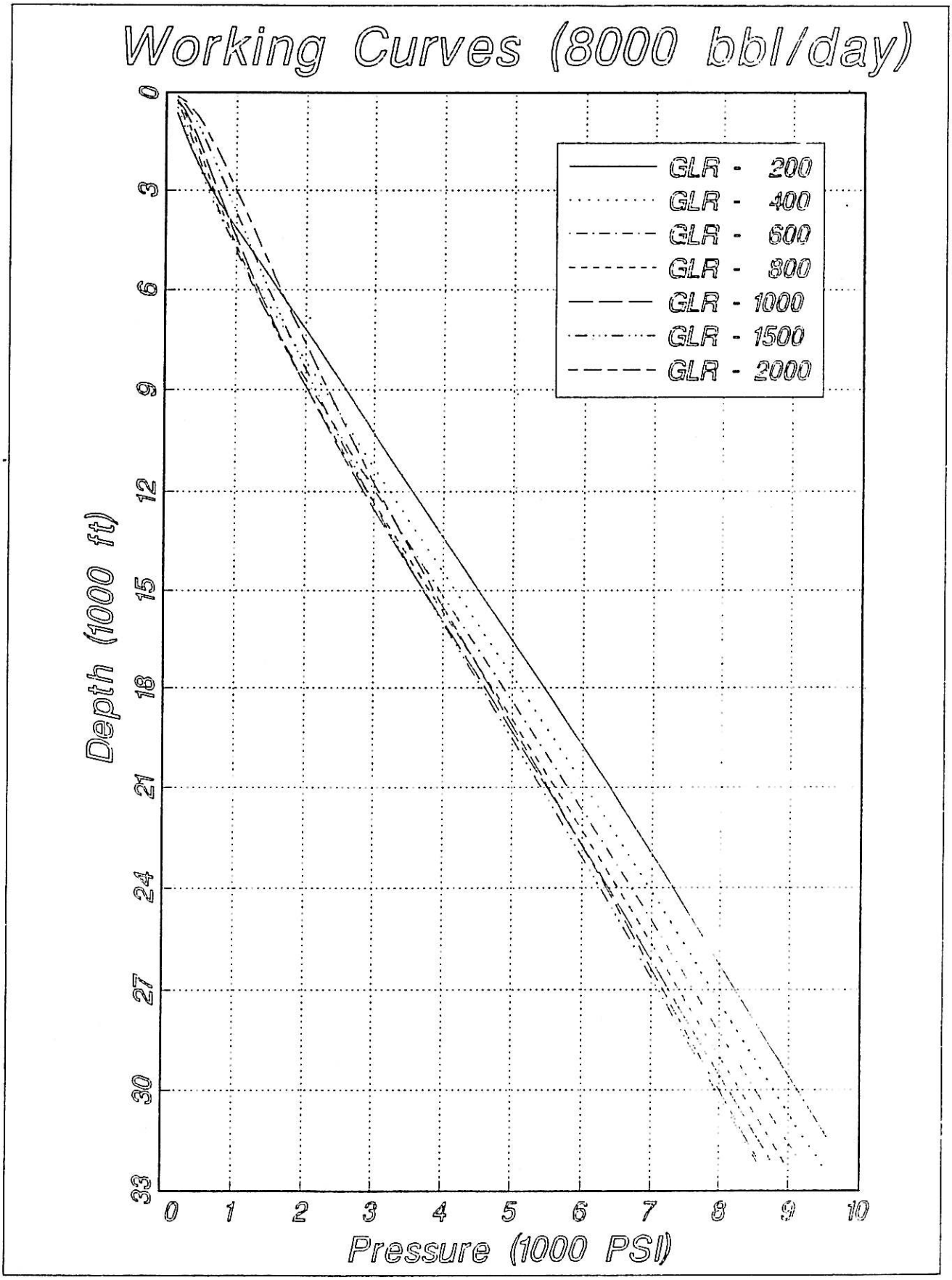
Poettmann & Carpenter



Poettmann & Carpenter



Poettmann & Carpenter



PRJ, Vol. 7 (January 1995); P. 31–34, 4 FIGS.

HYDROGEN EMBRITTLEMENT IN LOW CARBON STEELS

H.L. Rizkalla* and A. Abdulwahed*

القصافة الهيدروجينية في الصلب منخفض الكربون

هاني رزق الله و عياد عبدالواحد

تم شحن مجموعات من عينات الصلب المنخفض الكربون بالهيدروجين بطريقة مهبطية. وقيست صلادة جميع العينات عبر مقطعها العرضي بطريقة ميكرز وذلك لتعيين عمق تغلغل الهيدروجين. أظهرت نتائج الدراسة أن عدد الدورات التي تتحملها العينة تحت ظروف الكلال تتناقص بتزايد مقدار الهيدروجين المشحون بالعينات في نفس الوقت الذي تتزايد فيه المقاومة القصوى للشد نتيجة التأثير الإصلادي للهيدروجين. وقد أجريت عملية استعادة الهيدروجين من العينات واستخدمت الفترة الزمنية لإسترجاع عدد الدورات تحت ظروف الكلال الى 50% من قيمتها الأولى عند درجات حرارة مختلفة لحساب طاقة التحفيز لهذه العملية التي تبين أنها تتفق إلى حد كبير مع النتائج المذكورة في المصادر المختلفة.

ABSTRACT

Sets of low carbon steel (AISI 1015) fatigue specimens were cathodically charged with hydrogen. Transverse Vickers hardness profile was measured for each specimen to estimate the hydrogen penetration depth. The fatigue life and ductility decreased with increasing hydrogen content, while the UTS increased due to the hardening effect of hydrogen. Hydrogen baking time, to restore 50% of the fatigue life, was utilized in calculating the activation energy for the process. The estimated value for the activation energy through the use of this proposed technique proved to be in close agreement with the reported values in the literature.

INTRODUCTION

The damaging effect of hydrogen has long been recognized in ferrous metals. The phenomenon of hydrogen embrittlement (HE) of a metal is manifested primarily as a loss in the ability of a metal to undergo plastic deformation under the applied stress. Normally, it is measured as a decrease in the ductility of the metal [1]. One of the most intriguing aspects of the hydrogen embrittlement phenomenon is its sensitivity to strain-rate and temperature. Hydrogen embrittlement is enhanced by slow strain rate and moderately elevated temperature [2–3]. This is the opposite of the most common behavior where embrittlement is enhanced by high strain rate and low temperature. This slow strain rate and temperature sensitivity suggest that hydrogen embrittlement is mainly controlled by lattice diffusion of hydrogen. In addition, calculations have shown that hydrogen transport rates in association with dislocation motion can be several orders of magnitude than that associated with lattice diffusion [3]. Consequently, hydrogen embrittlement would have a major contribution in the cracking process. Generally, the presence of hydrogen does not change the flow stress or ultimate tensile strength, but it squeezes the true strain to failure. Hydrogen might have a hardening effect leading to an increase in the strength of low-alloy, low strength steels [4, 5]. On the contrary, maraging steels showed a decrease in strength when charged with hydrogen. Such behavior was attributed to the effect of stacking fault energy (SFE) and slip planarity where hydrogen is believed to lower (SFE) [6–7]. Different hypotheses have been proposed to explain the mechanism of hydrogen embrittlement [8–9]. A trial to calculate the activation energy for the process is attempted in the present work through the use of the fatigue behavior of the samples.

*Department of Materials and Metallurgical Engineering. Al Fateh University, P.O. Box 13292, Tripoli, Libya.

EXPERIMENTAL PROCEDURE

Fatigue Test

Sets of fatigue specimens were machined and shaped according to ASTM standards [10]. Some of the fatigue specimens were cathodically charged with different amounts of hydrogen in an electrolytic cell. The cell consisted of two similar electrodes (fatigue specimens) immersed in an electrolyte of 4% H_2SO_4 solution. The specimen to be charged was negatively polarized using constant voltage DC power supply, while the other specimen served as an anode to minimize contamination. All specimens were hydrogen charged under constant current density of 15 mA/Cm^2 for different times (10, 15, 20, 25 and 30 minutes). The fatigue life of the as received specimens was determined by using a rotary bending fatigue machine (Shimadzo). On the average, a minimum of three specimens were tested on each stress level. Thus, the stress vs. number of cycles up to failure (S–N curve) was established. Secondly, some of the cathodically charged specimens for different times were tested at a fixed stress of 275 MPa, which is above the experimentally determined endurance limit of the as received specimens. Then, the fatigue life as a function of the hydrogen content (charging time) was obtained. Thirdly, uncharged samples were heat treated at 225°C for 24 hours. Then, some of these heat treated samples were hydrogen charged for 30 minutes and their fatigue behavior was investigated. Finally, hydrogen charged specimens for 30 minutes, were baked as 125°C and 225°C for different baking periods (0.5, 7, 12 and 24 hours). The activation energy for the baking process was calculated provided that the time and temperature to restore 50% of the uncharged fatigue life were known.

Hardness Test

Small cylindrical sections ($\phi = 12$ mm) were cut from the gage length of untested hydrogen charged fatigue specimens. The transverse surface hardness was measured on a Zwick 3212 tester. The Hardness is taken at 1 mm intervals, starting from the edge towards the center of the specimen. The specimen was rotated at 90° and measurements were repeated. The change in hardness was used to give an indication about the hydrogen penetration depth.

Tensile Test

The ultimate tensile strength was measured as a function of charging time for the as received, and hydrogen charged specimens. Also, the percentage reduction in area as a function of the hydrogen content was calculated.

RESULTS AND DISCUSSION

Fatigue Results

The S–N curve for the as received samples showed that the endurance limit (fatigue life $> 10^7$ cycles) is 265 MPa which is 0.6 of the ultimate tensile strength. The deleterious effect of hydrogen appeared as a drop in the fatigue life, under constant stress of 275 MPa. Increasing the charging time up to 10 minutes did not produce a significant decrease in the fatigue life as can be shown in Fig. 1. Specimens charged for 15–25 minutes suffered from a remarkable decrease in the fatigue life. Further increase in charging time did not affect the fatigue life. This behavior is attributed to diffusion limitations where a period of 25 minutes of charging time would correspond to the amount of maximum hydrogen that can be absorbed by the steel due to the hydrogen fugacity that prevailed over the surface of the specimen under the prevailed charging conditions [7]. Consequently, this would represent the maximum degree of embrittlement beyond which little or no further embrittlement is observed. In addition, the fatigue behavior for the specimens that were heat treated at 225°C then charged with hydrogen for 30 minutes did not show any significant difference as compared to the fatigue behavior of the non heat treated specimens. Such behavior is in agreement with the previous argument.

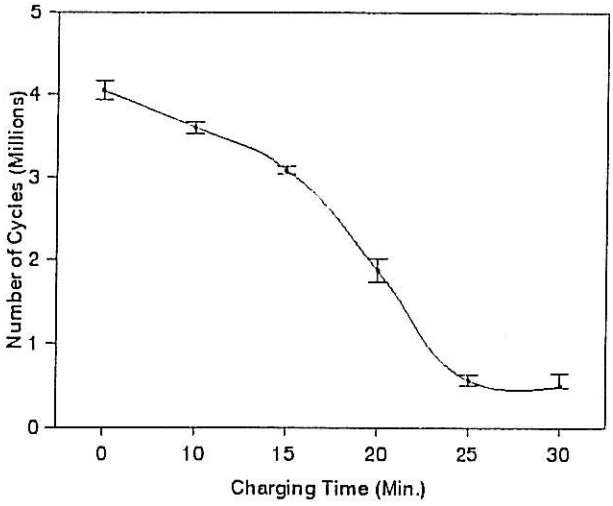


FIG. 1. The effect of hydrogen content (charging time) on fatigue life.

Transverse Hardness

The surface hardness increased with increasing the charging time, Fig. 2. This effect is mainly due to lattice distortion and hardening effect resulting from hydrogen diffusion. Hydrogen would be accumulated in regions of triaxial stress-state, or be associated with

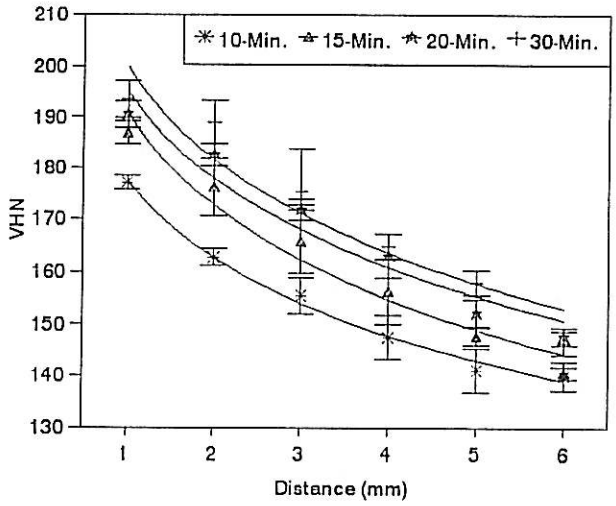


FIG. 2. Transverse hardness profile for different charging time.

dislocations. Hydrogen atoms can recombine and form H_2 molecules, accompanied by a pressure build up. Consequently, local regions would be under compressive state of stress, causing an increase in hardness. For constant charging time, hardness gradually decreased as the center of the specimen was approached, but the hardness level increased with increasing charging time as can be shown in Fig. 2.

Tensile Properties

An increase of approximately 20% in ultimate tensile strength (UTS) was observed between the as received and the maximum hydrogen charged specimens. The increase in UTS was accompanied by a 13% decrease in percent reduction in area as shown in Fig. 3. Similar behavior was reported by Oriani [11] in case of medium carbon steel (AISI 1035),

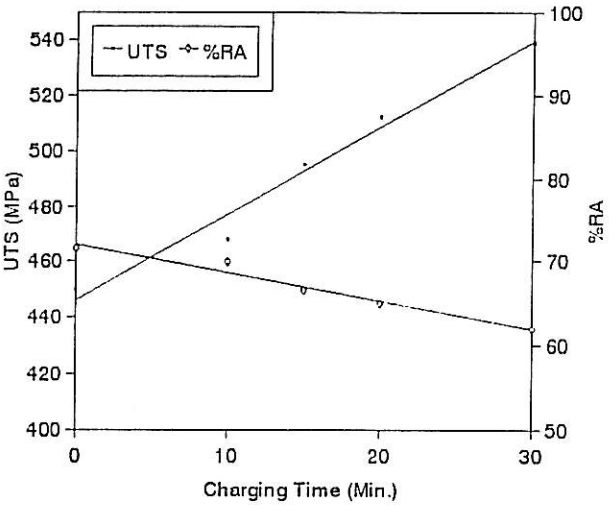


FIG. 3. The change in the tensile properties with increasing hydrogen content.

where an increase in the required stress to form and propagate Luders bands was observed. In general low-alloy, low strength steels show an increase in strength associated with decreased ductility due to hydrogen induced hardening effect. On the other hand, high strength steels exhibit a decrease in strength when charged with hydrogen [6–7].

Activation Energy

Hydrogen embrittlement is a reversible damage process. Therefore, charged specimens can restore their ductility if heated up in vacuum or left long enough in ambient conditions. Fig. 4 represents the restored fatigue life of the charged specimens when baked for different times at 125°C and 225°C. The baking time required to restore 50% of the fatigue life at different temperature was utilized in calculating the activation energy for the process where

$$\Delta H = R \ln\left[\frac{t_2}{t_1}\right]\left[\frac{T_1 \times T_2}{T_2 - T_1}\right]$$

and ΔH = activation energy, t_1, t_2 are the baking times at temperatures T_1 and T_2 respectively and R is the gas constant. The calculated activation energy $\Delta H = 3.7$ Kcal/mole turned out to be in good agreement with the reported values of ΔH for hydrogen diffusion in steel (ΔH reported = 4.2 KCal/mole [12]). Keeping in mind the statistical nature of the fatigue test and it's dependence on many variables other than the hydrogen content the above calculated ΔH would be a good approximation.

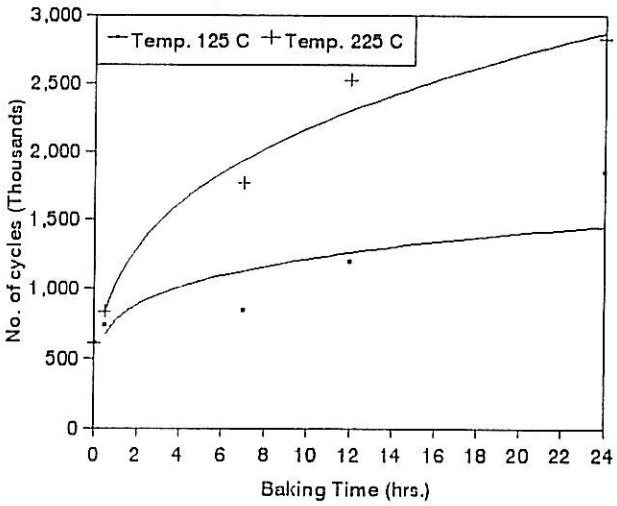


FIG. 4. The effect of baking time and temperature on the fatigue life.

CONCLUSION

1. The ultimate tensile strength of AISI 1015 increased with increasing the hydrogen content in

the samples; while the ductility and the fatigue life decreased.
2. The transverse hardness measurements proved to be effective in probing the hydrogen penetration into the sample.
3. The proposed technique for measuring the activation energy for hydrogen diffusion proved to be successful.

ACKNOWLEDGEMENT

The authors would like to thank the Department of Materials & Metallurgical Engineering for providing the facilities to carry out this work.

REFERENCES

[1] Troiano, A.R., 1973, Hydrogen in Metals, Proceedings of an international conference of the effect of hydrogen on materials properties and selection, ASM, p. 3.
[2] Dieter, G.E., 1986, Mechanical Metallurgy, 3/e., McGraw Hill, London.
[3] Tetelman, A.S. and McEvily, J., 1967, Fracture of structure Materials, Wiley, New York.
[4] Gosh, A. and Basu, A., 1988 U.K. Chatterjee and B. Sasmal, Trans. Ind. Inst. Metals 41, 519.
[5] Bowker, J., Piggett, M.R. and Wheatherly, G.C., 1984, Proceedings of the 6th International Conference on Fracture, New Delhi, Vol. 4 edited by K.N. Raju *et al.* p. 2371.
[6] Thompson, A.W. and Bernstein, I.M., 1980, Advances in Corrosion Science and Technology, Vol. 7, edited by M.G. Fontana, R.W. Staehle, Plenum Press, New York, p. 53.
[7] Reddy, K.G., Arumugam, S. and Lakshmanan, T.S., 1992, Hydrogen embrittlement of marging steel, J. Mats. Sci. 27, p. 5159–5162.
[8] Oriani, R.A., 1977, A review of proposed mechanisms for hydrogen assisted cracking in Metals, in Hydrogen Damage, edited by Cedric Beachem edited, Metals Park, Ohio, p. 301.
[9] Gilman, J.J., The Role of surface Hydrides in stress Corrosion Cracking, ibid.
[10] Dave, H.E., Troxell, C.E. and Wiskocil, C.T., 1964, The testing and inspection of Engineering Materials, McGraw Hill, New York.
[11] Oriani, R.A. and Josephic, P.H., 1980, Met. Trans. A, p. 1809–1820.
[12] Hertzber, R.W., 1986, Deformation and Fracture Mechanics of Engineering Materials, Wily, New York.

PRJ, Vol. 7 (January 1995); P. 35–41, 13 FIGS, 1 TABLE.

FRACTOGRAPHY EXHIBITED BY HYDROGEN EMBRITTLED AUSTENITIC STAINLESS STEELS

F.O. El-Shawesh*

أثر التصلد الهيدروجيني على التغير في طبيعة الكسر للفولاذ الأوستيني قليل الصداء

فوزي الشاوش

تم شحن عينات من الفولاذ قليل الصداء ، الأولى من نوع 304 في حالة ملدنة ومدرفلة وفي حالة حساسة (Sensitization) نتيجة ترسب الكربيدات ($C_{23}C_6$) في حدود الحبيبات والثانية في حالة ملدنة ومن نوع 310 ، بالهيدروجين عند درجة حرارة الغرفة وفي محلول مائي $1N\text{-}H_2SO_4$ مضاف إليه قليل من صوديوم ساينيد كعامل مساعد في إنتشار الهيدروجين في الصلب . تم عملية شحن العينات وهي معرضة لإجهادات شد بطيئة وبسرعات مختلفة (833.3 nm/s إلى 9.8 nm/s).

في حالة الصلب قليل الصداء نوع 304 أظهرت النتائج أن الكسر إنتشر خلال وعبر الحبيبات عند إجهادات شد بطيئة جداً (9.8 nm/s و83.3 nm/s) ، كما لوحظ أن معدل الكسر خلال الحبيبات يزداد بانخفاض سرعة الشد البطيئ . نفس ميكانيكية الكسر لوحظت في العينات المدرفلة من نوع 304 إلا أن معدل الكسر خلال الحبيبات كان أقل .

عينات الفولاذ من نوع 304 والتي حدود حبيباتها تحتوي على ($Cr_{23}C_6$) إعتمدت ميكانيكية الكسر فيها على زمن المعالجة الحرارية والسرعة المستخدمة في إجهاد الشد البطيئ . الكسر في عينات الصلب قليل الصداء في نوع 310 كان خلال وعبر الحبيبات وذلك عند تطبيق أجهاد الشد البطيئ جداً (9.8 nm/s) .

ABSTRACT

Annealed, sensitized and cold worked less stable 304 austenitic stainless steel and more stable 310 austenitic stainless steel in annealed condition were cathodically charged in 1N H_2SO_4 with addition of $NaAsO_2$ at current density of 0.4 mA/cm^2 while undergoing tensile strain over a wide range of crosshead speeds (833.3 nm/s to 9.8 nm/s) at room temperature.

Fracture surface of 304 austenitic stainless steel specimens exhibited both cleavage and intergranular fracture at low crosshead speeds of 83.3 nm/s and 9.8 nm/s. The extent of intergranular fracture was observed to increase with lowering in crosshead speed. Similar features were observed when cold worked 304 austenitic stainless steel specimens tested at the same condition. However, the extent of intergranular fracture was less compared to the non cold worked specimens.

Fracture surface of sensitized 304 austenitic stainless steel specimens exhibited different surface morphology and was found to depend on the sensitization time and the applied crosshead speed.

Both intergranular and quazi cleavage types of fracture modes were observed when stable 310 austenitic stainless steel specimens tested at the lowest corsshead speed of 9.8 nm/s.

INTRODUCTION

Ductility of many austenitic stainless steel is reduced by charging with hydrogen or by testing in a hydrogen atmosphere [1–4]. Embrittlement is substantial with ductility losses of up to 50% or higher, when 304 austenitic stainless steel is tested in high pressure hydrogen [1], strained while undergoing cathodic charging and when tensile tested after severly charged by hydrogen [1, 5]. Other varieties of austenitic stainless steel, such as type 310 austenitic stainless steel, is affected slightly under the same condition [3]. Explanation for the relatively high susceptibility of type 304 austenitic stainless steel to

*Petroleum Research Centre, P.O. Box 6431, Tripoli, G.S.P.L.A.J.

hydrogen embrittlement was attributed to the strain induced transformation to α-martensite [1, 2] or concentration of hydrogen at critical site by coplanar dislocation motion [6, 7].

Changes in fracture morphology have been observed in tensile specimens tested in hydrogen. Microvoid formation and coalescence leading to a dimpled fracture is the only fracture mode observed in hydrogen free type of 304 and 310 austenitic stainless steels [8, 9]. In contrast, fracture referred to as cleavage fracture [10] quazi cleavage [11, 12], intergranular fracture [2, 13, 14, 15], facets [16] have been reported for hydrogen embrittlement of 304 austenitic stainless steel. However, microvoid coalescence was the predominant fracture morphology for 310 austenitic stainless steel [8, 10].

This paper discusses the effect of strain rate (crosshead speed), microstructure and stability on the changes in the fracture morphology for less stable 304 and more stable 310 types of austenitic stainless steels as a result of hydrogen embrittlement.

EXPERIMENTAL

A commercial 304 and 310 austenitic stainless steel were used for this course of work. These alloys were selected in order to investigate the effect of different alloy stabilities on susceptibility to hydrogen embrittlement. The alloy 304 was selected because its austenite phase is less stable and would be expected to transform to both α and ε phases under either subzero cold working or cathodic charging. In the 310 alloy the austenite phase is anticipated to be highly stable. The chemical composition for these alloy steels are shown in Table 1. The samples were solution annealed at 1050 °C for 304 austenitic stainless steel and at 1100 °C for 310 austenitic stainless steel for 1 h followed by water quench. Some samples from 304 austenitic stainless steel were given an additional heat treatment (sensitization) at 650 °C for duration of 5 h and 24 h. This treatment cause chromium carbide ($Cr_{23}C_6$) to precipitate at the grain boundaries as a result of chromium and carbon depletion from the area adjacent to the grain boundaries.

A number of 304 austenitic stainless steel samples were cold worked up to 12% in order to examine the susceptibility of cold worked structure to the hydrogen embrittlement.

Table 1. Chemical Composition of the 304 and 310 Austenitic Stainless Steels

Materials	C%	Mn%	Si%	P%	S%	Cr%	Ni%
304	0.04	1.42	0.32	0.024	0.002	18.36	8.73
310	0.026	1.52	0.27	0.013	0.005	24.66	20.07

The material was received in the form of sheet with thickness of 0.8 mm. The specimens was then machined to required dimension and 60° V notch as introduced at the middle as shown in Fig. 1. All test specimens were tensile strained while undergoing cathodic charging at current density of 0.4 mA/cm² in 1*N* H_2SO_4 with addition of $NaAsO_2$ at room temperature. For comparison the same number of specimens were tested in air. The resulted fracture surfaces were cleaned in acetone using ultrasonic and then dried. A scanning electron microscope (SEM) was then used to examine the changes in the fracture morphology as a result of hydrogen embrittlement.

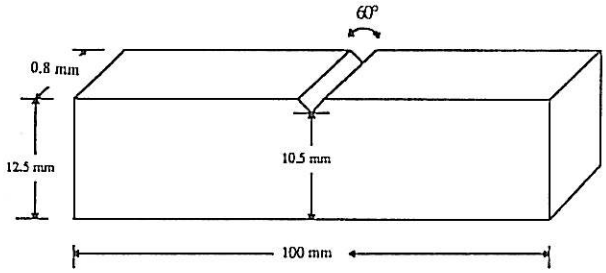


FIG. 1. Schematic representation showing the shape and dimensions (mm) of the type of specimen used in the hydrogen embrittlement test.

FRACTOGRAPHY

Three features were observed on the fracture surfaces of the tested specimens: dimples, cleavage and intergranular. Dimpled rupture was the only fracture mode observed on the specimens tested in air as shown in Fig. 2. The other two fracture modes were found only in specimens that were embrittled as a result of absorbed hydrogen.

The results will be classified into three main sections in order to clarify the different effects.

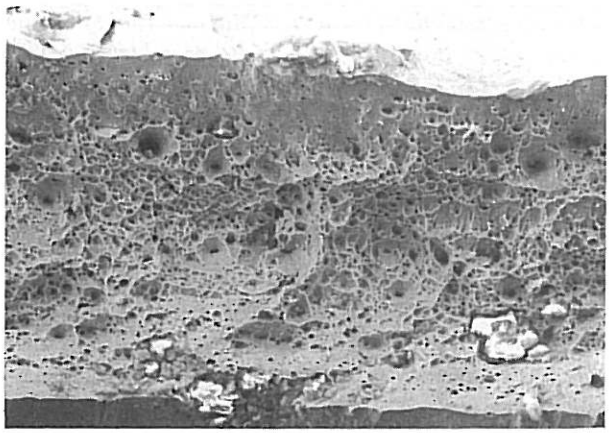


FIG. 2. S.E.M. fractography shows typical ductile fracture of stainless steel specimen fractured in air.

1. Effect of sensitization

Sensitized 304 austenitic stainless steel specimens exhibited higher susceptibility to hydrogen embrittlement compared when it is in the annealed condition. The degree of the susceptibility was found to depend on the sensitization time and used crosshead speed. The fracture surfaces for specimens sensitized for 24 h was predominantly intergranular particularly at two lowest crosshead speeds of 83.3 nm/s and 9.8 nm/s as shown in Fig. 3. The percentage of intergranular fracture was found to increase with lowering in crosshead speed. However, at these crosshead speed, cleavage fracture was predominant fracture mode for specimens sensitized for only 5 h as shown in Fig. 4.

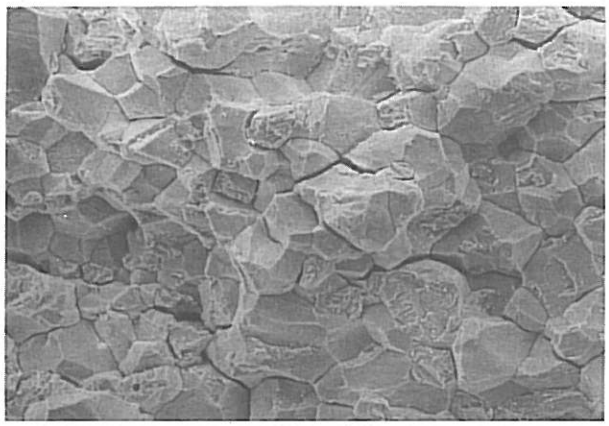


FIG. 3. S.E.M. fractograph of a 24 h sensitized 304 austenitic stainless steel specimen strained in solution at a crosshead speed of 9.8 nm/s. Fractograph shows faceted intergranular and little transgranular cleavage fracture.



FIG. 4. S.E.M. fractograph of a 5 h sensitized 304 austenitic stainless steel specimen strained in solution at a crosshead speed of 9.8 nm/s. Fractograph shows transgranular cleavage and little intergranular fracture.

2. Effect of cold work

Cold worked 304 austenitic stainless steel specimens exhibited pronounced embrittlement at lower crosshead speeds of (833.3 nm/s to 9.8 nm/s). The resulted fracture surfaces exhibited similar features to that observed for annealed specimens as shown in Fig. 5. Little ductile tearing was observed at the middle of fracture surface for specimens tested at the lowest crosshead speed of 9.8 nm/s.

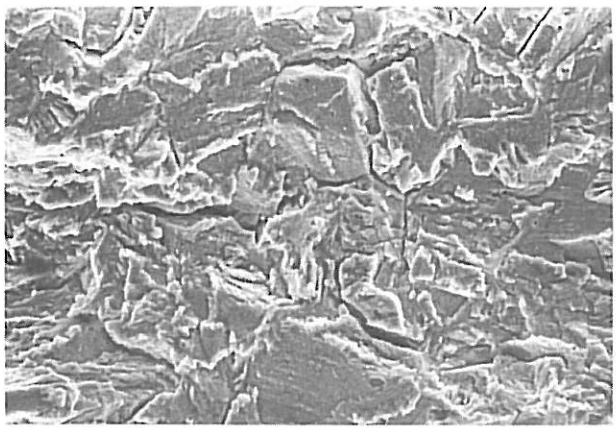


FIG. 5. S.E.M. fractograph of an 12% cold worked 304 austenitic stainless steel specimen strained in solution at a crosshead speed of 83.3 nm/s. Fractograph show both cleavage fracture and some intergranular fracture. Isolated areas of ductile tearing are observed.

3. Effect of stability

This section will show the effect of hydrogen on the two different stability austenitic stainless steels respectively less stable 304 and more stable 310 austenitic stainless steels. The degree of embrittlement was observed to increase with decreasing in crosshead speed and stability of the tested alloy. Less stable 304 austenitic stainless steel exhibited transgranular cleavage fracture and little intergranular fracture at low crosshead speeds (833.3 nm/s–83.3 nm/s) as shown in Fig. 6. Mixed mode transgranular cleavage fracture and faceted intergranular fracture was ob-

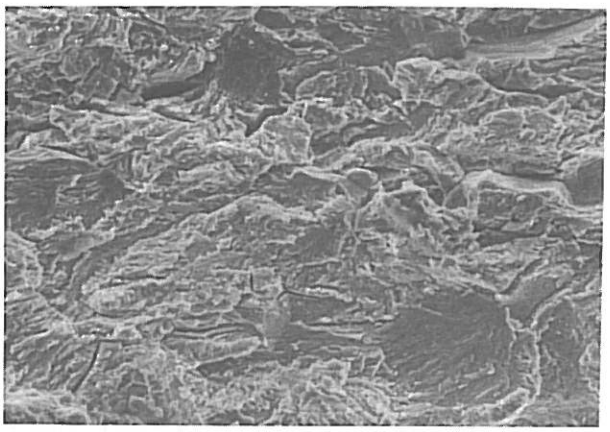


FIG. 6. S.E.M. fractograph of a 304 austenitic stainless steel specimen strained in solution at crosshead speed of 83.3 nm/s. Fractograph show cleavage fracture and some intergranular fracture.

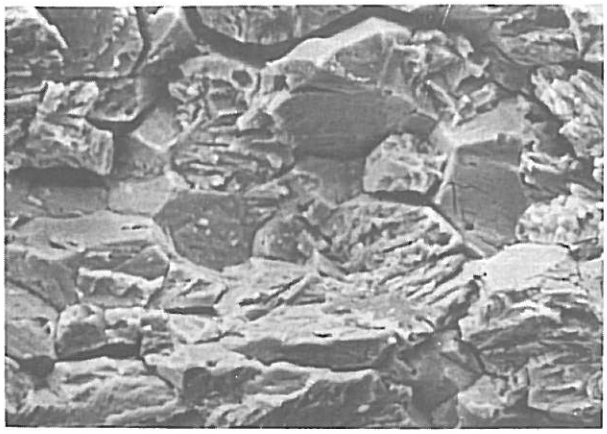


FIG. 7. S.E.M. fractograph of a 304 austenitic stainless steel specimen strained in solution at a crosshead speed of 9.8 nm/s. Fractograph show faceted intergranular fracture and some transgranular cleavage fracture.

served at the lowest crosshead speed of 9.8 nm/s as shown in Fig. 7. This faceted intergranular fracture was not reported earlier.

The more stable 310 austenitic stainless steel, which have high stacking fault energy (SFE) compare to less stable 304 austenitic stainless steel, shows less susceptibility to hydrogen embrittlement which is manifested in little changes in fracture morphology when only tested at the lowest crosshead speed of 9.8 nm/s. The change in fracture morphology was observed to be restricted at the areas in which high stress concentration attained e.g. notch and specimen edges. Both intergranular and quazi cleavage types of fracture modes were observed at these areas as shown in Figs. 8 and 9. This type of fracture was not reported earlier for this type of steel.

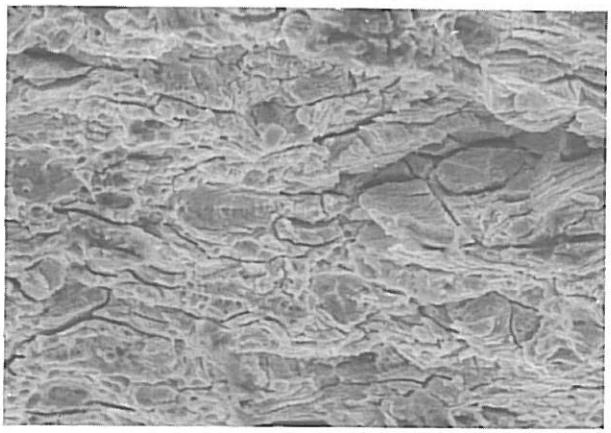


FIG. 8. S.E.M. fractograph of a 310 austenitic stainless steel specimen strained in solution at a crosshead speed of 9.8 nm/s. Fractograph shows details of fracture in the middle of the specimens, where quazi cleavage fracture and some intergranular fracture were visible.

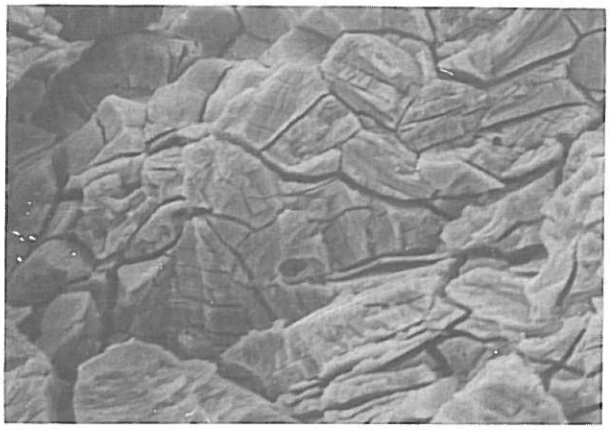


FIG. 9. S.E.M. fractograph of a 310 austenitic stainless steel specimen strained in solution at a crosshead speed of 9.8 nm/s. Fractograph show details of fracture at the specimen edge, where intergranular fracture and quazi cleavage fracture are visible.

SURFACE CRACK

Surface cracks on the surface of hydrogen embrittled less stable 304 austenitic stainless steel specimens in annealed, sensitized and cold worked condition and more stable 310 austenitic stainless steel specimens in annealed condition are shown respectively in Fig. 10–13. Both intergranular and transgranular cracks were observed on the surfaces of these tested specimens. Some of transgranular cracks were observed to propagate along or parallel to the slip bands as shown in Fig. 10 for 304 austenitic stainless steel specimens in annealed condition. Cold worked specimens exhibited less surface cracks compared to the annealed specimens as shown in Fig. 11. Sensitized specimens showed more transgranular cracks

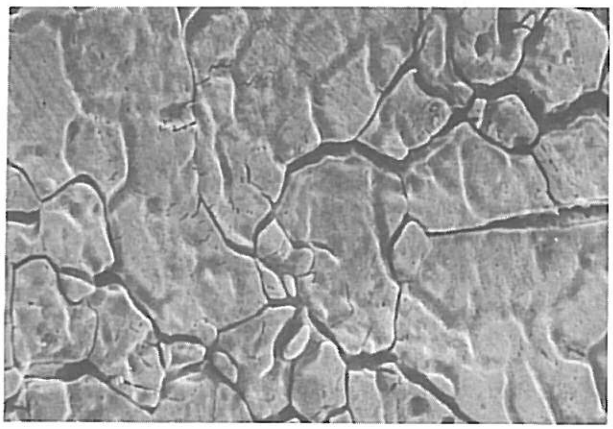


FIG. 10. S.E.M. micrograph of the surface of a 304 austenitic stainless steel specimen strained in solution at a crosshead speed of 9.8 nm/s. Micrograph show intergranular and many transgranular cracks. Some of transgranular cracks are appeared to be parallel to the slip bands.



FIG. 11. S.E.M. micrograph of an 12% cold worked 304 austenitic stainless and specimen strained in solution at a crosshead of 9.8 nm/s. Micrograph shows very little surface cracks.

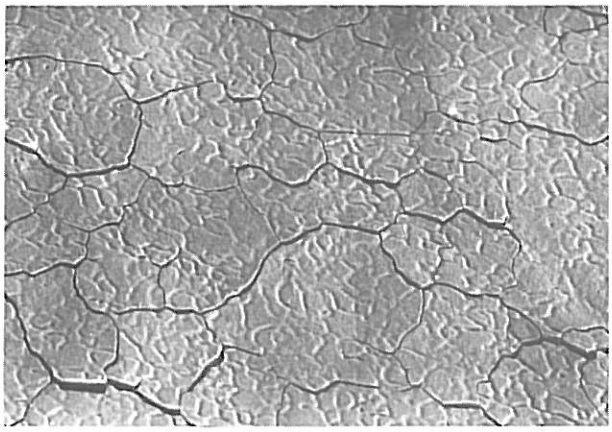


FIG. 12. S.E.M. micrograph of a 5 h sensitized 304 austenitic stainless steel specimens strained in solution at a crossheadspeed of 9.8 nm/s. Micrograph shows both transgranular and intergranular cracks.

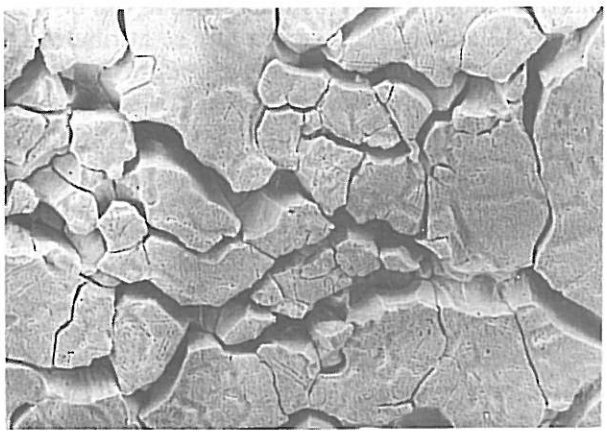


FIG. 13. S.E.M. micrograph of a 24 h sensitized 304 austenitic stainless steel specimen strained in solution at a crosshead speed of 9.8 nm/s. Micrograph show deep intergranular cracks and grain spall off. Transgranular cracks are visible.

compared to that observed for annealed specimens as shown in Fig. 12. Grain spall off was observed in specimens sensitized for 24 h as shown in Fig. 13. The extent of surface cracking for sensitized specimens was observed to increase with increasing in sensitizing time.

DISCUSSION

It is clear that the results naturally group themselves by heat treatment. If samples are aged (sensitized), the fracture mode is predominantly intergranular [13, 14, 15]. If the samples are only solution annealed, the crack usually proceeds along a transgranular path [10]. The intergranular fracture of sensitized specimens was attributed to the chromium depletion at the grain boundaries [13, 14]. This depletion makes the material at the grain boundaries, less stable, much more susceptible to α-martensite formation [14]. Since the martensite is much susceptible to hydrogen cracking, intergranular fracture occurs [14]. One should also note that martensite forms, at the grain boundaries, a continuous path for easy cracking through the sample [9]. This continuity is far more important than the volume percent of martensite [14].

The above discussion is in agreement with the observation of intergranular fracture only in the specimens sensitized for 24 h as shown in Fig. 2. Transgranular cleavage fracture was the predominant fracture mode for 5 h sensitized specimens. This results can be attributed to the less or/and non continuous martensite formation in 5 h sensitized specimens. Short sensitization time leads to less chromium depletion which in turn results in less martensite formation.

Faceted intergranular fracture was observed as well in the solution annealed 304 austenitic stainless steel specimens tested in hydrogen at the lowest crosshead speed of 9.8 nm/s as shown in Fig. 7. This result can be attributed mainy to the high hydrogen concentration at the grain boundaries as a result of dislocation bearing hydrogen piled-up at these boundaries [10]. Such clear faceted intergranular fracture was not reported before and may be produced as a result of using a very slow crosshead speed of 9.8 nm/s in this work which allow high hydrogen concentration to be attained.

Transgranular cleavage was observed in annealed and cold worked less stable 304 austenitic stainless steel specimens at low crosshead speeds (833.3 nm/s–9.8 nm/s) as shown in Figs. 5 and 6. This type of fracture can be attributed to the high hydrogen concentration on the cleavage plane of (100) owing to pile – up of hydrogen laden dislocations at this plane [17]. The extent of this fracture was observed to

increase with lowering in crosshead speed. At the lowest crosshead speed used (83.3 nm/s and 9.8 nm/s), cleavage fracture was observed to extend over the all fracture surfaces. In addition, intergranular fracture began to appear owing to availability of hydrogen due to long time to failure at these crosshead speeds.

Fracture surfaces for more stable 310 austenitic stainless steel specimens exhibited intergranular and quazi cleavage types of fracture at the lowest crosshead speed of 9.8 nm/s as shown in Figs (8 and 9). This result shows that even more stable austenitic stainless steel, with high SFE, can be embrittled when high hydrogen concentration is introduced to the sample. This type of fracture was not reported earlier and can be attributed to the severity of the embrittlement test. High hydrogen concentration changes the slip mode from easy cross slip to coplanar motion, which in turn makes dislocations bearing hydrogen to pile-up at the grain boundaries or any other obstacles to the dislocations movement, and increases the hydrogen concentration at these locations [17].

The effect of stability of austenitic stainless steel on the susceptibility to hydrogen embrittlement can be attributed to the differences in the austenite stability, which can be calculated using the emperical formula by Gladman *et al* [18].

$$Md_{30}(C) = 497 - 462(C+N) - 9.2(si) - 8.1(Mn) - 13.7(cr) - 20(Ni) - 18.5(Mc)$$

Utilizing the above formula shows that 304 austenitic stainless steel has Md_{30} above room temperature and its austenite phase is unstable and can be transformed to martensitic phases α^- and ε in presence of hydrogen [3, 9]. In contrast, more stable 310 austenitic stainless steel has more stable austenite phase and will only transform to ε phase owing to its very low Md_{30}. The presence of α^--martensite phase in less stable 304 austenitic stainless steel greatly enhances the hydrogen diffusivity owing to high hydrogen diffusivity of ferrite phase (bcc) structure [19] (10^{-8} cm^2/s) compare to only (10^{-12} cm^2/s) for austenite phase (fcc) structure [10].

The other important factor which controls the susceptibility of austenitic stainless steel to hydrogen embrittlement is the stacking fault energy (SFE) for the tested alloy [7]. The SFE of an alloy determines whether cross slip or coplanar motion is predominant. It is extensively reported in the literature that the hydrogen embrittlement of austenitic stainless steel resulted from lowering in SFE by absorbed hydrogen [8, 20]. Lowering in SFE energy leads to changes in slip mode, from easy cross slip to coplanar motion. Coplanar motion occurs in materials with low SFE and leads to dislocation pile-up at obstacles [7]. In the region of pile-up the hydrogen concentrations would be high.

In the current work, the stacking fault energy (SFE) for tested steels were measured using Schramm and Reed formula [21].

$$SFE\,(mJ/m2) = -53 + 6.2(Ni) + 0.7(cr) + 3.2(Mn) + 4.3(Mo)$$

The calculated values are 18 mJ/m^2 and 93 mJ/m^2 respectively for 304 and 310 austenitic stainless steels. This wide differences in the SFE values explain the differences in the susceptibility of these two steels to hydrogen embrittlement.

Surface cracks were observed on the surface of the annealed, sensitized and cold worked specimens. Intergranular cracks were observed and can be attributed to the action of hydrogen and the tensile test. Transgranular cracks were observed to propagate along or parallel to the slip bands as shown in Fig. 10. These cracks were observed by others and suggested to propagate along (110) and (111) planes [22, 23, 24]. This type of fracture may correspond to the fracture through the ε phase [23] or along ε/γ interface [23], since s phase forms in both alloys and has (111) habit plane.

Less cracking was observed in 12% cold worked 304 austenitic stainless steel compare to non cold worked specimens as can be seen by comparing Fig. 10 with Fig. 11. This can be attributed to the pre-existing of α martensite in the surface of cold worked specimens which may provide a rapid path for hydrogen to diffuse away from the specimen surface [25]. Thus preventing the build up of the critical concentration of hydrogen thought to be necessary for the formation of the expanded phases (γ^* and ε^*) [25, 26].

The surface of both 5 h and 24 h sensitized specimens exhibited more transgranular cracks than those on the surface of annealed specimens when the test was carried out at low crosshead speed as can be seen in Figs 12 and 13. This results can be attributed to the high content of martensite phases in sensitized specimens. These phases (α^- and ε) can act as crack initiation site or/and active path for hydrogen diffusion [10].

Specimens sensitized for 24 h showed more transgranular cracks and grain spall off compared to that for 5 h sensitized specimens. This result can be attributed to the embrittlement severity for 24 h sensitized specimens resulted from continuous precpitation of carbides and presence of high percentage of α^- martensite.

CONCLUSION

1. Less stable 304 austenitic stainless steel specimens exhibited both intergranular and transgranular

types of fracture mode when the test was carried out at low crosshead speeds of 83.3 nm/s and 9.8 nm/s.

2. 12% Cold worked 304 austenitic stainless steel specimens exhibited similar fracture morphology to that observed for non cold worked specimens over the most crosshead speed used.

3. Fracture surface of 5 h sensitized 304 austenitic stainless steel specimens exhibited cleavage fracture over all crosshead speeds used. However, intergranular fracture was the predominant fracture mode for 24 h sensitized specimens at low crosshead speeds of 83.3 nm/s and 9.8nm/s.

4. The extent of intergranular fracture insensitized specimens was observed to depend on both sensitization time and crosshead speed used.

5. More stable austenitic stainless steels can be embrittled in presence of high hydrogen fugacity.

6. Fracture surface of more stable 310 austenitic stainless steel exhibited both intergranular and quazi cleavage types of fracture node when tested at the lowest crosshead speed of 9.8 nm/s.

7. The results obtained in this work, support the observation of less surface cracking in hydrogen embrittled cold worked 304 austenitic stainless steel.

ACKNOWLEDGEMENT

I would like to express my sincere thanks to the Petroleum Research Centre for the Financial support while carrying out this work. Thanks are also extended to Professor John C. Scully at Leeds University, England for his constant interest and encouragement during the course of this work.

REFERENCES

[1] Vennett, R.M. and Ansell, G.S., 1969, Trans. ASM, 62, pp. 1007–1013.
[2] Benson, R.B., Dann, R.K. and Roberts, L.W., 1968, Trans AIME, 242, pp. 2199–2205.
[3] Holzworth, M.L. and Louthan, M.R., 1968, Corrosion, 24, pp. 110–124.
[4] Thompson, A.W., 1974, Hydrogen in Metals, I.M. Bernstein and A.W. Thompson eds., pp. 91–102, ASM, Cleveland, OH.
[5] Menta, M.L. and Burke, J., 1975, Corrosion, 31, pp. 108–110.
[6] Vaughan, D.A., Phalen, D.L., Beterson, C.L. and Boyd, W.K., 1963, Corrosion, 19, pp. 315t–325t.
[7] Odegard, B.C., Brooks, J.A. and West, J.A., 1976, Effect of Hydrogen on Behaviour of Materials, (A.W. Thompson and J.M. Bernstien eds.), pp. 631–641, AIME, New York, NY.
[8] Louthan, M.R. Caskey, G.R. Donovan, J.A. and Rawl, P.E., 1972, Mater. Sci. Eng., 10, pp. 357–368.
[9] Holzworth, M.L., 1969, Corrosion, 25, pp. 107–115.
[10] Tien, J.K., Thompson, A.W., Bernstien, I.M. and Richardson, R.V., 1976, Metall. Trans., 7A, pp. 821–829.
[11] Zheng, W. and Hardie, D., 1991, Corrosion Science, 32, pp. 23–26.
[12] Hannien, H. and Hakkarainen, T., 1980, Corrosion, 36, pp. 97–51.
[13] Briant, C.L., 1978, Metall. Trans., 9A, pp. 731–733.
[14] Briant, C.L., 1978, Scripta Met., 12, pp. 541–542.
[15] Hannula, S.P. Hanninen, H. and Tahtinen, S., 1984, Metall. Trans., 15A, pp. 2265–2211.
[16] Caskey, G.R., 1977, Scripta Met., 11, pp. 1077–1083.
[17] West, J.A. and Louthan, M.R., 1974, Metall. Trans., 10A, pp. 1675–1682.
[18] Pickering, F.B., Physical Metallurgy and the Design of Steels, Applied Science, Publishers Ltd., London, 1978, p. 229.
[19] Lange, K.W. and Konig, H.J., Proc. Second Int. Conf. on Hydrogen in Metals, 1977, p. 1A5, Pergamon, New York.
[20] Hartson, J.D. and Scully, J.C., 1970, Corrosion, 20, pp. 387–395.
[21] Schramm, R.E. and Reed, R.P., Metall. Trans., 6A, pp. 1345–1351.
[22] Liu, R., Narita, N., Altstetter, C.J., Birnabaum, H.K., 1980, Metall. Trans., 11A, pp. 1563–1574.
[23] Narita, N., Altstetter, C.J. and Birnabaum, H.K., 1982, Metall. Trans., 13A, pp. 1355–1365.
[24] Eliezer, D.E., Chakkrapani, D.G., Altstetter, C.J. and Pugh, E.N., 1979, Metall. Tans., 10A, pp. 935–941.
[25] Bently, A.P. and Smith, G.C., 1986, Scripta Met., 20, pp. 729–732.
[26] Bently, A.P. and Smith, G.C., 1986, Metall. Trans., 17A, pp. 1593–1600.

PRJ, Vol. 7 (January 1995); P. 43–59, 12 FIGS, 4 PLATES.

NAFOORA–AUGILA UNIT: RESERVOIR PERFORMANCE AND THE ROLE OF GRANITE PRODUCTIVITY-A CASE STUDY

N. A. Berruin* and Y. S. Gherryo**

الدور الإنتاجي للجرانيت في حقل النافوره–أوجله المشترك

نوري بالروين و يوسف السنوسي قريو

تراجع الورقة الدور الإنتاجي للجرانيت في حقل النافورة – أوجلة بليبيا.

ينتج الحقل من تراكيب ثلاثة ؛ تاقرفت (Tagrifet limestone) والباهي (Bahi sandstone/conglomorate) وصخور القاعدة الغرانيتية (Granite) المتشققة. تعتبر هذه التراكيب الثلاثة المنتجة كممكن واحد متصل.

بدأ الإنتاج في هذا الحقل سنة 1966 حيث تبع ذلك هبوط حاد في ضغط المكمن وارتفاع في نسبة الغاز إلى نسبة النفط كنتيجة لهبوط الضغط مما حتم استخدام تقنية حقن الماء لإعادة الضغط إلى المستوى المطلوب. جربت هذه العملية بالفعل على جزأ من المكمن، ثم عممت على كل المكمن. حدث نتيجة إلى استخدام هذه التقنية هبوط في انتاجية هذا الحقل الأمر الذي استوجب استخدام تقنية رفع الضغط باستخدام الغاز.

أنتج الحقل أكثر من 900 مليون برميل وكان أغلب الإنتاج من الآبار التي اخترقت تكوين صخور القاعدة الغرانيتية.

ABSTRACT

This paper discusses the role of Granite productivity in the Nafoora–Augila Unit, Nafoora Field, Libya. Three distinct lithologic members, Sandstone, Limestone and Granite constitute an interconnected single reservoir. To date this reservoir has produced more than 900 million barrels of oil. Wells penetrating Granite only have contributed significantly to this field performance. The salient characteristics of the Granite member in this reservoir are discussed along with the overall performance of this prolific reservoir.

INTRODUCTION

This paper reviews the reservoir performance of the Nafoora–Augila Unit in Nafoora Field, Libya. The Nafoora–Augila Unit is one of the largest oil fields in the southeastern part of the prolific Sirte Basin, located about 350 km southeast of Benghazi. The field was discovered in 1965 with the drilling of well G-2 in concession 51, and well D-1 in concession 102. As of November 2, 1971 the two fields were unitized, with the Arabian Gulf Oil Company (AGOCO) as the current operator of the Unit.

Production commenced in July of 1966. Initial production from this field resulted in a rapid decline in reservoir pressure, and a sharp rise in the field gas oil ratio due to the absence of pressure support which led to the decision of maintaining the reservoir pressure by water injection. Therefore, a waterflood pilot was initiated in May of 1969, which was developed into a full scale line-drive water injection by July of 1974. Also, well productivities started to decline and in anticipation of the increased water production due to the implementation of the waterflood, artificial

*Teknica (UK) Ltd., Holborn Tower, London WCIV 6PW.
**Arabian Gulf Oil Company, Benghazi, G.S.P.L.A.J.

lifting by gas lift was initiated early in the life of the field.

The field is productive from three distinct lithological members; the Tagrifet limestone, the Bahi sandstone/conglomorate complex both of Cretaceous age, and the fractured Granite basement of late Precambrian age. The Tagrifet pay is on top of the Bahi, or on top of the Granite where the Bahi is missing. The three oil-bearing horizons constitute a single and interconnected oil reservoir, which is called Tagrifet–Bahi–Granite reservoir (TBG).

The 35.5° API oil of the TBG is undersaturated with an average bubble point pressure of 2465 psig. The initial reservoir pressure is 4272 psig at depth of 8700 feet subsea. The original GOR is 463 Scf/STB. The original oil in place is estimated at 4.3 billion STB with an estimated recoverable reserves of about 1.78 billion STB. As of the end of 1989, 874 million STB of oil, or about 49.1% of the recoverable reserves has been produced.

Both of the sedimentary rocks and the granite are equally important in contributing to the field production. Production from the Granite comes mainly from fractures and possibly from zones of intergranular porosity believed to be associated with fractures. The vast difference between OOIP calculated by material balance and volumetrically calculated OOIP in the sediments (Tagrifet and Bahi) gives credence to the existence of oil in the Granite. The oil productivity of the Granite is further proven by prolific oil production from certain wells that are completed (open-hole) mainly in the Granite.

In relation to the sediments of the Tagrifet limestone and the Bahi sandstone, the Granite has historically been known to be a high rate producer with relatively high cumulative production at locations where the necessary reservoir quality parameters such as fracture-type porosity and good permeability are favorable.

GEOLOGICAL SETTING

The sedimentary rocks of the Nafoora–Augila Unit were deposited over the crest of an extensive Precambrian or early Paleozoic granite high. This regional high encompasses an area greater than a thousand square miles which had topographic relief in excess of two thousand feet in Upper cretaceous time, Fig. 1. During the general subsidence of the Sirte Basin, this large triangular block (as well as all other horst blocks in the basin) subsided more slowly than the areas on the down thrown sides of the faults forming the block. With continued subsidence, the large triangular block began to tilt slightly to the west, and the subsidence and westward tilting have continued to the present. As a result about 8500 feet of sediments were deposited over the highs in Nafoora and Augila Fields.

The Precambrian granite, encountered in Concessions 51 and 102, occurs as a chain of buried hills, uplifted and severely eroded during the hiatus prior to the deposition of, the unconformably overlaying, Cretaceous elastics and carbonates of the Bahi complex and Tagrifet Formation.

The basement rocks in this field are gradations of granophyre, granophyric granite as well as rhyolite. The rock types consist of quartz and alkali feldspars with biotite. Feldspars are granulitized along fractures and or seriticized and kaolinized to varying degrees from few feet to several hundred feet below the igneous suface. The lower areas on the land mass at the time of burial are represented by fresher granites as intense erosion stripped away much of the highly kaolinized upper portions of the granite.

Whether the granite basement is an emplacement mass or the product of granitization of early sediments, in which case grossly correlative log response characteristics might be retained, remains unstudied. That the basement complex has had a long and complex history of repeated periods of deposition and erosion have probably obliterated the evidence beyond recovery.

The granite is estimated to be of Early Paleozoic or late Precambrian (600–1250 million years) age, and it may have been affected by a subsequent hydrothermal tectonic events during the Lower Paleozoic. Porosity in the basement is the result of fracturing and weathering. Porosity distribution is currently not well defined, but production from the Granite indicates a large accumulation of oil. The quality of the basement reservoir is dependent upon fracturing and weathering. Fracture-type porosity with resulting fair to good permeability occurs along fracture zones. Good oil shows throughout zones within the granite also suggest secondary matrix porosity associated with weathering, some of which is probably related to zones of fracturing (Plates 1, 2, 3, and 4). It is probable that deep weathering of the granite took place along joints and fractures. It is likely that these fractures were developed either by stress release with removal of overburden and/or through tectonic forces coincident with movement along the Nafoora fault zone. Therefore, production from the granite is from fractures and zones of intergranular porosity believed to be associated with fractures.

Mudlog "shows" are frequent throughout the intervals of Granite penetration. The deepest such show is down to 10,020 feet, or about 1000 feet below the Granite top in well B-56-51, Fig. 2.

Pressure data, drill stem tests, sidewall cores, logs and several BHTV logs all show a deeply weathered basement complex, with numerous fractures. The basement produced in several wells (D-2, D-9, D-18,

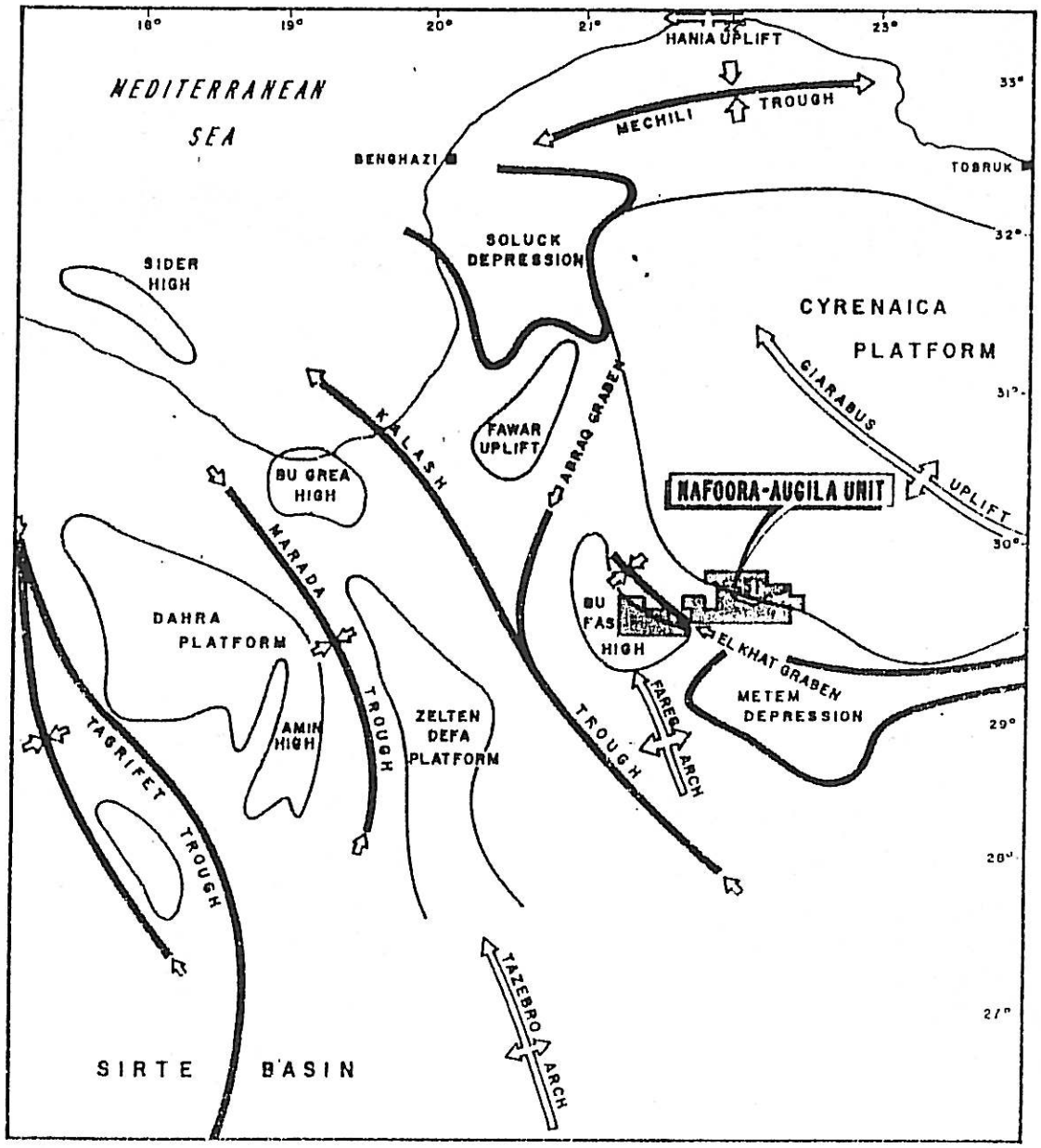


FIG. 1. Nafoora–Augila Unit location map.

D-42, G-13, G-20, G-30, G-54, G-62A, G-68, G-83, G-87, G-88, G-157, G-243, G-251, G-253, and G-254) and it also produces into the over-laying and on-lapping Bahi sands and Tagrifet Carbonates.

DETECTION OF FRACTURES

Fractures were detected with conventional logs. Although the tools do not detect fractures directly, experience gained in the evaluation of this field makes it possible to recognize fractures from the logs. The existence of fluids in the fractures cannot, however, be reliably determined.

The first log to be considered is the drillers log used during drilling of the well. The driller log usually indicates a significant timing decrease in fractured zones. The occurrence of partial loss of mud or drilling fluid is frequent. The following logs were often used for fracture identification:

—Gamma Ray
—Resistivity
—Acoustic
—Density
—PEF
—Natural Gamma Ray Spectrometry

Although not all productive intervals can be clearly picked from the logs, zones of apparent porosity are usually indicated on the Density, Neutron, and Sonic

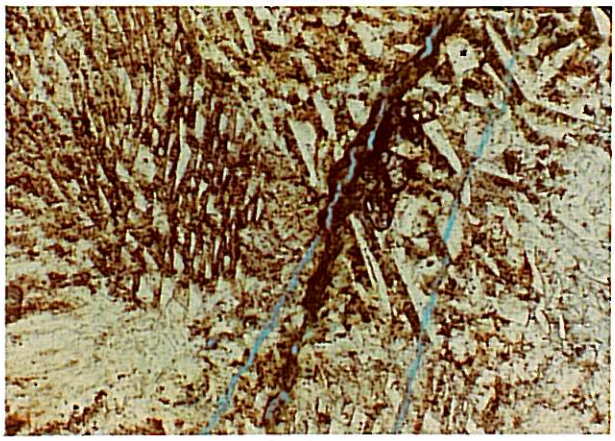


PLATE 1: Well: G253-51; Depth: 9065'; Lithology: Gph; Porosity: 3% est.; Magnification: × 160.

This view exhibits classic graphic texture typical of a granophyte. The graphic texture results from the intergrowth of quartz (clear) and feldspar (turbid, brown, sericitised) as they crystallised from the cooling magma. The granophyte is cut by hairline fractures partially filled with indeterminate, green authigenic clay (probably illite; 7F). Free fracture porosity is highlighted by the blue-dyed resin (8/9D).

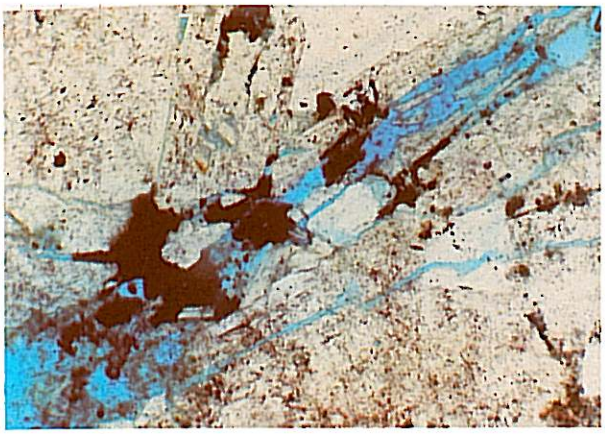


PLATE 2: Well: G2-51; Depth: 8733'; Lithology: HgG; Porosity: 2% est.; Magnification: × 160.

The plate illustrates a part-open, part-cemented fracture cutting a sample of micrographic granite. Free porosity in the fracture is highlighted by blue-dyed resin. The fracture is partially cemented by an opaque mineral (probably pyrite; 5G) and an indeterminate, green, authigenic clay (probably illite; 2J). The relative timing of the pyrite and illite cements cannot be determined from the evidence seen here.

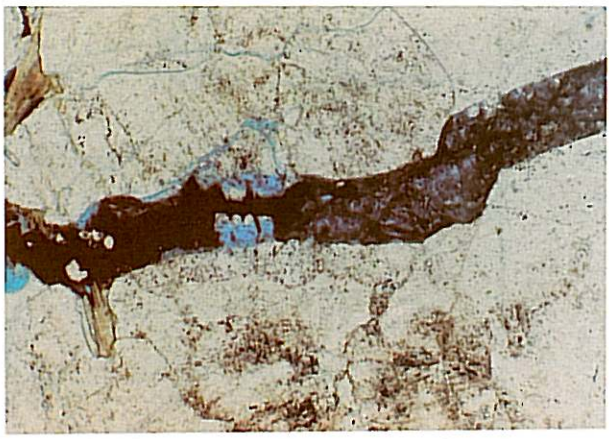


PLATE 3: Well: B2-102; Depth: 8822'6"; Lithology: GR; Porosity: 2% est.; Magnification: × 160.

The fracture illustrated here cross-cutting undeformed granite is partially cemented by blocky ferroan carbonate (blue-stained, probably calcite, e.g. 5F), and also part-filled by bitumen (black, e.g. 12E). Remaining open porosity is shown by the blue-dyed resin (1OE).



PLATE 4: Well: B2-102; Depth: 8822'6"; Lithology: GR; Porosity: 2% est.; Magnification: × 64.

This photomicrograph shows another fracture in the granite illustrated by Plate 73. In particular, it illustrates a hairline fracture part-filled by bitumen (e.g. 5G). Remaining open fracture (13D) porosity and small amounts of leached feldspar porosity is surrounding areas of the wallrock (4E, 5H, etc.) are highlighted by blue-dyed resin.

Logs and possible fractures are generally noted through log characteristics on the acoustic devices, Fig. 3. It is difficult however, to accurately position fractures and it is possible for fractures to remain undetected by the logs.

The Granite sections drilled and logged do exhibit distinctive porous interval responses. These zones of indicated porosity probably reflect well-bore intersections with fracture-planes along which deep solution and chemical "weathering" have induced the channels and void space which make the Granite a functional petroleum reservoir within the Nafoora–Augila Unit.

DRILLING AND COMPLETION

Due to the fact that fractures cannot be precisely identified and to avoid the possibility of cementing off fractures, casing was usually set few feet into the granite and the Granite was completed as an open-hole.

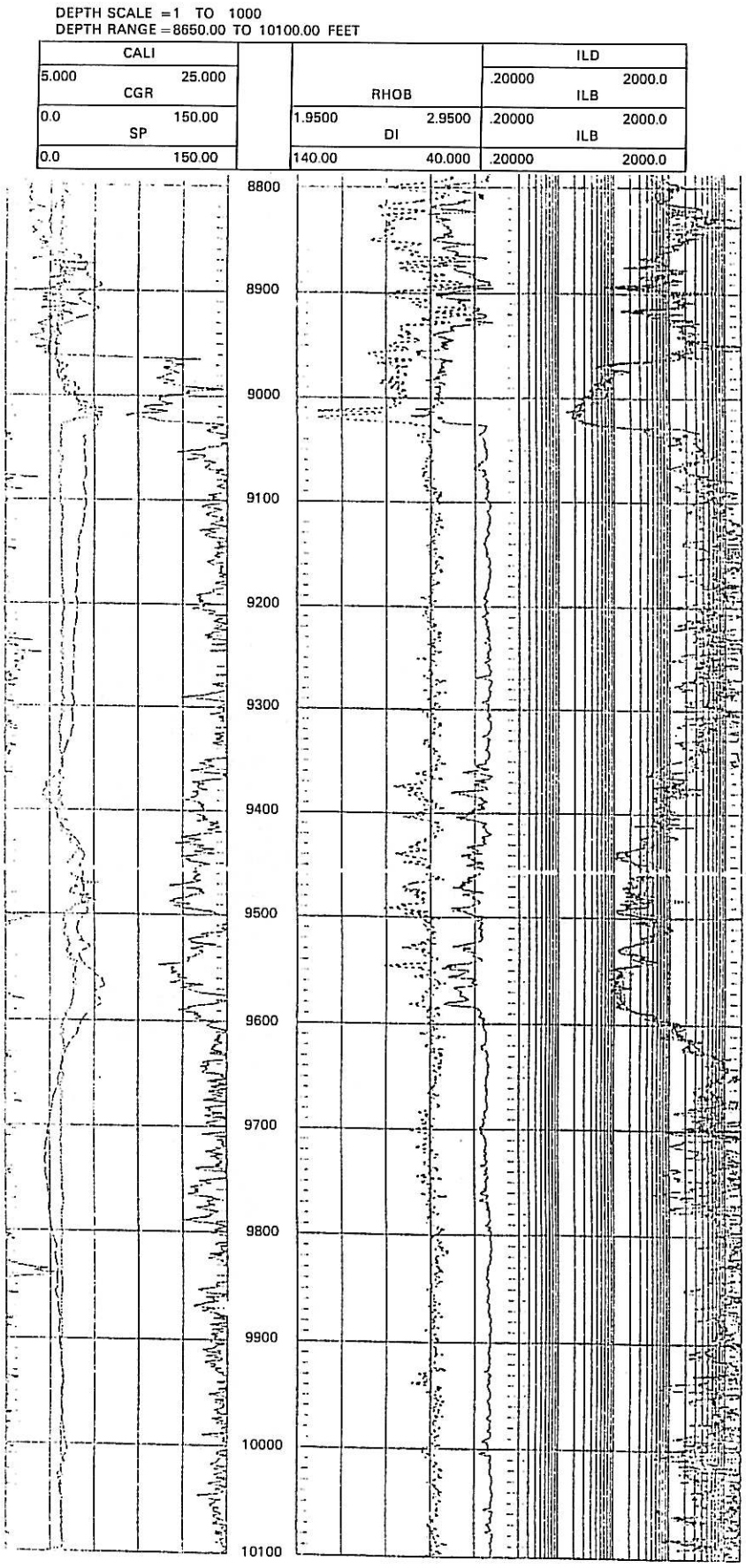


FIG. 2. Well G-56.

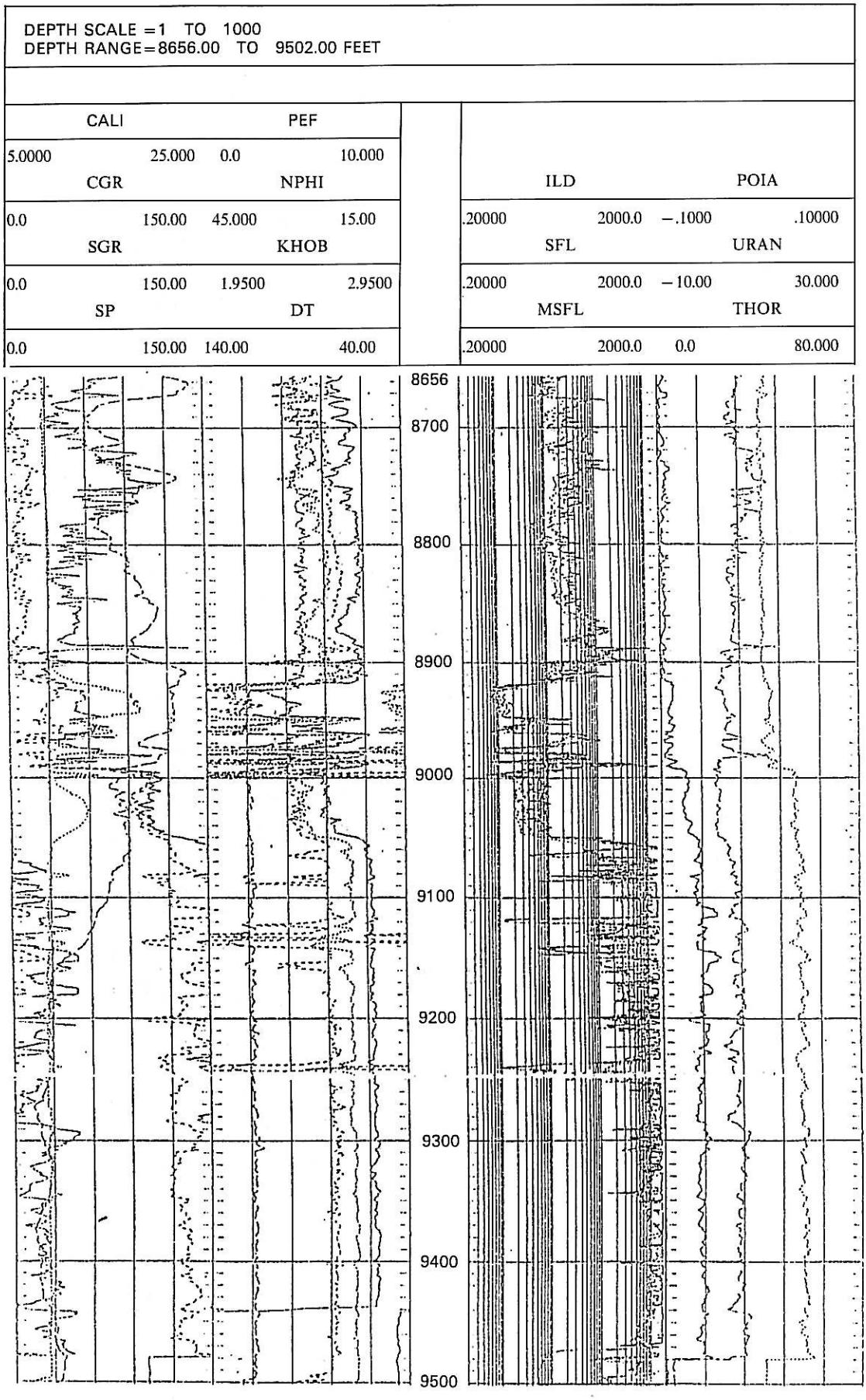


FIG. 3. Density, Neutron and Sonic logs (Well G-243).

RESERVOIR STUDIES

Numerous reservoir studies in the early life of the field were conducted mainly to evaluate the original oil in place, and the natural reservoir drive mechanism. Pressure maintenance by water injection was also investigated in these early studies in order to maintain high production levels, and eventually to improve the ultimate oil recovery.

These early studies concluded that, based on volumetrics and material balanced calculations, the Granite part of the TBG contained about 32% of the total OOIP. The rest of the OOIP was allocated to the sedimentary parts of the TBG.

As the number of drilled wells increased during the initial phases of field development, further reservoir studies continued for the same purpose. In 1971 through the use of a two dimensional areal simulator, the two operators jointly conducted a pre-unitization reservoir study of the TBG, which laid the grounds for the current Nafoora–Augila Unit. Among the conclusions of their study the OOIP was estimated to be 4300 MMSTB, the recovery mechanism was solution gas drive with an estimated recovery factor of 13%, and an ultimate oil recovery by a line-drive waterflood of 41%. The joint study had allocated 37% of the OOIP to the Granite, and 63% to the overlaying sedimentary rocks of the Tagrifet and the Bahi. Hence the current waterflood was implemented on these bases.

In 1982 a reservoir simulation study using a three-dimensional, three-phase model was conducted to provide AGOCO with an overall engineering and operating plan which would maximize oil production from the TBG reservoir. The study assumed that the OOIP within the unit boundaries to be 7000 MMSTB of oil, but did not attribute any of that to the Granite although significant production had come from wells that were completed mainly into the Granite. One of the problems that faced this study was the definition of the bottom layer, which was associated mainly with the granite. Therefore, this layer was omitted; a decision that was not agreeable to the operator.

The additional OOIP, which this study had come up with, was assumed to be attributed to a tight member in the Tagrifet limestone. However, this hypothesis was tested by performing some of the wells into the tight zones only. The completed intervals did not yield any significant amounts of fluids. But these wells were completed into other productive intervals.

Based on the earlier studies and on AGOCO's experience with the history of oil production from water injection into the Granite in many wells, it was agreed that the Granite should be considered as an oil bearing and/or a conduit in some areas of the field. Therefore a new scope of work was defined in order to perform a new study in phases. A consulting firm was contracted to conduct the first phase, which is concerned mainly with the reservoir geology, utilizing all geological, petrophysical, and production information collected since the last study. The main objectives of this study are to develop a better understanding of the reservoir geology of the TBG, to define the Granite as an oil reservoir, and to obtain a model layering consistent with geological layers to be used in the upcoming reservoir simulation study.

RESERVOIR PERFORMANCE

Fig. 4 shows the primary and waterflood performance of the TBG reservoir. The reservoir was initially above the bubble point pressure by about 1800 psi, and did not have any aquifer support. The reservoir primary performance was typical of solution gas drive mechanism, with some contribution from rock and fluid expansion, where the producing GOR had increased from an initial value of 463 scf/STB to a high of about 820 scf/STB after six years of production.

The reservoir production peaked within three years of development to reach 330,000 STB/day of oil. During this period the reservoir pressure had declined from an initial value of 4272 psia to lower than the bubble point pressure, particularly, in the center of the field where most of the profile producers are located. Beginning the middle of 1971, the field production started to decline rapidly concurrent with a continuous increase in the producing GOR.

In 1970, a water injection pilot by dump flooding was started with four wells, while efforts were made to study, design, and construct the surface injection facilities. The waterflood pilot was developed into a major line-drive flood injecting a maximum of 350,000 barrels per day of water by 1974. Prior to the initiation of the water injection water production was insignificant. Within two years of injection the decline in reservoir pressure and the increasing trend in GOR had been arrested. This was also affected by reducing oil production through control of field allowable.

By 1975, the producing GOR had stabilized, while the reservoir pressure continued to increase until it reached a value higher than 3150 psia in September of 1986. However, as the water injection facilities had undergone major revamping efforts, water injection into the TBG was ceased by the end of 1985. Hence the reservoir pressure started to decline but at a lower rate than the initial decline as the field production was curtailed at the same time in compliance with the OPEC quota which was allocated to the Nafoora field.

After the initiation of the waterflood, the water cut increased to 28% and remained constant at about the same value.

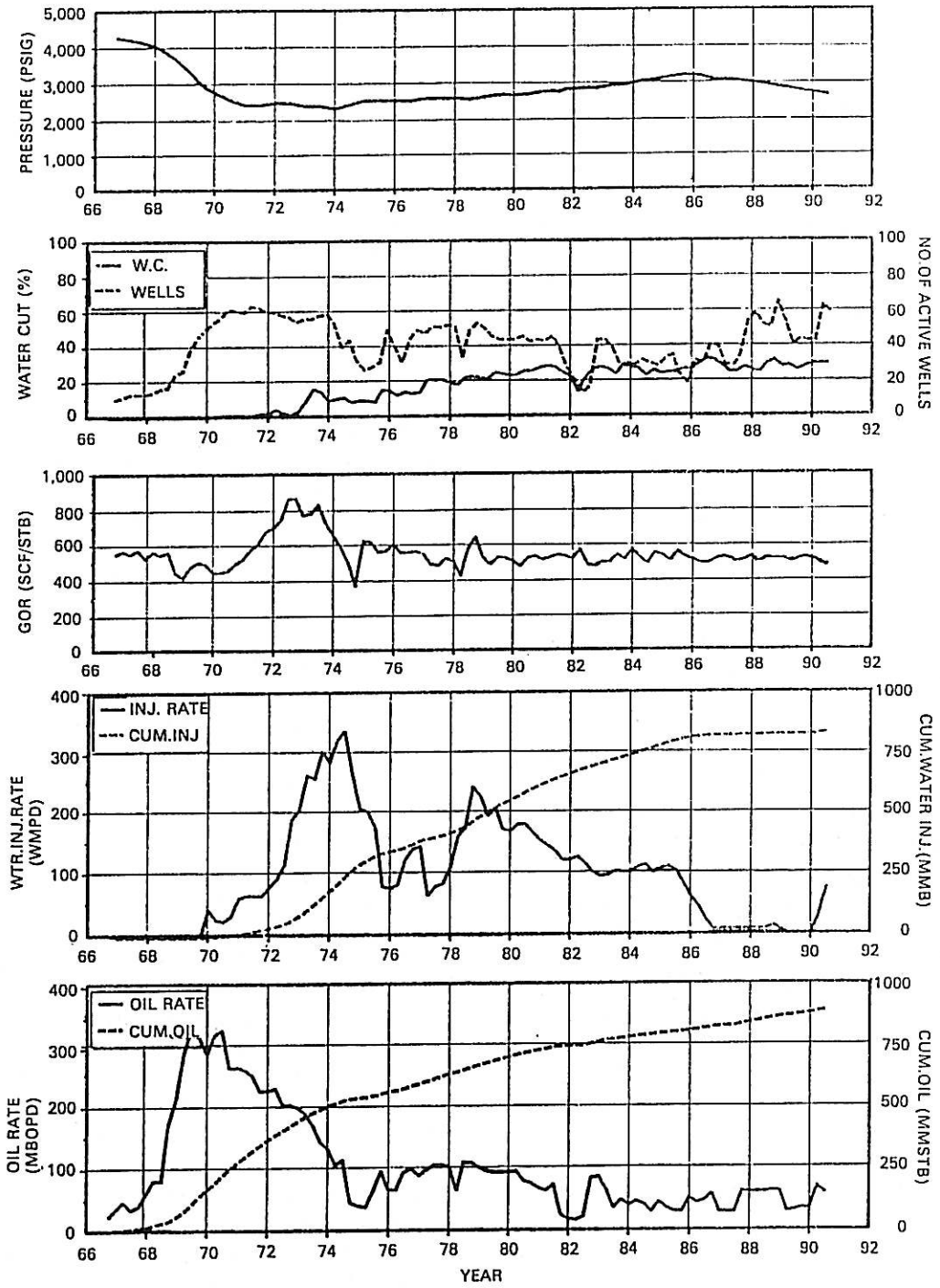


FIG. 4. Nafoora–Augila Unit/TBG Reservoir performance.

During periods of low production from the Unit the number of producing wells varied in an effort to control the level of pressure decline, and to maintain the GOR at an acceptably low values until the surface injection facilities are re-commissioned.

GRANITE OIL PRODUCTION

Indicators for granite production are taken from well completions, production tests, and production logs. Several wells have produced from the Granite, most significantly, wells G-20, G-54, G-62A, G-68, and G-243. Fig. 5 shows the location of these wells, and other wells that are known to have some flow contribution from the Granite.

Well G-20, which completed totally in the granite flowed initially at a rate of 3400 BOPD until it declined to 2000 BOPD as pressure dropped from 4300 to 2600 psi after 6 years of production. During this period it produced 5.5 MMSTB without any water production. It was then converted to an injector. No water production was observed.

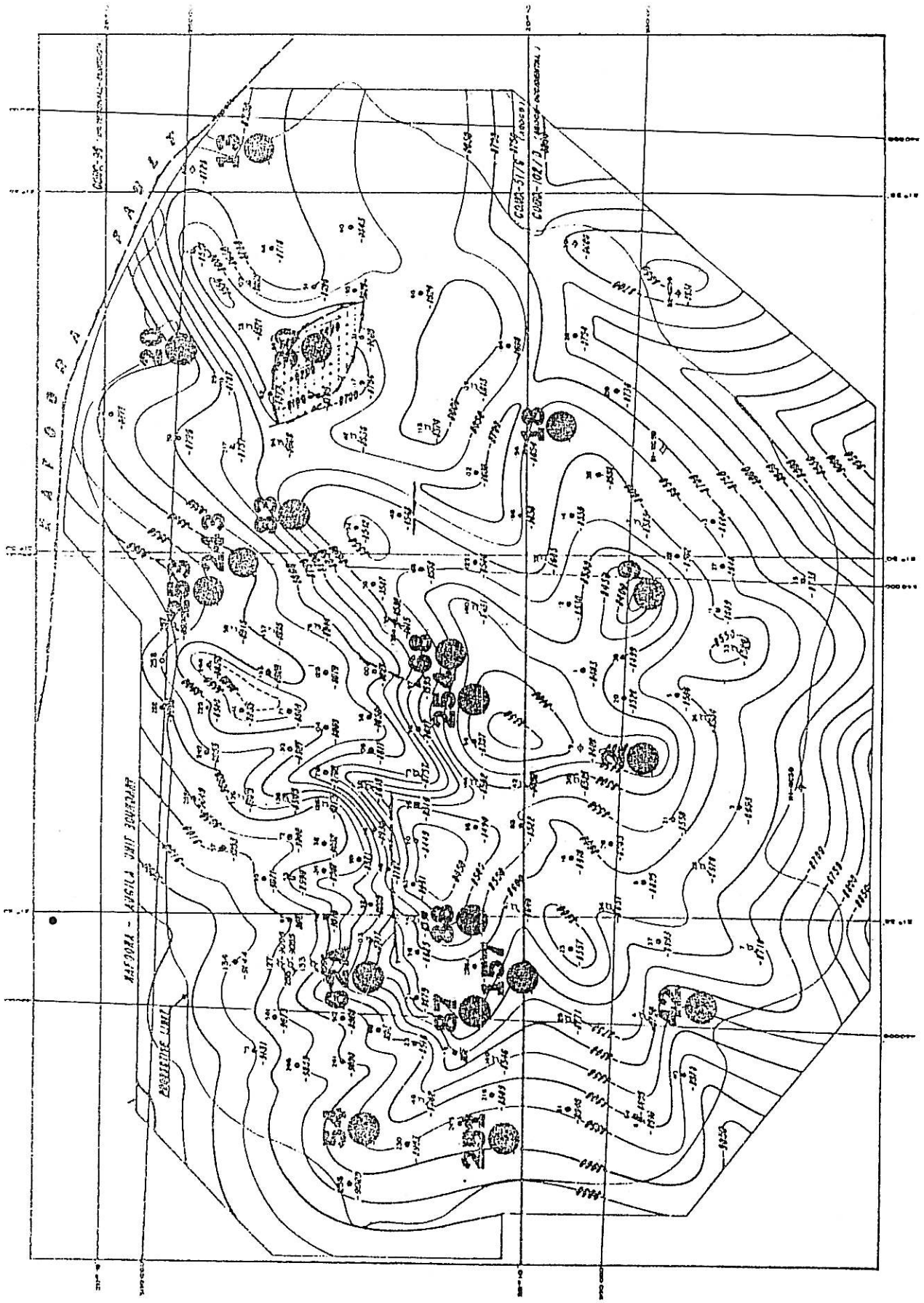


FIG. 5. Nafoora–Augila Unit (Granit STR Top). Well location.

Well G-54 flowed initially at a rate of 6950 BOPD, and declined to 3600 BOPD after four years of production That was caused by both, a drop in the reservoir pressure and an increase in water cut. Fig. 6 illustrates a cross section for this well. During this period it produced 7.3 MM STB before it was converted to an injector. Although this well was completed in the sedimentary rocks as well, production was only from the Granite as revealed from the production logs.

Well G-62a, flowed initially at a rate of 11405 BOPD declined to 7200 BOPD as the reservoir pressure dropped by 1800 psi and water cut increased to 15%. Water production in this well is attributed to water injection in the offset well G103-51 as suggested by the properties of the produced water. Well G-62a produced a total of 15.5 MMSTB before injection was initiated. Even though this well was also completed in the over-laying sediments, flowmeter surveys indicated that approximately 80% of the flow was coming from a set of perforation at the top of the granite.

Well G-68 was completed only in the granite, Figs. 7 and 8. This well flowed initially at a rate of 15750 BOPD, and then declined to 6900 BOPD with a cumulative production of 4.0 MMSTR. The reservoir pressure had also dropped by 1600 psi. The well was kept most of the time shut-in for nearly three years after the water cut increased to 70%. This water production was before the start of water injection in this area. The oil rate had fallen to a low of 1500 BOPD. As the reservoir pressure started to rise in response to waterflooding in the vicinity of well G-68, the water cut dropped to about 25% and the oil rate increased to an average of 5000 BOPD over the following ten years, Fig. 9. Production logs indicated that the flow was coming from several intervals down to 470 feet below the granite top, Fig. 10.

Well G-243, which was put on production in October of 1986, or about 20 years from the start of production from the field, had an initial rate of 4750 BOPD, declined to 1570 BOPD after cumulative production of 1.99 MMSTB. The decline was caused by a drop of 500 psi in the well's bottom-hole

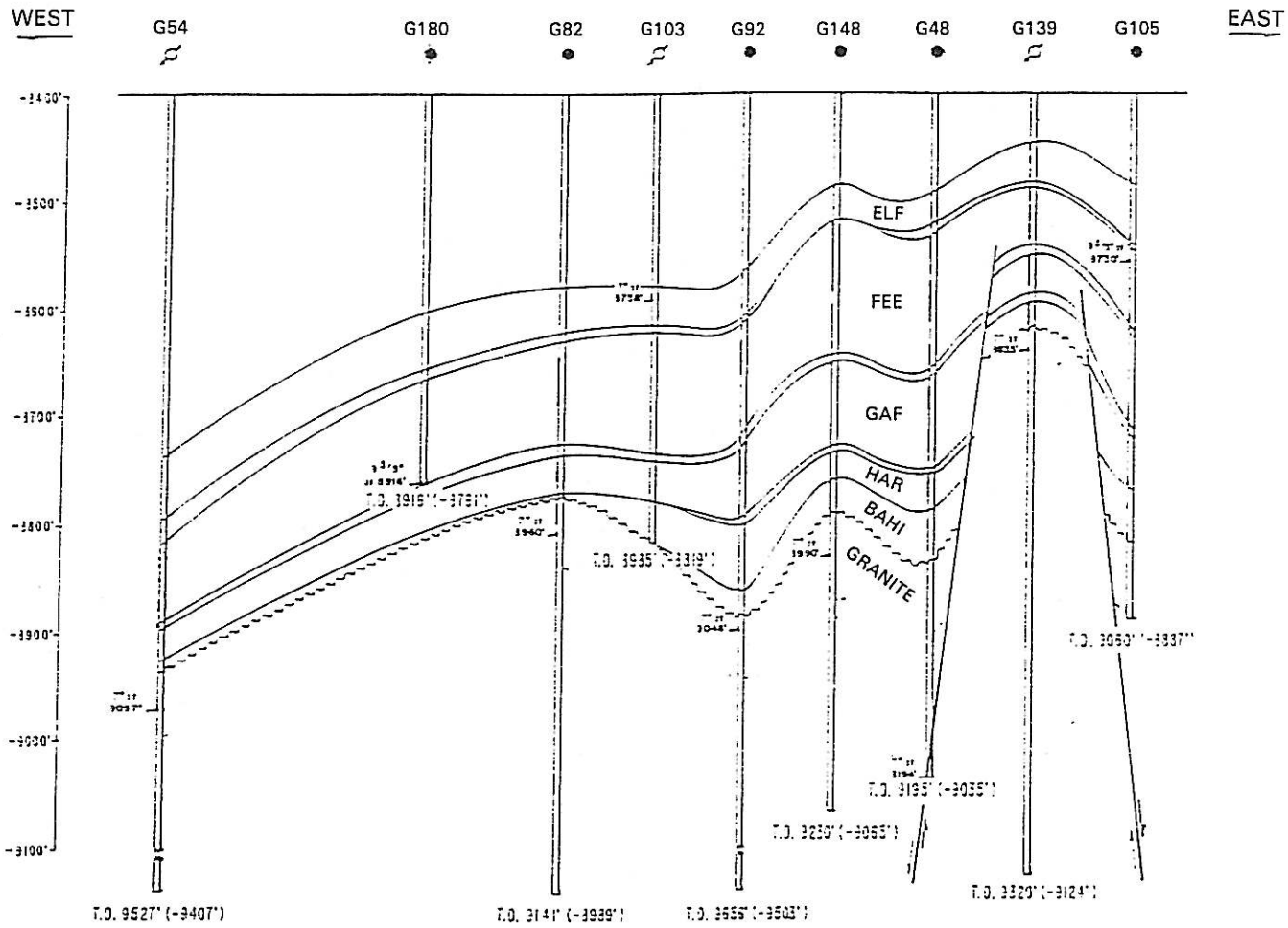


FIG. 6. Nafoora–Augila Unit structure cross section (Wells G54-G62).

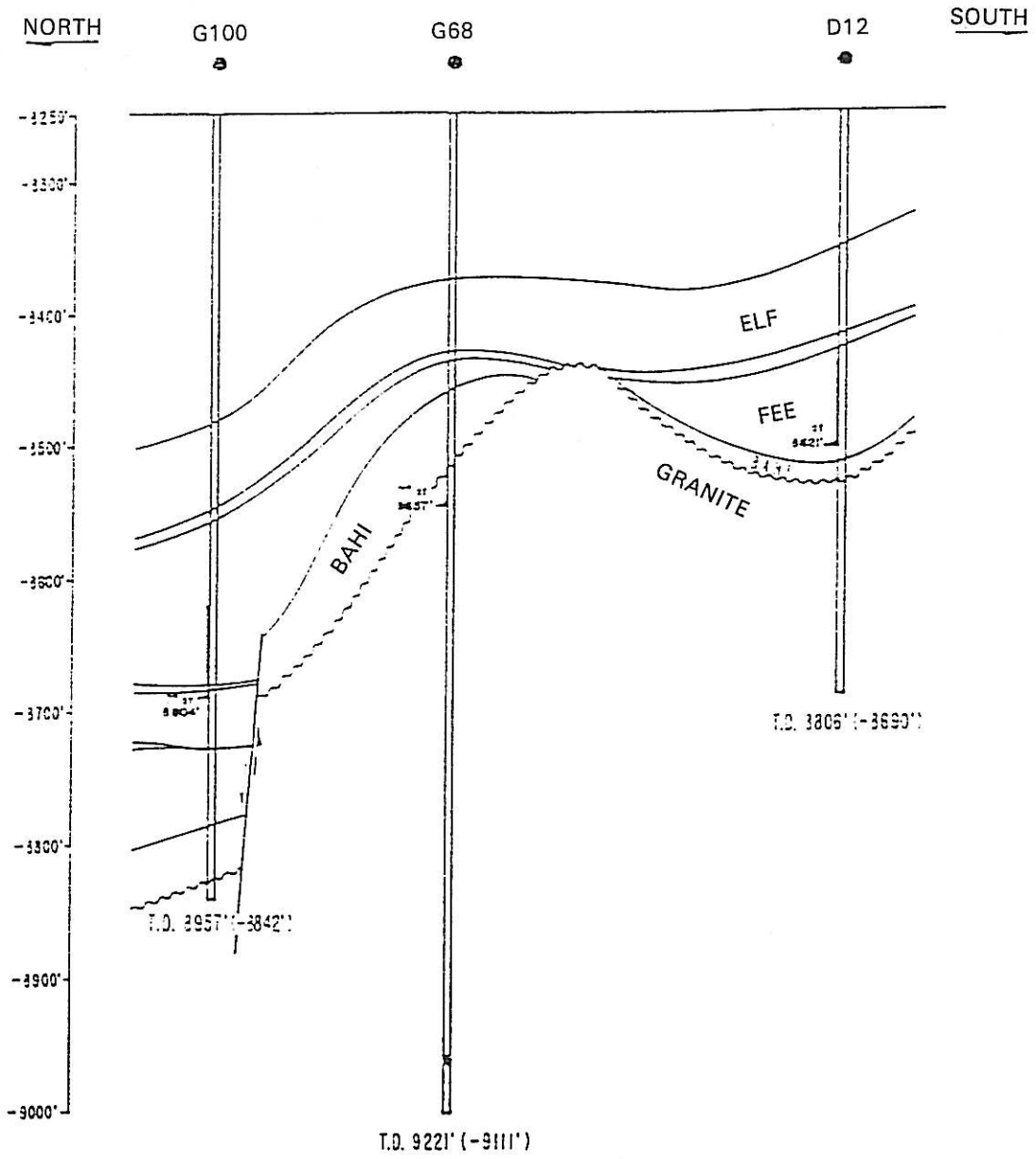


FIG. 7. Nafoora–Augila Unit structure cross-section (Wells G68) North-South.

pressure, which was 2970 psia when the well was first put on production in October of 1986, and an increase in water cut from 7 to 20%, Fig. 11. Production logs indicated that about 80% of the flow was coming from various granite intervals to a depth of 400 feet below the granite top, Fig. 12.

The productivity of these wells is a direct indication of Granite contribution to the field production, while the following is an indirect indication of the role of the granite as an important contributor to oil production:

1. The OOIP calculated by material balance is significantly higher than that obtained by volumetric calculations for the sedimentary rocks of the Tagrifet and the Bahi. The difference is accredited to the Granite.

2. Water cuts were observed to be quite low with reference to the large volumes of injected water in areas where the floodable pay is in very good communication with the granite.

3. A unique characteristic of wells producing exclusively from the granite is the very high salt content of the produced crude oil. This was also observed in some wells which are not known to be producing from the granite. It is believed that this could be as a result of oil being displaced from the granite to the overlaying sediments.

4. There are some wells that penetrated and were completed into the granite were not observed to be

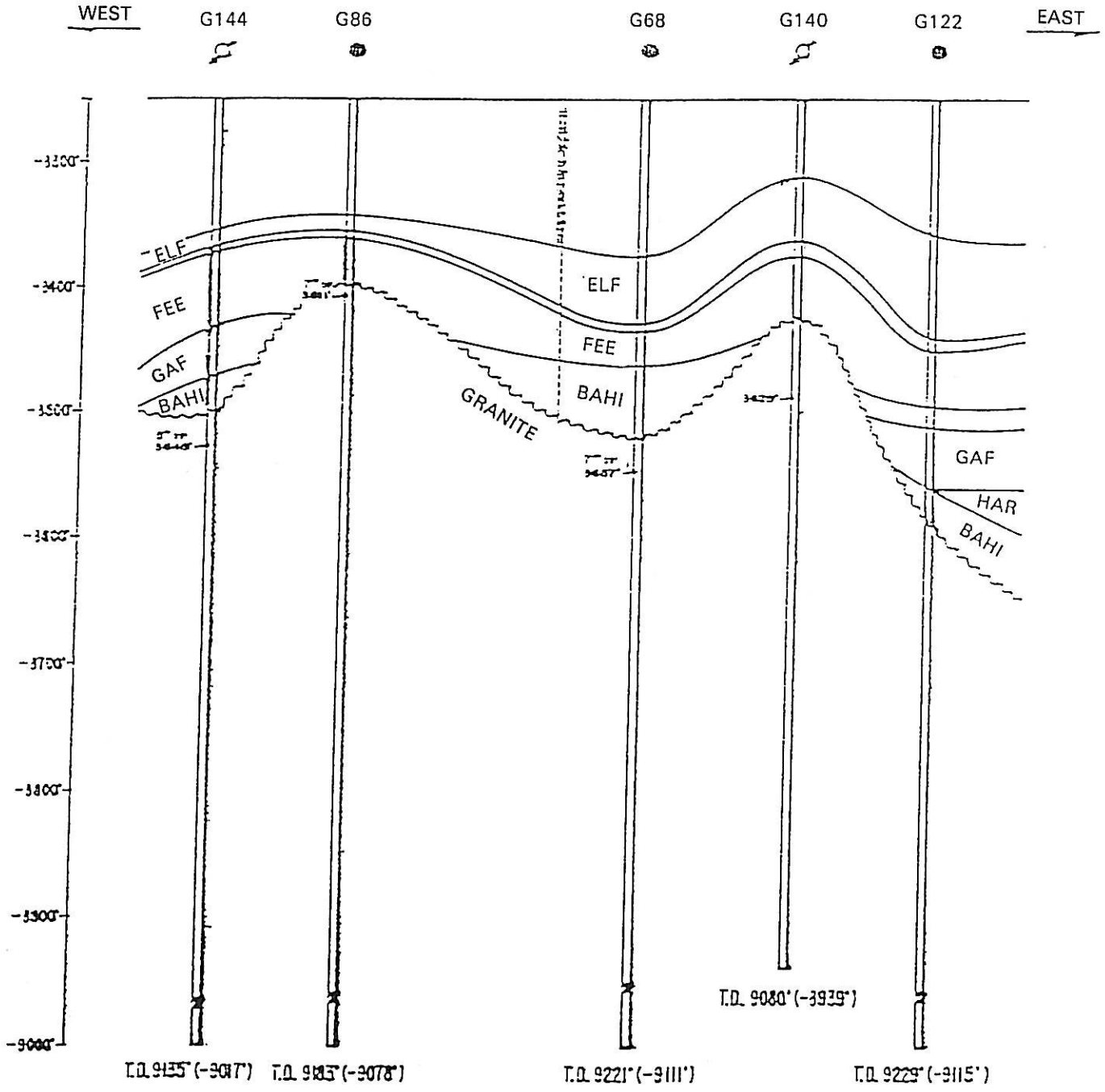


FIG. 8. Nafoora–Augila Unit structure cross-section (Well G-68) West-East.

producing from the granite. This may have been as a result of the fact that in some of these wells fracture intensity is so small that their production could not be detected by the flowmeter, and/or because of the lack of response to acid treatments due to extensive formation damage by drilling fluids, which could have plugged the fractures. Furthermore, exposure of the fractures to cement could cause permanent damage.

WATER PRODUCTION FROM THE GRANITE

Although no definite oil-water contact was established in the TBG reservoir of the Nafoora--Augila Unit, wells G-54 and G-68 starting cutting water after producing about 6.5 and 4.0 million barrels of oil, respectively, and before the start of water injection. This led to the belief that there could be a limited aquifer, but of low permeability, possibly existing

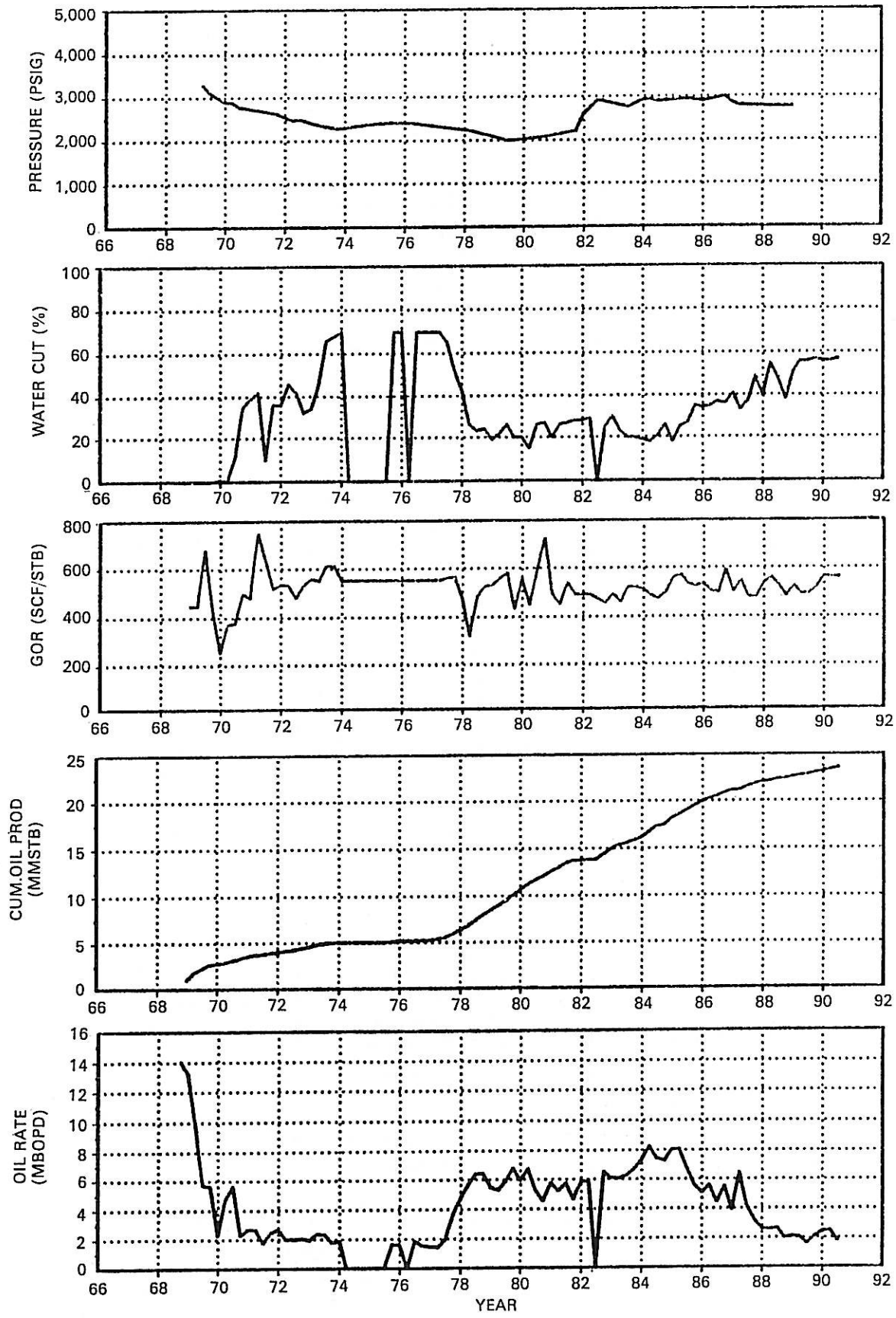


FIG. 9. (G-68) Well performance (Nafoora–Augila Unit).

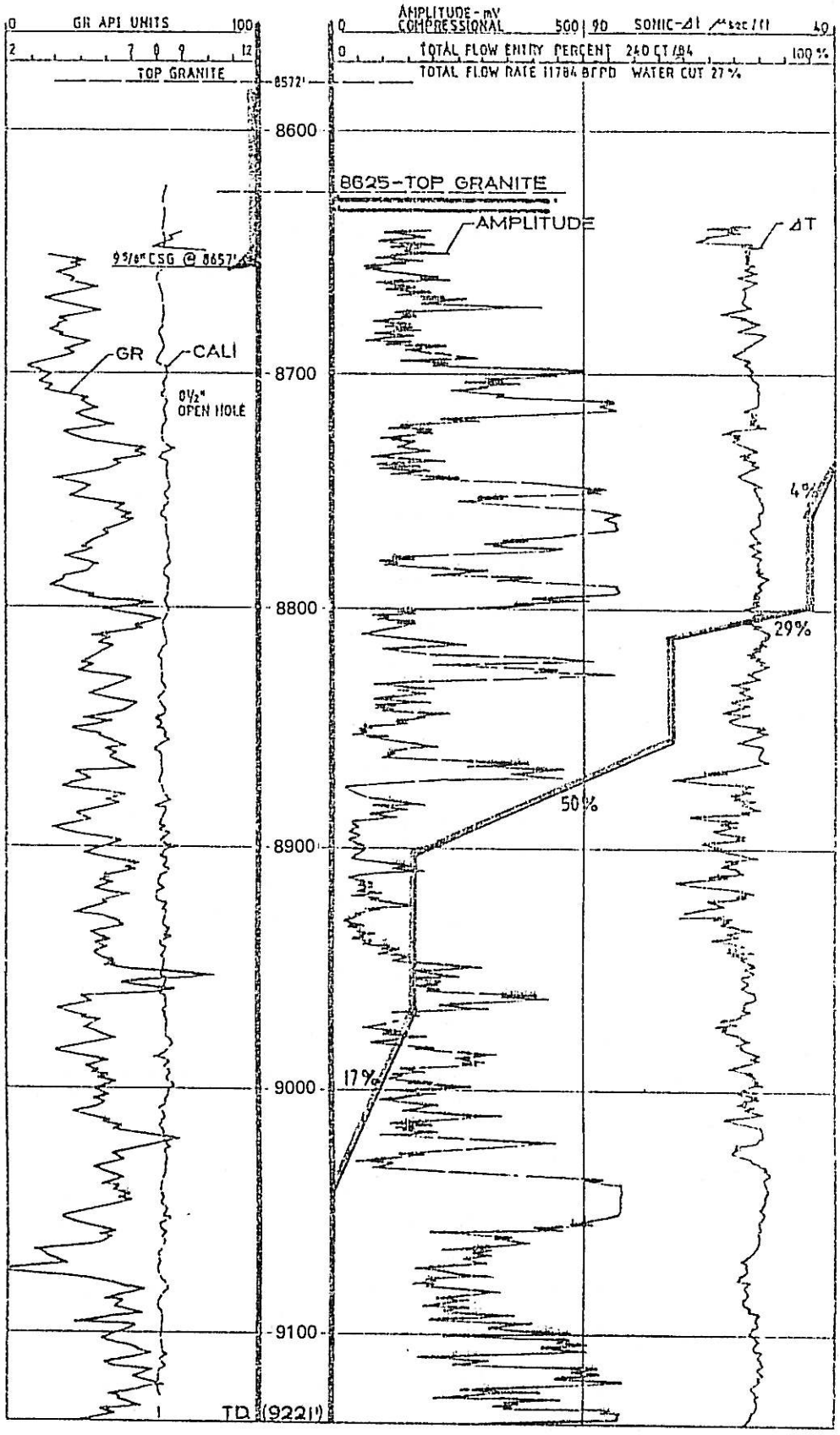


FIG. 10. Production logs (Well G-68).

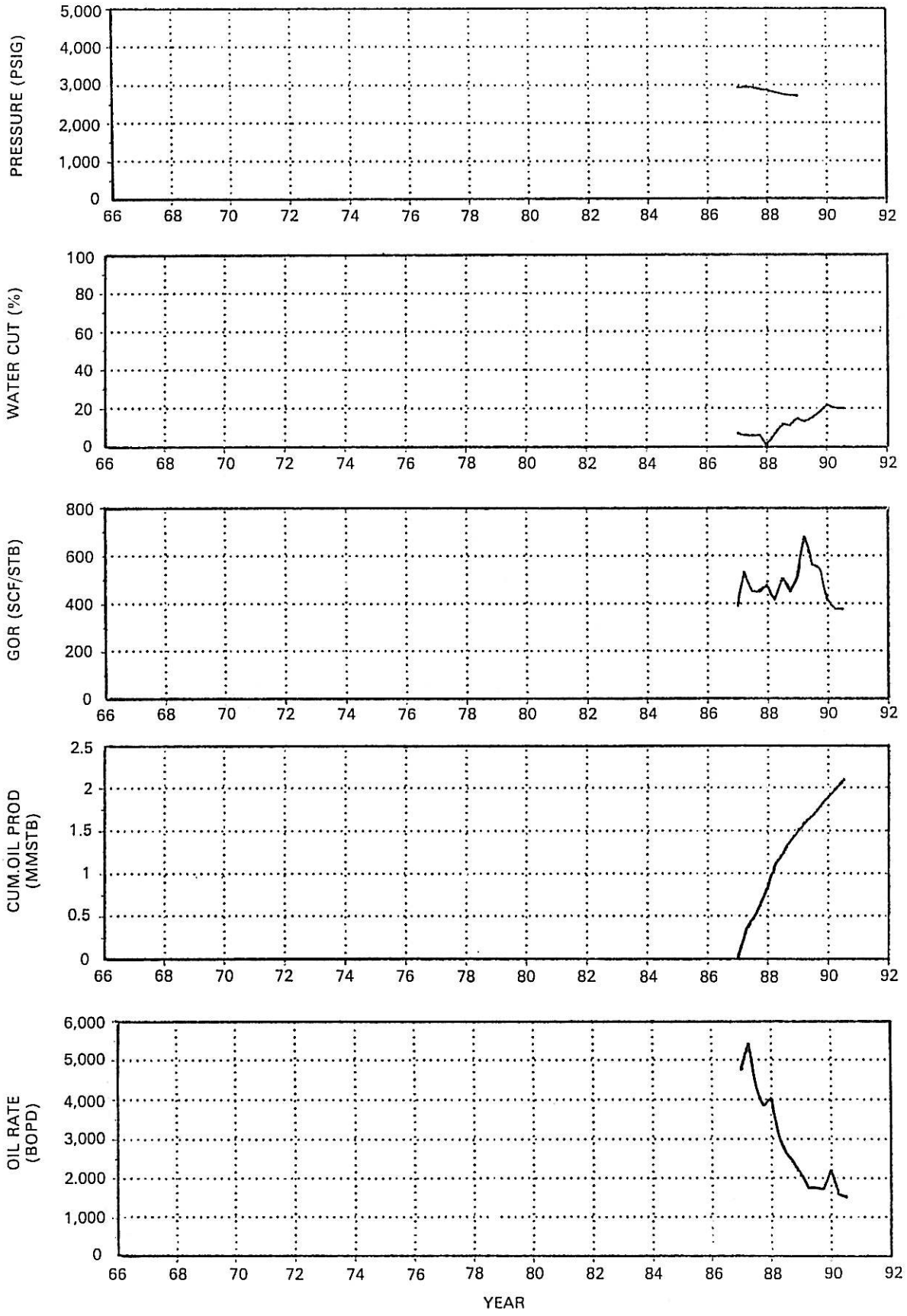


FIG. 11. (G-243) Well performance – Nafoora–Augila Unit.

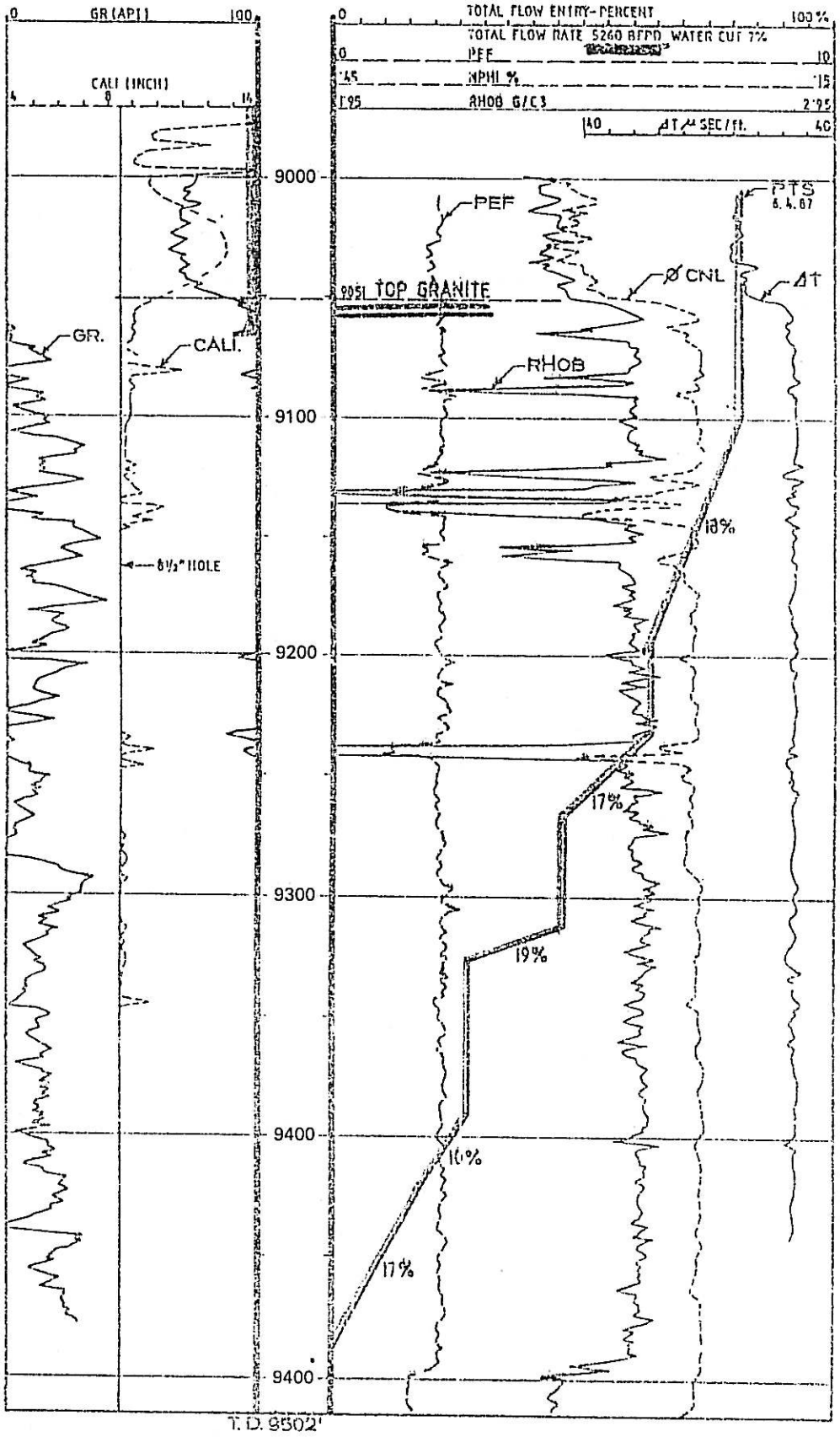


FIG. 12. Production logs (Well-G243).

within the fractured basement. Furthermore, water could have possibly channelled from the overlaying sediments with high initial water saturation.

CONCLUSIONS

- Fractured basement can be productive reservoirs under favorable geological conditions.
- The Granite of Nafoora--Augila Unit was found to be fractured and deeply weathered to as deep as 1000 feet below the Granite surface.
- Fractures can be detected by several Open-Hole logs, partial mud loss and a sudden decrease in drilling time.
- Direct and indirect indicators can be used to verify oil production from the Granite.

ACKNOWLEDGMENT

We thank AGOCO for permission to publish this paper, and the Reservoir Engineering Department for their help in preparation of this paper.

REFERENCES

[1] Perea, D., Giordano, J., June 5–8, 1988, "Igneous Rocks as Hydrocarbon Reservoirs in Malargue, Argentina", SPWLA Twenty-Ninth Annual Logging Symposium.

[2] Petrographic Study of Granite Cores From G86-51 WEH, Nafoora Field, Libya, June 18, 1969.

[3] William, J.: "The Sedimentary and Igneous Reservoirs of the Augila Oil Field, Libya" In Barr. F.T. (ed.), Geology and archaeology of Northern Cyrenaica, Libya, Petro. Explo. Soc. Libya, 10th Annual Field Conf., p. 197–205.

[4] Clarke, J., April 9, 1969, "Progress Report on a Study of the Precambrian Granite, in Nafoora Field, Gialo Concession 51".

[5] Mahner, C., August 1971, "Geologic Report for the Proposed Augila-Nafoora Unit", Occidental of Libya Inc., Internal Report.

[6] Hanners, A., November 19, 1969, "Oil Production from Granite, Nafoora Field, Libya".

[7] Bartlett, J., Scott, H., Singleton, A., December 2, 1973, "Correlation Study, Tagrifet-Bahi-Granite Reservoir, Nafoora-Augila Unit, Libyan Arab Republic".

[8] Van Poollen, H. K. and associates, Inc., January 1975, "Waterflood Evaluation as of June 1974, Tagrefit-Bahi-Granite Reservoir, Nafoora-Augila Unit".

[9] Applied Reservoir Technology, December 1982, "Reservoir Study and Operating Plan, Nafoora-Augila Unit".

[10] American Overseas Petroleum Ltd. and Occidental of Libya Inc., January 1971, "Technical Report and Water Injection Program for the Nafoora-Augila Unit".

PRJ, Vol. 7 (January 1995); P. 61–66, 4 FIGS.

ENHANCEMENT OF RESIDUAL TOTAL AEROMAGNETIC ANOMALIES – USING THE HILBERT TRANSFORM

M.R. Bakbak* and N.L. Mohan**

تحسين شاذات (إشارات) المغناطيسية الجوية باستخدام محول هلبرت

رضا البكباك و ن. ل. موهان

تم استخدام محول هلبرت بغرض تحسين شاذات المجال الكلي للمغناطيسية المتبقية، ولأول مرة، على إشارات من أكثر من 165 خط مسح جوي.

نتطرق في هذه الدراسة إلى العلاقات الرياضية التي تمثل محول هلبرت والمشتقة الأولى، واستنباط المرشح (Filter Generator).

مكنت النتائج المتحصل عليها للإشارات المحسنة من تحديد مصادر شاذات جديدة بالإضافة إلى تأكيد المصادر المحددة سابقاً. كذلك أعطت النتائج مؤشرات على التراكيب الجيولوجية الدفينة بالمنطقة كالفوالق، والتي لم تكن ظاهرة في الخريطة المغناطيسية المتبقية قبل إجراء عمليات التحسين عليها.

ABSTRACT

An attempt is made for the first time to demonstrate the applicability of the Hilbert transform in order to improve the signal resolution from aeromagnetic data over 165 profiles. Filter coefficients (M_j) were generated using the horizontal derivation (A) and its Hilbert transform (H), ($M_j = \Sigma A \times H$) for every profile and subsequently the filter was convolved with the horizontal derivative ($M \times A$) as well as its Hilbert transform ($M \times H$). The validity of the method is established by correlating the filtered aeromagnetic data with drill hole data in locations where anomalous zones are known. The enhanced signals enabled the delineation of new anomalous zones. The resolution of aeromagnetic anomalies, also, gave possible inference to the structural features like contacts and faults in the region.

INTRODUCTION

In continuation of the study of Hilbert transform application for geophysical signal resolution (Mohan *et al.* 1985, 1988; Rama Dass *et al.* 1987) an attempt was made to apply the Hilbert transform for the first time on aeromagnetic data.

The first horizontal derivative (A) and its Hilbert transform (H), were computed from the residual total aeromagnetic data over each profile; and the filter coefficients were cross multiplied with the horizontal derivative ($M \times A$) and its Hilbert transform ($M \times H$) separately. The enhanced signal peaks over a few profiles were correlated with the drill hole data in the area. A new zone was demarcated on the north-northwestern side from the filtered aeromagnetic signal peaks. Also, the signal peaks were correlated with prominent structural features like fault and contacts.

THE HILBERT TRANSFORM

The analysis of aeromagnetic anomalies, in the present case, was based on the Hilbert transform. It was established that the vertical magnetic field and horizontal magnetic field anomalies form the Hilbert transform pair; and equally true with the horizontal derivative and vertical derivative of any component of the magnetic field (Nabighian, 1972; Shuey, 1972; Cerveney and Zahradrik, 1975; and Mohan *et al.*, 1982).

*Geophysics Department, Al Fateh University, Tripoli, G.S.P.L.A.J.
**Centre of Exploration Geophysics, Osmania University, Hyderabad, India.

The Hilbert transform pair are defined by the relation (Erdelyi *et al.*, 1954),

$$A(x)=\frac{1}{\pi}\int_{-\infty}^{\infty}\frac{H(\mathcal{G})}{\mathcal{G}-x}\,d\mathcal{G} \tag{1}$$

and

$$H(\mathcal{G})=\frac{1}{\pi}\int_{-\infty}^{\infty}\frac{A(x)}{x-\mathcal{G}}\,dx \tag{2}$$

with the principle value to be taken at the singularity of the integrand. Also in the frequency domain, the Hilbert transform of any real function $f(x)$ is defined as

$$H(x)=\frac{1}{\pi}\int_{0}^{\infty}\{\text{Im}\,F(\omega)\cos\omega x-\text{Re}\,F(\omega)\sin\omega x\}\,d\omega \tag{3}$$

where $\text{Re}\,F(\omega)$ and $\text{Im}\,F(\omega)$ are real and imaginary components of the Fourier transform,

$$F(\omega)=\int_{-\infty}^{\infty}f(x)\,e^{-i\omega x}\,dx \tag{4}$$

and ω is the spatial frequency expressed in radians per unit length (Thomas, 1969). The computational procedure was well explained by Nabighian (1972), Shuey (1972) and Mohan *et al.* (1982). Here the Hilbert transform computations were carried out using the Shuey's (1972) FORTRAN IV program, based on convolution algorithm.

GENERATION OF FILTER

Filter generation was based on the following concept (Thomas, 1969). If $f(x)$ is a random process, then the autocorrelation function $R_{ff}(x, x+m)$ wax defined as

$$R_{ff}(x, x+m)=E(f(x).f(x+m)) \tag{5}$$

where $E(.)$ is the expectation operator.

Similarly, for two random processes, $f(x)$ and its Hilbert transform $H(x)$, the cross correlation function $R_{fH}(x, x+m)$ was defined as,

$$R_{fH}(x, x+m)=E(f(x).H(x+m)) \tag{6}$$

if the process $f(x)$ at least wide sense stationary, then eqn. (5) becomes

$$R_{ff}(x, x+m)=R_{ff}(m) \tag{7}$$

a function of the station interval, m, only. Also if $f(x)$ and its Hilbert transform, $H(x)$, are jointly at least wide sense stationary, then eqn. (6) becomes

$$R_{fH}(x, x+m)=R_{fH}(m) \tag{8}$$

By taking the cross correlation of $f(x)$ and its Hilbert transform $H(x)$ (eqn. (8)) with zero lag(i.e. $m=0$), an inner product, M_j, which is a measure of the product of first horizontal derivative, (A), and its Hilbert transform, (H) was defined as (Shimshoni and Smith, 1964; Mohan *et al.*, 1985, 1987, 1988),

$$M_j=\sum_{i=-n}^{n}A_{i+j}\times H_{i+j} \tag{9}$$

The inner product, M_j, gives a measure of the total signal power. The computation of the filter coefficients and subsequent cross multiplication with the horizontal derivative of the residual total aeromagnetic anomaly and its Hilbert transform was done as follows. Filter, M_j, is the summation of the cross multiplied values of the horizontal derivative of the anomaly and its corresponding Hilbert transform, three values at a time (3 point data window), from one end of the profile (eqn. (9)). The process was repeated by sliding the data window along the entire aeromagnetic profile. Each filter coefficient was attributed at the middle point of the data window.

Here the cross multiplication of $M_j\times A_j$ and $M_j\times H_j$ was defined as,

$$MA_l=\sum_{i=n-1}^{n+1}M_i\times A_{i+2} \tag{10}$$

and

$$MH_l=\sum_{i=n-1}^{n+1}M_i\times H_{i+2} \tag{11}$$

where

$$l=1, 2, 3, \ldots\ldots N-1$$
$$n=1, 2, 3, \ldots\ldots N-1$$

and $N=$ total number of values

The same procedure was adopted for convolving the filter coefficients (M_i) with the horizontal derivative (A_{i+2}) and its Hilbert transform (H_{i+2}) as was in the case of filter generation. However, the integration interval (or window length) either for generation of filter coefficients or for cross multiplication of the filter A and H was based on purely trial and error.

DATA AQUISITION AND PROCESSING

The aeromagnetic surveys were conducted along the northsouth profiles at a distance of 0.5 km inter-

vals; and tie-lines were oriented in E–W direction; spaced at 3 km intervals. The flight elevation was maintained at 122 ± 24 meters from the mean ground level. Profiles L-111 to L-275 (27°15′-27°45′; 13°15′–14°05′; Fig. 1) were considered for the present study. It may be seen from Fig. 1, towards northern side as well as western side, the significant magnetic anomalous features are absent unlike near the eastern part where anomalies are not only significant but also a lengthy patch, which is distributed up to the end of southern side.

In order to improve the signal resolution the first horizontal derivative of the residual total magnetic data of every profile was computed as

$$T'(x)=(T(x_{n+1})-T(x_n))/x \qquad (12)$$

where n represents the station numbers and x is the station interval in meters. Using eqn. (2), the Hilbert transform of the horizontal derivative was computed for every aeromagnetic profile. The filter, M_j, was computed from the summation of cross-multiplied values of the horizontal derivative of the residual total magnetic anomaly and its corresponding Hilbert transform three values each at a time (3 point data window), from one end of the profile, using equation (9). Each filter coefficient was attributed at the middle point of the data window. From equations (10) and (11), the filter, M_j, was convolved with the horizontal derivative ($M \times A$) and with its Hilbert transform ($M \times H$) and shown in Figures 2 and 3. A significant aspect of filter generation was "a self manipulation" of the observed data itself. Also, it may be noted here that neither the first horizontal derivative nor its Hilbert transform were smoothened prior to the filter generation. Evidently from Figures 2 and 3 the signal resolution was remarkable due to the self generated filter M_j, in all the profiles. This shows that even the noise generated by the first horizontal derivative and its Hilbert transform apart from the inherent noise, was substantially minimised.

DISCUSSION AND CONCLUSION

The signal enhancement procedure outlined above was applied on the 165 aeromagnetic profiles (L-111–L-275) (Fig. (1)). The validity of the method was established by correlating the enhanced signals of the residual total aeromagnetic anomaly with the presence of the anomalous zone in the south eastern side.

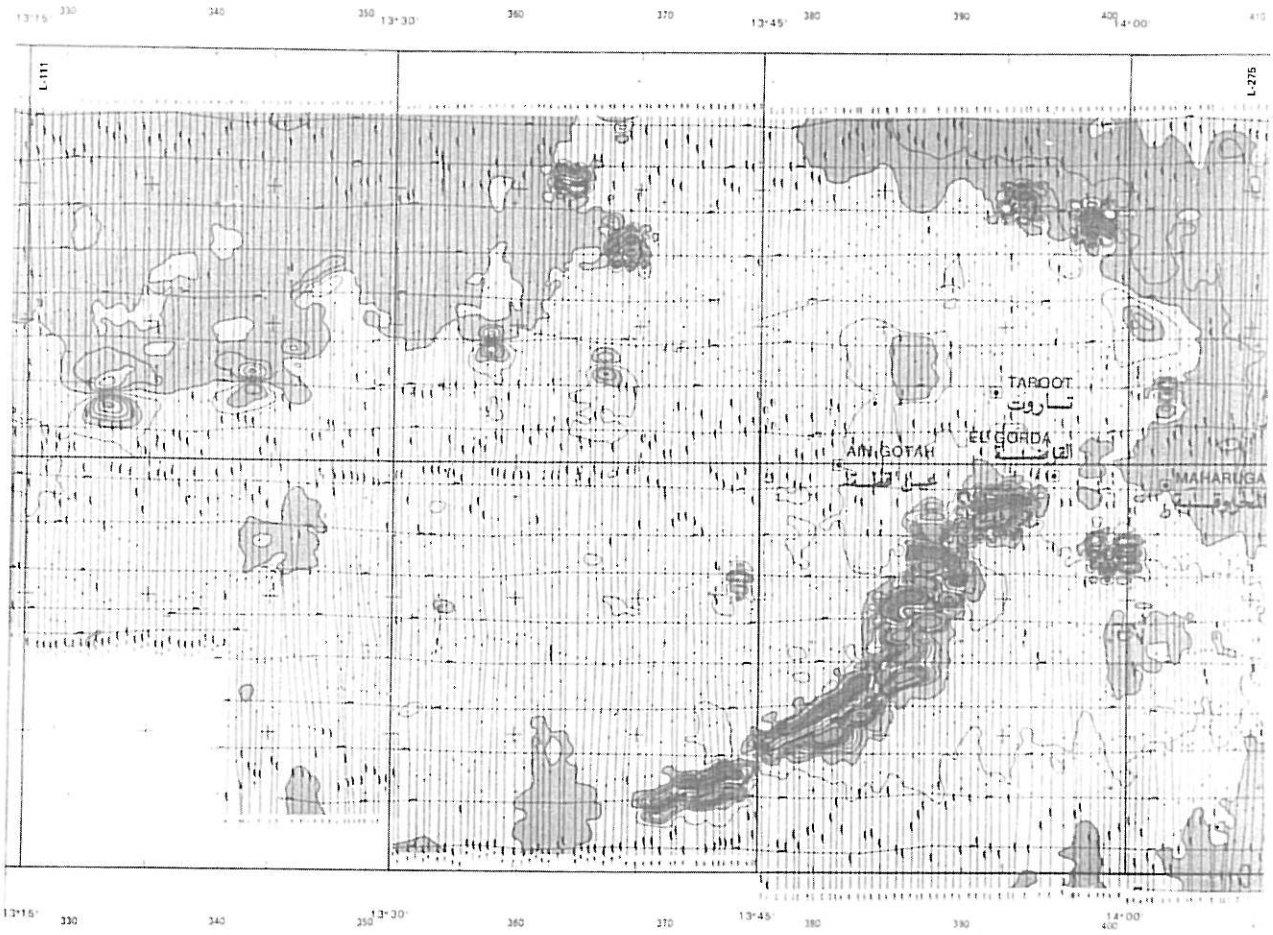


FIG. 1. Residual total magnetic intensity map of the area and profile line orientation.

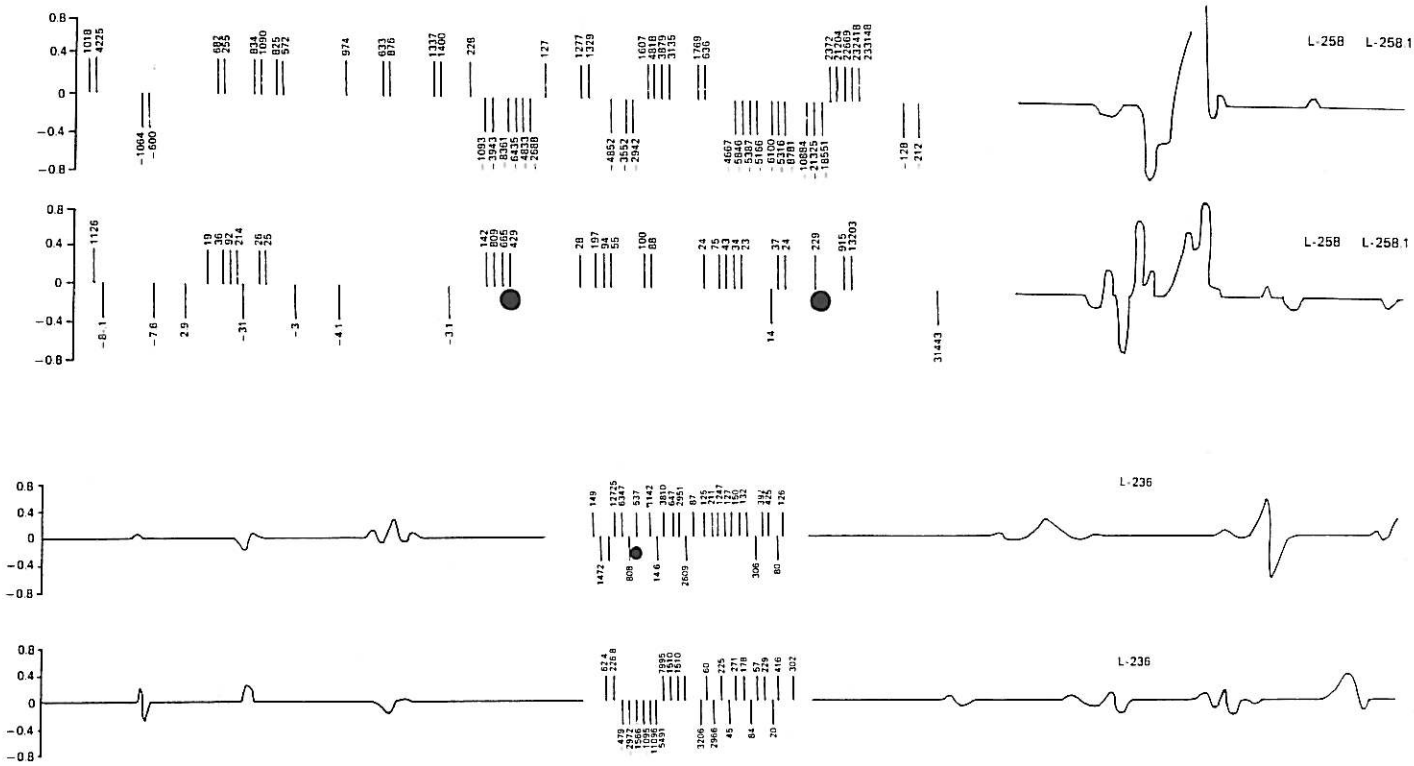


FIG. 2. Convolved horizontal derivative with filter ($M \times A$) and convolved Hilbert transform with filter ($M \times H$) of lines L-236 and L-258 over drill hole locations (solid dot) (L-258.1 is continuation of L-258 with short gap where no data is available).

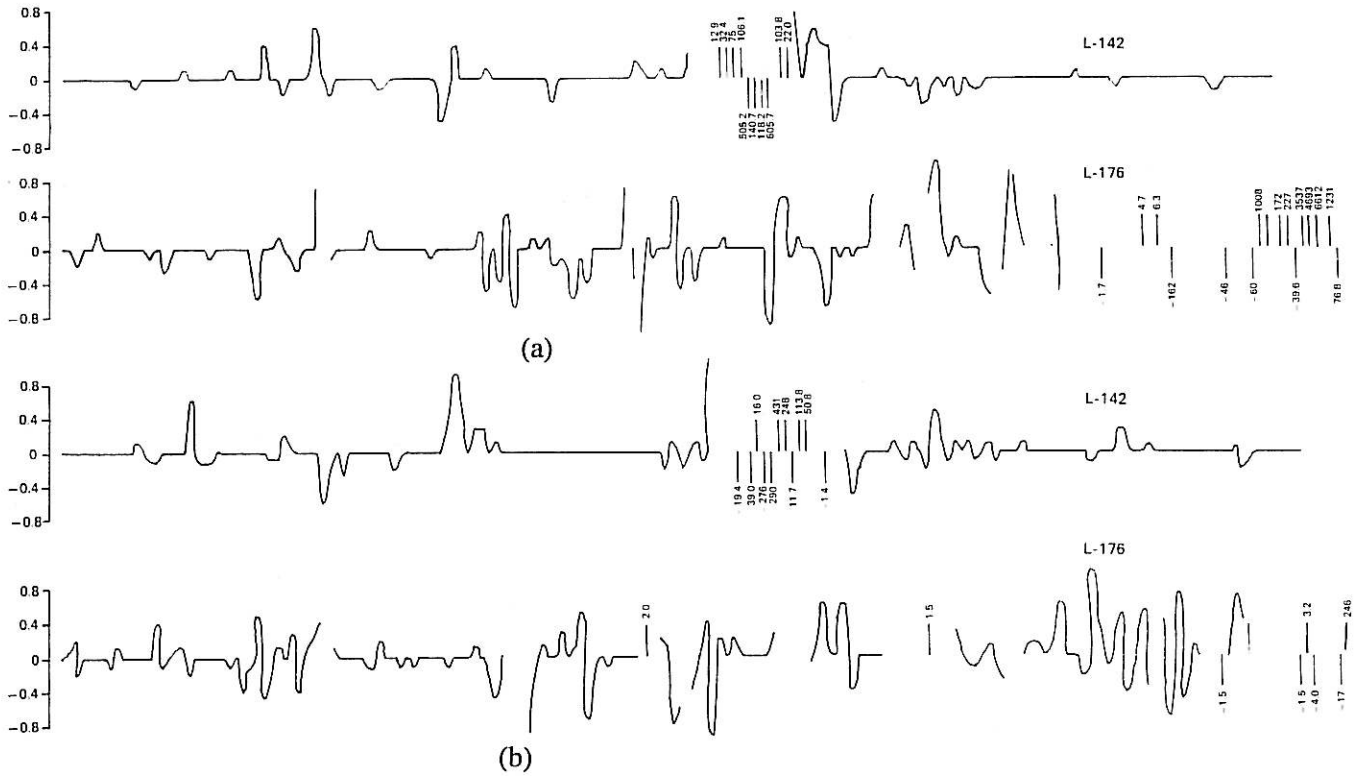


FIG. 3. (a) Convolved horizontal derivative with filter ($M \times A$) of L-142 and L-176 (profile lines through newly delineated zone), (b) Convolved Hilbert transform with filter ($M \times H$) of L-142 and L-176 (profile lines through newly delineated zone).

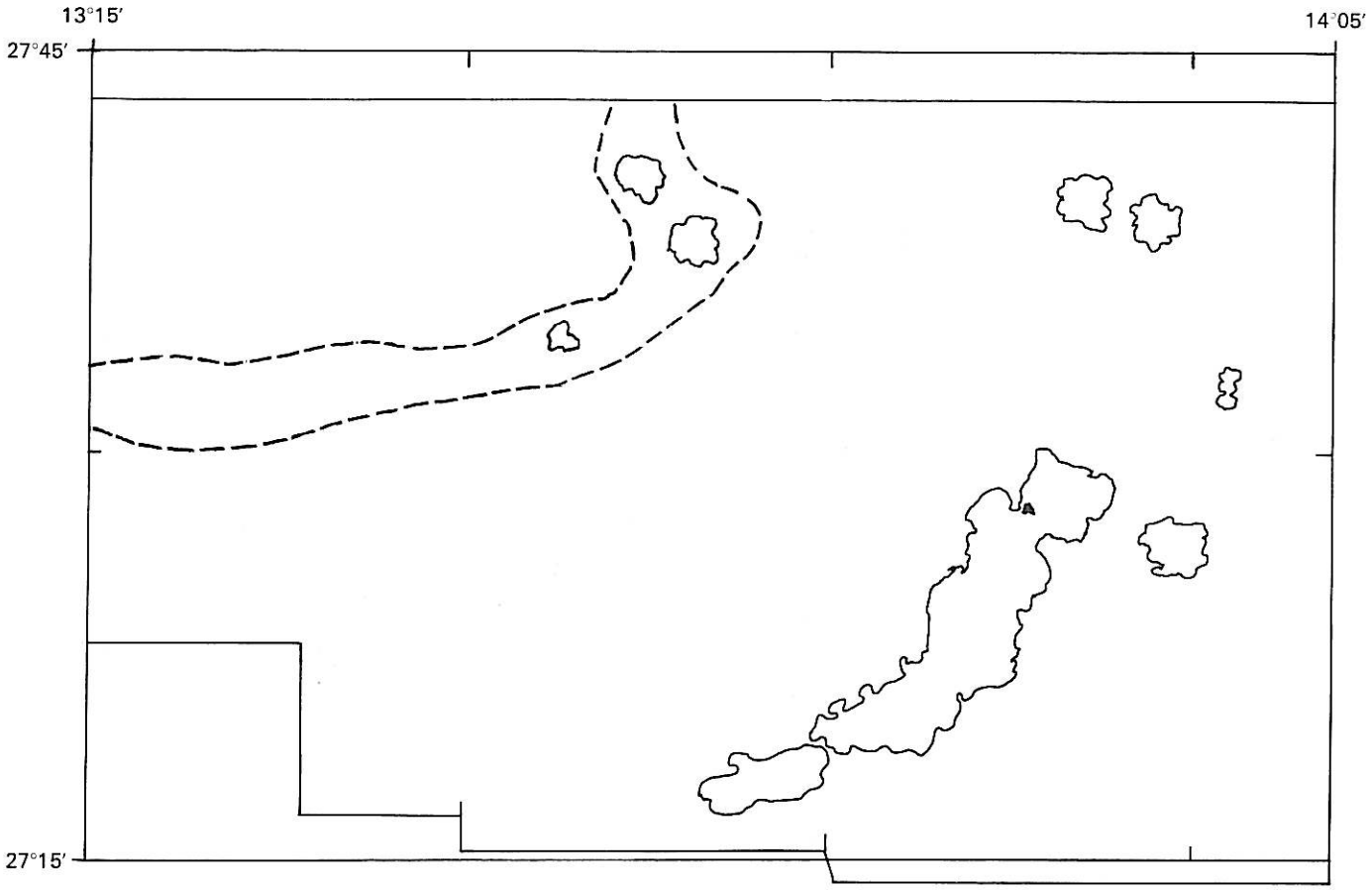


FIG. 4. Schematic outline of the anomalous zone (continuous line) and newly delineated zone (dashed line).

The enhanced signals ($M \times A$) and ($M \times H$) of two profiles (L-258) and (L-236) which pass over the drill holes are shown in Figure 2.

Figure 2 indicates that the signal resolution is quite predominant along the profiles over the drill holes.

The enhanced magnetic signals along profiles (L-111–L-195) delineate an anomalous zone extending north–northwest, where the pre-enhanced signals are very weak. The outline of the boundary of this zone is schematically shown in Figure 4.

As an example of the enhanced signatures outlining this zone, two profiles are shown in Figure 3. It is , also, important to note that the enhanced magnetic signatures over these profiles, although predominant, they are relatively low in magnitude compared to the profiles on the south eastern side, where the known anomalous zone is almost exposed near the surface (see Figure 2 and 3). This suggests that the new anomalous zone is deep seated and covered by the sand in the region.

It is pertinent to mention, also, that the analysis of the aeromagnetic data indicates a few patterns of enhanced signals at various locations. These signals appear to follow the structural features like faults and contacts, in the region.

The analysis of the filtered residual total aeromagnetic data using the Hilbert transform, not only enhanced the signals, verifying the known anomalous zone in the area, but also enabled the delineation of new zone trending north–northwest.

ACKNOWLEDGEMENT

The authors are highly indebted to the Industrial Research Centre of Libya for providing the aeromagnetic and drill hole data. Grateful appreciations are expressed to the computer centres of Zewitina and Oasis oil companies of Libya for extending excellent computational facilities.

REFERENCES

Cerney, V. and Zahradrik, K.J., 1975, Hilbert transform and its geophysical application, Acts. Uni. Math. Phys. 16, 67–81.

Erdelyi, A., and Magnus, W., *et al.*, 1954, Table of Integral transforms, Vol. II, McGraw-Hill Book Co., Inc.

Goudarzi, G.H., and Tschoepke, Dr. Ing. R., 1968, A geologic report on the iron deposit of the Shatti Valley area of Fezzan, Libya; Geological Section Bulletin No. 7, p. 9–10, Ministry of Industry, Libya.

Mohan, N.L., Rama Dass, G., and Varaprasada Rao, S.M., 1985, Resolution of gravimagnetic and radiometric regional anomalies of Cuddapah basin, A.P., India, using the Hilbert transform; accepted for European Association of Exploration Geophysicists Conference, Budapest, Hungary. Printed in the Abstracts booklet.

Mohan, N.L., Rama Dass, G., Varaprasada Rao, S.M., and Sunderarajan, N., 1988, Hilbert transform analysis for gravimagnetic and radiometric regional anomalies of Cuddapah basin, A. P., India – A qualitative study: Accepted for publication in Pure and Applied Geophysics

Mohan, N.L., Sunderarajan, N., and Seshagiri Rao, S.V., 1982, Interpretation of some two dimensional magnetic bodies using the Hilbert transform, Geophysics, 47, 376–387.

Nabighian, M.N., 1972, The analytic signal of two dimensional magnetic bodies with polygonal cross section, its properties and use for automated anomaly interpretation, Geophysics, 37, 507–512.

Rama Dass, G., Varaprasada Rao, S.M., and Mohan, N.L., 1986, Application of the Hilbert Transform in resolution of magnetic signals – A new technique: Australian Bulletin of Exploration Geophysicists, Vol. 17.

Shimshoui, M. and Smith, S. W., 1964, Seismic signal enhancement with three component detectors, Geophysics 29, 664–671.

Shuey, R.T., 1972, Application of Hilbert transforms to magnetic profiles: Geophysics, Vol. 37, No. 6, 1043–1045.

Thomas, J.B., 1969, An introduction to statistical communication theory, 639–657, John Wiley, New York.

PRJ, Vol. 7 (January 1995); P. 67–74, 3 FIGS, 1 TABLE.

PROBABILITY OF THE VALIDITY OF THE ROCK COMPONENT MODEL IN COMPLEX LOG INTERPRETATION

G. Szigeti*

إحتمالية صحة تطبيق نموذج المركبات الصخرية في تفسير سرود الآبار المعقدة

ج. زيقيتي

التقليل من الفارق بين السرود المسجلة والمحسوبة أو النظرية هو أساس التفسير للسرود. وفي حالة تعدد المركبات الصخرية في النموذج المستخدم لا يمكن مقارنة الفارق مباشرة، لذلك تم إدخال إحتمالية صحة أو تطبيق النموذج المستخدم لغرض المقارنة، كما تم دراسة تأثير التحديدات على حجم المعادن المحسوبة من النموذج المستخدم.

وتم تعديل توزيع «كاي» النظري واختبار حدود تطبيقاته في وجود هذه التحديدات، كما تم تطبيق نموذج الإحتمالية لغرض الإيضاح في تفسير السرود المسجلة من تكوين صخور رملية.

ABSTRACT

The minimization of the incoherence (the distance between measured and calculated logs) is a basic principle of complex well log interpretation. If lithological models with different numbers of unknowns (rock components) occur, however, the incoherences cannot be compared direclty.

The probability, α, of validity of rock component models is introduced as the basis of comparison. The effect of restrictions on the mathematically evaluated mineral volume fractions is discussed. The theoretical Chi-distribution is modified and the limits of its application are examined in case of restrictions.

The model probability, α, concept is applied for practical illustration in the interpretation of a well in a sandstone formation.

INTRODUCTION

The interpretation of geophysical data, in general, involves the comparison of the measured field data with that of the geologic geophysical model of the situation under study.

This comparison can be mathematically formulated as a minimization task where the goal is to minimize the distance, called incoherence, between the empirical and the theoretical model as a function of some model parameters. This idea leads to acceptable result for any fixed model but does not give a key, which model to accept. Indeed, in general, the more parameter considered by the model the less becomes the distance between the measured and calculated results. Defining too many parameters for the system of response functions, as might be known from practice, the determination becomes less definite.

On the other hand, as a property of any measuring system the experimental material consists of some degree of unavoidable uncertainty. Because of the presence of this uncertainty the statement about the validity of the interpretation model becomes a probability statement rather than a certain one. Having adequate definition for this probability and mechanism for its calculation we accept the maximum likelihood principle which means the choice of the model which has a higher probability of validity and which is not necessarily the model having the more parameters.

The objective of the present paper is to give a proper probability measure to the simple distance

*Petroleum Research Centre P.O. Box 6431, Tripoli, G.S.P.L.A.J.

concept, where this measure depends on the dimensions of the minimization task as well. The mathematical scheme applied in this work, based on the Fisher-Cochran theory, is close to that of decision making of mathematical statistics. Two specific features, however, influence the way of thinking. First, we have always low number of different logs in a given sample point, and second, the log readings represent a strong statistical average of a repeated observation.

The mathematical scheme developed does not give a key on how to set up rock component models, however, it is a useful tool to decide, when it is possible, which model to choose in a doubtful situation.

SETTING UP THE PROBLEM AND ESTABLISHMENT OF THE DECISION MAKING

Let the measured field data be denoted by ε concrete form, of which is indifferent at the moment, and suppose that two different geological-geophysical models A_1 and A_2 can be set up on the basis of the general knowledge about the situation under study. The question is which model describes better the real geological conditions on the basis of observation ε. Having the answer for two models, of course, we have the answer for any finite number of models.

We suppose at this point, in advance, that the probabilities of the involved events do exist, i.e. can be correctly defined later on. In this sense, $P(A_1)$ means the probability of the event that A_1 is the right model of the studied situation. The observed ε is the only sure thing about the studied situation, thus we need to compare the conditional probabilities

$$P(A_1|\varepsilon) \quad \text{and} \quad P(A_2|\varepsilon) \tag{1}$$

Because of the purely empirical character of ε, conclusion about the nature of the model cannot be drawn directly. A_1 and ε are mutually valid if within the ε event A_1 is valid, or if within the A_1 event ε is valid, this can be described using conditional probabilities by the equation

$$P(A_1\varepsilon)=P(\varepsilon)P(A_1|\varepsilon)=P(A_1)P(\varepsilon|A_1)$$

from which

$$P(A_1|\varepsilon)=\frac{P(A_1)}{P(\varepsilon)}*P(\varepsilon|A_1) \tag{2}$$

This is the simplest form of the Bayes theorem, for one hypothetical model A_1. Substituting (2) in (1) the answer to the problem lays in the comparison of quantities.

$$\frac{P(A_1)}{P(\varepsilon)}\cdot P(\varepsilon|A_1) \quad \text{and} \quad \frac{P(A_2)}{P(\varepsilon)}\cdot P(\varepsilon|A_2) \tag{3}$$

For this comparison $P(\varepsilon)$ does not play any role, $P(A_1)$ and $P(A_2)$ must reflect the knowledge about the area prior to the measurements. Often there is no evidence about the priority of one model over the other (e.g. clean and shaly sand equally possible at a given depth point of a sandstone area) and in this case (3) simplifies to the comparison of

$$P(\varepsilon|A_1) \quad \text{and} \quad P(\varepsilon|A_2) \tag{4}$$

The essential difference between (1) and (4) is that, unlike ε, A_1 (and A_2) is a theoretically defined complete situation, the model of the area under study, which gives the opportunity to define and calculate the probability of occurrence of the measured material ε.

Definition of the Probability of Occurrence of Given Measured Data at a Given Model of Interpretation

Now, the studied situation is the unit volume rock (true formation) which surrounds the bore hole at a given depth point. The measured data ε is the vector $\underline{\mathbf{b}}_M$ which consists of the number m log readings of different physical parameters at the same depth point. The model of the rock is the k number component of the rock (typically one fluid and k-1 solid component) and its linearized response function for each tool is in the form of the zone parameter matrix $\mathbf{Z}$ having m rows and k columns.

Because the model A_1 is valid (there is conditional probability in (4)) one defined independently from the exploration, but unknown k dimensional vector $\underline{\mathbf{x}}$ belongs to it, which gives the volumes of each components of the rock at the given depth. $\mathbf{Z}$ and $\underline{\mathbf{x}}$ together generate the ideal response vector $\underline{\mathbf{b}}$ in the form

$$\mathbf{Z}\underline{\mathbf{x}}=\underline{\mathbf{b}} \tag{5}$$

which gives m exact equations, without contradiction. If there is no inner connection between $\underline{\mathbf{b}}$ and $\underline{\mathbf{b}}_M$ then there is no way to know $\underline{\mathbf{x}}$. Consequently we make at this point the strong assumption that $\underline{\mathbf{b}}_M$ is an m-dimensional stochastic vector variable of Gaussian distribution with expectation $\underline{\mathbf{b}}$ and with a unit variation of each coordinates. The last assumption means, in practice, that the variation of each component is known and equation (5) have been already normalized according to this variations. Hence, instead of (5) we have;

$$\mathbf{Z}\cdot\underline{\mathbf{x}}=\underline{\mathbf{b}}_M \tag{6}$$

overdetermined system of equations. The best linear estimation for $\underline{x}$ is $\underline{\alpha}$ given by the Gaussian least square method (see e.g. [1]), which is the solution of the (ordinary) linear equation system

$$\mathbf{Z}^T \cdot \mathbf{Z}\underline{\alpha} = \mathbf{Z}^T \underline{b}_M \tag{7}$$

There is a strong connection between $\underline{x}$ and $\underline{\alpha}$, namely the expectation value of $\underline{\alpha}$ is $\underline{x}$, $E(\underline{\alpha}) = \underline{x}$. In equations (5), (6) and (7) $\mathbf{Z}$, $\underline{x}$ and $\underline{b}$ are deterministic values, while $\underline{b}_M$ is stochastic vector variable and $\underline{\alpha}$ is a linear combination of coordinates of $\underline{b}_M$ is stochastic variable as well.

Now, we are going to examine the distribution of the distance between the two sides of equation (6) around the $E(\underline{\alpha}(\underline{b}_M)) = \underline{x}$ point. Multiplying (5) by $\mathbf{Z}^T$ from the left and subtracting from (7), we get

$$(\underline{\alpha} - \underline{x}) = (\mathbf{Z}^T\mathbf{Z})^{-1} * \mathbf{Z}^T(\underline{b}_M - \underline{b}) \tag{8}$$

The incoherence I between the measured vector and the response function with the best statistical estimation $\underline{\alpha}$, using (5) and (8) can be written in the form

$$\begin{aligned} I &= \| \underline{b}_M - \mathbf{Z} \cdot \underline{\alpha} \| = \| (\underline{b}_M - \underline{b}) - \mathbf{Z}(\underline{\alpha} - \underline{x}) \| \\ &= \| (\underline{b}_M - \underline{b}) - \mathbf{Z}(\mathbf{Z}^T\mathbf{Z})^{-1} \cdot \mathbf{Z}^T(\underline{b}_M - \underline{b}) \| \\ &= \sqrt{\eta_1^2 + \eta_2^2 + \cdots \eta_m^2}, \end{aligned} \tag{9}$$

where $\| \ \|$ is the Euclidean distance in the m-dimensions, and $\eta_1, \eta_2, \ldots \eta_m$ are the coordinates of the incoherence, each one is a linear combination of the coordinates of the vector $\underline{b}_M - \underline{b}$. As a matter of our assumption, the coordinates of the stochastic vector $\underline{b}_M - \underline{b}$ are independent of each other, as their mutual distribution is a Gaussian distribution with the zero vector of expectation and with the unit (matrix) variation. The coordinates of the $\underline{\eta} = (\eta_1, \eta_2, \ldots \eta_m)$ incoherence vector are not independent from each other, because there is k number of linear relationship among them, namely,

$$\mathbf{Z}^T \cdot \underline{\eta} = \mathbf{Z}^T(\underline{b}_M - \underline{b}) - \mathbf{Z}^T \cdot \mathbf{Z}(\mathbf{Z}^T \cdot \mathbf{Z})^{-1} \cdot \mathbf{Z}^T(\underline{b}_M - \underline{b}) \equiv 0$$

To suppose more linear relationships among the coordinates of $\underline{\eta}$ contradicts with the independence of $\underline{b}_M - \underline{b}$. According to the Fisher-Cochran theorem [1], from this situation it follows for $\underline{\eta}$, examining it in a properly chosen orthonormal basis, that its m-k coordinates vary freely, while the remainder k coordinates equalise each other to zero. From this it follows that the distribution of the right side expression of (9) is the distribution of the distance of m-k number of independent Gaussian distributions, each one with zero expectation and unit variation. In other words we got the theoretical distribution of the incoherence I for the A_1 model (represented by the $\mathbf{Z}$ matrix). This incoherence is a stochastic scalar variable, let it be denoted by ξI_{A_1} and its distribution is the Chi-distribution belonging to the m-k parameter, i.e.

$$\xi I_{A_1} = \| \underline{b}_M - \mathbf{Z} \cdot \underline{\alpha} \| = \chi_{m-k} \tag{10}$$

The distribution of the Chi random variable χ_n is well known, and for small values of $\mathbf{n}$ is characteristic for the complex log interpretation application, and can be expressed by the following form [2]

$$P(\chi_n < x) = \int_{-\infty}^{x} h_n(t)\,dt$$

$$h_n(t) = \begin{cases} 0 & t \leqslant 0 \\ g_n(t) & t > 0 \end{cases}$$

$$g_1(t) = \sqrt{\frac{2}{\pi}} \cdot e^{-(t^2/2)}; \qquad g_2(t) = t \cdot e^{-(t^2/2)} \tag{11}$$

$$g_3(t) = \sqrt{\frac{2}{\pi}} \cdot t^2 \cdot e^{-(t^2/2)}; \quad g_4(t) = \tfrac{1}{2} \cdot t^3 \cdot e^{-(t^2/2)}$$

$$g_5(t) = \frac{1}{3}\sqrt{\frac{2}{\pi}} \cdot t^4 \cdot e^{-(t^2/2)}.$$

In this way we established the theoretical distribution of the incoherence as a result of the uncertainty of observation $\underline{b}_M$. This distribution is a function of the only variable $DF = m - k$ degree of freedom which reflects the dimension of the observations and the dimension of the applied model of interpretation.

On the other hand, substituting the only measured value for the vector $\underline{b}_M$ into formula (9) we get the experimental incoherence

$$I_{\underline{b}_M} = \| \underline{b}_M - \mathbf{Z} \cdot \underline{\alpha} \|$$

using the $\underline{\alpha}$ statistical estimation of $\underline{x}$ defined by (7).

Now it is clear, the smaller the $I_{\underline{b}_M}$ empirical incoherence the more reason to accept the choice for model A_1, thus we define the probability of validity of the rock component model A_1 as the probability measure of the event that the theoretical distribution is higher than the experimental one, and denoting this probability by α we estasblish

$$\alpha = P(\varepsilon = \underline{b}_M \mid A_1) = P(\xi I_{A_1} \geqslant I_{\underline{b}_M}) \tag{12}$$

Substituting (10) into (12), using (11) and some elementary features of any distribution function, and also changing the notation of the experimental $I_{\underline{b}_M}$ for I_{exp}, we get

$$\alpha = P(\xi I_{A_1} \geq I_{\underline{b}_M}) = 1 - P(\xi I_{A_1} < I_{\underline{b}_M})$$
$$= 1 - P(\chi_{m-k} < I_{exp})$$
$$= 1 - \int_0^{I_{exp}} g_{m-k}(t)\, dt \qquad (13)$$

Returning to the original problem (4), the observation $\underline{b}_M$ out of the models A_1 and A_2 verify that model, and that estimation $\underline{\alpha}$ given by the model, for which the probability α of (13) is higher. In (13) m is the number of logs involved into the interpretation, while I_{exp} and k depend very much on the models A_1 or A_2 used for interpretation purpose. Figure 1 demonstrate, the probability α as a function of DF and I_{exp}.

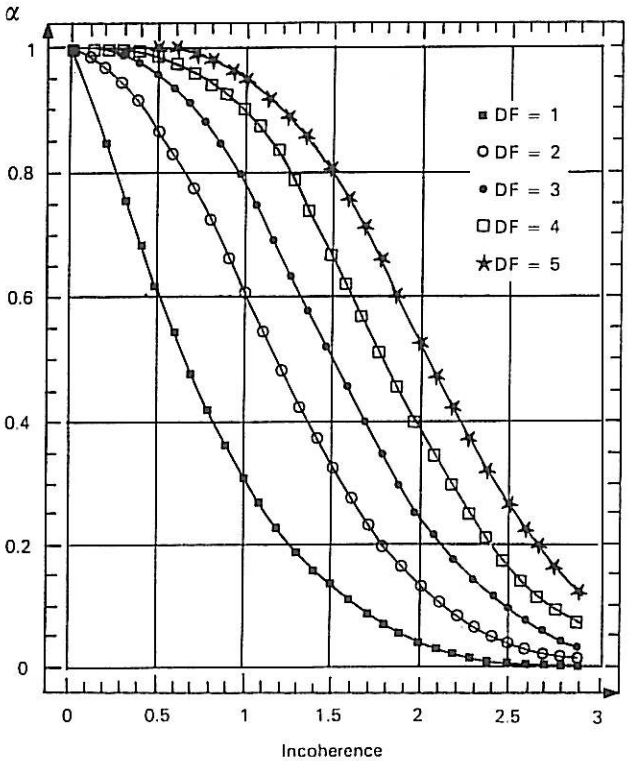


FIG. 1. Probability of validity of rock component model as a function of degree of freedom and incoherence.

Effect of Restrictions on the Degree of Freedom and the Exactness of the Calculation of Probability α

In real practice of complex log interpretation instead of equation system (6) we solve more complete task. In fact, we use one more equation, the material balance equation

$$x_1 + x_2 + \cdots x_k = 1 \qquad (14)$$

and we require all the volume fractions to be non negative, $x_i \geq 0$, $i = 1, 2, \ldots k$, having in this way the set of so called logical restrictions [3].

The new equation (14) simply means that in (13) we have to put $m+1$ instead of m in the definition of degree of freedom, since the deterministic equation (14) is a limit of a stochastic equation tending to zero variance on its right side, see [4].

In equations (8) and (9) the $\mathbf{Z}(\underline{\alpha} - \underline{x}) \in \mathbf{R}^m$ vector represents the projection of the $\underline{b}_M - \underline{b} \in \mathbf{R}^m$ vector to the k dimensional hyper plain $\kappa(\underline{z}_1, \underline{z}_2, \ldots \underline{z}_k)$ of $\mathbf{R}^m$, defined by the all possible linear combinations of vectors $\underline{z}_1, \underline{z}_2, \ldots \underline{z}_k$ which are the column vectors of matrix $\mathbf{Z}$. Until the projection of the decisive mass of the m dimensional Gaussian distribution of $\underline{b}_M - \underline{b}$ is inside of the domain allowed by restrictions i.e. the projection is given in the form $\underline{z}_1 x_1 + \underline{z}_2 x_2 + \cdots + \underline{z}_k x_k$, where all $x_i \geq 0$, then the theoretical distribution of the incoherence is undisturbed and is the Chi-distribution as given by (10). However, when the projection of the only measured $\underline{b}_M$ vector is outside or inside but close to the boundaries of the allowed domain then the projection we calculated for the theoretical distribution in (9) is not completely inside the allowed domain and so in formula (9) $\underline{\alpha}$ loses its meaning and, in this way, our definition for ξI_{A_1} fails.

Now we show that having the solution, as in [3], for the minimising task with restrictions we can avoid the case when the ordinary projection of the measured $\underline{b}_M$ vector (which is the solution (7) of the minimization task without restrictions) is outside the allowed domain. Indeed, suppose that the exact solution of the minimising task with restrictions is $\hat{\underline{x}} \in \mathbf{R}^k$ contain n_0 number of zeros ($n_0 < k$). In this case we redefine the interpretation model by leaving off the zone parameters belonging to the zero values in $\hat{\underline{x}}$, having in this way the $\mathbf{Z}'$ matrix of m rows and $k - n_0$ columns. Now the solution with restrictions for the $\mathbf{Z}'$ model is evidently given by $\hat{\underline{x}}$ (without the zeros in it) because the minimum is given by $\hat{\underline{x}}$ even on a wider set. From this it follows that for the real geophysical task with logical restrictions and with the material balance equation (14) the correct definition of the degree of freedom in the formula (13) for the probability of the model validity is

$$DF = (m+1) - (k - n_0) \qquad (15)$$

where n_0 is the number of zeros in the solution of the minimization task with logical restrictions.

Analysing the case when the ordinary projection of the measured $\underline{b}_M$ is inside the allowed domain but close to the boundary, we confine ourselves to giving estimation for the minimum distance which guarantees that we can use formula (13) with degree of freedom given by (15) for calculating the probability α with a satisfying accuracy. We construct this estimation only for the most important, (i.e. most frequent) case in practice, when the projection is near to only one boundary, given by the $x_i \geq 0$ condition, and far from all the others. As long as the projection of $\underline{b}_M - \underline{b}$ at the calculation of the theoretical distribu-

tion is inside the allowed domain, vector $\underline{\alpha}$ keeps its original meaning, and formula (9) is valid. This projection is still a Gaussian distribution around $\underline{b}$ with a unit variation and with $k-n_0$ independent coordinates. Let us denote the distance of $Z\underline{\alpha}$ from the i-th boundary by μ_b. In this case it can be shown easily that $\Phi(\mu_b)$ part of the distribution is undistrubed by the i-th boundary, where Φ is the error function, the distribution function of the one dimensional Gaussian distribution. For example at $\mu_b=2$, $\Phi(\mu_b)=0.9772$ that is, for this part of the distribution $\underline{\alpha}$ still represents a model point, so the calculation of the probability α in (13) is satisfactorily accurate.

So we need to calculate the distance of the $Z\underline{\hat{x}}$ point from the i-th boundary, where $\hat{\underline{x}}$ is the solution of the minimization task with logical restrictions (which is the same as $\underline{\alpha}$ calculated after the dimension reduction described in (15)). We can avoid repeating the calculation for each $\hat{\underline{x}}$ solution at different depth points, noticing that if we calculate only once the distance D_i of $\underline{z}_i$, the vertex of the allowed simplex domain, from the $\kappa(\underline{z}_1, \dots \underline{z}_{i-1}, \underline{z}_{i+1}, \dots \underline{z}_{k-n_0})$ hyper plane then the distance we are looking for becomes x_i part of D_i, where x_i is the i-th co-ordinate of $\underline{x}$. This statement is a direct consequence of the fact that $t\underline{z}_i+\kappa(\underline{z}_1, \dots \underline{z}_{i-1}, \underline{z}_{i+1}, \dots \underline{z}_{k-n_0})$ represents parallel planes, distance of which is regulated linearly by the t parameter alone. In this way the formula (13) remains valid, despite of the restriction conditions, with accuracy governed by μ_b if

$$x_i > \frac{\mu_b}{D_i} \tag{16}$$

for $i=1, 2 \dots k-n_0$.

To calculate the D_i distances we have to find the projection of $\underline{z}_i$ for the $\kappa(\underline{z}_1, \dots \underline{z}_{i-1}, \underline{z}_{i+1}, \dots \underline{z}_{k-n_0})$ hyper plane, which is again given by the best statistical estimation of the

$$(Z_{i-})\cdot\underline{y}=\underline{z}_i \tag{17}$$

overdetermined system of equation, where Z_{i-} is the Z matrix after neglecting its i-th column, and the unknown $\underline{y}$ has $k-1$ coordinates. Thus if we express the projection of vector $\underline{z}_i$, as in (7), then we get the distance

$$D_i=\| \underline{z}_i - Z_{i-}(Z_{i-}^T Z_{i-})^{-1}\cdot Z_{i-}^T \underline{z}_i \| \tag{18}$$

where $\| \ \|$ is the m-dimensional Euclidean distance.

If we have a component in $\hat{\underline{x}}$ different from zero volume component which does not satisfy inequality (16), that occurs for a fairly defined zone parameter matrix only at a lower percentage of all the depth points of interpretation, then for the calculation of α, instead of the Chi-distribution of (11), we use more sophisticated boundary distributions, which is not the subject of the present paper.

For the sake of conciseness let us introduce besides the degree of freedom in (13) the symbolical degree of freedom as follows:

If DF′ and DF″ are two positive integers and β' and β'' two real numbers, then the statement that we apply (13) with the symbolical degree of freedom

$$DF=\beta'\cdot DF' \oplus \beta''\cdot DF'' \tag{19}$$

means that

$$1-\alpha=\beta'\int_0^{l_{exp}} g_{DF'}(t)\,dt+\beta''\cdot\int_0^{l_{exp}} g_{DF''}(t)\,dt \tag{20}$$

Now, suppose that for all the $i=1, 2, \dots k-n_0$ (16) is satisfied except one i for which x_i tends through positive numbers to zero. In this case one restriction effects the determination of the theoretical distribution of incoherence. Using the symmetry of this special case it is not difficult to realise that we get the proper calculation for the model validity probability by applying (13) with the symbolic degree of freedom

$$\overline{DF}=\tfrac{1}{2}\cdot DF \oplus \tfrac{1}{2}(DF+1) \tag{21}$$

where the meaning of multiplication and 'plus' is given by (19) and (20), and DF is given by (15).

In the case, when (16) is satisfied for all $i=1, 2, \dots k-n_0$ except of two for which x_i and x_j tend to zero, and the angle defined in the m-dimensional Euclidean space by the $\kappa(\underline{z}_1, \dots \underline{z}_{i-1}, \underline{z}_{i+1}, \dots \underline{z}_{k-n_0})$ and $\kappa(\underline{z}_1, \dots \underline{z}_{j-1}, \underline{z}_{j+1}, \dots \underline{z}_{k-n_0})$ hyper planes is φ, then the probability α is given by (13) with the symbolic degree of freedom

$$\overline{\overline{DF}}_{\varphi}=\frac{\varphi}{2\pi}\cdot DF \oplus \tfrac{1}{2}(DF+1)\oplus\frac{\pi-\varphi}{2\pi}(DF+2) \tag{22}$$

When in (22) φ tends to π, then $\overline{\overline{DF}}_{\varphi}$ tends $\overline{DF}$ given by (21), since in this case the two hyper planes are in coincidence.

ILLUSTRATION OF THE USE OF THE MODEL VALIDITY PROBABILITY IN SANDSTONE FORMATION

Our general experience related to the usage of the probability concept above shows that depending on the geological circumstances, on the quality of the field measurements, and on the applied models of interpretation very different relations can be obtained among the probability curves. Accordingly, the intention here is just to give some illustration about the practical application of those curves, for the determination of mineral composition of drilled through formation. We have the density, neutron porosity,

acoustic, photoelectric index and the thorium and potassium spectral gamma ray logs ($m=6$) of one well in Hamada North area for complex interpretation. For the geophysical modelling of the drilled sandstone we define a set of models in the following way. Suppose that the basic part of the matrix is given by sand (Sd) and by dolomite (Dol) while the pore volume is filled up with interstitial water (Por). Additionally the matrix contains or may contain silt (Sil), different type of clays like illite (Ill) or kaolinit (Kao) and/or some iron bearing minerals like limonite (Lim), hematite (Hem). The response values for the measurements of this materials are given by laboratory data of the studied formation and by general tables, based on calculations and on laboratory measurements [5]. We can include a "mineral" into our mineral composition model only in the case if it has at least one significantly different value among its zone parameters from the zone parameter values of the sand and dolomite and from all the other included materials as well. Using this mineral set we define two component models {Por, Sd} and {Por, Dol}, for the sake of completeness, as the possible simplest formation; the basic clean sandstone without clay component {Por, Sd, Dol}; models for shaly sandstone {Por, Sd, Dol, Ill} or the same but Kao instead of Ill; models with iron hydroxides or oxides as {Por, Sd, Dol, Lim} or the same but Hem instead of Lim. We also define a larger number of five component models, combining the clay and iron bearing minerals. Thus we have a model set with different number of components; $k=2, 3, 4$ or 5, and according to formula (15) $DF=5, 4, 3$ or 2. Comparing for example the {Por, Sd, Dol} and the {Por, Sd, Dol, Ill} models often we experience that in a given depth point for the volumetric fraction of illite we get zero, $x_4=0$, and in this way as $n_0=1$, expression (15) reduces DF by one and the latter model compeletely simplifies to the three component model {Por, Sd, Dol} with exactly the same numerical value for α. But this possibility does not mean that the three component model is superfluous. Indeed, frequently we get that x_4 does exist ($x_4>0$) in the four component model but the probability α belonging to this model is less than that of the three component model. In this situation we conclude that even though the very existence of the illite component in the geological reality at the given depth can not be excluded, the illite component does not exist in a statistically significant quantity at the given depth.

Selecting the most appropriate model for interpretation we have a double aim. Our basic parameter for the oil industry and the most robust one is the porosity and we try to determine its value with the highest possible accuracy. Often we experience that different sandstone models give porosity percentages very near to each other while the probabilities belonging to the models differ significantly. This emphasizes again the high stability of porosity estimation from logs. In this situation we have enough reason to say that using a wider set of logs ($m=5, 6, 7$) we can determine not only the volumetric percentages of given minerals, but also decide certain alternatives related to the composition of the rock, therefore giving additional useful information about the formation for the reservoir engineer.

We note that in the calculation of α typical boundary distances defined by (16) and (18), belonging to the practically yet acceptable $\mu_b=1$ value, are $x_i=0.024$ for the porosity, $x_2\cong x_3=0.23$ for sand and dolomite, $x_4=0.044$ for shale and $x_5=0.03$ for iron oxides.

In Fig. 2 we demonstrate the model validity probability for the above models as a function of the

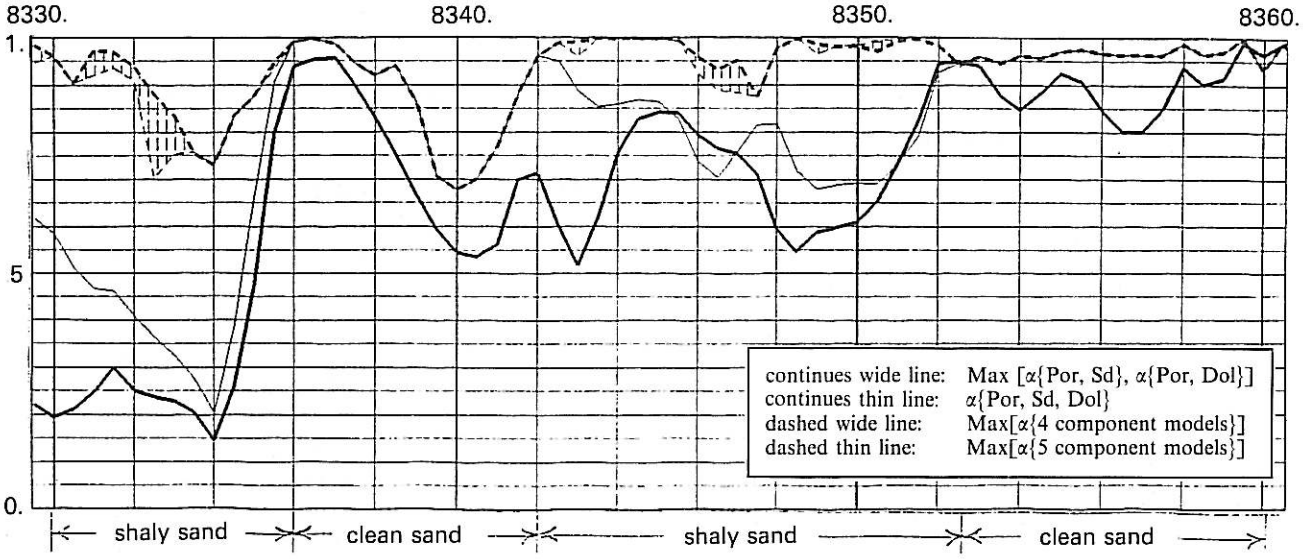
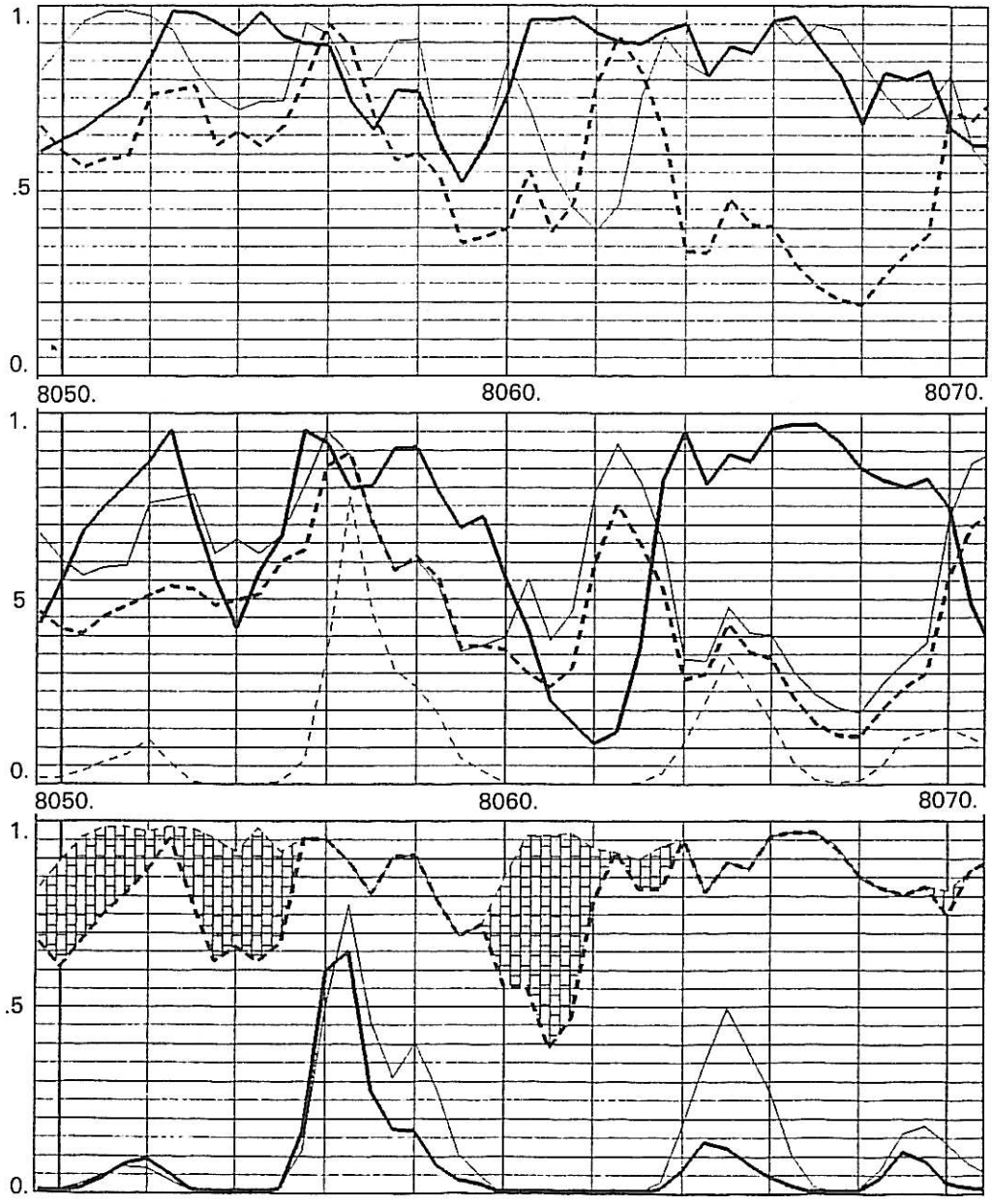


FIG. 2. Probability of validity of different sandstone models as a function of number of mineral components involved into the model in a well of sandstone formation.

number of components establishing the curves of maximum α value of all the two, four and five component models respectively, and using the only one three component model as well. In this interval the best two component model already gives relatively high probabilities, but almost everywhere the {Por, Sd, Dol} basic model works better. In the 8336.–8342. feet and in the 8352.5–8360. feet intervals any four or five component model gives the same probability as the basic model (because, in fact, they simplify to the basic model) which clearly indicates that in this intervals we have clean sand formation. In the two remaining intervals the best four component models give much higher probabilities than the basic model, thus here we have definitely shaly sand.

In the 8330.5–8333.5 feet and 8345.5–8347.5 feet intervals (shaded area in the figure) any fifth component definitely reduces the probability, because here the fifth component does not vanish but statistically is not significant.

More complex rock development is indicated in Fig. 3, where the two and three component models are failing. From 8050.0–8055.5 and from 8059.5–8064, feet (shaded area) without five components we cannot give complete explanation of our measurements, while on the remaining sections four component models give this explanation. In the mentioned five component intervals Kao plus Hem and Kao plus Sil appear in the formation. In the intervals 8057.–8059.5 and 8064.–8070. feet Kao is the type of the clay in formation, while in the interval 8055.5–



c, five component models: the basic model plus Kao, Sil for the continues wide line; the basic model plus Kao, Hem for the continues thin line; the basic model plus Ill, Hem for the dashed thin line.

b, four component models: the basic model {Por, Sd, Dol} plus Kao for the continues wide line; the basic model plus Ill for the continues thin line; the basic model plus Sil for the dashed wide line; and the basic model plus Hem for the dashed thin line

a, same curves as in Fig. 2

FIG. 3. Probability of validity of different sandstone models in the same well.

8057.0 the presence of Kao, Ill or Sil cannot be distinguished.

Table 1 shows in details the determined volumes

Table 1. Volume Fractions and the Probability of Validity Given by Different Sandstone Models at 8054 feet

Por	Sd	Dol	Kao	Ill	Si	Hem	Alfa
0.0971	0.6204	0.1028	0.1798	×	×	×	0.42
0.1581	0.3195	0.3438	×	×	0.1789	×	0.5
0.0923	0.6688	0.0358	×	0.2031	×	×	0.66
0.0923	0.6688	0.0358	×	0.2031	×	0	0.66
0.0975	0.7111	0	0.1718	×	×	0.0144	0.72
0.1251	0.4466	0.2236	0.0983	×	0.1064	×	0.92

and probabilities belonging to different models; at 8054 feet here the Kao, Sil combination alone give the definite maximum probability on a three feet long section, thus the presence of those minerals are proved; their presence at this depth effects the porosity determination relatively strongly.

CONCLUSION

- As far as we work with models of different dimensions for complex log interpretation, we have to develop the minimum incoherence concept into the maximum model validity probability concept.
- For the calculation of the model validity probability, despite of the presence of restriction conditions, for the most depth points we can use the Chi-distribution with a modified degree of freedom. However in certain cases more sophisticated boundary distributions are necessary for the same calculations.
- Using the model validity probability concept we can increase the accuracy of porosity estimation and decide certain alternatives related to the rock development as well.

ACKNOWLEDGEMENT

I would like to thank the management of the Petroleum Research Centre for the support of the present research. The author highly acknowledge the numerous consultations with Prof. Zoltan Barlai.

REFERENCES

[1] Vincze, I., 1968, Matematikai statisztika ipari alkalmazasokkal [Mathematical Statistics with Industrial Applications] Muszaki Konyvkiado Budapest (Technical Book Company).

[2] Renyi, A., 1966, Valoszinusegszamitas [Theory of Probability] Tankonyvkiado Budapest (Text Book Company).

[3] Szigeti G., 1994, Restriction Conditions in Well Log Interpretation, Petroleum Research Journal, Vol. 6., Tripoli, G.S.P.L.A.J.

[4] Szigeti, G., 1993, Improvement of the Accuracy of Statistical Well Log Interpretation Using the material Balance Equation, Petroleum Research Journal Vol. 5, Tripoli, G.S.P.L.A.J.

[5] Barlai, Z., Zilahi-Sebess, L., 1993, Report on the Sheet Silicates and their Effects on the Basic Reservoir Parameters of Shaly Sandstone and Barrier Shales, Petroleum Research Centre Internal Report, Tripoli, G.S.P.L.A.J.

PRJ, Vol. 7 (January 1995); P. 75–93, 5 FIGS, 3 PLATES

CRETACEOUS BIOSTRATIGRAPHY AND PALAEOGEOGRAPHY OF NORTH EGYPT AND NORTHEAST LIBYA

M.I. Ibrahim*, E. Schrank** and M.R. Abdel-Kireem*

الطبقية الحياتية والجغرافيا القديمة لصخور الحين الكريتاسي المبكر والمتأخر بشمال مصر وشمال شرقي ليبيا

محمد إبراهيم ، إ. شرانك و محمد عبدالكريم

هناك تشابه كبير بين الحشود الباينولوجية وحشود المنخربات ، التي ترجع إلى الحين الكريتاسي المبكر والمتأخر، بشمال مصر وشمال غربي ليبيا. وقد تحكم في نمط الرسوبيات بهذه المنطقة ومحتواها الباينوجي ومستحاثات المنخربات موقع الشاطئ القديم لبحر التيش.

وقد تمّ إعداد مجموعة من الخرائط تمثل الجغرافيا القديمة لعدة فترات زمنية أثناء الحين الكريتاسي وذلك بناء على نطاقات المستحاثات الباينوجية والمنخربات. وقد إستنتج من هذه الخريطة أيضاً مراحل تجاوز وانحسار مياه البحر أثناء ذلك الحين.

كما قسمت الرسوبيات الأبتية — السينومانية بشمال مصر وليبيا إلى أجزاء بناء على محتواها من حبوب اللقاح والأبواغ والسوطيات الدوارة. وتدل بالينومورفات الحين الكريتاسي الأوسط على ظروف ترسيبية محصورة ودور فاعل للرسوبيات المستمدة من اليابسة في الأحواض الترسيبية ، الأمر الذي وقف حائلاً أمام عدم وفرة المنخربات الهوائم بشمال مصر وشمال شرقي ليبيا وفي حوض سرت في ذلك الوقت. وقد تميزت المرحلة السينومانية بوجود أعداد كبيرة من المنخربات القاعية ذات الأصداف الملتحمة من الجنس Thomasinella ، كما شملت البالينومورفات المرشدة أنماط الألتيراتات والجنس Afropollis والنوع Classopollis brasiliensis.

وتوضح الرسوبيات التورونية — الماسترختية إنتقالاً واضحاً إلى بيئة بحرية مفتوحة وانتشار المنخربات الهائمة وبعض السوطيات الدوارة وحبوب اللقاح والأبواغ.

ABSTRACT

The Cretaceous palynological and foraminiferal assemblages from northern Egypt show an intimate resemblance to their respective counterparts from northeastern Libya. The Lower Cretaceous to Cenomanian deposits in northern Egypt and Libya were subdivided and dated by means of pollen, spores and dinoflagellates. The Neocomian is distinguished palynologically from the Late Jurassic by the first occurrence of ***Impardecispora*** *and* ***Pilosiporites trichopapillosus*** *spores.* ***Dicheiropollis etruscus*** *is a characteristic late Neocomian–Barremian guide pollen as in northern Gondwana. The Barremian is also characterized by the first incoming of* ***Ephedripites*** *pollen and primitive angiosperm pollen like* ***Clavatipollenites***, ***Asteropollis***, ***Retimonocolpites*** *and* ***Liliacidites***. *The percentage of angiosperm pollen increases during the Aptian;* ***Afropollis***, ***Brenneripollis***, *and tricolporate pollen appear. The Albian microflora is dominated by* ***Crybelosporites pannuceous***, ***Afropollis jardinus***, ***Balmeisporites*** *and* ***Ephedripites***. *Tricolporate angiosperm and elater-bearing elements are present in the middle to late Albian and become abundant in the early-middle Cenomanian. The Aptian-Albian palynomorphs indicate restricted marine conditions and high terrestrial input into the sedimentary basins. These conditions prevented the full development of planktonic foraminiferal assemblages in northern Egypt as well as in western Libya and the Sirt Basin.*

*Geology Department, Faculty of Science, Alexandria University, Egypt.
**TU Berlin, SFB 69, Ackerstr. 71–76, 13355 Berlin, Germany.

The Cenomanian is often characterized by the occurrence of large agglutinated benthonic foraminifer ***Thomasinella****, in addition to guide palynomorphs such as* ***Afropollis****,* ***Stephanocolpites****,* ***Dichastopollenites*** *and* ***Classopollis brasiliensis****. The Turonian–Maastrichtian sediments show a sharp environmental shift towards open marine conditions with abundant and well diversified planktonic foraminiferal and only subordinate dinoflagellates, pollen and spores.*

The Cretaceous sediments with their palynological and foraminiferal contents are greatly influenced by the position of the ancient shoreline of the Tethys Sea. On the basis of the palynological and foraminiferal zonation and other stratigraphical and sedimentological data available, a chronological series of maps reconstructing the Cretaceous shorelines have been prepared. The maps also provide information about the transgression-regression phases of the Cretaceous.

INTRODUCTION

The Cretaceous has been one of the main targets of oil exploration in Egypt and Libya. The Cretaceous strata are widely distributed in the area as surface exposures or concealed under the surface as recorded in many wells. In general, the Lower and Upper Cretaceous strata are represented by two main facies, the continental to shallow marine "Nubian" facies of the Lower Cretaceous and the typical deep marine shale and carbonate facies of the Upper Cretaceous.

A large quantity of new sedimentological, micropalaeontological, palynological and palaeogeographical data from the Mesozoic strata of northern Egypt and northeastern Libya have contributed to a better understanding of the transgression/regression cycles in this part of the African continent.

The aim of the present paper is to present a report on the Cretaceous biostratigraphy based on published and unpublished palynological and foraminiferal data from northern Egypt and northeastern Libya including the Sirt Basin.

1 CRETACEOUS BIOSTRATIGRAPHY

Many papers dealing with Cretaceous palynological and foraminiferal data from Egypt have been published, e.g. Beckmann *et al.* (1969), Abdel-Kireem (1971, 1986), Soliman and Sultan (1976), Saad and Ghazaly (1976), Urban *et al.* (1976), Saad (1978), Sultan (1978, 1985, 1986, 1987), Aboul Ela (1978, 1979), Abdel-Kireem and Abdou (1979), Abdelmalik *et al.* (1981), Schrank (1982, 1983, 1984a, 1984b, 1984c, 1987, 1988, 1991, 1992), Penny (1986, 1988a, 1988b, 1989, 1991), Sultan and Aly (1986), Abdel-Kireem and Ibrahim (1987), Abdel-Kireem and Sultan (1988), El-Shamma (1988), El-Shamma and Arafa (1988), Abdel Mohsen (1991), El-Beialy *et al.* (1990), Omran *et al.* (1990) and Abdel-Kireem *et al.* (1993).

Relatively few palynological and foraminiferal works on the Cretaceous of Libya have been published. Early Cretaceous to Cenomanian palynomorphs from NE Libya have been treated by Batten and Uwins (1985), Thusu and Van Der Eem (1985), Thusu *et al.* (1988) and Uwins and Batten (1988). The most important and valuable foraminiferal works have been published by Barr and Gohrbandt (1967), Phillips 1969, Barr (1971, 1972), Barr and Hammuda (1971) and Eliagoubi (1979).

I.1 Neocomian

The Lower Cretaceous deposits of both Egypt and Libya are usually barren of planktonic foraminifera. Consequently, palynomorphs have been most commonly used for biostratigraphical subdivisions.

Neocomian marginal marine sediments (Cyrenaica and Matruh Basins) can be distinguished by the dinocysts *Phoberocysta neocomica*, *Pseudoceratium pelliferum*, *Oligosphaeridium complex*, *Muderongia simplex*, and *Cyclonephelium distinctum*. Contemporaneous terrigenous spores include *Impardecispora apiverrucata* and *Pilosisporites trichopapillosus*.

The deposits of the upper Neocomian are distinguished by the first appearance of the gymnosperm pollen *Dicheiropollis etruscus* and the angiosperm pollen *Clavatipollenites hughesii*. The latter angiosperm species was recorded only in the upper Neocomian of NE Libya (Thusu *et al.* 1988).

I.2 Barremian

Barremian miospore spectra from Egypt and Libya were recorded by Saad (1978), Abdelmalik *et al.* (1981), Thusu and Van Der Eem (1985), Sultan (1986), Penny (1986, 1991), Schrank (1987), Thusu *et al.* (1988), Uwins and Batten (1988), El-Shamaa and Arafa (1988), El Sheikh and Aly (1988), El-Beialy *et al.* (1990) and Omran *et al.* (1990).

The most striking element in the late Neocomian-Barremian is the gymnosperm pollen *Dicheiropollis etruscus*. In the Barremian, *Ephedripites* and the first angiospermous pollen such as *Clavatipollenites*, *Asteropollis*, *Liliacidites*, *Retimonocolpites*, *Stellatopollis barghoornii*, and *Tucanopollis crisopolensis* appear. The dinocysts are represented by *Pseudoceratium anaphrissum*, *P. retusum*, *Coronifera oceanica*, *Cerbia tabulata*, *Systematophora silyba*, *Cribroperidinium edwardsii* and *C. orthoceras* as recorded in assemblage IB (marine) from NE Libya (Uwins and Batten, 1988).

I.3 Aptian

The Aptian palynoassemblage comprises the new incoming angiosperms of the reticulate monocolpate

or monocolpate-derived types such as *Brenneripollis*, *Schrankipollis* (formerly "*Retimonocolpites*"), the *Clavatipollenites/Asteropollis* group, *Afropollis operculatus*, *A. zonatus* and *Reyrea polymorpha*. The first tricolpate pollen also occur. The marine Aptian sediments are characterized by a dinoassemblage with *Pseudoceratium regium*, *P. securegerum*, *P. retusum*, *Aptia polymorpha*, *A. plera*, *Subtilisphaera ventriosa*, *Florentinia mantellii*, *Odontochitina aperculata*, *Cribroperidinium edwardsii*, *C. orthoceras* and *Kiokansium hydra*.

I.4 Albian

The most noteworthy feature of the Albian miospore spectra in Egypt as well as in Libya is the first appearance of *Crybelosporites* (Perotrilites) pannuceus (Gabonisporis sensu Batten and Uwins 1985, Uwins and Batten 1988) and *Balmeisporites holodictyus*. *Ephedripites jansonii* and *Afropollis jardinus* are also present. Elaterate pollen (*Elaterosporites*, *Elatercolpites* and *Elateroplicites*), tricolporate and tricolporoidate pollen characterize the late Albian.

The dinocyst assemblage of the Albian is characterized by *Xenascus ceratioides*, *X. plotei*, *Coronifera alberti*, *Oligosphaeridium porosum*, *O. djenn*, *Spiniferites multibrevis*, *Subtilisphaera perlucida*, *S. terrula*, *S. zawia*, *Trichodinium* spp., *Xiphophoridium alatum*, *Cyclonephelium vannophorum* and *Palaeohystrichophora infusorioides*. The latter species is of Vraconian age in the Tethyan province (Williams and Bujak, 1985; Uwins and Batten, 1988).

The Albian sediments in northern Egypt and Libya are usually barren of foraminifera as is the case in the older Lower Cretaceous sediments except in the area of northern Cyrenaica where abundant planktonic foraminifera diagnostic of the *Ticinella roberti* Zone (Albian) were recorded from the lower Hilal Shale (Barr and Hammuda, 1971).

I.5 Cenomanian

Early to middle Cenomanian sporomorphs are characterized by the first appearance of the polycolpate pollen *Stephanocolpites* and the gymnosperm *Classopollis brasiliensis* while circumaperturate pollen (*Dichastopollenites*) and triporate angiospermous pollen characterize the late Cenomanian. Other important sporomorphs extending from the late Albian to the early and middle Cenomanian include: elaterate pollen (*Elaterosporites*, *Elaterocolpites*, *Elateroplicites*, *Galeacornea* and *Sofrepites*) and *Cretacaeiporites polygonalis*.

The late Cenomanian of northern Gondwana is distinguished by the occurrence of the marker triporate pollen *Triorites africaensis* (Jardine and Magloire, 1965; Herngreen, 1973, 1975; Jardine *et al.*, 1974; Belsky *et al.*, 1975; Brenner, 1976; Boltenhagen, 1980; Lawal and Moullade, 1986; Muller *et al.*, 1987; Lawal, 1991). Unfortunately, this species has not been recorded until now in either Egypt or Libya, but similar triporates such as *Triporopollenites* and *Proteacidites* were recorded from the late Cenomanian of the Western Desert of Egypt (Ibrahim, 1986, 1992). Most of the dinocyst assemblages recorded from the Cenomanian are long-ranging species (Uwins and Batten, 1988; Ibrahim, 1992) such as *Florentinia resex*, *F. radiculata*, *F. mantellii*, *F. laciniata*, *F. clavigera* in addition to *Cyclonephelium vannophorum*.

There are no published palynological data for the upper Cenomanian and younger strata of Libya. However, the planktonic and benthonic foraminifera are the most reliable biomarkers for the Late Cretaceous of the working area.

The marine Cenomanian sediments in both Egypt and Libya are characterized by the occurrence of the large-sized agglutinated index foraminifer *Thomasinella* (Barr and Gohrbandt, 1967; Abdel-Kireem and Sultan, 1988; Andrawis, 1990; Hataba and Ammar, 1990; Abdel-Kireem *et al.*, 1993). The Cenomanian planktonic biomarkers *Rotalipora* spp. were recorded only from the Marsa al Hilal area (Barr, 1972). Other planktonic foraminifers characteristic of the Egyptian Cenomanian are *Hedbergella delrioensis*, *H. planispira*, *H. simplex*, *Heterohelix moremani*, *Praeglobotruncana delrioensis* and *Globigerinelloides ultramicra* (Abdel-Kireem *et al.*, 1993).

I.6 Turonian

Turonian palynological data in NE Africa are scarce. Recent studies (Schrank 1991, 1992; Ibrahim 1992) have shown that the Turonian sediments are characterized by an association of large members of the *Foveotricolpites giganteus-F. gigantoreticulatus* group with triporate and tricolporate pollen. *Classopollis*, the elaterates and other Cenomanian types are no longer present. Turonian dinocysts in northern Egypt include *Spiniferites porosus*, *S. ramosus*, *Dinogymnium vozzhennikovae*, *Florentinia* spp., *Odontochitina striatoporifera*, *Silicisphaera torulosa*, *Kleithriasphaeridium readei*, *Litosphaeridium siphoniphorum* and *Cordosphaeridium latispinosum*.

As a result of the deep marine conditions prevailing during the Turonian, the planktonic foraminiferal assemblage became rich and diversified. Abdel-Kireem *et al.* (in press) divided the Turonian into three planktonic zones, namely the *Whiteinella Archaeocretacea*, *Praeglobotruncana helvetica* and *Marginotruncana schneegansi* zones which they equated with the *Praeglobotruncana helvetica* and the *Globotruncana sigali* zones of Libya (Barr, 1972).

I.7 Coniacian

The spinose tetrad of *Droseridites senonicus* repesents an index pollen for the Coniacian to Santonian of northern Gondwana (Jardine and Magloire, 1965; Belsky *et al.*, 1975; Jan Du Chêne *et al.*, 1978; Morgan, 1978; Mebradu, 1982; Sultan, 1985; Sultan *et al.*, 1986; Lawal and Moullade, 1986; Odébdódé, 1987; Salard-Cheboldaeff, 1990; Abdel Mohsen, 1991; Schrank, 1992). Furthermore, tricolpor(oid)ates, triporates and the *Foveotricolpites giganteus-F. gigantoreticulatus* group are also present in the Coniacian sediments (Schrank 1987, 1991, 1992, Ibrahim, 1992).

In the marine microfloras the following dinocytes made their first appearance in the Coniacian: *Odontochitina porifera, Dinogymnium undulosum, D. albertii, D. longicornis, D. heterocastatum, D. cretaceum, D. microganulosum, Trigonopyxidia ginella* and *Hystrichosphaeridium atlasiense* (Ibrahim, 1992).

The Coniacian planktonic foraminiferal assemblage is represented by *Dicarinella primitiva, D. concavata, Marginotruncana coronata* and *Archaeoglobigerina cretacea.* The first two species are the zonal marker species for the Coniacian-early Santonian (Abdel-Kireem *et al.*, in preparation).

I.8 Santonian

The palynologic transition from the Coniacian to the Santonian stage is difficult to assign by means of pollen and spores. It was determined, however, by the dinocyst assemblage where the Santonian is characterized by the first evolutionary appearance of *Spinidinium sverdrupianum, Gillinia hymenophora* and *Alisogymnium euclaense* which are associated with *Glaphyrocysta divaricata, Dinogymnium sibiricum,* and *Amphigymnium cooksoniae.*

The early Santonian planktonic foraminiferal assemblage is similar to that of the Coniacian and is dominated by *Dicarinella concavata.* Upper Santonian sediments seem to be absent in the studied sections due to the absence of the late Santonian zonal planktonic species *Dicarinella asymetrica* as previously recorded by Abdel-Kireem and Ibrahim (1987) and Abdel-Kireem *et al.* (1993).

I.9 Campanian–Maastrichtian

Palynologically it is difficult to distinguish between the Campanian and Maastrichtian because they are characterized by similar microfloras. These were studied in Egypt by Aboul Ela (1978); Sultan, (1985), Abdel Mohsen (1987), El-Beialy and Kora (1987), Schrank (1984b, 1984c, 1987, 1988, 1991, 1992), Schrank and Perch–Nielsen (1985), and Ibrahim (1992). The Campanian–Maastrichtian pollen assemblage can easily be distinguished from older assemblages by the presence of pollen such as *Crassitricolporites brasiliensis, Spinizonocolpites echinatus, Echitriporites, Retidiporites, Syncolporites, Periretisyncolpites* and *Echimonocolpites.*

The Campanian–Maastrichtian phytoplanktonic assemblage is represented by *Phelodinium tricuspis, Cannosphaeropsis utinensis, Isabelidinium cretaceum, I. cooksoniae, Dinogymnium muticum, D. digitus, D. acuminatum, Thalassiphora pelagica, Amphigymnum cooksoniae, Cerodinium granulostriatum, Odontochitina porifera, O. operculata, Cladopyxidium saeptum, Conosphaeridium striatoconus, Spiniferites* spp., *Florentinia spp.*, and *Glaphyrocysta* spp.

On the other hand, the planktonic foraminiferal assemblages recorded from the Campanian–Maastrichtian in Egypt and Libya are readily distinguishable. The Campanian planktonic foraminiferal assemblage is characterized by *Globotruncanita elevata, Globotruncana ventricosa, G. linneianna, G. mariei, Globotruncanita calcarata, G. subspinosa, Contusotruncana fornicata, C. morozovae, Rugoglobigerina rugosa, Globigerinelloides prairehillensis, Heterohelix globulosa, H. striata, H. semicostata* an *Pseudotextularia elegans* (Barr, 1972; Abdel-Kireem and Abdou, 1979; Abdel-Kireem, 1986; Abdel-Kireem and Ibrahim, 1987; Andrawis 1990; Abdel-Kireem *et al.* ,1993).

The Maastrichtian planktonic foraminiferal assemblage is characterized by *Globotruncana aegyptiaca, G. arca, G. bulloides, G. falsostuarti, G. orientalis, Globotruncanita stuarti, G. stuartiformis, Gansserina gansseri, Contusotruncana contusa, Abathomphalus mayaroensis* and other distinctive forms (Barr, 1972; Eliagoubi, 1979; Abdel-Kireem and Abdou, 1979; Abdel-Kireem 1986; Abdel-Kireem *et al.*, 1993).

II CRETACEOUS PALAEOGEOGRAPHY

The Cretaceous Period in coastal NE Africa witnessed four major transgressive cycles during the Aptian, Cenomanian, Coniacian and Campanian–Maastrichtian. The Cretaceous palaeogeography of Egypt and/or Libya in general was dealt with many authors, notably: Said (1962), Barr (1972), El Shazly (1977), Van Houten (1980), Van Houten *et al.* (1984), Klitzsch and Wycisk (1987), Luger and Schrank (1987), Thusu *et al.* (1988), Uwins and Batten (1988), Klitzsch and Squyres (1990) and Said (1990). The following sections give a generalized palaeogeographic picture (Figs 1–4) of the limits and extension of the Tethys in NE Africa during the Cretaceous Period.

II.1 Neocomian–Barremian

The Lower Cretaceous sedimentation in northeast Africa was dominated by a major regressive phase

(Van Houten, 1980). The uplands in the south supplied significant amounts of sandy material to form widespread non-marine to marginal or shallow marine deposits along the unstable pericratonic margins towards the north (Thusu *et al.*, 1988).

The Lower Cretaceous "Nubian" facies in northern Egypt and NE Libya, including southeast Sirt Basin, is the most extensively developed facies encountered in numerous deep wells. In the northern Western Desert this facies is represented by the Alam El Buieb Formation or Burg El Arab Formation. In general, this "Nubian" facies consists mostly of multicoloured sandstone and shale and overlies the Pre-Cambrian basement and the Palaeozoic sediments or the Jurassic strata, while underlying the marine Upper Cretaceous shales and carbonates.

Biogeographically, two main facies are distinguishable for the Early Cretaceous in northern Egypt and NE Libya:

(1) A marginal marine facies in the northern Western Desert, i.e. Matruh Basin (Sidi Barrani and Matruh Formations) and the Cyrenaica Basin (including Jabal Al-Akhdar trough) with dinocytes, acritarchs, tasmanitids and microforaminiferal linings in certain horizons suggesting periodic incursion of the Tethys onto the platform. In this period the Tethys shoreline did not exceed lat 31°N (Fig. 1).

(2) A non-marine to fluviatile facies with miospores and dark brown terrestrial humic kerogen (wood and cuticle). These deposits are usually referred to the "Nubian" Formation (or Messak Formation in NE Libya). The Lower Cretaceous non-marine sands have provided reservoirs for several major oil fields in the Egyptian Western Desert and the Sirt Basin.

II.2 Aptian

The Aptian in northern Egypt and NE Libya shows the first major transgressive cycle of the Cretaceous Period. These marine conditions allowed the deposition of carbonates, the dolomites of the Alamein Formation, followed by the shales of the Dahab Formation in the northern Western Desert. On the other hand, a large part of the southern Western Desert was under the influence of a shallow sea where the Abu Ballas Formation was deposited.

In Libya, continental conditions allowed the deposition of the Lower Cretceous continental beds (alluvial and fluviatile sediments) of the wood-bearing

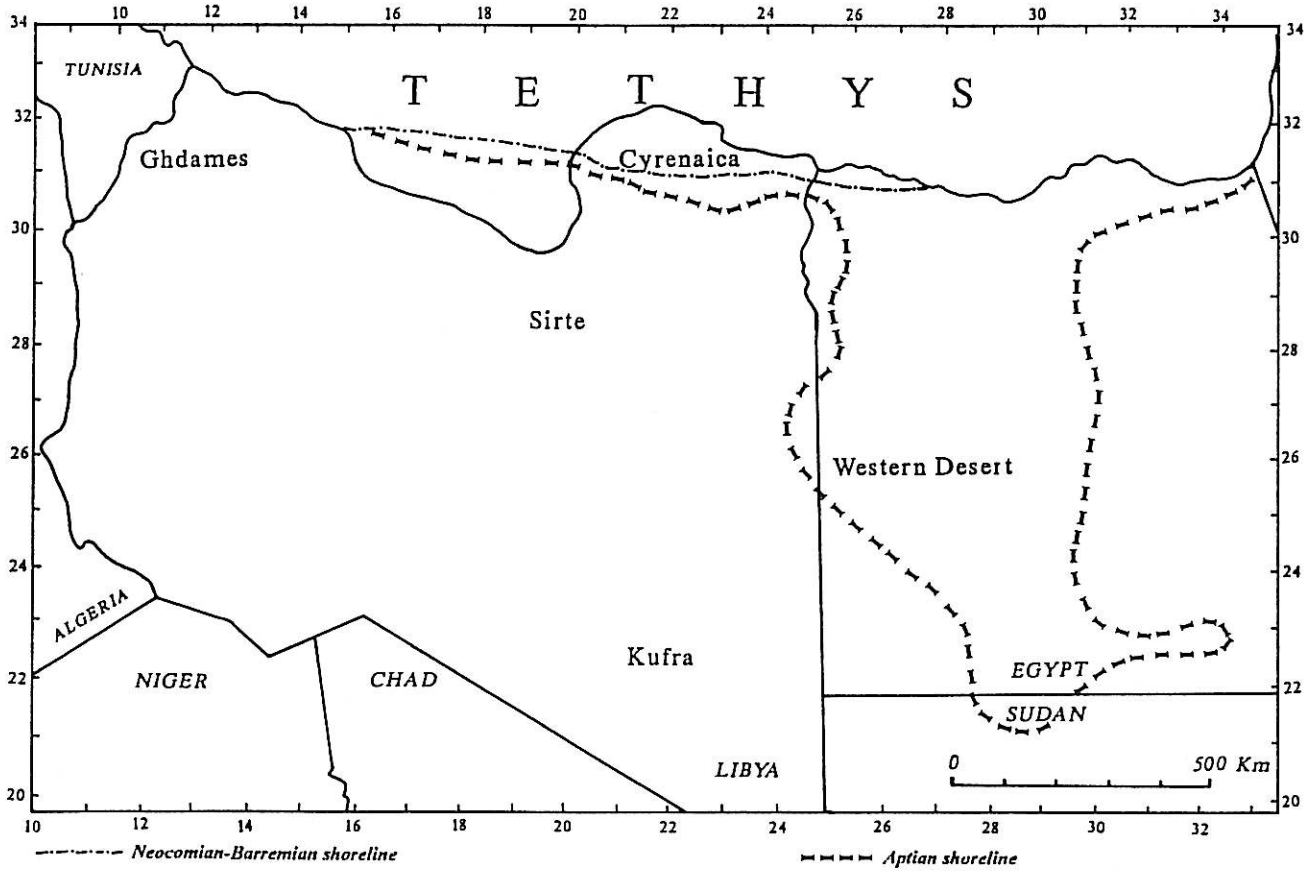


FIG. 1. A map showing the position of the tethys shorelines during the Neocomian-Barremian and Aptian in Egypt and Libya (based on Baarr, 1972; Klitzsch and Wyeisk, 1987; Uwins and Batten, 1988; Said, 1990, and others).

Chicla Formation covering most of the southern region (Barr and Weegar, 1972). An exception is the Jabal Akhdar trough across northern Cyrenaica (Barr, 1972) which was deposited under marine conditions. The Tethys shoreline during the Aptian was restricted to the area north of approximately 30.5°N in NE Libya and may have reached to lat 29°N in the northern Western Desert of Egypt. An Aptian Tethyan arm invaded most of the Western Desert to lat 21°N (Klitzsch and Wycisk, 1987; Said 1990, see Aptian shoreline Fig. 1).

II.3 Albian

The Albian, in general, represents a regressive phase in which the Tethys withdrew northward as in pre-Aptian time. Except in the Matruh, Sidi Barrani and the Cyrenaica areas, fluvial deposits which resulted from the eroding of an elevated massif to the south were formed in most of Egypt and Libya. Marine deposits, represented by carbonates and shales in and around the Matruh and Cyrenaica basins, were formed in areas north of lat. 30.5°N (Albian shoreline, Fig. 2). This palaeogeographical picture was supported by Barr and Hammuda (1971) who have described planktonic foraminiferal taxa from the lower part of the Hilal Shale belonging to the *Tricinella roberti* Zone (Albian).

II.4 Cenomanian

The Cenomanian stage witnessed the second major marine phase in large parts of northern Egypt and Libya (Fig. 2).

The formation of the Sirt Basin commenced at the dawn of the Cenomanian (Berggren, 1969; Barr, 1972). The Sirt Basin Arch underwent extreme tensional stress. This positive area collapsed into a series of alternating grabens and horst blocks generally oriented NNW–SSE. Several of the principal grabens are about 150 to 200 miles in length and 25 to 30 miles in breadth (Barr, 1972). These dimensions and orientations are similar to contemporaneous structures in the Gulf of Suez which was differentiated at the same time into its eastern and western embankments, the sites of the shallow marine Raha and Galala Formations. In northern Sinai, the thick marine calcaerous sediments of the Halal Formation were deposited, while in the northern Western Desert the Baharija Formation was formed and comprises tidal flat, estuarine to fluviatile deltaic deposits with frequent marine intercalations (Dominik, 1985). In the

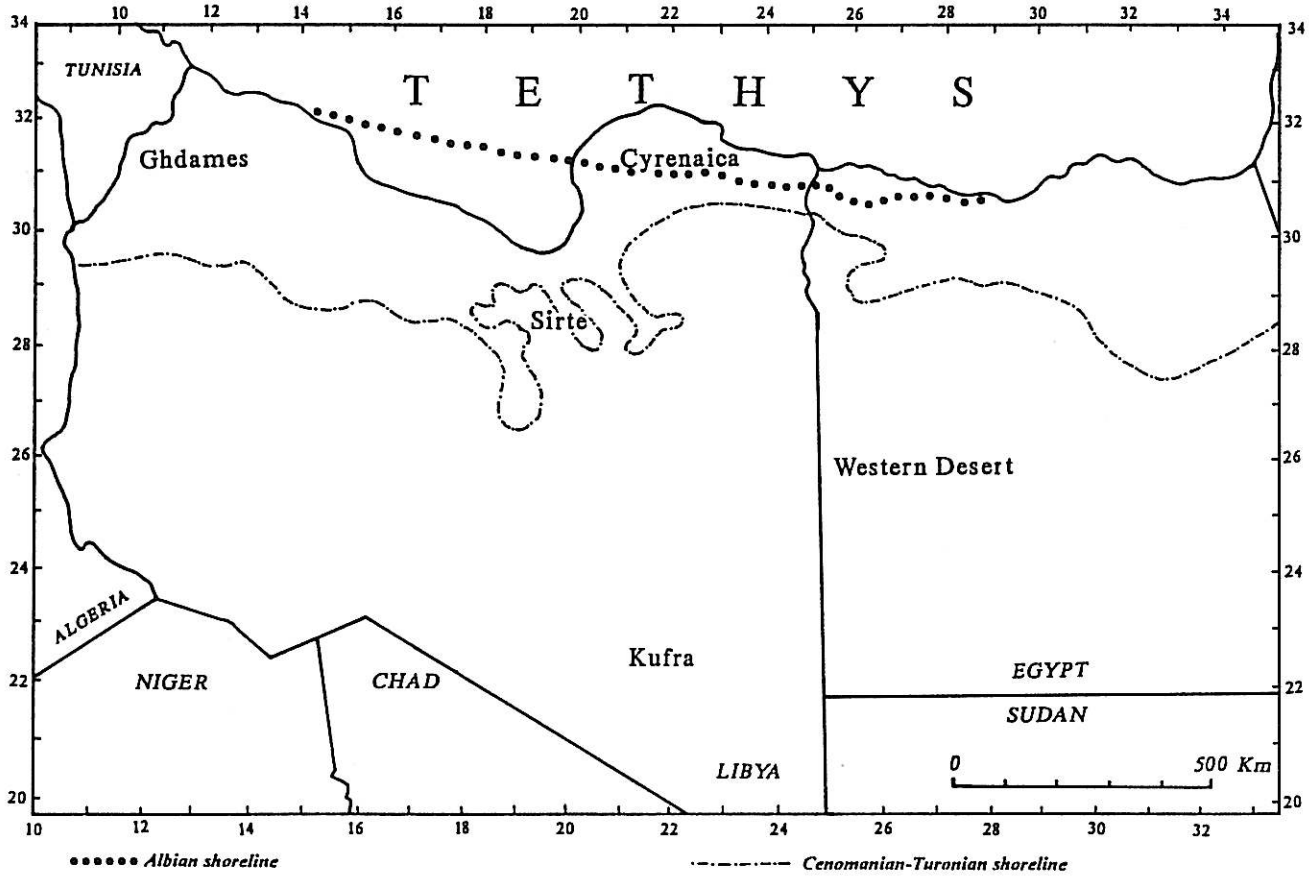


FIG. 2. A map showing the position of the Tethys shorelines during the Albian and Cenomanian-Turonian in Egypt and Libya (based on Barr, 1972; Van Houten, 1980; Klitzsch and Wycisk, 1987; Uwins and Batten, 1988; Said 1990; and others).

late Cenomanian, the marine influence was even stronger resulting in the deposition of the lower part of the Abu Roash Formation "member G" in the subsurface, which is equivalent to the El-Heiz Formation in the south (Hanter, 1990).

In north Libya, the Cenomanian transgression caused the deposition of shallow marine carbonates together with subordinate amounts of clay, lime clay and sand along the grabens of the Sirt Basin. Along the edges of these troughs, sabkhas developed locally, resulting in the deposition of dolomite and evaporites (Barr, 1972). In northeastern Libya (Cyrenaica) the sea advanced a short distance to the south of the Lower Cretaceous basin. The Cenomanian is represented by deep marine shales belonging to the lower part of Hilal Shale (Barr and Hammuda, 1971; Barr and Weegar, 1972) while farther south, the shallow marine deposits are represented by carbonates (Ain Tobi Limestone) and marls of the lower Jardas Formation (late Cenomanian).

II.5 Turonian

The marine conditions that prevailed during the late Cenomanian continued into the Turonian in both northern Egypt and Libya, as suggested by the abundance of planktonic foraminifera.

The marine Turonian in the Gulf of Suez area is represented by a lower shale unit, the Abu Qada Formation, and an upper solid limestone unit, the Wata Formation. In the subsurface of the northern Western Desert the Turonian is represented by the Abu Roash D, E and F members.

In the Sirt Basin, the Turonian embayments largely became areas of sabkha evaporitic deposition. In the northern Sirt Basin, western Libya and northern Cyrenaica, shallow marine carbonate (Argub Carbonate) and thin bedded carbonates, shale, anhydrite, and siltstone (Etel Formation) were formed (Barr and Weegar, 1972).

II.6 Coniacian

The Coniacian represents the third major transgressive cycle over most of Egypt and Libya following a minor regression at the end of the Turonian (Fig. 3). In northern Egypt and Libya the Coniacian sediments were deposited under fairly deep water, open marine conditions, as suggested by planktonic foraminifera and dinocysts which became increasingly abundant.

The marine Coniacian in northern Egypt and in

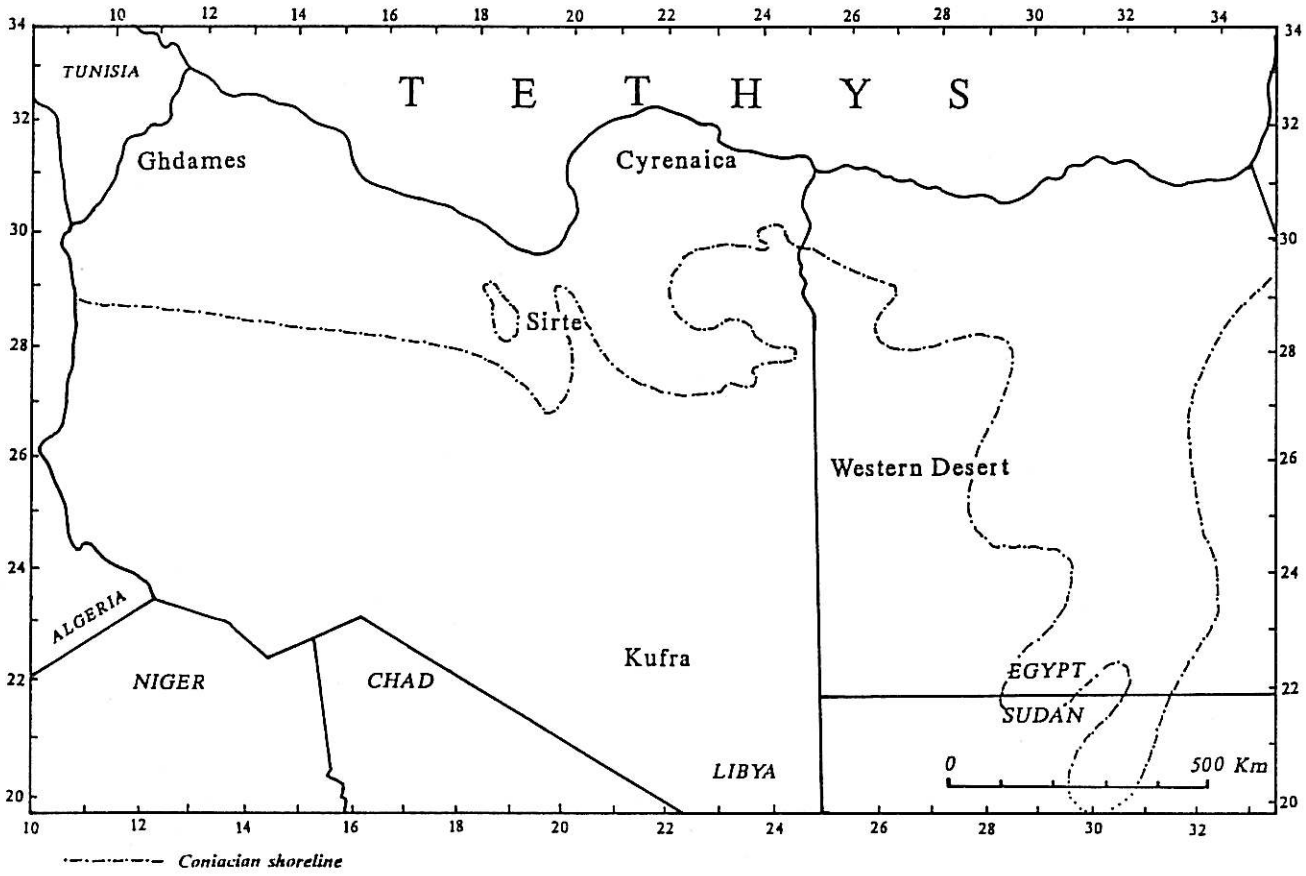


FIG. 3. A map showing the position of the Tethys shoreline during the Coniacian in Egypt and Libya (based on Barr, 1972; Klitzsch and Wycisk, 1987; Said, 1990; and others).

the Gulf of Suez area is represented by the Abu Roash B and C members and by the Matulla Formation, respectively, while in the Nile embayment and in the Wadi Qena area shallow marine epicontinental deposits alternate with fluvial sediments of the Timsah and Hawashiya Formations (Said, 1990).

In parts of the northern Sirt Basin argillaceous carbonates and clays were deposited. In the Marsa al Hilal area of northern Cyrenaica about 183 m of the upper Hilal Shale and 18.3 m of the basal Atrun Limestone belong to the Coniacian (Barr, 1972).

II.7 Santonian

During the early Santonian a short time regression took place which was followed by a renewed transgression. While the Santonian sea advanced far to the sourth covering most of northern Egypt and Libya, a number of small areas remained emergent as islands in northern Egypt and the Sirt Basin (Fig. 4). This explains the absence of Santonian deposits in most deep wells of the northern Western Desert (Abdel-Kireem and Ibrahim, 1987; Hanter 1990; Abdel-Kireem *et al.*, 1993).

In the Gulf of Suez the Santonian is represented by the St Anthony Chalk and by the upper beds of Matulla Formation (Said, 1990). In the northern, Western Desert the Santonian is represented by the Abu Roash "A" member which is recorded only in those basins which became clearly distinct between the major highs.

In Sirt Basin and northeastern Libya a considerable thickness of dark brown clays and shales (Rachmat Formation, Coniacian–Santonian) were deposited with rare planktonic foraminifera and common small *Neobulimina* (Barr, 1972).

II.8 Campanian–Maastrichtian

During the Campanian–Maastrichtian the sea had reached its maximum sothern extension as a result of the fourth and last major transgressive phase of the Cretaceous Tethys (Figs 4, 5). The transgression reached its maximum extent during the middle to late Maastrichtian.

Two main facies characterize the Campanian–Maastrichtian sediments in NE Africa. (1) The deep marine facies to the north of lat. 28°N represented by chalky limestones, the Sudr in northern and central Sinai and the Gulf of Suez area, and the Khoman

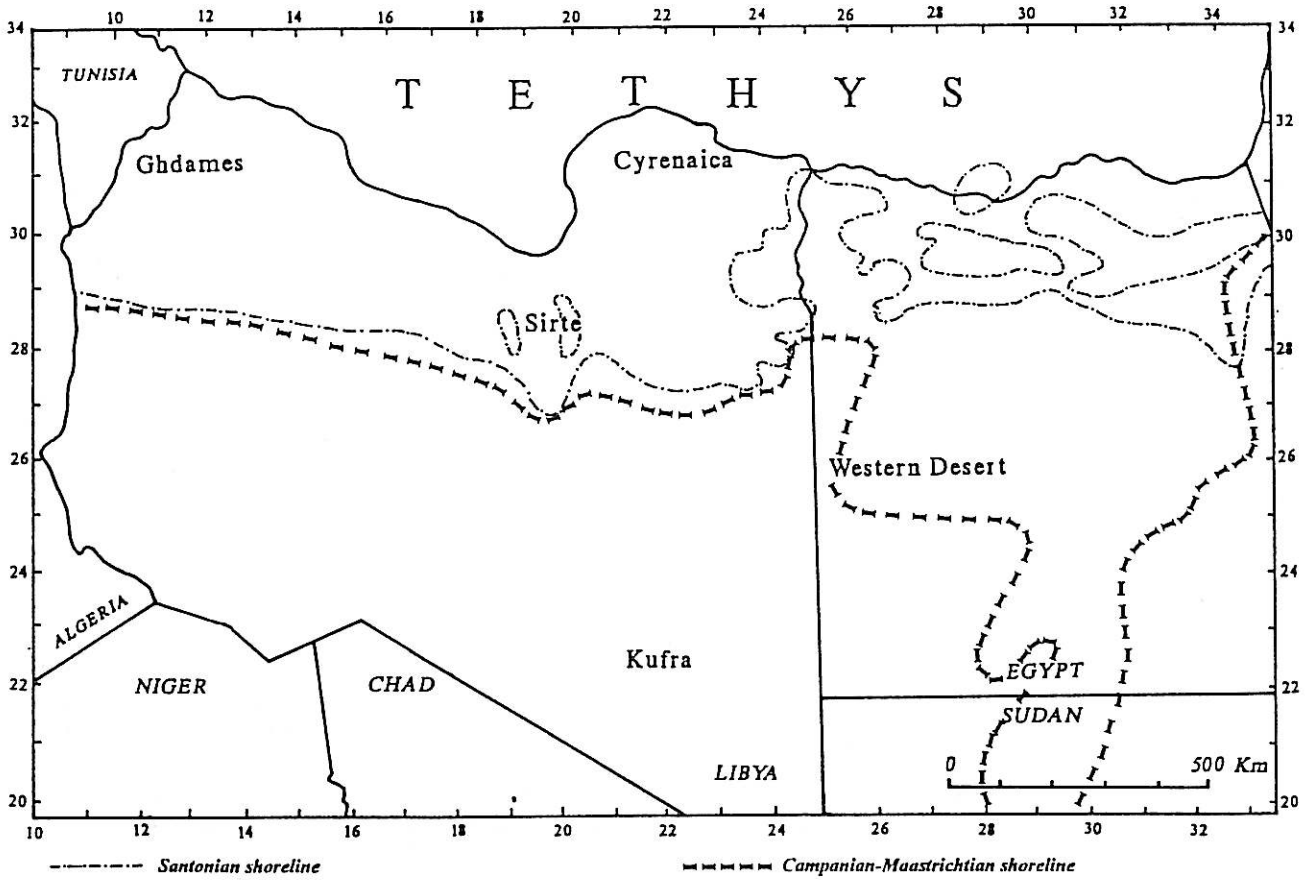


FIG. 4. A map showing the position of the Tethys shorelines during the Santonian and Campanian-Maastrichtian in Egypt and Libya (based on Barr, 1972; Litzsch and Wycisk, 1987; Said, 1990; and others).

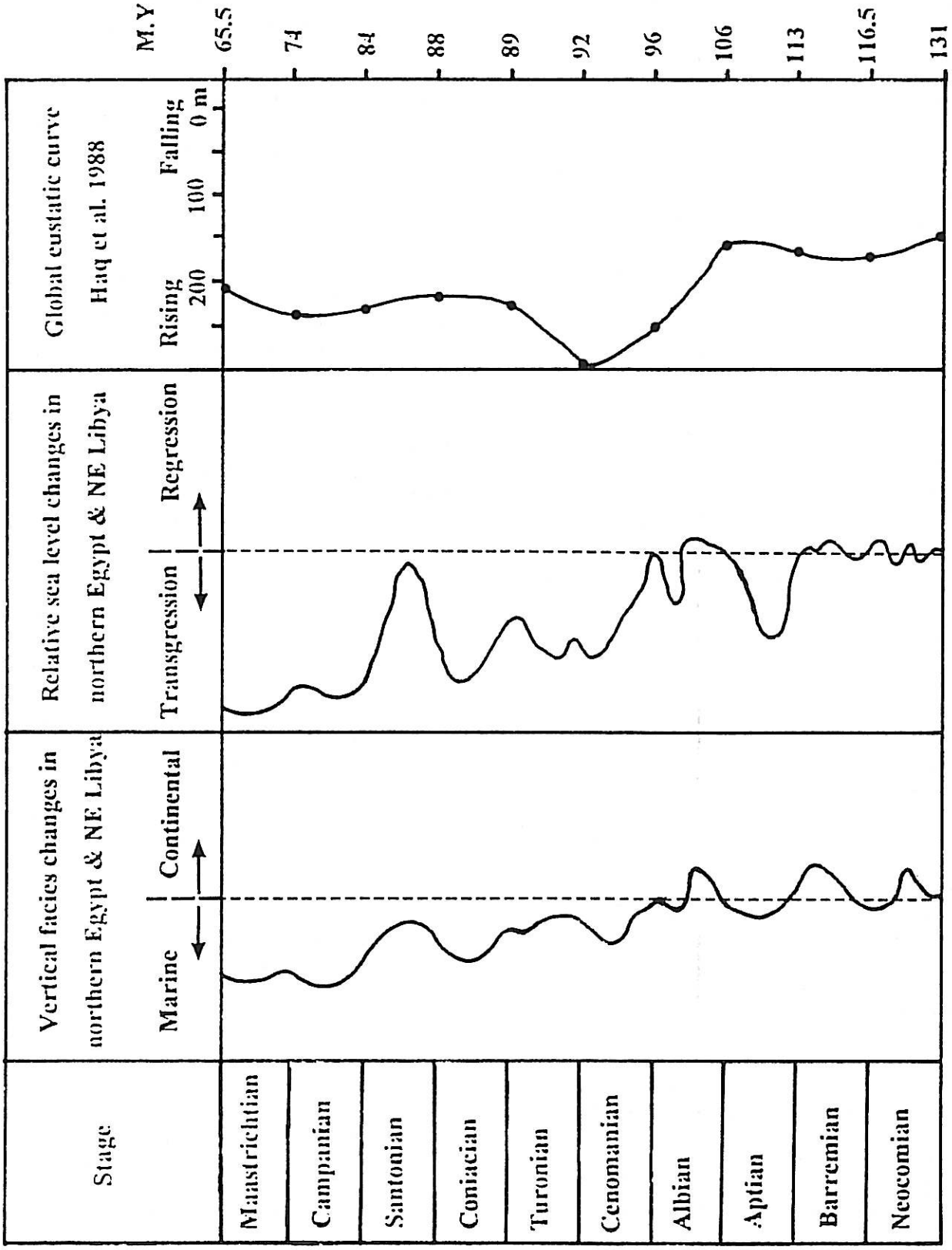


FIG. 5. Reconstructed Cretaceous transgression-regression phases in northern Egypt and NE Libya with the global custatic sea level changes, after Haq *et al.*, 1988.

Formation in northern Eastern and Western Desert. (2) The shallow marine facies to the south of lat. 28°N represented by phosphate deposits (Duwi Formation) and shales (Rakhiyat, Quseir and Dakhla formations). In the Gulf of Suez the Campanian marl section includes phosphatic beds and was named Gebel Thelmet Formation (Brown limestone by oil company geologists).

In northern Libya the Campanian–Maastrichtian sediments are represented by dark brown clays in the lower Campanian and by calcereous shales (Sirte Shale) in the upper Campanian–Maastrichtian. The Maastrichtian is represented by limestone (Atrun Limestone-Kalash Limestone-Waha Limestone) with a high percentage of planktonic foraminifera which suggests an open sea, neritic environment of deposition (Barr and Weegar, 1972).

CONCLUSIONS

In northern Egypt and NE Libya the Cretaceous sedimentary sequences with their microflora and microfauna have a more or less similar depositional picture. The Cretaceous sea level and the vertical facies changes in northern Egypt and NE Libya were compared with the global eustatic sea level changes of Haq *et al.*, 1988. The detailed studies on the Cretaceous microfloral and foraminiferal contents of northern Egypt and NE Libya led to the following conclusive remakrs:

(1) The Neocomian–Barremian in Egypt and Libya was dominated by a major regressive phase. Two facies could be distinguished: (a) a non-marine to fluviatile "Nubian" facies with its peculiar spores and pollen, and (b) a marginal marine facies containing dinocysts as well as pollen and spores. The Neocomian terrigenous spores include *Impardicispora apiverrucata* and *Pilosisporites trichopapillosus.* The gymnosperm pollen *Dicheiropollis etruscus* is the most striking element in the late Neocomian-Barremian. In the Barremian, *Ephedripites* and the first angiospermous pollen appear. The dinocysts include *Phoberocysta neocomica*, and *Muderongia simplex* in the Neocomian, while the Barremian is distinguished by *Pseudoceratium anaphrissum*, *P. retusum*, *Coronifera oceanica*, *Cerbia tabulata*, and *Cribroperidinium.*

(2) The Aptian Tethys shoreline was restricted to the area north of approximately 30.5°N in NE Libya and Egypt. A Tethyan arm invaded most of the Western Desert to lat. 21°N. The Aptian palynoassemblage includes *Brenneripollis*, *Afropollis zonatus*, *A. operculatus* and *Reyrea.* The Aptian dinoassemblage is dominated by *Pseudoceratium*, *Aptia polymorpha*, *A. plera*, *Subtilisphaera ventriosa*, *Odontochitina operculata*, and *Kiokansium hydra.*

(3) The Albian in general represents a regressive phase in which the Tethys withdrew northwards as in pre-Aptian time. The Albian sediments in northern Egypt and Libya are usually barren of foraminifera as is the case of the older Lower Cretaceous sediments. The Albian palynomorphs in Egypt as well as in Libya are represented by *Crybelosporites (Perotrilites) pannuceus* and *Balmeisporites holodictyus*, *Ephedripites jansonii* and *Afropollis jardinus.* Elaterate pollen, tricolporate and tricolporoidate pollen characterize the late Albian. The dinocyst assemblage of the Albian is characterized by *Xenascus ceratioides*, *X. plotei*, *Oligosphaeridium porosum*, *O. djenn*, *Spiniferites multibrevis*, *Subtilisphaera perlucida*, *S. terrula* and *S. zawia.*

(4) The Cenomanian showed the second major marine transgression in large parts of northern Egypt and Libya. The formation of the Sirt Basin commenced at the beginning of the Cenomanian. Early to middle Cenomanian sporomorphs are characterized by the polycolpate pollen *Stephanocolpites* and the gymnosperm *Classopollis brasiliensis*, while circumaperturate pollen (*Dichastopollenites*) and triporate angiospermous pollen characterize the late Cenomanian. The marine Cenomanian sediments in both Egypt and Libya are characterized by the occurrence of the large-sized agglutinated index foraminifer *Thomasinella.* The Cenomanian planktonic biomarkers *Rotalipora* spp. were recorded only from the Marsa al Hilal area, NE Libya. The Egyptian Cenomanian planktonic biomarkers are characterized by *Hedbergella*, *Heterohelix* and *Praeglobotruncana delrioensis.*

(5) The marine conditions that prevailed during the late Cenomanian continued into the Turonian in both northern Egypt and Libya. The Turonian sediments are characterized by an association of large members of the *Foveotricolpites giganteus-F. gigantoreticulatus* group. Turonian dinocysts in northern Egypt include *Spiniferites porosus*, *S. ramosus* and *Dinogymnium vozzhennikovae.* The recorded planktonic foraminifera are distinguished by the zonal marker species *Whiteinella archaeocretacea*, *Praeglobotruncana helvetica* and *Marginotruncana schneegansi.*

(6) The Coniacian represents the third major transgressive cycle over most of Egypt and Libya. The Coniacian sediments were deposited under fairly deep water, open marine conditions, as suggested by planktonic foraminifera and dinocysts which became increasingly abundant. *Droseridites senonicus* with the *Foveotricolpites giganteus-F. gigantoreticulatus* group are the index pollen recorded from the Coniacian sediments. The following dinocysts made their first appearance in the Coniacian: *Odontochitina porifera*, *Dinogymnium undulosum*, *D. albertii*, *D. longicornis*, *D. heterocastatum*, *D. cretaceum*, *D. microgranulosum* and *Trigonopyxidia ginella.* The Coniacian planktonic

foraminiferal assemblage is characterized by the zonal markers *Dicarinella primitiva* and *D. concavata.*

(7) The Santonian sea advanced far to the sourth covering most of northern Egypt and Libya, but a number of small areas remained emergent as islands in northern Egypt and the Sirt Basin.

The dinocysts are characterized by the first evolutionary appearance of *Spinidinium sverdrupianum, Gillinia hymenophora* and *Alisogymnium euclaense.*

The early Santonian planktonic foraminiferal assemblage is similar to that of the Coniacian and is dominated by *Dicarinella concavata.* Upper Santonian sediments seem to be absent in the studied sections due to the absence of the late Santonian zonal planktonic species *Dicarinella asymetrica.*

(8) During the Campanian–Maastrichtian the sea had reached its maximum southern extension as a result of the fourth and last major transgressive phase of the Cretaceous Tethys. The transgression reached its maximum extent during the middle-late Maastrichtian.

The Campanian–Maastrichtian pollen assemblage can easily be distinguished from older assemblages by the presence of pollen such as *Crassitricolporites brasiliensis, Spinizonocolpites, Echitriporites, Retidiporites* and *Periretisyncolpites.* The phytoplanktonic assemblage is represented by *Phelodinium tricuspis, Cannosphaeropsis utinensis, Dinogymnium acuminatum, D. digitus, D. muticum, Thalassiphora pelagica, Amphigymnium cooksoniae* and *Cerodinium granulostriatum.*

On the other hand, the Campanian planktonic foraminiferal assemblage is characterized by *Globotruncanita elevata, Globotruncana ventricosa* and *Globotruncanita calcarata.* The Maastrichtian planktonic foraminiferal assemblage is characterized by *Globotruncana aegyptiaca, G. falsostuarti, Gansserina gansseri, Contusotruncana contusa* and *Abathomphalus mayaroensis.*

REFERENCES

Abdel-Kireem, M.R., 1971. Contribution to the stratigraphy of Gebel Thelmet area, south Galala Plateau, Eastern Desert, Egypt. Bull. Fac. Sci., Alexandria University, 11: 71–86.

Abdel-Kireem, M.R., 1986. Microfaunastic parameters of the Chalk Formation (Upper Cretaceous), Bahariya Oasis, Egypt. Rev. Esp. Micropal., 18(1): 27–46.

Abdel-Kireem, M.R. and Abdou, H.F., 1979. Upper Cretaceous-Lower Tertiary planktonic foraminifera from South Galala Plateau, Eastern Deser, Egypt. Rev. Esp. Micropal., 11(2): 175–222.

Abdel-Kireem, M.R. and Ibrahim, M.I.A., 1987. Late Cretaceous biostratigraphy and palaeobathymetry of the Betty Well No. 1, Western Desert, Egypt. In: G. Matheis & H. Schandelmeir (Editors), Current Research in African Eart Sciences. Balkema, Rotterdam, Bookfield: 165–169.

Abdel-Kireem, M.R., Samir, A.M. and Ibrahim, M.I.A., (in prep.). Upper Cretaceous foraminiferal zonation and correlation in the northern Western Desert of Egypt.

Abdel-Kireem, M. R., Schrank, E., Samir, A.M. and Ibrahim, M.I.A., 1993. Cretaceous plaeoecology, palaeoclimatology and palaeogeography of the northern Western Desert of Egypt. In Thorweihe & Schandelmeier (Editors), Geoscientific Research in Northeast Africa, Balkema, Rotterdam: 375–380.

Abdel-Kireem, M.R. and Sultan, I.Z., 1988. Cenomanian agglutinated foraminifera from Baharija Oasis Western Desert, Egypt. Rev. Paléobiologie, 2: 259–270.

Abdelmalik, W.M., Aboul Ela, N.A. & El-Shamaa, A.G., 1981. Upper Jurassic-Lower Cretaceous Microflora from the North-Western Desert, Egypt. N. Jb. Geol. Paläont. Abh., 162(2): 244–263.

Abdel Mohsen, S., 1987. Palynological studies of the Lower Esna Shale Formation (Cretaceous) in the Tushka Basin, Southern Egypt. N. Jb. Geol. Paläont. Mh., 6: 357–370.

Abdel Mohsen, S., 1991. Microfloras from the Upper Cretaceous near Aswan, southern Egypt. N. Jb. Geol. Paläont. Mh., 12: 711–727.

Aboul Ela, N.M., 1978. The palynological characteristics of the Upper Cretaceous sediments in Abu Tartur Plateau, Kharga Oasis, Egypt. Rev. Espan. Micropaleont., 10(3): 421–442.

Aboul Ela, N.M., 1979. Lower Cretaceous microflora from the North-Western Desert of Egypt. N. Jb. Geol. Paläont. Mh., 10: 586–595.

Andrawis, S.F., 1990. Tables of foraminiferal biozones. In: R. Said (Editor), The Geology of Egypt. Balkema, Rotterdam, Brookfield: 639–648.

Barr, F.T., 1971. The foraminiferal genus *Bolivinoides* from the Upper Cretaceous of Libya. Jour. Paleontol., 44(4): 462–654.

Barr, F.T., 1972. Cretaceous biostratigraphy and planktonic foraminifera of Libya. micropaleontol., 18(1): 1–46.

Barr, F.T. and Gohrbandt, K.H.A., 1967. *Thomasinella punica*, a Tethyan foraminifer from the Cenomanian of central Tunisia. In: Martin, L., Ed., Guide-book to the geology and history of Tunisia. Tripoli: Petrol. Expl. Soc. Libya: 153–158.

Barr, F.T. and Hammuda, O.S. 1971. Biostratigraphy and planktonic zonation of the Upper Cretaceous limestone and Hilal Shale, northeastern Libya. Internat. Conf. Planktonic Microfossils, 2*nd*, Rome, Proc: 27–40.

Barr, F.T. and Weegar, A.A. 1972. Stratigraphic nomenclature of the Sirte Basin, Libya. Tripoli, Petrol. Expl. Soc. Libya: 179 pp.

Batten, D.J. and Uwins, P.J.R., 1985. Early-Late Cretaceous (Aptian–Cenomanian) palynomorphs. J. micropal., 4(1): 151–168.

Beckman, J.P., El-Heiny, I., Kerdany, M.T., Said, R. and Viotti, C., 1969. Standard planktonic zones in Egypt. Proc. 1*st* Inter. Conf. Plank. Microf., Geneva: 92–103.

Belsky, C.Y., Jardiné, S., Prestat, B., Durif. P., Grosdidier, E., Casson, J.P. and Gillmann, M., 1975. Etude stratigraphique et sédimentologique d'une coupe du Crétacé-Tertiaire au large du Surinam. Oroc. IX Inter Guyana Geol. Conf. Bol. Geol. Venezuela: 179–197.

Berggren, W.A., 1969. Biostratigraphy and planktonic foraminiferal zonation of the Tertiary System of the Sirte Basin of Libya, North Africa. Proc. 1*st* Plank. Conf. Geneva (1967): 104–120.

Boltenhagen, E., 1980. Palynologie du Crétacé supérieur du Gabon. Com. Trav. Inst. Sci., Mém. Sec. Sci., Pris, 7: 1–191.

Brenner, G.J., 1976. Middle Cretaceous floral provinces and early migration of angiosperms. In: C.B. Beck (ed.): Origin and early evolutionh of angiosperms, 23–47. New York: Columbia Univ. Press.

Dominik, W., 1985. Stratigraphie und Sedimentologie (Geochemie, Schwermineralanalyse) der Ober-Kreide von Baharija und ihre Korrelation zum Dakhla-Becken (Western Desert, Ägypten). Berliner geowiss. Abh., (A), 62: p. 1–173.

El-Beialy, S.Y., and Kora, M., 1987. Cretaceous-Early Tertiary palynomorphs from Dark El Arbain, Southern Egypt. Bull. Fac. Sci., Mansoura University, 14(2): 343–358.

El-Beialy, S.Y., Ayyad, S.N., and Kholeif, S.E., 1990. Mesozoic-Tertiary palynomorphs and planktonic foraminifera of the subsurface section of the Sindy-1 well, eastern Nile Delta, Egypt. Newsl. Strati., 22(2/3): 71–85.

Eliagoubi, B., 1979. Systematic paleontology of Maastrichtian foraminifera (Upper Cretaceous) from Northcentral and Northwestern Libya. Arab Development Institute, Tripoli: 79 pp.

El-Shamma, A.E. and Arafa, A.A., 1998. Early pollen angiosperm from the Lower Cretaceous sediments in the northern part of the Western Desert, Egypt. Egypt. J. Geol., 32, 1–2: 263–272.

El Shazly, E.M., 1977. The Geology of the Egyptian Region. In: A.E.M. Nairn, W.H. Kanes and F.G. Stehli (Editors), The Ocean Basins and Margins. Plenum Press 4(A): 379–444.

El Sheikh, H.A. and Aly, S.M., 1988. Nannoplankton and palynological biostratigraphy of the Early Cretaceous rocks of Monaga Well No.1, east of the Nile Delta. Egypt. JH. Geol., 32, 1–2: 243–261.

Hanter, G., 1990. North Western Desert. In: R. Said (Editor), The Geology of Egypt. Balkema, Rotterdam, Brookfield: 293–320.

Haq, B.U., Hardenbol, J. and Vial, P.R., In collaboration with others, 1988. Mesozoic and Cenozoic chronostratigraphy and cycles of sea-level change. Soc. Econom. Paleontol. Mineral., Spec. Publ. (42): 71–108.

Hataba, H. and Ammar, G., 1990. Comparative stratigraphic study on the upper Cenomanian-lower Senonian sediments between the Gulf of Suez and the Western Desert, Egypt. EGPC Tenth Expl. Prod. Conf., Cairo: p. 1–16.

Herngreen, G.F.W., 1973. Palynology of Albian-Cenomanian strata of borehole 1-QS-1-MA, state of Maranhao, Brazil. Pollen Spores, 15(3–4): 515–555.

Herngreen, G.F.W., 1975. Palynology of Middle and upper Cretaceous strata in Brazil. Meded. R.G.D., N.S. 26(3): 39–91.

Ibrahim, M.I.A., 1986. Mesozoic Palynological and Foraminiferal studies of Betty well No.1, Western Desert, Egypt. M.Sc. thesis (unpublished), Geology Dept., Faculty of Science, Alexandria University: 1–258.

Ibrahim, M.I.A., 1992. Palynological and foraminiferal studies in the subsurface Cretaceous of the northern Western Desert, Egypt. Ph. D. thesis (unpublished), Geology Dept., Faculty of Science, Alexandria University: 1–270.

Jan Du Chené, R.E., Adegoke, O.S., Adediran, S.A. and Petters, S.W., 1978. Palynology and foraminifera of the Lokoja Sandstone (Maastrichtian), Bida Basin, Nigeria. Rev. Esp. Micropal., 10: 379–393.

Jardiné, S., Kieser, G. and Reyre, Y., 1974. l'individualisation progressive du continent Africain vue a'travers les données palynologiques de l'ére secondaire. Sci. Géol., Bull., 27(1–2): 69–85.

Jardiné, S., and Magloire, L., 1965. Palynologie et stratigraphie du Cretacé des Bassins du Senegal et de Cote d'Ivoire. Mem. Bur. Rech. Geol. Min., 32: 187–245.

Klitzsch, E.H. and Wycisk, P., 1987. Geology of the sedimentary basins of northern Sudan and bordering areas. Belriner geowiss. Abh., (A), 75.1: 97–136.

Klitzsch, E.H. and Squyres, C.H., 1990. Paleozoic and Mesozoic geological history of northeastern Africa based upon new interpretation of Nubian strata. AAP≃G Bull., 74(8): 1203–1211.

Lawal, O., 1991. Palynological age and correlation of a black shale section in the Eze-Aku Formation, Lower Benue Trough, Nigeria. J. Afr. Earth Sci., 12(3): 473–482.

Lawal, O. and Moullade, M., 1986. Palynological biostratigraphy of Cretaceous sediments in the upper Benue Basin, N.E. Nigeria(1). Rev. Micropal., 29(1): 61–83.

Luger, P. and Schrank, E., 1987. Mesozoic to Paleogene transgressions in middle and southern Egypt–Summary of paleontological evidence. In: G. Matheis & H. Schandelmeir (Editors), Current Research in African Earth Sciences. Balkema, Rotterdam, Brookfield: 199–202.

Mebradu, S., 1982. Stratigraphic palynology of Obi (Lafia), Plateau State of Nigeria. Rev. Palaeobot. Palynol., 36: 317–323.

Morgan, R., 1978. Albian to Senonian palynology of Site 364, Angola Basin. Init. Repts. DSDP, 40: 915–951.

Muller, J., De Di Giacomo, E. and Vn Erve, A.W., 1987. A palynological zonation for the Cretaceous, Tertiary, and Quaternary of northern South America. AASP Contr. Ser. (19): 7–75.

Odébódé, M.O., 1987. Palynological dating of the Lamja Sandstone (Benue Basin, Nigeria) and its geological significance. J. Afr. Earth Sci., 6(4): 421–426.

Omran, A.M., Soliman, H.A., and Mahmoud, M.S., 1990. Early Cretaceous palynology of three boreholes from northern Western Desert (Egypt). Rev. Palaeobot. Palynol., 66: 293–312.

Penny, J.H.J., 1986. An Early Cretaceous Angiosperm pollen assemblage from Egypt. Paleont., Spec. Papers No.35: 121–134.

Penny, J.H.J., 1988a. Early Cretaceous Acolumellate semitectate pollen from Egypt. Palaeont., 31(2): 373–418.

Penny, J.H.J., 1988b. Early Cretaceous striate tricolpate pollen from the Borhole Mersa Matruh 1, North West Desert, Egypt. J. micropal., 7(2): 201–215.

Penny, J.H.J., 1989. New Early Cretaceous forms of the angiosperm pollen genus *Afropollis* from England and Egypt. Rev. Palaeobot. Palynol., 58: 289–299.

Penny, J.H.J., 1991. Early Cretaceous angiosperm pollen from the borehole Mersa Matruh 1, North West Desert, Egypt. Palaeontog. Abt. B, 222: 31–88.

Phillips, R.W., 1969. Biostratigraphic study in the Sirte Basin, Libya. Proc. 3*rd* African Micropaleontol. Colloquium, Cairo, 1968: 503–508.

Saad, S.I., 1978. Palynological studies in the Egyptian Western Desert: Umbarka IX Borehole. Pollen Spores, 20(2): 261–301.

Saad, S.I. & Ghazaly, G., 1976. Palynological studies in Nubia Sandstone from Kharga Oasis. Pollen Spore, 18(3): 407–470.

Said, R., 1962. Geology of Egypt. Elsevier Publ. Co., N.Y., Amsterdam, 337 pp.

Said, R., 1990. Cretaceous paleogeographic maps. In: R. Said (Editor), The Geology of Egypt. Balkema, Rotterdam, Broodfield: 439–449.

Salard-Cheboldaeff, M., 1990. Intertropical African palynostratigraphy from Cretaceous to Late Quaternary times. J. Afr. Earth Sci., 11(1/2): 1–24.

Schrank, E., 1982. Kretazische Pollen und Sporen aus dem "Nubischen Sandstein" des Dakhla-Beckens (Ägypten). Berliner Geowiss. Abh., (A), 40: 87–109.

Schrank, E., 1983. Scanning electron and light microscopic investigations of Angiosperm pollen from the Lower Cretaceous of Egypt. Pollen Spores, 25(2): 213–242.

Schrank, E., 1984a. Paleozoic and Mesozoic palynomorphs from the Foram 1 Well (Western Desert, Egypt). N. Jb. Geol. Paläont. Mh., 2: 95–112.

Schrank, E., 1984b. Organic-walled microfossils and sedimentary facies in the Abu Tartur Phosphates (Late Cretaceous, Egypt). Berliner geowiss. Abh., (A), 50: 177–187.

Schrank, E., 1984c. Organic-Geochemical and palynological studies of a Dakhla shale profile (Late Cretaceous in Southeast Egypt: Part A: Succession of microfloras and depositional environment. Berliner geowiss. Abh., (A), 50: 189–207.

Schrank, E., 1987. Paleozoic and Mesozoic palynomorphs from Northeast Africa (Egypt and Sudan) with special reference to Late Cretaceous pollen and dinoflagellates. Berliner Geowiss. Abh., (A), 75.1: 249–310.

Schrank, E., 1988. Effects of chemical processing on the preservation of Peridiniod Dinoflagellates: a case from the Late Cretaceous of NE Africa. Rev. Palaeobot. Palynol., 56: 123–140.

Schrank, E., 1991. Mesozoic palynology and continental sediments in NE Africa (Egypt and Sudan) – a review. J. Afr. Earth Sci., 12(1/2): 363–373.

Schrank, E., 1992. Nonmarine Cretaceous correlations in Egypt and northern Sudan: palynological and palaeobotanical evidence. Cret. Res., 13: 351–368.

Schrank, E. and Perch-Nielsen, K., 1985. Late Cretaceous Palynostratigraphy in Egypt with comments on Maastrichtian and Early Teriary Calcareous Nannofossils. Newsl. Stratig., 15(2): 81–99.

Soliman, H.A. and Sultan, I.Z., 1976. Spores et Pollen des Gres de Baharia, Desert Ouest, Egypte. Rev. Micropaleont., 19(2): 108–111.

Sultan, I.Z., 1978. Mid-Cretaceous plant microfossils from the Northern part of the Western Desert of Egypt. Rev. Palaeobot. Palynol., 25: 259–267.

Sultan, I.Z., 1985. Palynological studies in the Nubia Sandstone Formation, east of Aswan, southern Egypt. N. Jb. Geol. Paläont. Mh., 10: 605–617.

Sultan, I.Z., 1986. Palynostratigraphy of Lower Cretaceous sediments in the Nile Delta region, Egypt. Rev. Espan. Micropal., 18(1): 55–70.

Sultan, I.Z., 1987. Palynology of Albian-Cenomanian strata in Mersa Matruh Well, Western Desert, Egypt. J. Afr. Earth Sci., 6(5): 665–675.

Sultan, I.Z. and Aly, S.M., 1986. Palynological zonation of Albian-Cenomanian sediments in the Northern part of the Western Desert of Egypt. Bull. Fac. Sci. Alex. Univ., 26(3): 80–101.

Sultan, I.Z.; Aly, S.M. and Arafa, A.A., 1986. Palynostratigraphy of the Turonian-Lower Senonian sequence, Gulf of Suez Area, Egypt. Bull. Fac. Sci. Alex. Univ., 26(3): 1–17.

Thusu, B. and Van Der Eem, J.G.L.A., 1985. Early Cretaceous (Neocomian-Cenomanian) palynomorphs. J. Micropal. 4: 131–151.

Thusu, B., Van Der Eem, J.G.L.A., El-Mhdawi, A. and Bu-Argoub, F., 1988. Jurassic-Early Cretaceous palynostratigraphy in northeast Libya. In: A. El-Arnauti, B. Owens, and B. Thusu (Editors), Subsurface Palynostratigraphy of northeast Libya. Garyounis Univ. Publ.: 171–214.

Urban, L.L.; Moore, L.V. and Allen, L.M., 1976. Palynology, Thermal alteration and source rock of three Wells from Alamein Area, Western Desert, Egypt. *5th* EGPC Expl. Seminar, November 1976, 1–31 pp.

Uwins, P.J.R. and Batten, D.J., 1988. Early to mid-Cretaceous palynology of northeast Libya. In: A. El-Arnauti, B. Owens, and B. Thusu (Editors), Subsurface Palynostratigraphy of northeast Libya. Garyounis Univ. Publ.: 215–258.

Van Houten, F.B., 1980. Latest Jurassic-Early Cretaceous regressive Facies, northeast Africa Craton. AAPG Bull., 64 (6): 857–867.

Van Houten, F.B., Bhattacharyya, D.P. and Mansour, S.E.I., 1984. Cretaceous Nubia Formation and correlative deposits, eastern Egypt: Major regressive-transgressive complex. Geol. Soc. Amer. Bull., 95: 397–405.

Williams, G.L. and Bujak, J.P., 1985. Mesozoic and Cenozoic dinoflagellates. In: H.M. Bolli, J.B. Saunders and K. Perch-Nielsen (Editors), Plankton Stratigraphy, Cambridge, Cambridge Univ. Press 1985: 847–964.

PLATE 1

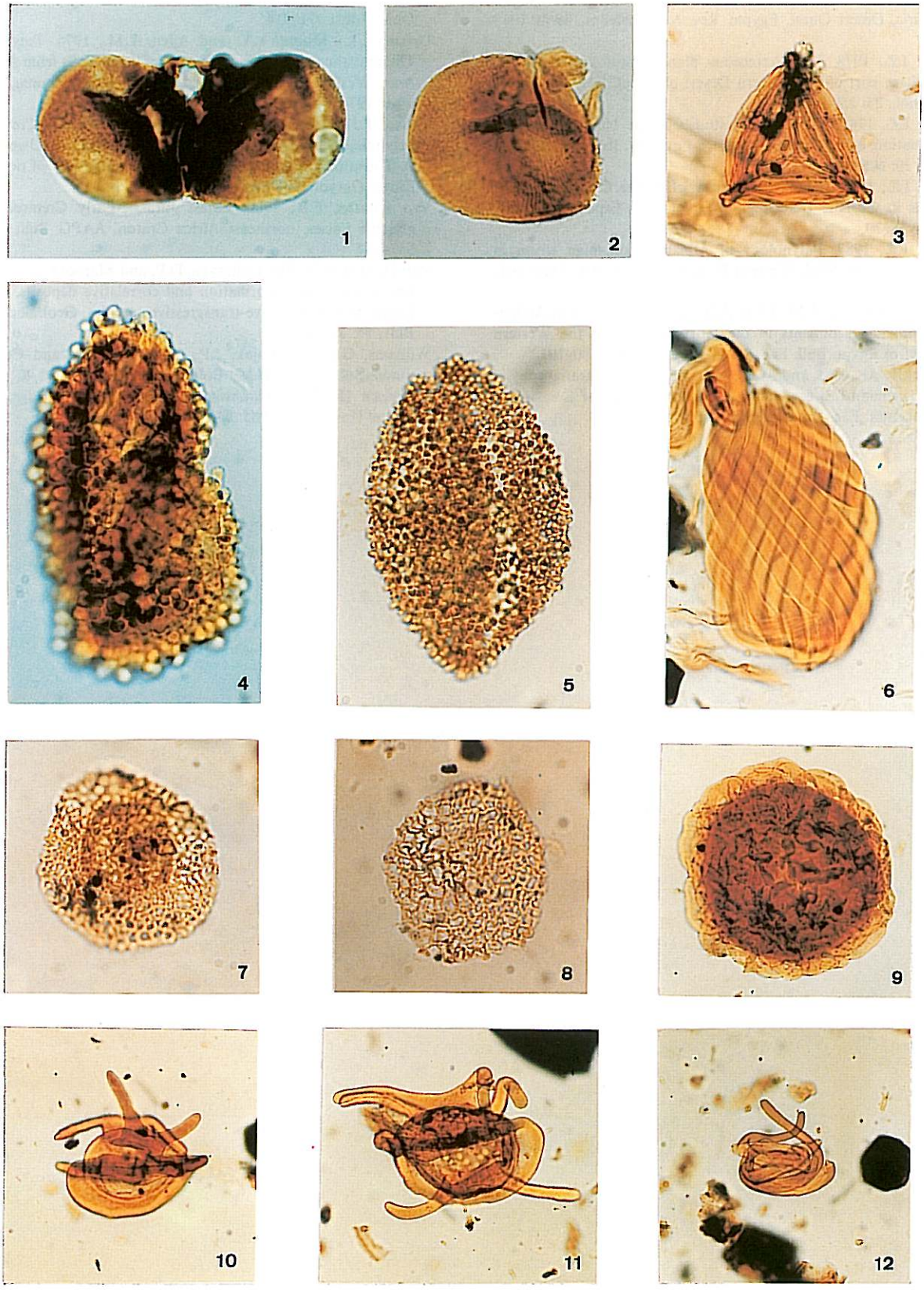


PLATE 1

Fig. 1. *Dicheiropollis etruscus* Trevisian, 1972. Kahraman-1, Sample 149, 11800 ft., Slide 2, × 1000, (late Neocomian–Barremian).

Fig. 2. Half grain of *Dicheiropollis etruscus* Trevisian, 1972. Kahraman-1, Sample 143, 11460 ft., Slide 1, × 1000, (late Neocomian–Barremian).

Fig. 3. *Appendicisporites potomacensis* Brenner, 1963. Kahraman-1, Sample 118, 9250 ft., Slide 2, × 500, (Albian-Cenomanian).

Fig. 4. *Reyrea polymorphus* Herngreen, 1973. Kahraman-1, Sample 106, 8600 ft., Slide 2, × 1000, (Aptian-Albian).

Fig. 5. *Sellatopollis barghoornii* Doyle *et al.*, 1975. Kahraman-1, Sample 96, 7500 ft., Slide 2, × 1000, (Aptian-Cenomanian).

Fig. 6. *Ephedripites jansonii* (Pocock) Muller, 1968. Kahraman-1, Sample 96, 7500 ft., Slide 3, × 800, (Albian-Cenomanian).

Fig. 7. *Afropollis operculatus* Doyle *et al.*, 1982. Kahraman-1, Sample 115, 9030 ft., Slide 3, × 1000, (Aptian).

Fig. 8. *Afropollis aff. jardinus* Doyle *et al.*, 1982. Kahraman-1, Sample 110, 8700 ft., Slide 2, × 1000, (Aptian-Albian).

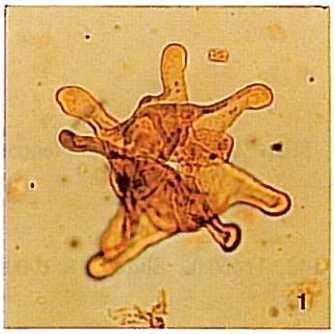
Fig. 9. *Crybelosporites pannuceus* (Brenner) S.K. Srivastava, 1977. Kahraman-1, Sample 82, 6900 ft., Slide 1, × 500, (Albian-Cenomanian).

Fig. 10. *Elaterosporites klaszi* (Jardine and Magloire) Jardine, 1967. Kahraman-1, Sample 82, 6900 ft., Slide 1, × 500, (Albian-Cenomanian).

Fig. 11. *Elaterosporites verrucatus* (Jardine and Magloire) Jardine, 1967. Kahraman-1, Sample 87, 7100 ft., Slide 2, × 500, (Albian-Cenomanain).

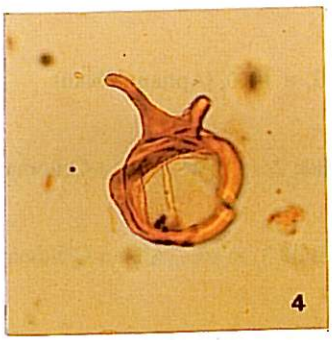
Fig. 12. *Elateroplicites africaensis* Herngreen, 1973. Kahraman-1, Sample 72, 6400 ft., Slide 1, × 500, (late Albian-Cenomanian).

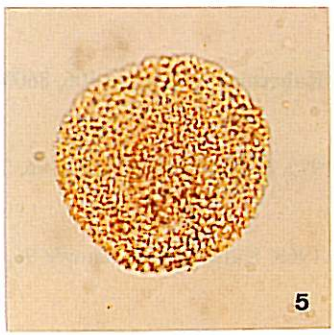
PLATE 2

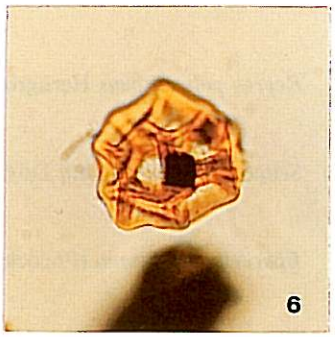


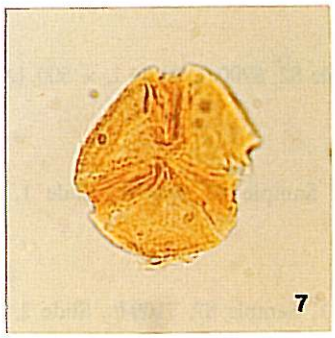


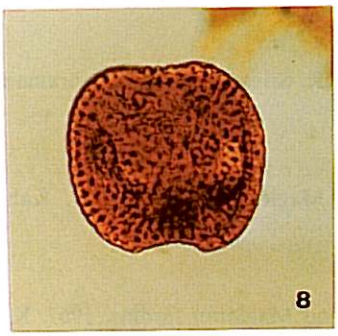


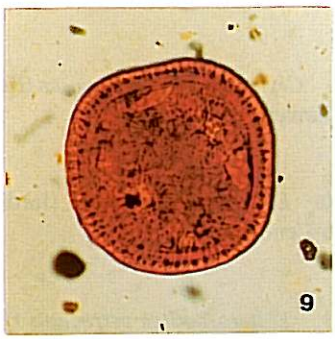












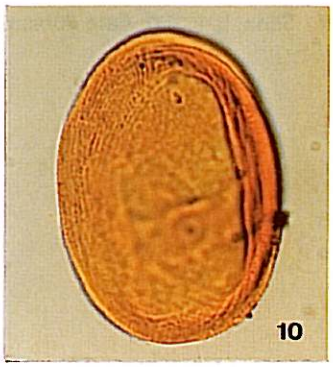






PLATE 2

Fig. 1. *Elaterocolpites castelaini* Jardine and Magloire, 1965. Kahraman-1, Sample 74, 6500 ft., Slide 2, × 500, (late Albian–Cenomanian).

Figs 2, 3. *Galeacornea* cf. *causea* Stover, 1963, high and low focus. Kahraman-1, Sample 98, 7600 ft., Slide 2, × 800, (late Albian-Cenomanian).

Fig. 4. *Galeacornea clavis* Stover, 1963. Kahraman-1, Sample 80, 6800 ft., Slide 1, × 500, (late Albian-Cenomanian).

Fig. 5. *Afropollis jardinus* (Brenner) Doyle *et al.*, 1982 (fine reticulation variety). Kahraman-1, Sample 80, 6800 ft., Slide 2, × 1000, (late Albian-Cenomanian).

Fig. 6. *Cretacaeiporites polygonalis* (Jardine and Magloire) Herngreen, 1973. Kahraman-1, Sample 89, 7200 ft., Slide 2, × 1000, (late Albian-Cenomanian).

Fig. 7. *Nyssapollenites albertensis* Singh, 1971. Kahraman-1, Sample 74, 6500 ft., Slide 1, × 1000, (Cenomanian).

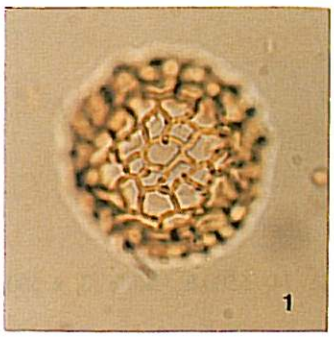
Figs 8, 9. *Stephanocolpites* sp., Kahraman-1, Samples 87 and 96, 7100 and 7500 ft., Slides 3 and 1 respectively, × 1000, (Cenomanian).

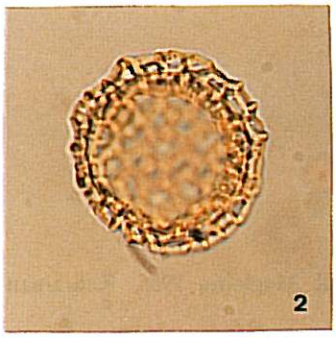
Fig. 10. *Classopollis brasiliensis* Herngreen, 1975. Kahraman-1, Sample 68, 6200 ft., Slide 1, × 1000, (Cenomanian).

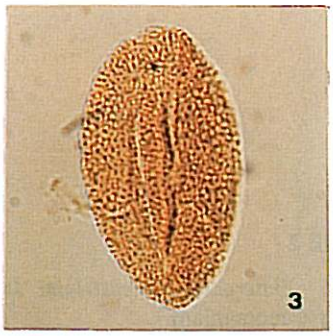
Fig. 11. *Tetracolpites* sp., Kahraman-1, Sample 91, 7300 ft., Slide 1, × 1000, (Cenomanian).

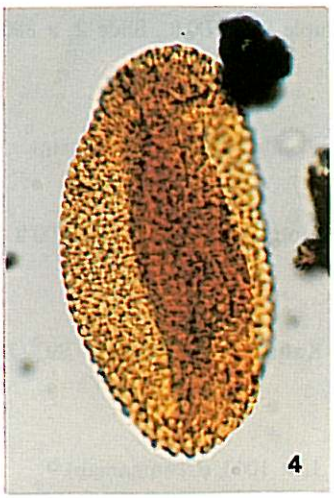
Fig. 12. *Triporopollenites* sp., Kahraman-1, Sample 29, 4250 ft., Slide 1, × 1000, (late Cenomanian-Maastrichtian).

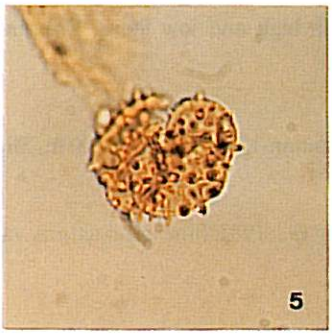
PLATE 3

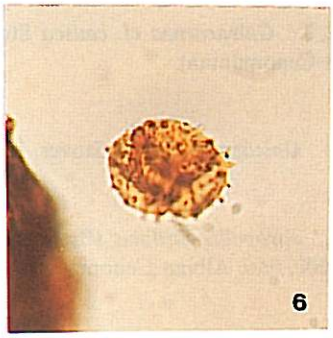


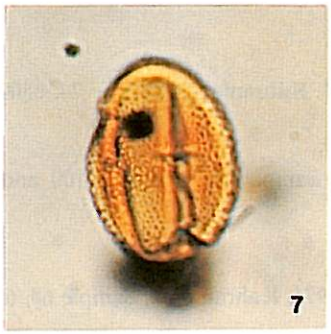


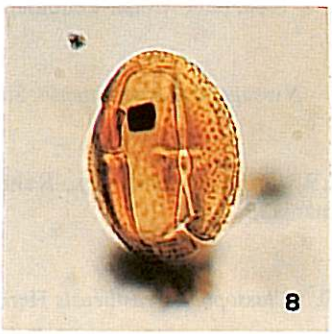




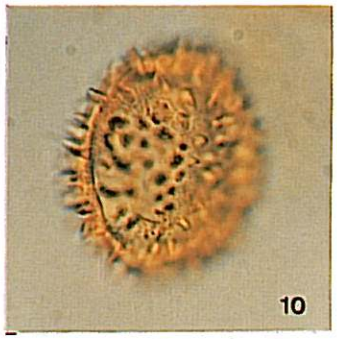












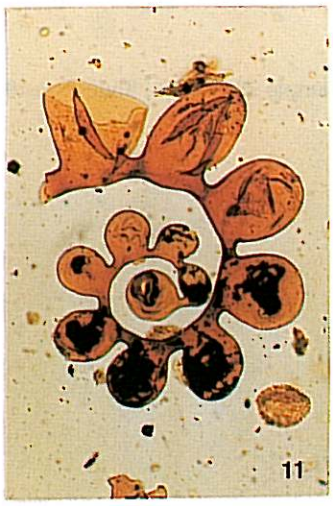




PLATE 3

Figs. 1, 2. *Dichastopollenites* cf. *dunveganensis* Singh, 1983 (high and low focus). Ghazalat-1, Core 5, 2112–2115 ft., Slide 1, × 1000, (late Cenomanian).

Fig. 3. *Faveotricolpites gigantoreticulatus* (Jardine and Magloire) Schrank, 1987. Kahraman-1, Sample 24, 4000 ft., Slide 1, × 1000, (Turonian-Santonian).

Fig. 4. *Foveotricolpites giganteus* (Jardine and Magloire) Jan Du Chene *et al.*, 1978. Abu Gharadig-18, Sample 15, 8900 ft, Slide 2, × 1000, (Turonian-Santonian).

Figs. 5, 6. *Droseridites senonicus* Jardine and Magloire, 1965. Abu Gharadig-18, Sample 15, 8900 ft., Slide 1, × 1000, (late Turonian-Santonian).

Figs. 7, 8. *Crassitricolporites brasiliensis* Herngreen, 1972. Kahraman-1, Sample 18, 3700 ft., Slide 2, × 1000, (Campanian-Maastrichtian).

Figs. 9, 10. *Spinizonocolpites* cf *echinatus* Muller, 1968. Kahraman-1, Sample 16, 3600 ft., Slide 2, × 1000, (Campanian-Maastrichtian).

Fig. 11. Microforaminiferal lining. Kahraman-1, Sample 32, 4400 ft., × 250.

Fig. 12. Scolecodont. Kahraman-1, Sample 24, 4000 ft., Slide 1, × 500.

PRJ, Vol. 7 (January 1995); P. 95–99, 7 FIGS, 1 TABLE.

FOSSIL PHYTOCLASTS IN OILS FROM MESSLAH AND BOURI OIL FIELDS – LIBYA: A PRELIMINARY STUDY

R.N. Sinha* and H.B. Eland*

متحجرات الفتات النباتية في نفط حقول الميسلي والبوري — ليبيا : دراسة أولية

ر. ن. سنها وهـ. ب. ايلاند

يحتوي النفط المنتج من آبار حقول الميسلي والبوري على رواسب يحتمل أن يكون مصدرها الصخور المولدة ، الخزانات النفطية وبقية الصخور التي إنتقل النفط خلالها عبر الأزمنة الجيولوجية.

إن دراسة الفتات النباتية المحتواة في النفط الخام يمكن أن تساعد على ربطها بالصخور المولدة. تم دراسة الجزء الفتاتي ومحتوياته في المتحجرات البالينولوجية في حقول الميسلي والبوري. وقد تم استخدام تقنيات مخبرية متطورة لفصل واستخراج المتحجرات البالينولوجية من النفط الخام.

المحتويات الفتاتية في عينات النفط التي تم دراستها قليلة جداً والفتات النباتية كذلك قليلة جداً. وقد شوهدت متحجرات بالينولوجية نذكر منها نوع البسيلانراليس ونوع السايكودونيس وحبوب اللقاح الرباعية ويحتمل كذلك وجود نوع ريترايكولبايتس. أما بقية الفتات النباتية فتحوي بقايا نباتية وبالينولوجية ومادة عضوية ذات لون أسود إلى بني عميق. كما أن المتحجرات البالينومورفية المكتشفة ذات عمر جيولوجي طويل ، إلاّ أنه يصعب تحديد عمرها بدقة.

وتجدر الإشارة بأن عينات النفط التي إستخدمت في هذه الدراسة قد جمعت بعد الفصل (Separators) وهذا يفسر قلة الفتات النباتية والبالينولوجية في هذه العينات. وللحصول على نتائج أشمل وأدق يستوجب دراسة كل من العينات المجمعة قبل الفصل وكذلك الرواسب المتبقية في الفاصل (Separator).

ABSTRACT

Oils produced from wells contain sediments possibly drived from source, reservoir and such other rocks through which the oil migrated during the geologic past. Study of phytoclasts in the particulate content of oils may thus be helpful in relating it to the most probable source rocks. Clasitic fraction and its palynofossil contents in oils of Messlah and Bouri fields were studied. To extract and separate the palynofossils from the crude oils a special laboratory technique has been evolved.

The sediment content in oil is very low and that of the fossil phytoclasts, extremely poor. Only a very few palynofossils were recovered. These include ***Psilatriletes*** *sp.,* ***Cycadopites*** *sp. tetralete pollen grain and possible* ***Retitricolpites*** *sp. The rest of the fossil phytoclasts comprise plant remains, possible palynomorphs and black to dark brown organic matter. The recovered palynofossils are long ranging in age and it is not possible to relate them to any specific age.*

The studied oil samples were collected after the separators and this could explain the overall extremely low yield of phytoclasts and palynofossils. It seems necessary to study oil samples collected before the separators and also, the sediments retained by the separators for more meaningful and conclusive results.

*Petroleum Research Centre, P.O. Box6431, Tripoli, G.S.P.L.A.J.

INTRODUCTION

The onshore Sirte Basin of Libya hosts many oil fields. Some of these produce gas. Fourteen oil fields are classified as giants (Table 1) and each of these have reserves exceeding 500 mill. bbls. (Halbouty *et al.*, 1970 and AGOCO, 1980).

Offshore oil production is from the Bouri Oil Field. Oil is produced from various stratigraphic units ranging in age from Cambro-Ordovician to Oligocene. It is also produced from fractured Precambrian igneous-metamorphic basement.

Geochemical studies by Robertson Research International (1979) and subsequent evaluation of avail-

Table 1. Source and Reservoir Rocks of Oil in Giant Oil Fields, Libya

Oil field	Reservoir rock[1]		Source rock[3]		Rec.
	Lithology	Age	Lithology	Age	Reserves (Mill. Blls)
AMAL	Sandstone	Early Cret. & older	Unnamed Shale	Triassic	
AUGILA-NAFOORA	Carbonate (metam basem)	Eocene Precambrium	Sirte Shale	Campanian Cret	5200[1]
BUATTIFEL	Sandstone	Early Cret.	Variegated shale	Early cret.	1000[1]
DAHRA+HOFRA	Carbonate	Paleocene	Shale	Campanian	700[1]
DEFA	Carbonate	Paleocene	Shale	Campanian	2000[1]
GIALO	Sandstone Carbonate	Oligocene Eocene	**Shale**	Carmpanian	2000[1]
INTESAR 'A'	Carbonate	Paleocene	Shale	Campanian	1500[1]
INTESAR 'D'	Carbonate	Paleocene	Shale	Campanian	1200[1]
MESSLA	Sandstone	Early Cret	Shale	Campanian	1500[2]
RAGHUBA	Carbonate	Late Cret.	Shale	Campanian	1000[1]
	Sandstone	Cambro-Ord.	Shale	Campanian	
SAMAH	Carbonate	Late Cret.	Shale	Campanian	1305[1]
	Sandstone	Cambro-Ord.	Shale	Campanian	
SARIR	Sandstone	Early Cret	Shale	Campanian	8000[1]
			Variegated Shale	Early Cret.	
WAHA	Carbonate	Paleocene	Shale	Campanian	1000[1]
ZELTEN	Carbonate	Paleocene	Shale	Campanian	2280
BOURI	Carbonate	Early Eocene[3]	Shale & Marl	Maastrichtian[4]	?

1. After Halbouty et al., 1970. 2. After AGOCO, 1980.
3. After Robertson Research Int., 1979 & Al-Alami et al., 1989.
4. After I.Y. Meraheel, Petroleum Research Centre,- personal discussion, 1992.

able geochemical data (Hamayouni *et al.*, 1984) indicate that the oil of the Sarir Field (Table 1) was possibly generated by the Early Cretaceous Middle Nubian variegated shales as well as the Campanian Sirte Shale; the oil in the Nubian Sandstone of Buattifel Field was generated by the Early Cretaceous Middle Nubian variegated shales. The Triassic shales (unnamed) might have sourced the oil of the Amal Field. The oils of the giant Augila-Nafoora, Dahra-Hofra, Defa, Gialo, Intesar-A, Intesar-D, Raghuba, Samah, Waha and Zelten fields and the rest of the smaller onshore fields are thought to have been generated by the Campanian Sirte Shale (Al-Alami *et al*, 1989). Oil in the Early Eocene limestone and dolomites of Jedier and Jerami formations of the Bouri Field in the offshore could have been generated by the mostly Maastrichtian shales and marls of Al Jurf Formation (Hammuda *et al.* 1985).

Oils, in general, contain 0.1% or less (by weight) of sediment fraction. These are eliminated as far as possible by separators. Some of these, however, escape the separators and get into the flow line.

The detrital fraction of the oil, which contains fossil phytoclasts, is contributed by sedimentary sequences comprising the source, reservoir and other rocks through which the oil migrated or came in contact during the geologic past. Thus a study of fossil phytoclasts in oil is likely to offer valuable clues on the age and environment of source and reservoir sequences as well as rocks of immigration path. It was with this notion that the present study was undertaken. The results, herein reported, are based on the study of 54 permanent mounts of clastic fraction isolated from six oil samples from the Messlah and Bouri oil fields. It should be emphasised that these samples were collected after the separator. Their clastic content is, hence, very scarce. Consequently, the recovered fossil phytoclasts cannot be expected to yield a conclusively representative assemblage of clastics and fossil phytoclasts.

SEPARATION OF CLASTICS

Nearly 200 cc. of the oil sample, mixed with 100 cc. of carbon tetrachloride (CC14), was heated to about 50°C and centrifuged at 2000 RPM for 15 minutes before filtering through Whatman filter paper no. 54. The retained clastic fraction was extracted for 6–8 hours with a 10:1 mixture of Benzene:Toluene. Final extraction was carried with Hexane for one hour. The extracted clastic fraction was treated with Hydrofluoric Acid (HF), washed and mounted on glass slides. The quantity of the recovered clastic fraction was generally very scarce and it was thought prudent to avoid separation using $ZnBr_2$. In some cases if the material was extremely fine and low in quantity, it was neither treated with HF nor subjected to separation. Permanent mounts were prepared using "Eukitt" a commercial mounting media.

ASSEMBLAGE OF CLASTIC MINERALS IN OIL

1. Messlah Oil

The yield, though poor, is relatively more than that recorded from Bouri Oil. Ore minerals are fairly scarce and include hematite, limonite, possibly magnetite and rarely a few grains of mutually interfering crystal aggregates of pyrite. The non-opaque suite comprises quartz and chlorite and very scarce to rare feldspars, chloritoid and micas. Quartz and micas generally display strain shadows.

2. Bouri Oil

Clastic minerals are very rare. These include few ore minerals and possible some grains of quartz.

ASSEMBLAGE OF PHYTOCLASTS IN OIL

The yield of fossil phytoclasts is fairly low to very low. Black to very dark reddish brown coloured, at times almost opaque, dull, angular to subangular and even irregularly shaped, amorphous to nonstructured, compact organic material is fairly common. Pale-brown, yellowish brown, reddish brown, dark amber and dark to very dark raddish brown and at times almost opaque grains suspected to be resin/resinous matter are observed. Dark brown to black coloured filamentous organic matter is also observed. Pale brown structured organic matter displaying cellular features are noticed. Their specific identification was, however, not possible.

Recovery of identifiable fossil palynomorphs from the oil samples is extremely poor. They were generally not recorded in most of the slides. The following enlists those which could be recognized.

Figure 1. *Psilatriletes* sp, Messlah Field, X1250. Amb is triangular with very slight convex sides, not very clear trilete mark.

Figure 2. Possible palynomorph, Messlah Field, X1250.

Figure 3. *Psilatriletes* sp., Messlah Field, X500. Amb is triangular with convex sides. Commissure is simple. Exine is possible scabrate.

Figure 4. Tetralete pollen grain, Bouri Field, X1250, Scale bar = 6 μm. The diameter is 27 μm. The single cell measures 19.2 μm. Exine is possibly scabrate.

Figure 5. Palynomorph or recent contamination, Bouri Field, X1250.

Figures 6. and 7. Pieces of palynomorphs, Bouri Field, X1250. The sizes are: 9 × 18 μm and 15 × 24 μm respectively, the wall is dark brown.



FIG. 1. *Psilatriletes* sp, Messlah Field, X1250.



FIG. 2. Possible palynomorph Messlah Field, X1250.

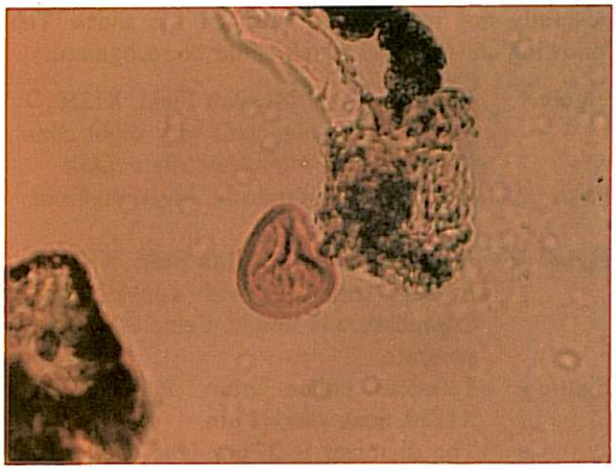


FIG. 3. *Psilatriletes* sp. Messlah Field, X500.

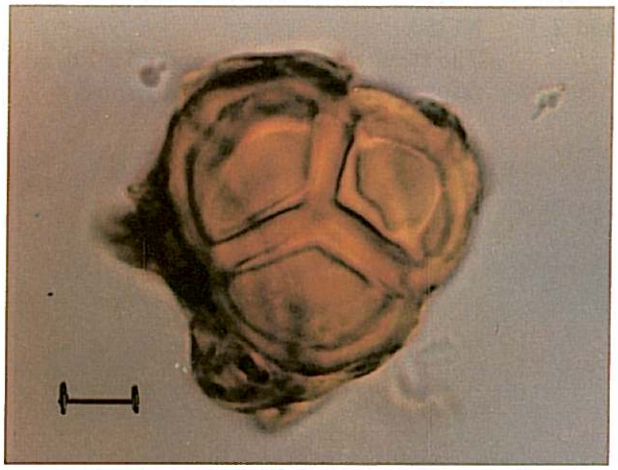


FIG. 4. Tetralete pollen grain, Bouri Field, X1250, Scale bar = 6 μm.

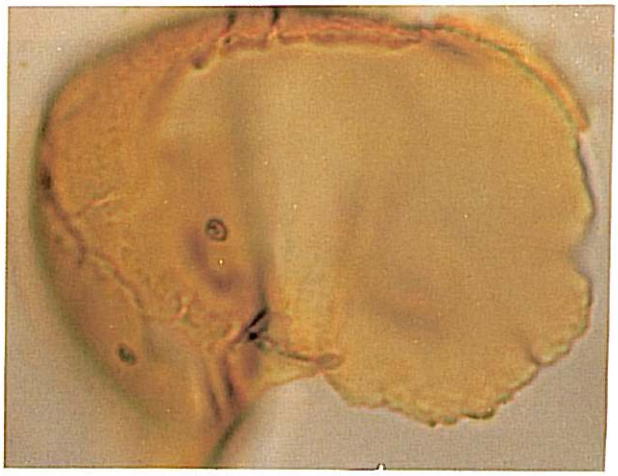


FIG. 5. Palynomorph (or recent contamination), Bouri Field, X1250.

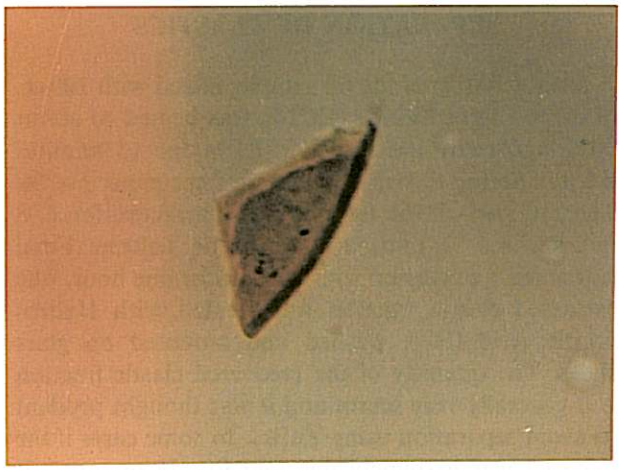


FIG. 6. Piece of palynomorph, Bouri Field, X1250.



FIG. 7. Piece of palynomorph, Bouri Field, X1250.

DISCUSSION

The study establishes presence of fossil phytoclasts and palynofossils in the clastic residues isolated from crude oils of Messlah and Bouri oil fields. The recovered palynofossils could be contributed either by the source or reservoir rocks or by others through which oil has migrated during the geologic past. The recorded phytoclasts are long ranging and non-diagnostic of any specific age. Their colour range to dark brown which pertains to a mature facies. They seem indigenous to the source or reservoirs or others through which the oil migrated or came in contact.

The studied samples were collected after the separators which trap almost all the sediments. This reasons out the low rare yield of the clastics and consequently, the fossil phytoclasts and palynofossils. For a more objective and possible conclusive results, it is necessary to study oil samples obtained before the

separators and also the clastics trapped by the separators since these are likely to yield a better palynofossil assemblage, both qualitatively and quantitatively. It may be more rewarding to study a large number of such samples preferably collected from closely spaced wells producing liquid hydrocarbons from the same reservoir.

CONCLUSIONS

- A laboratory technique to extract palynofossils from the sediment fraction in crude oils has been evolved after extensive experimentation.
- The present study establishes that the clastic fraction in oil contains palynofossils. These could be utilized to inform the age and environment of the more probable source – reservoir rocks of hydrocarbons.

ACKNOWLEDGMENTS

The authors would like to acknowledge Mr. M. Idris, General Manager, P.R.C. Mr. M. Al Bakai and Mr. A.S. Saghier, P.R.C. for their encouragement. To Mr. M.K. Koni, P.R.C. for laboratory facilities. They are grateful to Dr. Iftikhar for providing oil samples from Bouri Oil Field as well as valuable help in evolving the technique of separation of sediments. Dr. N.A. Farooqui was kind to spare some samples from the Messlah Oil Field.

REFERENCES

Al-Alami, M.S. Rahouma, and A.A. Butt, 1989, Hydrocarbon Habitat in the Sirte Basin Northern Libya, Petroleum Research Journal, Vol. I, pp. 17–200.

Arabian Gulf Oil Co., 1980, Geology of a Stratigraphic Giant – The Messlah Oil Field, *in* Salem, M.J. and Busrewil, M.T., Eds. Proc. Second. Symp. Geology of Libya, VII, pp. 521–536.

Halbouty, M.I., Meyerhoff, A.A., King, R.E., Dott, R.H. (Sr.), Klemme, H.D. and Shabad, T., 1970, World's Giant Oil and Gas Field, Geologic Factors Affecting their Formation, and Basin Classification, in Geology of Giant Petroleum Fields.: AAPG Mem. 14, pp. 502–555.

Hammuda, O.S., Sbeta, A.M., Mouzughi, A.J. and Eliagoubi, B.A., 1985, Stratigraphic Nomenclature of the Northwestern Offshore of Libya: Earth Sciences Society of Libya, Tarabulus, Libya, 166 p.

Hamyouni, E.A., Amir, I.A., Riani, M.A. El Ghull, A.B., and Rahouma, S.A., 1984, Source and Habitat of Oil in Libyan Basins, *in* Proc. Seminar on Habitat of Petroleum in the Arab Countries, Kuwait (7–11 Oct., 1984), pp. 127–180.

Robertson Research International, 1979, The petroleum geochemistry of oils and source rocks in the Southeastern Sirte Basin, Libya: V.I & II (unpublished).

PRJ, Vol. 7 (January 1995); P. 101–106, 3 FIGS, 9 TABLES.

POSSIBILITY OF MANUFACTURING LUBE BASE STOCKS FROM BREGA CRUDE OIL

I. Ahmad*, A.A. Tuwil*, M. Buseiffi*, S. Dabah* and A. Balat*

إمكانيـة إنتـاج زيـوت الأسـاس مـن نفـط خـام البريقـة

إفتخار أحمد ، عادل الطويل ، محمد البوسيفي ، سالم الدباح ، وعلي بلاط

تم تقييم إنتاج زيوت الأساس الكامنة في نفط خام البريقة من ناحية النوعية والكمية. فقد تم تحضير المتبقى تحت الضغط الجوي العادي (340+°C) وكذلك تم تقييم هذا المتبقى بهدف إستخدامه في الحصول على زيوت الأساس ذو تصنيفات مختلفة.

وجد أن نسبة المتبقى في نفط خام البريقة بالوزن تحت الضغط الجوي العادي هي 43.00%. كذلك تم تقطير المتبقى إلى عدد تسعة قطفات ذات مدى حراري مختلف وتم تقييم هذه القطفات قبل وبعد عملية نزع الشمع والمواد العطرية وتم أيضاً حساب نسبتها بالوزن في المتبقى من خام البريقة.

ABSTRACT

Lube base stocks production potential of Brega crude oil has been assessed both in terms of quality and quantity. Atmospheric residue (340+°C) of Brega crude oil was prepared and evaluated for manufacturing lube base stocks for different classes. The yield of 340+°C of atmospheric residue was found to be 43.00 wt% on crude oil. The atmospheric residue was further distilled into nine different fractions. The yield and properties of raw cuts, dewaxed cuts and dewaxed and solvent extracted cuts were determined and evaluated for lube base stocks production. Some views on possible utilisation of Brega lube base stocks are also presented.

INTRODUCTION

The finished lubricant contains a base stock, additives to impart certain performance characteristics and may contain a carrier for the additives. Mineral oils have been used as base stock for manufacturing of different types of lubricating oils for a long time and they will probably continue to be used for considerable time to come. The base stock are generally prepared from crude oils. In Libya there is a plant to produce engine oil but the base stock and additives used in this plant to produce engine oils are imported. As a result of this situation an attempt has been made to look into the likely availability of lube base stocks from Libyan crudes both in respect to yield and quality.

This paper presents likely yield potential and available viscosity range of lube base stocks from Brega crude oil. This also presents views on utilisation aspects, based on the current developments in lubricant formulations and application aspects.

* Petroleum Research Centre P.O. Box 6431, Tripoli, G.S.P.L.A.J.

EXPERIMENTAL

Experimental work reported herein was carried out using Brega crude oil sample obtained from the field. Physico-chemical data of Brega crude oil are reported in Table 1. Brega crude oil has API 41.2 and having characterisation factor (Kuop) of 12.10.

Preparation of Atmospheric Residue

The atmospheric residue was prepared by distillation of Brega crude oil through a distillation column, which conforming to ASTM D2892 method, for atmospheric distillation to remove naphtha, kerosene

Table 1. Characteristics of Brega Crude Oil

Test Method	Test Description	Result
ASTM D1298	Specific gravity at 15.6/15.6 °C	0.8194
ASTM D1298	API gravity	41.2
ASTM D1796	Water and sediment content, vol.%	Nil
ASTM 129	Sulphur content, wt.%	0.352
ASTM 97	Pour point ,°C	- 6
ASTM D445	Kinematic viscosity at 37.8 °C, cSt	2.9
IP 143	Asphaltene content, wt.%	0.09
ASTM D189	Conradson carbon residue, wt.%	1.34
ASTM D482	Ash content, wt.%	0.0092
UOP D375	Characterisation factor	12.10
IP 77	Salt content, ppm	23.94
Shell Method	H_2S, ppm	63.92

and gas oil fractions boiling up to 340°C. The left over portion in distillation flask remains as atmospheric residue. The yield of atmospheric residue was found to be 43.00 wt.% on crude oil.

Preparation of Lube Distillate Cuts

The eight distillate cuts ranging from 340 to 550°C and vacuum residue of Brega crude oil were prepared by distillation of atmospheric residue (340+°C) using a batch distillation apparatus made according to ASTM D1160 method. The position of cuts on composite TBP up to 550°C is shown in Fig. 1. The boiling range and yield of these distillate cuts are presented in Table 2. The properties of distillate cuts are given in Table 3.

Deasphalting of Vacuum Residue

The vacuum residue (550+°C) was propane deasphalted using a batch four litre capacity extractor at 60°C. The solvent to oil ratio used was 5:1 by volume. The deasphalted oil (DAO) was separated from the solvent initially in the extractor and subsequently by evaporation with a nitrogen purge at

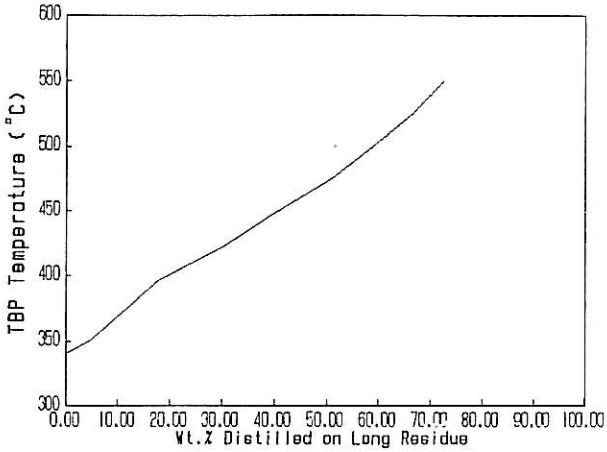


FIG. 1. Composite TBP curve up to 550°C.

Table 2. Yields of Raw and Processed Cuts of Brega Crude Oil

Distillate Cuts Corresponds to Atm. Distillation (ASTM D2892) (°C)	Yield on Atmospheric Residue (wt.%)		
	Raw Cut	Dewaxed Cut	Dewaxed and Solvent Extracted Cut
340 - 351	4.67	3.74	2.25
351 - 396	13.08	10.46	6.38
396 - 422	12.39	9.91	6.10
422 - 450	10.65	8.73	5.95
450 - 475	10.16	8.33	6.09
475 - 500	7.88	6.54	4.71
500 - 525	7.92	6.57	5.09
525 - 550	5.76	4.84	3.48
550+ (Deasphalted Oil)	10.44	8.77	6.58

150°C. The yield of oil and asphalt were found 10.44 and 17.01 wt.% on atm. residue, respectively.

Processing of Distillate Cuts and Deasphalted Oil (DAO)

Distillate cuts and deasphalted oil were processed according to the following steps:

Step 1: Dewaxing (to improve the low temperature properties)
Step 2. Solvent extraction (to improve viscosity index and quality)

Table 3. Properties of Raw Distillate Cuts

Distillate Cuts Correspond to Atm. Residue (°C)	Spec. gravity at 15.6°C	API gravity	Kin. Viscosity at 40 °C		Kin. Viscosity at 100 °C		Pour Point (°C)	Total Sulphur, (wt.%)
			(cSt)	(SUS)	(cSt)	(SUS)		
340 - 351	0.8497	35.0	7.22	49.5	2.26	33.7	12	0.220
351 - 396	0.8568	33.7	9.19	56.1	2.44	34.1	18	0.258
396 - 422	0.8729	30.6	14.3	74.6	2.97	36.1	27	0.290
422 - 450	0.8776	29.7	29.9	141	4.75	41.9	39	0.327
450 - 475	0.8973	26.2	-	-	6.10	46.1	42	0.368
475 - 500	0.9056	24.8	-	-	8.10	52.7	45	0.442
500 - 525	0.9117	23.7	-	-	11.1	63.1	48	0.481
525 - 550	0.9139	23.3	-	-	13.9	73.8	51	0.584
550+(Deasphalted Oil)	0.9219	21.9	-	-	46.7	218	63	1.600

The above sequence may be altered during the process design.

Dewaxing

The mixture of methyl ethyl ketone (MEK) and toluene in the ratio of 70:30 percent by volume was used for dewaxing of all distillate cuts. Dewaxing temperature was 12 ± 2°C and the ratio of the solvent to feed was maintained as 3:1 by volume. The chilled solvent was mixed with the preheated feed and cooled to – 12°C with agitation. The mixture was allowed to stand for about 2 hours and then filtered using No. 4 sintered glass filter. The wax cake was washed three times with the solvent and the extract was stripped out of the solvent in a rotary vacuum separator. The wax cake was stripped out from the filter and weighed to determine the yield of the slack wax. The yields of oils after dewaxing and their properties are given in Tables 2 and 4, respectively.

Solvent Extraction

The majority of lubricating oil refining technologies use furfural, phenol and N-methyl-pyrrolidone (NMP) as a solvent. It is generally known that the

Table 4. Properties of Dewaxed Distillate Cuts

Distillate Cuts Correspond to Atm. Residue (°C)	Spec. gravity at 15.6°C	API gravity	Kin. Viscosity at 40 °C		Kin. Viscosity at 100 °C		Viscosity Index	Pour Point (°C)	Total Sulphur, (wt.%)
			(cSt)	(SUS)	(cSt)	(SUS)			
340 - 351	0.8631	32.4	7.99	52.1	2.19	33.5	65	- 6	0.42
351 - 396	0.8717	30.8	10.5	60.5	2.65	35.0	65	- 6	0.47
396 - 422	0.8824	28.7	15.8	80.3	3.29	37.1	58	- 9	0.49
422 - 450	0.8932	26.9	27.5	130	4.69	41.7	80	- 9	0.51
450 - 475	0.8994	25.8	48.3	225	6.32	46.9	70	- 6	0.56
475 - 500	0.9049	24.9	75.8	352	8.73	54.9	84	- 6	0.58
500 - 525	0.9153	23.1	186	859	14.2	74.8	64	- 6	0.72
525 - 550	0.9244	21.6	288	1332	17.7	88.9	54	- 6	0.77
550+(Deasphalted Oil)	0.9353	19.8	358	1658	65.7	306	75	0	0.45

thermal stability of furfural is low, while phenol has undesirable safety and health aspects. NMP is considered more advantageous, for it is nontoxic, its physical and chemical characteristics are more favourable, and it dissolves the aromatics more selectively than either phenol or furfural. The main characteristics [1] of the most widely used solvents: phenol, furfural and NMP are summarised in Table 5.

Table 5. Characteristics of Refining Solvents

Property	Furfural	Phenol	NMP
Molecular weight	96.1	94.1	99.1
Density at 25 °C, kg/l	1.159	1.132	1.027
Boiling point, °C	161.7	181	202
Freezing point, °C	-38.7	40.9	24.4
Flash point, °C (M) (PM)	60 -	- 75	95 -
Heat of evaporation, kJ/kg	450.6	485.3	532.6
Solution characteristics	good	very good	excellent
Selectivity	good	good	very good
Stability	good	very good	excellent
Corrosivity	low	medium	low
Toxicity	mildly	very toxic	nontoxic
Biodegradability	good	good	good
Solubility in water	partial	partial	complete
Azeotrop formation (with water)	yes	yes	no

Keeping all those points into consideration dry NMP was selected as solvent for extraction to improve viscosity index and quality of the base oils. The conditions used for solvent extraction are shown in Table 6. The dewaxed oil (50 ml) and an appropriate amount of NMP solvent were mixed and agitated at 58 ± 1°C for 20 minutes. The mixture was allowed to stand for 30 minutes to settle down. The upper layer (raffinate) containing the product was separated and stripped using initially a rotary vacuum evaporator and subsequently using a stream stripper. GLC analysis of the oil was performed which indicated that the solvent content has been reduced to traces in the base oil. The yield and properties of the oil after solvent extraction are tabulated in Tables 2 and 7, respectively.

Table 6. Conditions Used for Solvent Extraction of Dewaxed Oil

Solvent oil ratio	2 : 1
Temperature, °C	55 - 58
Number of stages	1
Extraction time, min.	20
Settling time, min.	30

Table 7. Properties of Processed (Dewaxed and Solvent Extracted) Distillate Cuts

Distillate Cuts Correspond to Atm. Residue (oC)	Spec. gravity at 15.6°C	API gravity	Kin. Viscosity at 40 °C		Kin. Viscosity at 100 °C		Viscosity Index	Pour Point (°C)	Flash Point, (°C)	Total Sulphur, (wt.%)	Conradson Carbon Residue, (wt.%)
			(cSt)	(SUS)	(cSt)	(SUS)					
340 - 351	0.8434	36.3	7.60	5.07	2.25	33.7	104	- 6	152	0.088	0.0001
351 - 396	0.8528	34.4	10.1	59.2	2.66	35.1	97	- 6	170	0.107	0.0001
396 - 422	0.8618	32.8	15.1	77.6	3.43	37.6	101	- 9	192	0.200	0.0016
422 - 450	0.8695	31.2	25.7	122	4.70	41.7	99	- 9	210	0.247	0.0054
450 - 475	0.8813	29.1	44.4	207	6.56	47.7	98	- 6	226	0.251	0.0123
475 - 500	0.8901	27.5	77.3	358	9.31	56.8	95	- 6	244	0.257	0.0130
500 - 525	0.8923	27.1	109	507	11.6	64.8	93	- 6	270	0.280	0.0155
525 - 550	0.8991	25.9	170	788	15.7	80.7	94	- 6	302	0.291	0.0176

DISCUSSION

The atmospheric residue (340+°C) of Brega crude oil was distilled using a batch distillation apparatus made according to ASTM D1160 method. The eight distillate cuts ranging from 340 to 550°C were prepared and vacuum residue as also collected. The vacuum residue (550+°C) was then propane deasphalted and the oil was separated. It was found to be 10.44 wt.% on atmospheric residue. This oil and eight distillate fractions were subjected to dewaxing and solvent extraction. The plot of cumulative yield of raw, dewaxed and solvent extracted of distillate fractions versus TBP temperature is shown in Fig. 2. The properties of oils obtained after treatment are given in Table 7. The plot of mid wt.% of yield versus kinematic viscosity at 40°C of processed oils is shown in Fig. 3. The yields of different grades of base stocks have been calculated and the cut range corresponds to these yields were calculated and presented in Table 8.

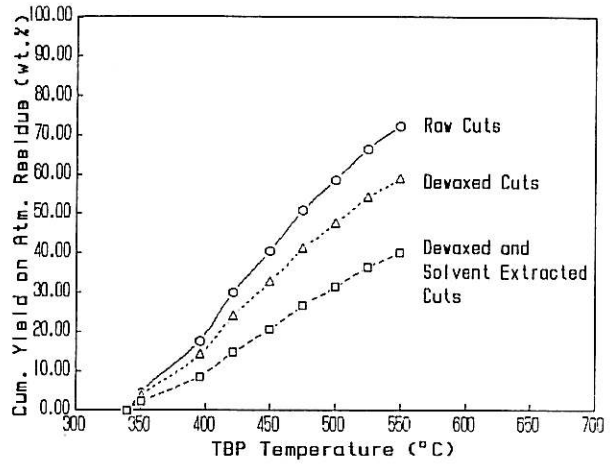


FIG. 2. Yield versus TBP temperature of raw, dewaxed and solvent extracted cuts.

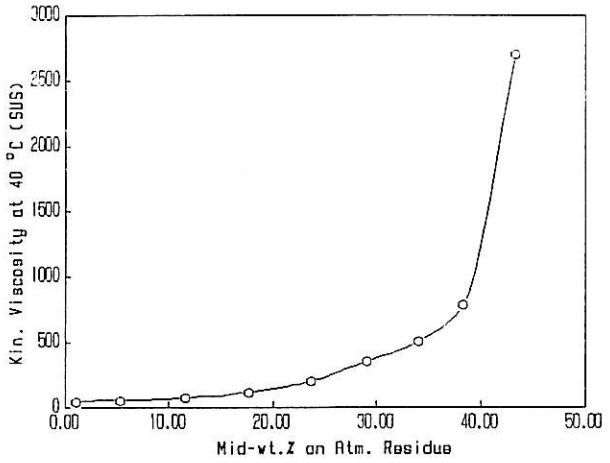


FIG. 3. Kinematic viscosity versus mid wt.% of yield.

Table 8. Distillation Range and Yield of Different Class of Base Oils

Base Oil	Distillation Range (°C)	Yield on Atm. Residue (wt.%)	Yield on Crude oil (wt.%)
Base stock for light lubricants	340 - 430	16.41	7.06
N 150	430 - 456	5.88	2.53
N 250	456 - 478	5.39	2.32
N 500	478 - 550	11.96	5.14
Bright Stock	550^{+} (Deasphalted oil)	6.45	2.77

All distillate fractions after processing (dewaxing and solvent extraction) had viscosity index between 93 to 104, and pour point −6 to −9°C. The deasphalted oil obtained from vacuum residue after dewaxing and solvent extraction had pour point −3°C. The material balance of the processes showing the yields of lube base stocks, wax content, aromatic content and asphalt content is given in Table 9. The yield of base stock to produce light viscosity range lubricants was found to be 16.41 wt.% on atm. residue (7.06 wt.% on crude oil). Recent reports in the literature [2] indicate that base oils of lower viscosity are required by the automotive sector to meet the need of fuel efficient multigrade oils. However, the volatility of such base oils needs to be carefully controlled to avoid excessive oil consumption. Reports further indicate that friction modifiers have been found to respond best in low viscosity oils.

Table 9. Material Balance of the Process

Product	Yield on 340^{+}°C (wt.%)	Yield on Crude (wt.%)
Base oil for light viscosity lubricants	16.41	7.06
N 150	5.88	2.53
N 250	5.39	2.32
N 500	11.96	5.14
Bright Stock	6.45	2.77
Wax content	15.06	6.48
Aromatic Extract	21.24	9.13
Asphalt	17.01	7.31

The above trends make the situation favourable towards the use of lube base stocks from Brega crude oil, major potential of which is in lower viscosity range. The volatility characteristics of these base oils can be improved by careful control of vacuum unit operation so that oils produced have less low boiling material.

Although it is difficult to make any firm statement on the application aspect of formulated lubricants from Brega lube base stocks in the absence of any performance data, however, it is possible to state that it appears possible to formulate multigrade motor oil like, 20W50, 20W40, 15W40, and alike with low volatility improved oil consumption characteristics, wear protection and deposit control in combination with the following:

(a) By the use of modern additive package of enhanced viscosity increasing power.
(b) By the use of synthetic esters and polyalphaolefins as components in the base oil blend.

CONCLUSIONS

Evaluation results obtained indicate that Brega crude oil is suitable for manufacturing of different grades of lube base stocks. A substantially large amount (16.41 wt.% on atmospheric residue; 7.06 wt.% on crude oil) of the Brega lube base stocks production potential lies in the light viscosity range. Such type of base oils according to the recent trends can be used in the fuel efficient multigrade motor oil formulations along with the proper additive package and synthetic lubricants.

ACKNOWLEDGEMENT

The authors are thankful to the staff of the Industrial Processing Department for preparation of lube cuts and determining their properties. The authors are also thankful to PRC management for providing facilities and encouragement.

REFERENCES

[1] Gardos, G., Kovacs, M., Szabo, T.K., Denes, F. and Miko, F., 1982, Investigation on energy conserving lubricating oil producing processes, Hung. J. Ind. Chem., vol. 10, pp. 257–266.

[2] Singh, H., Gupta, P.C., Anwar, M., Chaudhry, G.S., Kishore, K., Kaushik, R.S., Kumar, M.M., and Lal, M., 1985, Possibility of manufacturing lube base stocks from BH crude, Pet. Asia J., Vol. 7, pp. 150–157.

PRJ, Vol. 7 (January 1995); P. 107–109, 4 FIGS, 2 TABLES.

Short Note

OXYGEN CAUSES CORROSION FAILURE OF HEAT EXCHANGER

M.L. Mehta*, T.S. El-Mendelssi,** and A.M. El-Houde**

ظاهـــرة إخفـاق أنبـــوب مبـادل حـــراري

م. مهتا، التومي ساسي المندلسي، وعبد الرزاق محمد الهود

تم إجراء فحوصات مجهرية ودراسات ميثالوروجية وبعض التحاليل الكيميائية لنوع المعدن ونواتج التآكل لتحديد سبب ونوع التآكل لأحد أنابيب المبادلات الحرارية المصنوعة من الفولاذ الكربوني، هذا وأظهرت النتائج أن سبب التآكل هو وجود عنصر الأكسجين الموجود في الماء المستخدم في عمليات التبريد.

INTRODUCTION

Tubes of a shell and tube heat exchanger failed after one month of operation due to underscale oxygen attack despite chemical inhibition. Investigation revealed that localized oxygen attack caused severe operational problems associated with the exchanger unit frequent failure. Micro and macroscopic analysis of the problems are presented.

PROCESS DESCRIPTION

The heat exchanger is used to heat raw water pumped from a storage tank on the shell side. Hot crude oil as the heating medium is circulated through the tube side. The raw water is treated upstream of the pumps with corrosion, scale inhibitors as well as oxygen scavenger, (Fig. 1) is a schematic representation of the process.

The heat exchanger shell and tubes are made of cold brown seamless low carbon steel pipes as per ASTM A 179 [1–2]. The tubes are 19 mm in outside diameter with a wall thickness of 2.7 mm. The operational data of the exchanger are presented in Table 1. Table 2 gives the water chemical analysis.

FAILURE CASE

As received tube sample showed pitting to varying depth on its external surface. Fragile scale, black at some places and brown at others, is evident.

Cluster of pits were visible in some places, and their growth had led to coalescene resulting in a wider pits causing leaks. Macroscopic examination of transverse section through a pit revealed a hemispherical morphology. The internal tube side exposed to the heating oil did not show any corrosion attack.

Deep pits were found underneath the scale layer and filled with black scale indicative of bacterial growth. The top layer of the scale was brownish and soluble in HC1 acid confirming the formation of iron oxides.

Upon Microscopic examination it was clear that the grain structure in the tube steel had suffered elongation due to plastic deformation. Such deformation could be attributed to either the manufacturing process of the tubes, or to the localized internal stresses due to the volume expansion when the pits

*Previously with the Petroleum Research Centre, Tripoli, G.S.P.L.A.J.
**Petroleum Research Centre, P.O. Box 6431, Tripoli, G.S.P.L.A.J.

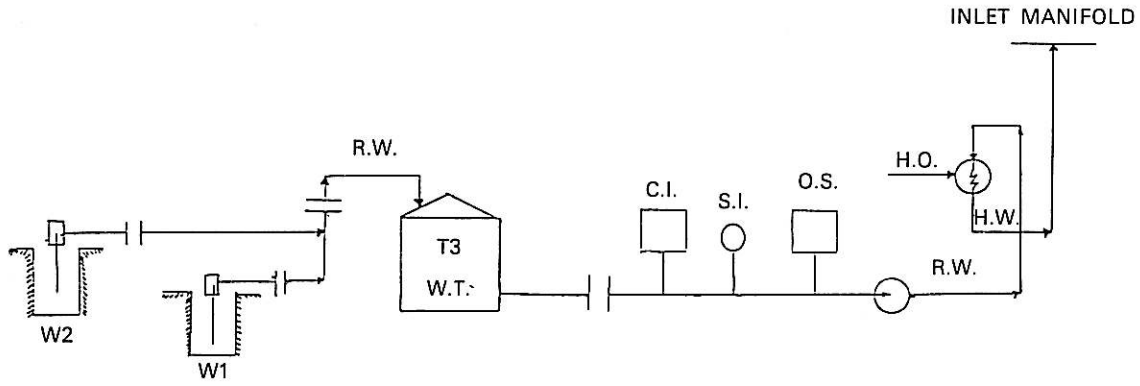


FIG. 1. Schematic exchanger flow diagram.

Table 1. Heat Exchanger Operational Data

Water side t emp. (inlet)	15 C°
Water side temp. (outlte)	60 C°
Hot oil side temp. (inlet)	120 C°
Hot oil side temp. (outlet)	110 C°
Discharge rate water pump	24 M^3/h
Tube outside diameter	19 mm
Tube thickness	2.7 mm

Table 2. Raw Water Analysis

PH			7.51
Conductivity		(US)	5210
Salinity	(Nacl)	mg/1	2326
Total hardnees		F.C.	116
Chlorid	(CL)	mg/1	1411
Sodium	(Na)	=	710
Calcium	(Ca)	=	241
Magnesium	(Mg)	=	136
Sulphte	(S04)	=	600
Hydroxide	(OH)	=	NIL
Carbonate	(C03)	=	12
Bicarbonate	(HC03)	=	122
Iron (Total)	(Fe)	=	0.15
Oxygen	(02)	=	1.0
Hydrogen sulphide	(H2S)	=	NIL
Total suspended solid		=	5.19
Total dissolved solid		=	3232

were filled with the corrosion products. (Fig. 2 shows pitting corrosion of tube section). Highly elongated grain structure is representative of high degree of deformation, as is the case shown in (Fig. 3a and Fig. 3b).

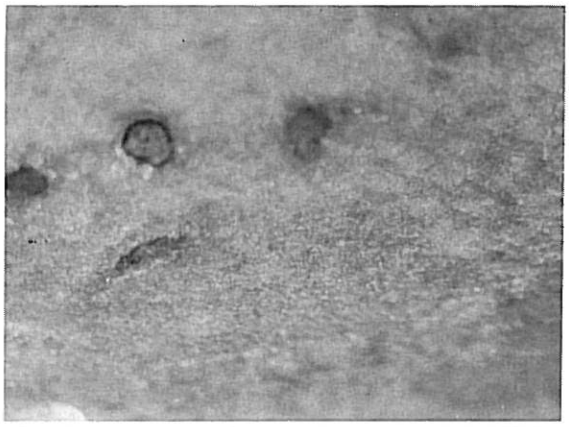
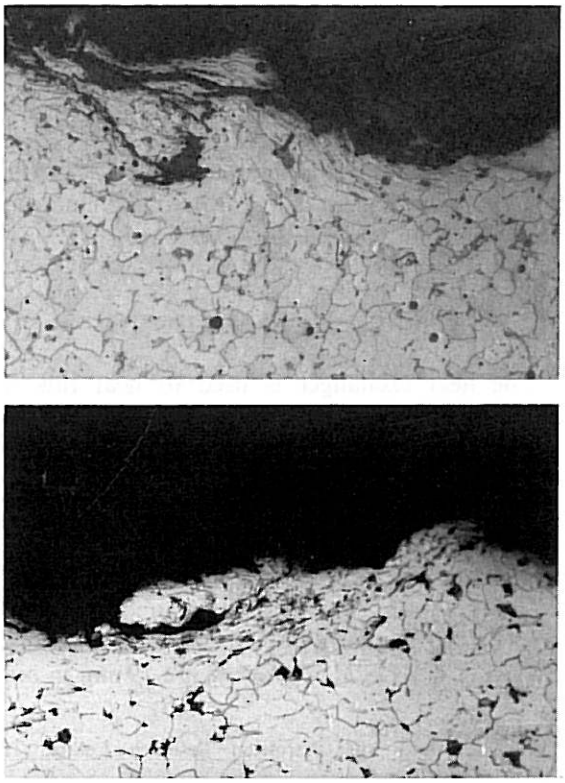


FIG. 2. Pitting corrosion of tube section.



(a)

(b)

FIG. 3a,b. Deformed grain structure of tube section.

CONCLUDING REMARKS

Underscale oxygen attack of the external tube surface was mainly of the pitting type. The scale chemistry and the presence of soluble oxygen in the water confirm the oxygen attack. The severity of the attack is promoted with the setup of the oxygen concentration cells on the scale layer. The presence of layered scale has also activated sulfide reducing bacteria growth. The chemical treatment of the raw water is definitely ineffective and it is recommended that the oxygen ingress be eliminated at the source of entry prior to any inhibition program.

ACKNOWLEDGEMENT

The authors would like to thank the Petroleum Research Centre management for support and encouragement.

REFERENCES

[1] N.P. Cheremisinoff, 1984, Heat Transfer Pocket, Handbook, p. 119–121.

[2] ASTM, Part 1, 1979, Steel Piping, Tubing, fitting, p. 33–81.

PRJ, Vol. 7 (January 1995); P. 111–113, 1 FIG, 3 TABLES.

Short Note

LEAD LEVELS IN SURFACE LAYERS OF NEARSHORE SEDIMENTS OF THE WESTERN COAST OF LIBYA

A.K. El Hinsheiry*, N.S. Kumar*, S.A. El Jawashi* and I. Ahmad*

مستويات تركيز الرصاص في تراكمات الطبقات العليا من الساحل الغربي للجماهيرية

عبد الله خليفة الهنشيري ، ن. س. كومار، سالم عبد الله الجواشي و إفتخار أحمد

تم قياس تركيز نسبة الرصاص في التراكمات الرملية القريبة من السواحل الغربية للجماهيرية في المنطقة بين الزاوية وتاجوراء وذلك باستعمال طريقة طيف الإمتصاص الذري. تراوح التركيز بين 0.2 إلى 57.0 مايكروجرام/جرام على أساس الوزن الجاف وتراوح المعدل بين 2.0 إلى 24.2 مايكروجرام/جرام على نفس الأساس.

كما أجريت معاملة إحصائية للنتائج وتم مقارنتها مع نتائج منشورة لأماكن أخرى على سواحل البحر الأبيض المتوسط.

INTRODUCTION

Lead levels in nearshore sediments of the western coast of Libya (i.e. Az-Zawiya to Tajoura) have been determined by atomic absorption spectrophotometry. The observed values range from 0.2 to 57.0 μg^{-1} dry weight. The mean values at different locations were found to range from 2.0 to 24.2 μg^{-1} dry weight. The frequency distribution has been determined. The data were also compared with those reported in the literature for other places in the Mediterranean coast. This work presents the analysis of lead in sediments of the coastal area of the western part of Libya i.e. from Az-Zawiya to Tajoura including the capital city, Tripoli. A number of industrial plants discharge their effluents after some degree of treatment. The coastal area also receives waste-water from domestic sewage and agricultural runoff. There is a main road parallel to the sea coast on which a large number of vehicles use for transportation. These vehicles use leaded gasoline. During the raining season the runoff water of this road also goes to the sea. Such discharges usually contain potentially harmful substances including lead which can be sorbed by particulate matter and assimilated by organisms, eventually reaching the sediments.

* Petroleum Research Centre, P.O. Box 6431, Tripoli, G.S.P.L.A.J.

EXPERIMENTAL

Sediment samples were collected from sixteen locations. Sampling sites are given in Table 1. The collected samples were airdried for 24 hours, grounded and passed through 80 mesh sieve. Standard procedure, described in ASTM D4698 was followed for the total digestion of sediment samples for chemical analysis of various metals.

A 0.5 g of finely grounded sample of sediments was taken into a 100 mL TFE-fluorocarbon beaker, 6 mL HNO_3 (sp. gr. 1.41) was added and placed on a hot plate for approximately 30 min. The hot plate was previously adjusted to produce a surface temperature of 200°C. The beaker was removed from the hot plate and waited for 5 min. A portion of 6 mL of HF (sp. gr. 1.19) and 2 mL of $HClO_4$ (sp. gr. 1.67) were added to the beaker and returned to the hot plate. The

Table 1. Locations of Sediment Sampling

Site No.	*Location*	*No. of Samples*
1	Janzour area, near Pipe Factory	10
2	Janzour area, near Textile and Soap Factory	10
3	Janzour area, near Fish Canning	10
4	Girgarish area, Beach no. 1	10
5	Girgarish area, near Muntada ElAkhdar	10
6	Tripoli City, before harbour, near Datul Imad building	10
7	Tripoli City, after harbour, near hotel Shatul Naqil	10
8	Tajoura area, near Marine Research Centre	10
9	Tajoura area, after Tourist City	10
10	3 km from refinery towards West (Sabrata)	8
11	5 km from refinery towards West (Sabrata)	
12	Az-Zawiya Refinery, near harbour	9
13	Az-Zawiya Refinery	9
14	2 km from Az-Zawiya Refinery towards east (Tripoli)	9
15	Jodayem (Scout Hall)	9
16	Almaya	9

beaker was heated until the evolution of white perchloric fumes and the solution had reached incipient dryness. The beaker was then removed from the hot plate and waited for 5 min. 2 mL of $HClO_4$ (sp. gr. 1.67) was added and the beaker was returned again to the hot plate. Heating was continued until the solution had reached incipient dryness. The beaker was removed from the hot plate, and temperature was lowered to 100°C. 2 mL of HCl (50 vol.%) was added, followed by 10 mL water. The solution was put on the hot plate and the residue was dissolved completely. The solution was, then, transferred to a 50 mL volumetric flask and filled by adding distilled water. This solution represents concentration of 10 g of sample per litre of solution.

The above solution was analysed for lead content by using flame ionisation atomic absorption spectrophotometer (AAS). Atomic Absorption Spectrophotometer (Varian AA 1475) was used throughout this study. Varian high intensity hollow cathode lamp was used for lead. The operating conditions used were as recommended by the manual of the instrument.

RESULTS AND DISCUSSION

Sixteen sites were selected for the determination of lead content in surface sediments of the western Libyan coast. For each location ten samples were collected unless otherwise reported in Table 1. Each sample was prepared for analysis according to the procedure described in ASTM D4698. The range of lead contents of ten replicates from each of the sixteen locations are given in Table 2. The minimum and maximum observed lead content in sediments were found to be 0.2 and 57.0 μg^{-1} dry weight, respectively. The mean concentration of lead of ten replicates from each location is given as a range ($X \pm S.D.$) in Table 2. The highest mean concentration of lead (24.2 μg^{-1} dry weight) is found at location 6 which is near Datul-imad building in Tripoli city. This is the location where domestic sewage is discharged to sea after treatment. The location is also near the coastal road of the city. Other higher concentration of lead (15.3 μg^{-1} dry weight) was observed at location 7 which is near the city harbour. This location is also close to the coastal road of Tripoli city. These observations indicate that the major source of lead may be attributed to combustion of leaded gasoline. It should be noticed, however, that the mean value of lead content found in the western Libyan coastal sediments is below the reported values (Table 3) of

Table 2. Concentration (µg/g dry weight) of Lead in Sediments of Western Coast of Libya

Site No.	*Concentration (µg g^{-1} dry weight) (Min. – Max.)*	*Average concentration ($\bar{X} \pm S.D.$)*
1	0.8–5.1	2.0±1.3
2	0.4–5.0	2.6±1.3
3	2.6–20.4	8.1±5.8
4	2.0–7.6	4.3±2.4
5	2.4–21.1	10.3±4.8
6	17.2–57.0	24.2±12.3
7	0.8–42.8	15.3±12.3
8	1.5–4.0	2.6±0.8
9	1.3–3.2	2.5±0.6
10	1.9–7.4	3.8±1.7
11	1.8–4.3	3.2±0.8
12	2.6–8.2	5.0±1.9
13	1.6–4.4	3.0±0.9
14	2.5–20.3	7.5±5.2
15	1.3–2.9	2.0±0.7
16	0.2–3.3	2.0±1.0

Table 3. Concentrations (µg/g dry wet) of Lead in Surface Layers of Nearshore Sediments in Different Locations of the Mediterranean Sea

Location	*Value*	*Reference*
Mediterranean	4.5–280	UNEP, 1986
Adriatic	5.3–96	Donazzdo et al., 1984
Ligurian Sea	36–180	Cosma et al., 1982
Sicily	4.5–17	Castagna et al., 1982
	7.5–20	Castagna et al., 1987
Spain	4.8–550	Modamio, 1986
Thermaicos, Greece	18–246	Voutsinou-Taliadouri & Satsmadjis, 1983

nearshore sediment of different locations in the Mediterranean sea. The frequency distribution of lead content in nearshore sediments is given in Fig. 1.

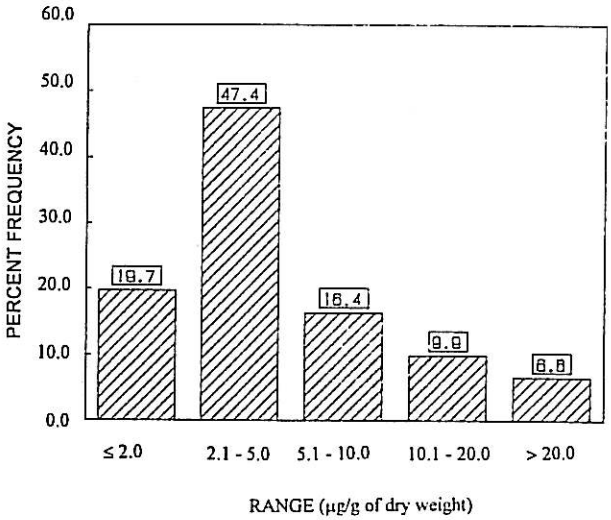


FIG. 1. Frequency distribution of lead in coastal sediments of the western coast of Libya.

CONCLUSIONS

Lead levels in nearshore sediments of the western coast of Libya (i.e. Az-Zawiya to Tajoura) have been determined by using atomic absorption spectrophotometric technique. The observed values range from 0.2 to 57.0 μg^{-1} dry weight.

The sediment samples were collected from sixteen locations and analysed for lead content. The mean values at different locations were found to range from 2.0 to 24.2 μg^{-1} dry weight. These values are below the reported values of nearshore sediments of different locations in the Mediterranean sea.

ACKNOWLEDGEMENT

The authors are grateful to PRC management for providing facilities, encouragement and permission to publish this work.

REFERENCES

Castagna, A., Sinatra, F., Zanini, A., De Sanctis, N. and Giardinelli, S., 1987, Surface sediments and heavy metals from the Sicily Channel Coast, Mar. Poll. Bull., v.18, p. 136–140.

Castagna, A., Sinatra, F. and Console, E., 1982, Heavy metal distribution in sediments from the Gulf of Catania (Italy), Mar. Poll. Bull., v.13, p. 432–434.

Cosma, B., Frache, R., Baffi, F. and Dadone, D., 1982, Trace metals in sediments from the Ligurian coast, Italy, Marine Poll. Bull., v.13, p. 127–132.

Donazzolo, R., Merlino, H., Menegazzo, V.L. and Pavoni, B., 1984, Heavy metal content and lithological properties of recent sediments in the Northern Adriatic. Mar. Poll. Bull., v.15, p. 93–101.

UNEP, 1986, Coordinated Mediterranean Pollution Monitoring and Research Programme (MED POL – Phase I), Final report 1975–1980. Map. Tech. Rep. Ser., No. 9, UNEP, Athens.

Voutsinou-Taliadouri, F. and Satsmadjis, J., 1983. Metals in polluted sediments from the Thermaikos Gulf, Greece, Mar. Poll. Bull., v.14, p. 234–236.